Contribution to Aerothermal Study of a Film Cooling Geometric Design using ZnO Phosphorescence Thermography and Numerical Simulations

Arunprasath Subramanian

THÈSE

Pour l'obtention du grade de

DOCTEUR DE L'ÉCOLE NATIONALE SUPÉRIEURE DE MÉCANIQUE ET D'AÉROTECHNIQUE

(Diplôme National - Arrêté du 25 Mai 2016)

École Doctorale : Sciences et Ingénierie en Matériaux, Mécanique, Energétique

Secteur de Recherche : TRANSFERTS THERMIQUES

Présentée par

Arunprasath SUBRAMANIAN

Contribution to aerothermal study of a film cooling geometric design using ZnO phosphorescence thermography and numerical simulations

Thesis director : **Mme. Eva DORIGNAC**
Co-Supervisor : **M. Gildas LALIZEL**

Planned date of defence 25 April 2022

JURY

Antonio ANDREINI	Assoc. Prof., University of Florence, Italy	Reviewer
Beatrice PATTE-ROULAND	Professor, Université de Rouen,Rouen	Reviewer
Benjamin REMY	Professor, Université de Lorraine, Nancy	Examinator
Laurent DAVID	Professor, Université de Poitiers,Poitiers	Examinator
Eva DORIGNAC	Professor, Institut P', Poitiers	
Gildas LALIZEL	Asst. professor, Institut P', Poitiers	
Patrick BERTERRETCHE	Research engineer, Institut P', Poitiers	Guest
Charlie KOUPPER	Research engineer, Safran Helicopter Engines, Bordes	Guest

Dedicated to my family, whose constant support I cherish

Acknowledgements

The last three years have been a roller coaster journey but I have enjoyed this ride completely despite all struggles due to a lot of people who have helped me all along the way.

The first and foremost (million) thanks goes to my supervisors Dr. Eva Dorignac and Dr. Gildas Lalizel who have always been available for me when I needed their support. I can never forget Eva's kindness and support all along, many times going out of the way to help me in ways I am always grateful for. I found a friend and a pillar to lean on in Gildas, an exceptional human with incredible patience. Gildas' love for science and his way to explain difficult things in the simplest ways inspire me. I would like to profoundly thank my teachers without whom it would have been impossible to finish this thesis on time considering the pandemic that has had a profound effect on our lives.

An important person for my thesis to happen in the first place is Patrick Berterretche, a nice human with a huge heart. I would like to thank him for all the scientific help, financial support and all the push he has given to propel this project. I will cherish the conversations, lunches and talks in between little work!

I also take this opportunity to thank the Jury for being present for my thesis defence. Many thanks to Dr.Antonio Andreini and Dr. Beatrice-Patte Rouland for accepting to review the thesis and provide technical comments. I am grateful to the jury members Dr. Benjamin Remy, Dr. Laurent David, Mr. Charlie Koupper for their presence and valuable inputs.

Many thanks to friends and colleagues at PROMETEE lab...Redouane Kari, Romain Bouju, Damien Esseyric, Romain Pelligrino, Thomas, Patrick Laurent, Nicolas for helping me with some difficult experiments and friendly chats!

A big thank you to Dr. Lorenzo Mazzei, a friend and guide in many ways for all the useful technical suggestions related to numerical simulations and moral (memes) support over the course of this thesis. I would also like to say thanks to a friend for life Dr.Tommaso Lenzi who also helped me in experiments related to ZnO calibration. I also thank Dr. Christopher Abram for all the valuable inputs.

Special thanks to Alain Claverie the laser man of ENSMA. I am always grateful for all the precise suggestions related to measurement techniques, the numerous material I got and more importantly, warm smiles and jokes! Thank you to Hervé Arlaud, Catherine Fuentes, Yann Thomas for the support related to ZnO experiments.

Huge thanks to two partners in crime... Aurelien (Darling) and Viiincent for the mutual support at work and laughter all these years. Of course, thanks to crazy Tamaraaaa and our beautiful friendship there was never really a tough time. Many many thanks to my superb friends Gabi (good bowling bro), Nam, Clement, Raji, Alex, Armando, Yann, Di bao (Panna cotta?), Prasad, Flavio for a very nice company. The pain of writing was cured due to Yassine, a true friend who gave me nice company and support. I am blessed to meet such nice people.

Away from work, there are very many people who indirectly helped me with the thesis in many ways. I would really like to thank Jenn, who helped me during frustrating times with uncountable study sessions, affectionate company and motivation. I am proud of who you are! All the apéros with family away from family David, Cedric, Marie-Noelle, Yves and Yvette helped me immensely to finish this manuscript smoothly. I would also like to thank all my friends and well-wishers for attending the presentation of this thesis and I cherish all the support I received! Thank you in a big way!

Last but the best I want to thank my Amma, Appa, Gokul, Keerti, and my family for ever being with me and helping me in every possible way to do this thesis. Nothing else matters other

than the happiness of my family, and I very well know that during the period of this thesis, I have drained the energy of my family. No one can ask for a better support system than what I received and the diplomas I have today are due to the sacrif ces of my parents. I would like to thank all people I may have missed here who helped me in this journey. Alone, I could have gone fast, But together I could go far! Thank you once again!

Arun

Le Projet S3A PROMETEE (convention n° P-2020-BAFE-91) est cofinancé par l'Union européenne avec le Fonds Européen de Développement Régional (FEDER)

Contents

1 Introduction to film cooling **1**
1.1 Need for film cooling . . . 2
1.2 Basic understanding of film cooling . . . 3
1.3 Objectives and scheme of the thesis . . . 4

2 Literature review of Jet In Cross-Flow system **7**
2.1 Jet In Cross-Flow . . . 8
2.1.1 JICF parameters and flow classification . . . 8
2.1.2 Vortex systems in a JICF . . . 10
2.2 Factors affecting film cooling performance . . . 13
2.2.1 Blowing ratio . . . 14
2.2.2 Mainstream turbulence . . . 14
2.2.3 Injection angle . . . 15
2.2.4 Hole shape . . . 15
2.3 Anti-vortex film cooling configurations . . . 15

3 Auxiliary holes position optimisation: RANS study **19**
3.1 Introduction . . . 20
3.2 Numerical setup . . . 22
3.2.1 Geometry . . . 22
3.2.2 Solver and Boundary conditions . . . 22
3.2.3 Mesh Validation . . . 23
3.3 Results . . . 25
3.3.1 Adiabatic Film Cooling Effectiveness . . . 25
3.4 Heat transfer characteristics . . . 26
3.4.1 Adiabatic film cooling effectiveness . . . 26
3.4.2 Heat transfer . . . 28
3.5 Analysis of flow aerodynamics . . . 33
3.5.1 Vortex intensity . . . 33
3.5.2 Streamlines analysis . . . 35
3.5.3 Boundary layer characteristics . . . 35
3.6 Review . . . 37

4 Novel thermometry technique: Phosphor thermometry **39**
4.1 Need for Phosphor thermometry . . . 40
4.2 Phosphors - working principles . . . 41
4.2.1 Basic overview and definitions . . . 41
4.2.2 Working mechanism . . . 42
4.2.3 Factors affecting precision in phosphor thermometry . . . 43
4.2.4 Phosphor thermometry techniques . . . 45
4.2.5 Phosphor types . . . 48
4.3 ZnO properties . . . 49
4.3.1 Liquid phase . . . 49
4.3.2 Gas phase . . . 50

4.4 Experimental setup . . . 51
4.5 Study of ZnO phosphor properties . . . 52
4.6 Spectral properties of ZnO . . . 53
4.6.1 Effect of ZnO temperature . . . 54
4.6.2 Effect of ZnO concentration . . . 54
4.6.3 Effect of laser fluence . . . 55
4.6.4 Luminescence decay properties . . . 56
4.6.5 Exploration of a novel technique . . . 59
4.7 Development of two-color spectral intensity ratio method . . . 60
4.7.1 Image acquisition . . . 62
4.7.2 Calibration procedure . . . 62
4.7.3 Validation and accuracy . . . 66
4.8 Application: Raleigh-Bénard convection . . . 67

5 Analysis of film cooling using Experimental methods 69
5.1 Concept of BATH . . . 70
5.2 Description of BATH Test rig . . . 71
5.2.1 Test facility components . . . 71
5.2.2 Seeding system . . . 75
5.3 Calibration of BATH test rig . . . 79
5.3.1 Presentation of measurement techniques used for calibration purposes . . . 79
5.3.2 Working points of BATH test rig . . . 81
5.3.3 RANS simulations: effect of step . . . 85
5.4 Film cooling: 2-D temperature measurements . . . 86
5.4.1 Film cooling geometry . . . 87
5.4.2 Film cooling: Boundary conditions . . . 87
5.4.3 Experimental setup . . . 88
5.4.4 Calibration . . . 91
5.4.5 Results: 2-D temperature fields . . . 91

6 Large Eddy Simulations and discussion of results 103
6.1 Large Eddy simulations . . . 104
6.1.1 Geometry and boundary conditions . . . 104
6.1.2 Solver and Mesh sizing . . . 105
6.2 Results . . . 106
6.3 Discussion of flow physics . . . 110

7 Summary and perspectives 121
7.1 General synthesis . . . 122
7.1.1 Overview of objectives . . . 122
7.1.2 RANS studies . . . 122
7.1.3 Phosphor thermometry development . . . 122
7.1.4 Experimental film cooling studies . . . 123
7.1.5 LES simulations . . . 123
7.2 Perspectives . . . 123

Résumé étendu i

Abstract xiii

List of Figures

1.1 Representation of a modern gas turbine engine: Cross-sectional view of GE9X . . 1
1.2 Chart showing the increase in the absolute CO_2 emission and a relative contribution to the total emission from all other sources (given in percentage). Lee *et al.* (2021) 2
1.3 Gas turbine entry temperature evolution Virginia (2018) 3
1.4 Illustration of a gas turbine blade with film cooling holes Beale (2012) and an illustration of the film cooling process in a single discrete hole obtained from in house LES simulations. 3
1.5 Illustration of the proposed auxiliary holes system 4
1.6 Overview of the work carried out in this thesis 5

2.1 Instantaneous three-dimensional visualizations of the flow field in a perpendicular Jet in Cross-Flow arrangement. Ruiz *et al.* (2015) 7
2.2 Arrangement of a Jet In Cross-Flow system. 8
2.3 Illustration of the effect of velocity ratio on the jet trajectory 9
2.4 Representation of JICF with vortex configurations New *et al.* (2006) 10
2.5 Trajectories of the horseshoe vortices at low Reynolds number Kelso *et al.* (1996*a*). Right: Horse shoe vortex and the ensuing wake region visualisation around a round transverse jet. The smoke is injected in the cross-flow boundary layer Fric & Roshko (1994) 11
2.6 Side view of a jet in cross flow configuration with standing vortices clearly seen. The dots represent the trajectory of the jet at a velocity ratio VR=4 Fric & Roshko (1994). Right: Upright vortex formation from the channel floor shear layer, their lifting from the topological critical points Sau *et al.* (2004) 11
2.7 Left: Transverse jet shear-layer structure visualised by use of smoke injection in jet. Right: Transverse jet shear-layer structure visualised by use of smoke streaklines injection in the transverse flow Fric & Roshko (1994). Three dimensional vortex structures can be seen in the figures (c) and (d) based on LES simulations from Milani *et al.* (2020) 12
2.8 Visualisation of a Counter Rotating Vortex Pair by experiments by Gogineni *et al.* (1996) and numerically by an in-house RANS simulation 13
2.9 Origin of the CRVP as proposed by Kelso *et al.* (1996*a*). (a) the large-scale vortex ringlike roll-up and (b) the reorientation of the shear layer vorticity leading to the folding of the cylindrical vortex sheet 13
2.10 Adiabatic film cooling effectiveness of a single inclined cylindrical hole configuration at various blowing ratios by Sultan (2011). 14
2.11 Results of the experimental study on the effect of freestream turbulence on the adiabatic film cooling effectiveness by Mayhew *et al.* (2003) 14
2.12 Results of the experiment obtained at different distances from the nozzle exit in the wall-normal direction showing the formation of a CRVP Yuen & Martinez-Botas (2003) 15
2.13 Film cooling hole configurations: (a) simple cylindrical hole (b) Fan shaped hole (c) Laid-back hole (d) Console hole (e) Tri-pod hole (f) Crater hole. Citations: Gritsch *et al.* (1998), Barigozzi *et al.* (2010), Azzi & Jubran (2007), Ramesh *et al.* (2016), Kalghatgi & Acharya (2015). 16

2.14 Left: Representation of an auxiliary hole configuration. Right: Adiabatic film cooling effectiveness of simple cylindrical hole and two streamwise injection angles for a configuration where auxiliary holes placed are along the lateral axis of the main hole by Park *et al.* (2014). 16

3.1 Flow visualisation of streamlines from auxiliary holes configuration seen from upstream location. (in-house simulation) 19
3.2 Geometrical parameters frequently used in film cooling studies. 20
3.3 Film cooling study from a previous work. (a) Velocity contour, (b) Temperature contour, (c) mesh used in few of the cases are shown. 21
3.4 Geometrical representation of the three configurations tested.(not to scale) 22
3.5 Illustration of the computational domain with the boundary conditions. 23
3.6 Side view of the mesh where the three refinement zones are clearly seen. 24
3.7 Centerline adiabatic film cooling effectiveness for single hole case at M=1 for the three meshes used in the GCI study. 25
3.8 Comparison of numerical and experimental results: Evolution of centerline (left) and lateral AFCE (right) along the X-axis for various blowing ratios: M=0.65; M=1; M=1.25 25
3.9 Evolution of centerline (a-c) and lateral AFCE (d-f) along the X-axis for various blowing ratios. (a,d) M=0.65; (b,e) M=1; (c,f) M=1.25 27
3.10 Top view of adiabatic film cooling effectiveness contours along the streamwise direction for the three configurations at different blowing ratios 29
3.11 Evolution of adiabatic film cooling effectiveness along the streamwise direction for the three configurations at different blowing ratios. Note: the planes perpendicular to the stream show non-dimensional temperature θ. 30
3.12 Temperature field along the symmetry plane for the various film cooling configurations at different blowing ratios : M=0.65 (a-c); M=1 (d-f); M=1.25 (g-i). Figures (j) and (k) are a zoom of (g) and (i) to highlight the jet trajectories of the single hole and Auxiliary hole Case 2. 31
3.13 Evolution of centerline (a-c) and laterally averaged NHFR (d-f) values along the longitudinal axis (X-axis) for various blowing ratios. (a,d) M=0.65 (b,e) M=1 (c,f) M=1.25 32
3.14 Upstream view of CRVP formation at the hole exit in a single hole case from RANS simulations for M=1.25 33
3.15 Contour plot of the temperature profile for the single hole case at M=1 showing the various locations used for the vortex intensity measurements (Z/D=0.5,1) and the boundary layer study locations (X/D=1.5,5.5) 34
3.16 Evolution of laterally averaged vortex intensities along the longitudinal axis (X-axis) at a height of Z/D=0.5 (a,b,c) and Z/D=1 (d,e,f) for various blowing ratios. (a,d) M=0.65; (b,e) M=1; (c,f) M=1.25. 34
3.17 Visualisation des lignes de courant du courant libre et du jet pour le cas de trou unique (a-d) et le cas de trou auxiliaire 2 (e-i) à différents plans :(a,e) X/D=1; (b, f) X/D=3; (c,g) X/D=5 avec les contours de température sur les plans. Les figures (d) et (h) montrent la vue de dessus des lignes de courant libres près de la paroi, et (i) les lignes de courant du jet injecté dans la configuration du trou auxiliaire 2. . 36
3.18 Evolution of non-dimensional velocity boundary layer at X/D=1.5 (a,b,c) and X/D=5.5 (d,e,f) for various blowing ratios: (a,d) M=0.65; (b,e) M=1; (c,f) M=1.25. The corresponding evolution of the normalised temperature is also marked by colored dots to represent the jet and freestream fluids. Higher value indicates higher presence of injected jet. 37

4.1 Metrology studies at Institut P': Real time emission of ZnO particles in water (phosphorescence) mixed with rhodamine-B (fluorescence), upon excitation with a 266nm laser. (In-house experiments) 39

4.2 Schematic representation of the absorption and emission processes in a phosphor with Activators(A) and sensitizers(S) . . . 41
4.3 The Jablonski diagram to represent the transitions between the energy states of an electron. (1) light absorption, (2) vibrational relaxation, (3) internal conversion (IC), (4) intersystem crossing (ISC), (5) radiative transition, and (6) non-radiative transition Shigeo Shionoya (2006) . . . 42
4.4 Working principle of Spectral intensity ratio method. As the temperature increases, the emission spectrum moves towards longer wavelengths. . . . 45
4.5 Spectral intensity ratio method: A typical experimental setup. . . . 46
4.6 Working principle of decay time method. The lifetime becomes shorter when the temperature increases. . . . 47
4.7 Methods to perform phosphor thermometry by exploiting the spectral and temporal emission dependence on temperature. . . . 49
4.8 Emission spectrum of ZnO particles at 23°C using 266nm and 355 nm excitation, and 355 nm excitation at 95°C (Abram *et al.* (2016)). . . . 50
4.9 Temperature dependence of the normalized ZnO:Zn emissions. Left: spectra obtained at different temperatures normalized at each spectrum maximum value. Right: Normalised emission intensity for various temperatures Frattina (2019) . . . 50
4.10 Schematic representation of the test cell and actual image of the test cell. . . . 51
4.11 Schematic representation of the experimental setup with various components used. 52
4.12 Emission spectrum of ZnO in water at two different temperatures and an image of the emission as seen visually is shown on the right. . . . 52
4.13 Particle size distribution of the selected lot of ZnO particles made by Malvern analysis. . . . 53
4.14 Spectral and emission intensity dependence with respect to temperature of ZnO and water mixture. . . . 54
4.15 Spectral and emission intensity dependence with respect to concentration of ZnO phosphor in water. . . . 55
4.16 Spectral and emission intensity dependence with respect to total laser energy (measured before the laser sheet generator). . . . 56
4.17 Quantum Efficiency Curves for Gen 3 Image Intensifiers for the ANDOR iStar sCMOS camera. . . . 57
4.18 (a) Timing diagram for a constant gating width of 2ns and variable delay (δt) introduced before camera aperture (b) Timing diagram for a variable gating width and constant delay (δt) before camera aperture. T_0 is the instant at which the laser pulse is fired. . . . 57
4.19 (a) Total emission intensity (I)vs time after laser pulse (b) Change in emission intensity (E) vs time after laser pulse. (c) Normalised emission intensity in the decaying arm of the emission vs camera gating width. (d) Evolution of the time constant τ vs temperature. . . . 58
4.20 (a) Total emission intensity (I) vs time after laser pulse for various temperatures (b) Emission intensity ratio for various temperatures (see text for explantion) (c) calibration curve for the proposed decay-rise time ratio method: Normalised emission intensity vs temperature. . . . 59
4.21 (a) Representative image of an imaginary setup for the proposed decay-rise time ratio method (b) Timing diagram for the laser and cameras for the proposed method. 60
4.22 Quantum efficiency of Princeton camera with the superposition of the emission spectrum of ZnO phosphor. . . . 61
4.23 Timing diagram for the laser fire and camera gating. . . . 62
4.24 Percentage standard deviation as a function of gating width/ intensification and Gaussian filtering. Note: In all cases, the image intensity was kept at a constant level so as to be comparable between different cases. . . . 63
4.25 (a) Working of Optosplit. (b) Example of a raw image containing two filtered images. 63
4.26 Image showing the various processes involved in the calibration procedure. . . . 64

4.27 Representation of the averaging process. The zones with the particles are alone considered for obtaining the mean image. . . . 65
4.28 Representation of the 'block averaging' process. Each block has its own temperature vs intensity ratio calibration curve following 4.7. . . . 65
4.29 Validation of the calibration process by testing the process at constant temperature cases at various temperatures. A frequency distribution of temperature for the entire calibration zone is shown below each case. . . . 66
4.30 Instantaneous temperature fields at 5s (a) and 10s (b). Mean temperature field and the corresponding temperature distribution is seen in (c) and (d) respectively. (e) Mean temperature field with superimposed velocity vectors: adapted from Silano *et al.* (2010) . . . 67

5.1 Aerial view of the PROMETEE platform (PROgramme et Moyens d'Essais pour les Transports, l'Énergie et l'Environnement) at Poitiers. . . . 69
5.2 BATH test rig: CAD view . . . 70
5.3 BATH test rig: assembled view of premix and combustion zone, dilution and expansion chambers. . . . 71
5.4 Schematic view of the Bath test rig components . . . 71
5.5 Picture of the electric heater system. . . . 72
5.6 CAD view of the premix chamber with the injectors. Right picture shows the actual view of the pre-mix chamber . . . 73
5.7 CAD view of the combustion chamber. Right picture shows the actual view of the combustion chamber . . . 73
5.8 CAD view of the dilution zone. Right picture shows the actual view of the pre-mix chamber . . . 74
5.9 Illustration of the modular test section with the various features. . . . 75
5.10 Picture showing the seeding chamber with supports. . . . 76
5.11 Illustration of the bypass system. . . . 76
5.12 Evolution of velocity and thermal response time with respect to temperature and pressure for different particle sizes. Figures A and B are a zoom for the particle sizes less than 5 μm . . . 78
5.13 Illustration of the the triple probes used to calibrate the test bench. . . . 79
5.14 CAD representation of the test section with the locations where triple probe measurements were conducted. L=16cm here. . . . 80
5.15 Illustration of a classical PIV setup. Raffel *et al.* (2018) . . . 81
5.16 Illustation of the PIV setup. A 532nm laser is used to generate the green laser sheet. 82
5.17 (a) Velocity profile and (b) Temperature profile at the horizontal centerline for a mass flow rate of 500g/s and 1000g/s at 20°C and 150°C at the entry of the test section. Vertical dotted lines denote the extremities of the test section dimension. . 83
5.18 Velocity contour at the entry of test section for a mass flow rate of 500g/s at 20°C. Vertical dotted lines denote the extremities of the test section dimension. . . . 83
5.19 Left: Turbulence intensity evolution for Y=0 at 500g/s and 20°C. Right: PSD at the central point of the test section at 500g/s and 20°C. . . . 84
5.20 (a) velocity profile along the Y direction at X=30 . . . 84
5.21 Representation of the test section with and without a step . . . 85
5.22 Representation of the geometry used for the RANS simulations with boundary conditions . . . 86
5.23 Velocity flow field analysed numerically using RANS simulations: (a) without and (b) with presence of a step. . . . 86
5.24 Illustration of the film cooling modules used in this thesis and their corresponding hole shape from the top view is shown below each module with geometrical parameters. 87
5.25 Schematic representation of the working of an orifice tube. . . . 88
5.26 Calibration curve for the 2mm orifice . . . 88
5.27 Andor iStar sCMOS camera: Depiction of various parts in the intensifier and the functioning of Micro Channel Plate. . . . 89

5.28 (a)Illustration of the PIV/ phosphor thermometry setup. (b) Actual image of the inside of the test section during the phosphor thermometry image acquisition. (c) CAD illustration of the laser path in the test section 90
5.29 (a) Schematic representation of the working of optosplit device. (b) Raw image obtained on the ANDOR camera with two filtered images of the ZnO emission obtained during film cooling experiments. 91
5.30 Intensity ratio vs temperature calibration curve for the ZnO phosphor in air. . . . 92
5.31 The locations of the XZ plane in the lateral direction where 2-D phosphor thermometry was conducted. 92
5.32 Phosphor thermometry: Non-dimensional temperature contours for M=3 for single hole case at Y/D=0. (a) Mean flow field. (b-d) instantaneous flow fields at different instances. 93
5.33 Phosphor thermometry: Non-dimensional temperature contours for M=3 for single hole case at Y/D=0.4. (a) Mean flow field. (b-d) instantaneous flow fields at different instances. 95
5.34 Phosphor thermometry: Non-dimensional temperature contours for M=3 for single hole case at Y/D=0.8. (a) Mean flow field. (b-d) instantaneous flow fields at different instances. 96
5.35 Phosphor thermometry: Non-dimensional temperature contours for M=3 for single hole case at Y/D=1.2. (a) Mean flow field. (b-d) instantaneous flow fields at different instances. 97
5.36 Phosphor thermometry: Non-dimensional temperature contours for M=3 for Auxiliary hole case 2 at Y/D=0. (a) Mean flow field. (b-d) instantaneous flow fields at different instances. 98
5.37 Phosphor thermometry: Non-dimensional temperature contours for M=3 for Auxiliary hole case 2 at Y/D=0.4. (a) Mean flow field. (b-d) instantaneous flow fields at different instances. 99
5.38 Phosphor thermometry: Non-dimensional temperature contours for M=3 for Auxiliary hole case 2 at Y/D=0.8. (a) Mean flow field. (b-d) instantaneous flow fields at different instances. 100
5.39 Phosphor thermometry: Non-dimensional temperature contours for M=3 for Auxiliary hole case 2 at Y/D=1.2. (a) Mean flow field. (b-d) instantaneous flow fields at different instances. 101

6.1 Iso-contours of Q-criterion colored with local temperature values. (in-house simulations) 103
6.2 Geometrical representation of the domain. The two geometric hole configurations are shown at the bottom. 104
6.3 (a) Determination of Taylor length scale from RANS simulation. (b) View of the mesh with 2 refinement zones. (c) Close-up view of the coolant exit region showing prism layers 105
6.4 (a) Convective Courant number distribution (b) Wall Y+ distribution on the base wall. 106
6.5 Mean non-dimensional 2-D temperature contours in the XZ plane at **Y/D=0** for the single hole configuration (a, c, e) and the auxiliary hole configuration (b, d, f). The figures (a) and (b) are obtained using phosphor thermometry, (c) and (d) are obtained through LES simulations, (e) and (f) are obtained using RANS simulations. 107
6.6 Mean non-dimensional 2-D temperature contours in the XZ plane at **Y/D=0.4** for the single hole configuration (a, c, e) and the auxiliary hole configuration (b, d, f). The figures (a) and (b) are obtained using phosphor thermometry, (c) and (d) are obtained through LES simulations, (e) and (f) are obtained using RANS simulations. 108
6.7 Mean non-dimensional 2-D temperature contours in the XZ plane at **Y/D=0.8** for the single hole configuration (a, c, e) and the auxiliary hole configuration (b, d, f). The figures (a) and (b) are obtained using phosphor thermometry, (c) and (d) are obtained through LES simulations, (e) and (f) are obtained using RANS simulations. 109

6.8 Adiabatic film cooling effectiveness evolution for M=3. 109
6.9 Adiabatic film cooling effectiveness contours for M=3. Top: Single hole, bottom: Auxiliary hole case 2 110
6.10 Instantaneous non-dimensional 2-D temperature contours in the XZ plane at **Y/D=0** for the single hole configuration (a and c) and the auxiliary hole configuration (b and d). The figures (a) and (b) are experimentally obtained using phosphor thermometry and (c) and (d) are obtained through LES simulations. 111
6.11 Instantaneous non-dimensional 2-D temperature contours in the XZ plane at **Y/D=0.4** for the single hole configuration (a and c) and the auxiliary hole configuration (b and d). the figures (a) and (b) are obtained using phosphor thermometry and (c) and (d) are obtained through LES simulations. 112
6.12 Instantaneous non-dimensional 2-D temperature contours in the XZ plane at **Y/D=0.8** for the single hole configuration (a and c) and the auxiliary hole configuration (b and d). The figures (a) and (b) are obtained using phosphor thermometry and (c) and (d) are obtained through LES simulations. 113
6.13 Mean velocity contour in the central plane (Y/D=0) for the single hole case (left) and the auxiliary hole configuration (right). 113
6.14 Variance contours for the single hole configuration and auxiliary hole configuration in the central plane. (a) and (b) present the variance in temperature; (c) and (d) present the variance in velocity magnitude; (e) and (f) present the variance in the i component of velocity; (g) and (h) present the variance in the j component of velocity; (i) and (j) present the variance in the k component of velocity. 115
6.15 Front view of the mean helicity contours for the single hole and the auxiliary hole configuration at various planes (a) X/D=-1, (b) X/D=0, (c) X/D=1, (d) X/D=3. 116
6.16 Instantaneous velocity (a, c) and vorticity (b,d) contours for the single hole and auxiliary hole configuration at X/D=3 plane. Figures (a) and (b) represent the single hole case, while (c) and (d) represent the auxiliary hole configuration. 117
6.17 Top view of the iso-contours of Q-criterion colored with helicity values. Note: the color bar is limited to -50000 and 50000 to better highlight the vorticity features of the film cooling configurations. 117
6.18 Side view of the iso-contours of Q-criterion colored with helicity values. Note: the color bar is limited to -50000 and 50000 to better highlight the vorticity features of the film cooling configurations. 118
6.19 Illustration of the working mechanism in the single hole and auxiliary hole configurations. 118

7.1 Various activities carried out in the framework of this thesis. 121
7.2 Aperçu des travaux réalisés dans cette thèse ii
7.3 Représentation de JICF avec des systèmes de vortex New *et al.* (2006) iii
7.4 Visualisation des lignes de courant de l'écoulement principal et de l'écoulement injecté pour le cas du trou unique (a-d) et le cas des trous auxiliaires 2 (e-i) à différents plans :(a,e) X/D=1 ; (b, f) X/D=3 ; (c,g) X/D=5 avec les contours de température sur les plans. Les figures (g) et (h) montrent la vue de dessus des lignes de courant de l'écoulement principal près de la paroi, et (i) les lignes de courant du jet injecté dans la configuration des trous auxiliaires 2. v
7.5 Méthodes pour effectuer la thermométrie au phosphore vii
7.6 Validation du processus d'étalonnage en testant le processus dans des cas à température constante à différentes températures. Une distribution de fréquence de la température pour l'ensemble de la zone d'étalonnage est indiquée sous chaque cas. vii
7.7 Illustration des modules de refroidissement par film utilisés dans cette thèse et leur forme de trou correspondante de la vue de dessus est montrée en dessous de chaque module avec leurs paramètres géométriques. viii
7.8 Thermométrie au phosphore: contours de température non dimensionnels pour M=3 pour le cas d'un seul trou à Y/D=0,4. (a) Champ d'écoulement moyen. (b,c) Les champs température instantanés ix

7.9 Contours de vitesse instantanée (a, c) et de vorticité (b, d) pour la configuration à trou unique et trou auxiliaire au plan X/D=3. Les figures (a) et (b) représentent le cas d'un seul trou, tandis que (c) et (d) représentent la configuration du trou auxiliaire. x
7.10 Contours de température 2D instantanés non dimensionnels dans le plan XZ à **Y/D=0** pour la configuration à un seul trou (a et c) et la configuration à trou auxiliaire (b et d). Les figures (a) et (b) sont obtenues expérimentalement à l'aide de la thermométrie au phosphore et (c) et (d) sont obtenues par des simulations LES. xi
7.11 Illustration du mécanisme dans les configurations à trou unique et à trou auxiliaire. xi

Chapter 1

Introduction to film cooling

The thesis begins by introducing the problem statement and a general introduction about film cooling and its applications are presented. Furthermore, the objectives and contents in this thesis are highlighted to understand the context of the thesis.

Figure 1.1: Representation of a modern gas turbine engine: Cross-sectional view of GE9X

Contents

1.1 Need for film cooling **2**

1.2 Basic understanding of film cooling **3**

1.3 Objectives and scheme of the thesis **4**

1.1 Need for film cooling

Gas turbine engines are the most commonly used propulsion systems in modern commercial and military aircraft. Due to various technological advances, drastic increases in cycle efficiencies have been made possible since the advent of the turbojet engine Boyce (2011). In spite of these advancements, there is always a need to reduce specific fuel consumption rates. This is not only due to the immense pressure from the regulatory point of view but also an urgent need to reduce green house gas emissions in order to slow down the rapid increase in global atmospheric temperatures.

Figure 1.2 shows the contribution of aviation to global carbon dioxide emissions representing about 2-3% . Although this percentage is growing at a relatively low rate, the total absolute emission has increased by four times since 1966. In addition to carbon dioxide emission, aviation contributes directly and indirectly to global warming through the emission of water vapour, soot particles, NOx related ozone and methane, sulfate aerosols and other minor greenhouse gases Lee *et al.* (2021). Moreover the formation of contrails and cirrus cloud formation due to contrail seeding can cause a warming effect due to the entrapment of heat within the atmosphere. Hence, it is evident for the need to reduce carbon emission, or in other words the reduction in fuel consumption.

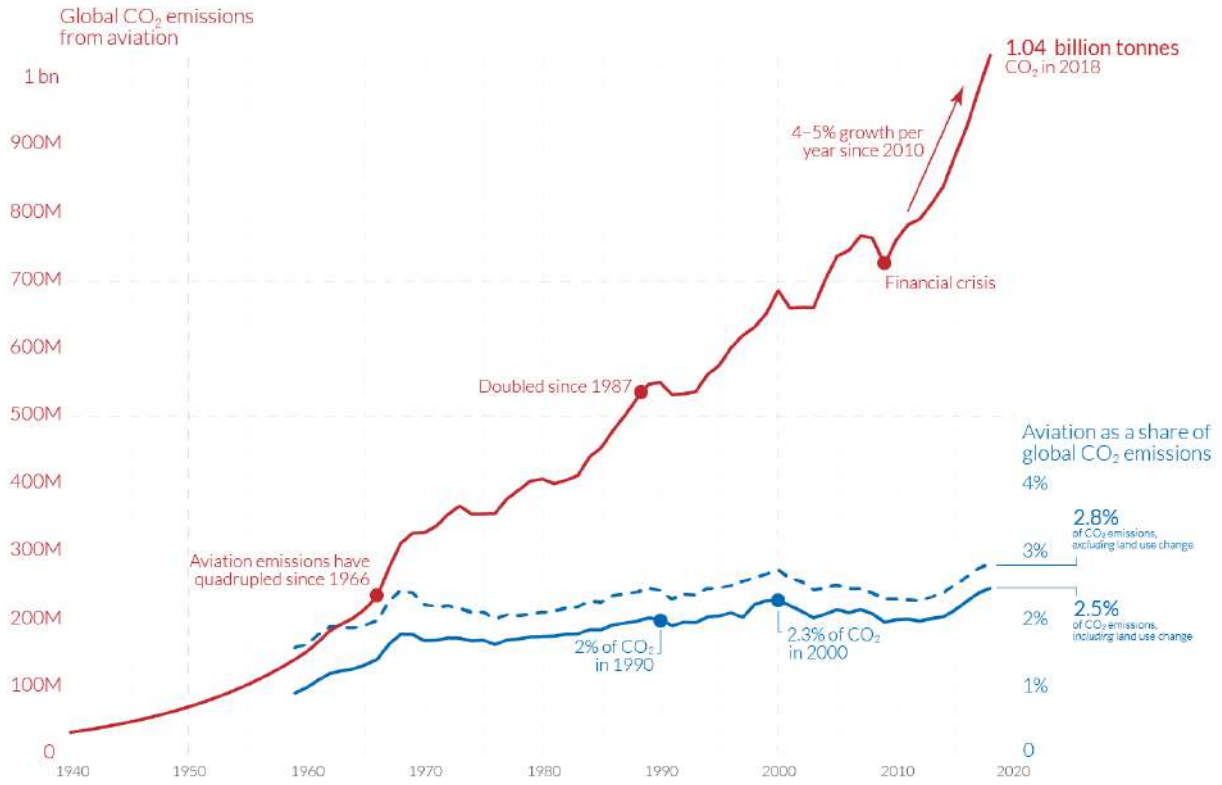

Figure 1.2: Chart showing the increase in the absolute CO_2 emission and a relative contribution to the total emission from all other sources (given in percentage). Lee *et al.* (2021)

Studies have shown that combustion at stoichiometric conditions (where the total molar mass of the reactants equals the total mass of the products) enhances the efficiency of the engines and can also immensely reduce the NOx and soot emissions. However, in this case, the temperature of the exiting gases at the combustion chamber is the maximum possible due to stoichiometric combustion, this temperature is very high and hence can cause the materials to fail as they exceed the melting point of metal alloys used. Moreover, the turbine blades are subjected to very high mechanical loads too and the combination of the thermal and mechanical forces requires the operating temperatures to be limited to 800°C. Han *et al.* (2012)

This brings us to the concept of turbine blade cooling technologies. Since the early gas turbine engines, research has been made to improve the temperature tolerance of turbine blades as in Figure 1.3. The two ways to improve the material resistance to temperatures are by using novel

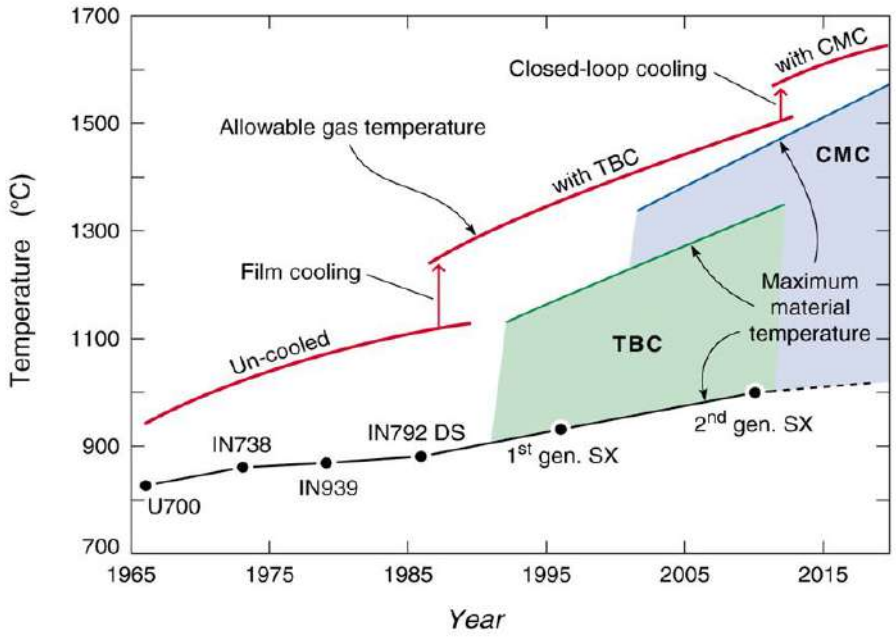

Figure 1.3: Gas turbine entry temperature evolution Virginia (2018)

materials like CMC (Ceramic Matrix Composites) or TBC (Thermal barrier coating) to fabricate the turbine blades and the other is by the improvement of Turbine Blade Cooling strategies. This thesis focuses on the improvement of an external turbine blade cooling technique called film cooling.

1.2 Basic understanding of film cooling

Film cooling is currently the most commonly used external cooling technique which employs discrete holes at specific locations to protect the outer surface of the turbine blade and inner surfaces of a combustion chamber Bunker (2005).

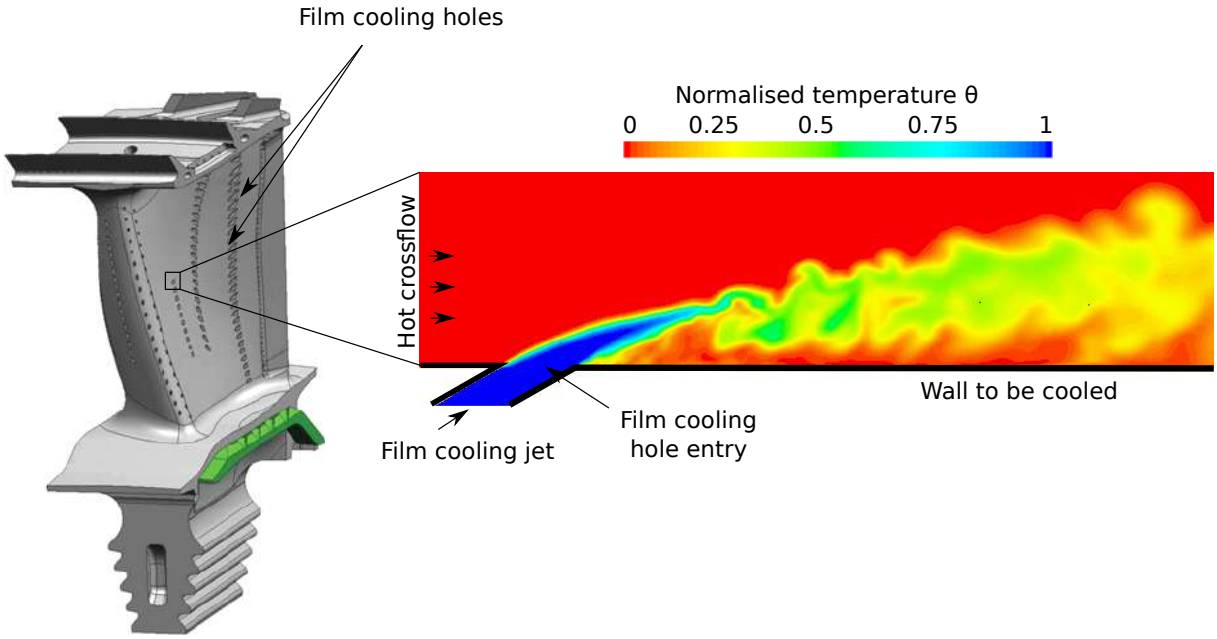

Figure 1.4: Illustration of a gas turbine blade with film cooling holes Beale (2012) and an illustration of the film cooling process in a single discrete hole obtained from in house LES simulations.

The aim of film cooling is to provide a layer of coolant gas, typically extracted from the

compressor stage, over the surface of the turbine blade so as to limit the contact of the turbine blade with the hot gases in the main stream flow. Figure 1.4 shows a typical high pressure gas turbine blade with the discrete holes in them. An instantaneous flow-field from in-house L.E.S simulations in a single hole is shown, with a normalised temperature contour. The normalised temperature is given as

$$\Theta = \frac{T_\infty - T}{T_\infty - T_c} \tag{1.1}$$

where T_∞ is the mainstream temperature, T_c is the temperature of the coolant injected and T is the local temperature.

The objective of the film cooling process is to protect the blade from the extreme temperature and eventually reduce the heat transfer into the wall of the turbine blade. The jet mixes with the mainstream as it flows along and the temperature of the coolant jet increases continuously due to this mixing process implying lesser thermal protection downstream of the hole. The thermal effectiveness of the film cooling configuration is determined using a parameter called the adiabatic film cooling effectiveness which will be used extensively in this thesis. (Smith *et al.* (2006))

$$\eta = \frac{T_\infty - T_{aw}}{T_\infty - T_c} \tag{1.2}$$

where T_∞ is the mainstream temperature, T_c is the temperature of the coolant injected and T_{aw} is the local adiabatic wall temperature. A value of 1 for η means perfect cooling performance and value 0 indicates the absence of the coolant air over the surface to be protected. The various factors influencing the film cooling performance and the vortex systems induced are discussed in detail in Chapter 2. The Jet In Cross Flow (JICF) is a simplification of the film cooling problem where just the jet arising from one hole is analysed to understand the thermal implication due to the aerodynamic characteristics of the jet. There is a need to improve the film cooling process and hence the study of film cooling physics of newer hole shapes and techniques to improve efficiency. Laboratory studies to understand film cooling are usually conducted on a flat plate instead of an actual turbine blade so as to reduce geometrical complexity.

1.3 Objectives and scheme of the thesis

One of the major coherent structures detrimental to the film cooling effectiveness is the presence of a vortex system called Counter Rotating Vortex Pair (CRVP) which will be presented in Chapter 2.

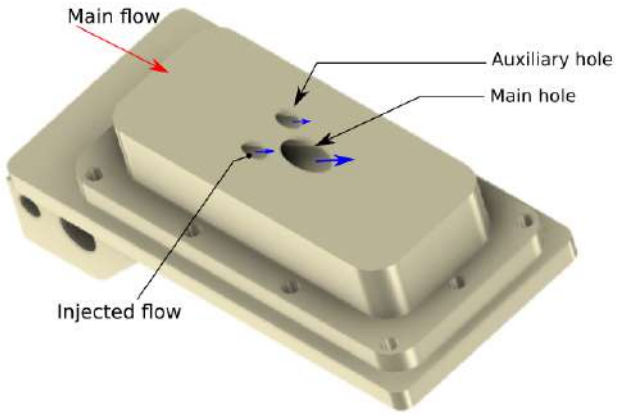

Figure 1.5: Illustration of the proposed auxiliary holes system

With the objective of reducing the intensity and the height of the CRVP, a new geometric configuration of holes distribution called the auxiliary holes film cooling configuration (a main hole supported by two smaller holes upstream as in figure 1.5) is proposed and studied in this

thesis. The overall objective of this thesis is to evaluate the performance of this non-conventional film cooling configuration and to understand the various aero-thermal characteristics of this configuration. To this end, auxiliary holes film cooling arrangements are proposed and their film cooling performance parameters are compared numerically and experimentally with a single cylindrical hole arrangement with the help of preliminary RANS simulations using OpenFOAM 7 or StarCCM+.

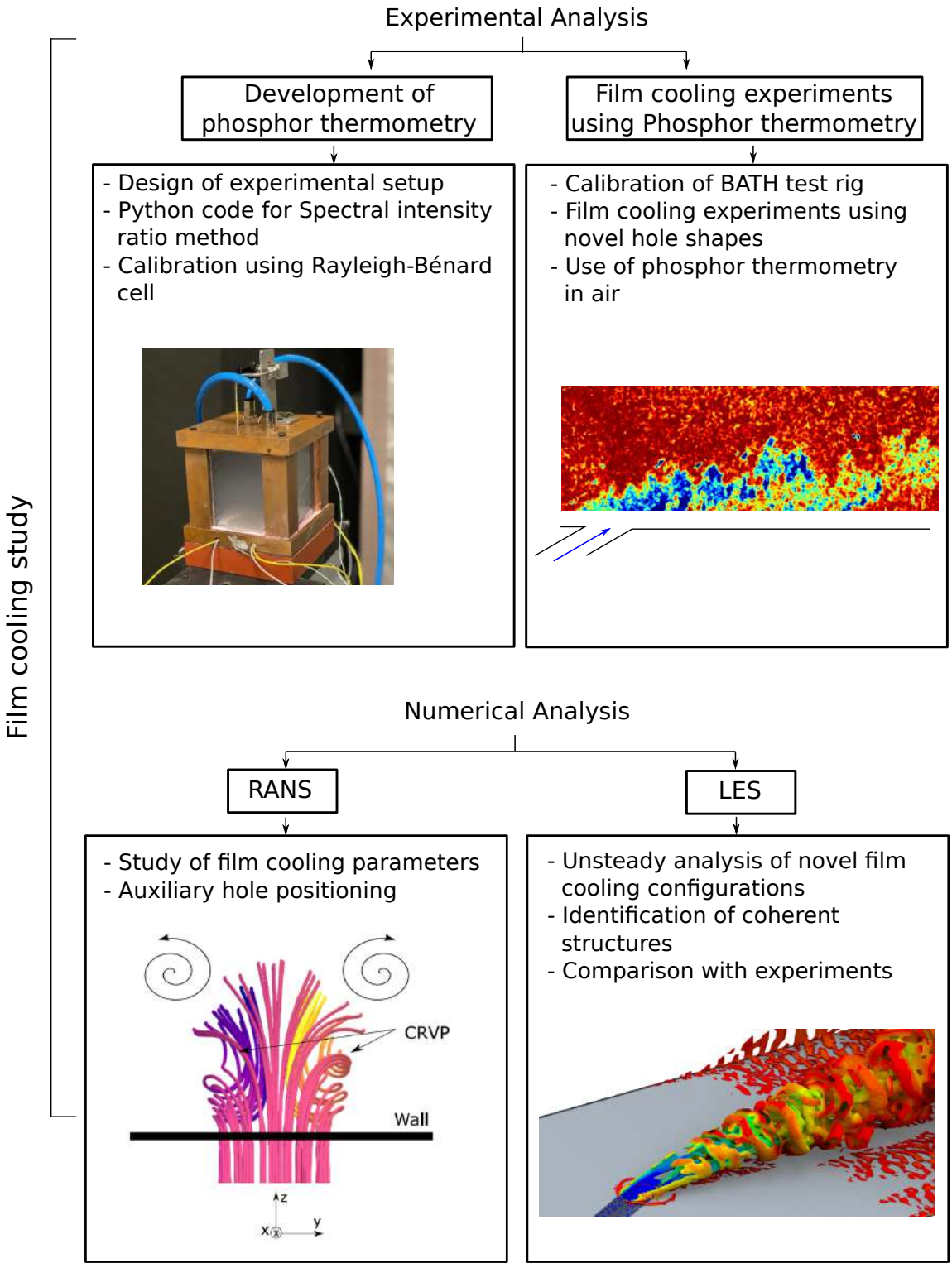

Figure 1.6: Overview of the work carried out in this thesis

To understand the underlying physics of the interaction of coherent structures better, experiments using the proposed film cooling arrangement are necessary. Very frequently, Particle Image

Velocimetry (PIV) is used to analyse the velocity flow field (for example Lenzi *et al.* (2019)) and infrared thermometry to analyse wall temperatures to study film cooling configurations. However, currently very few studies exist to analyse the instantaneous flow temperatures non-intrusively. To achieve this, a recent thermometry technique called 'Phosphor thermometry' is developed for the first time at Institut P'. A novelty in this development is the use of a single camera and a code to post-process the raw images is to be developed from scratch and a robust calibration process defined in detail. Zinc Oxide phosphor thermometry is developed by the use of a test cell where the ZnO particles are suspended in water. The validated thermometry method is then reused to study film cooling process where air is the working medium. Film cooling experiments are carried out in a completely new test bench called BATH (Banc Aéro-THermique) at Institut P' laboratory. Finally, the results obtained experimentally are compared with Large eddy simulations performed using StarCCM+ to study instantaneous and average flow fields. Figure 1.6 provides a compact listing of the tasks carried out in the framework of this thesis.

Chapter 2 provides a bibliographic review concerning Jet in Cross-Flow configuration and the parameters affecting film cooling performance. A state of the art review on the auxiliary holes configuration is described.

Chapter 3 describes a numerical analysis in order to choose the positioning and dimension of the auxiliary holes using RANS simulations.

Chapter 4 provides an introduction to phosphors and the factors influencing the working of a phosphor. This is followed by a short description of ZnO phosphor and its properties. A discussion of the calibration of zinc oxide thermographic phosphor and the validation through a Rayleigh-Benard cell is provided. The various measurement strategies, experiments conducted and the results obtained along with post processing techniques are discussed.

In **Chapter 5**, a detailed description is provided for the BATH test rig where the film cooling experiments are conducted. The various essential features of the test rig are highlighted and a calibration of the test section is discussed. Various film cooling configurations are studied with the application of ZnO phosphor thermometry. Instantaneous and mean 2D temperature fields are provided.

Chapter 6 is a discussion of the results obtained from the experimental and numerical methods to analyse the aero-thermal properties quantitatively and qualitatively. Large Eddy Simulations help in the identification of the various vortex systems and comparison with experiments.

Chapter 7 provides a summary of the methodologies used, results obtained and inferences to be taken from this thesis along with perspectives.

Thesis statement

The use of auxiliary hole configuration is beneficial to the film cooling processes in aircraft turbine blades due to beneficial CRVP features. The complex physical processes arising out of this relatively simple hole configuration is currently inadequately understood and necessitates a thorough understanding by use of experiments and time resolved numerical simulations. By developing and implementing novel non-intrusive thermometry technique called the phosphor thermometry and comparison with LES simulations, the cross flow-jet interactions in the auxiliary hole configuration is analysed.

Chapter 2

Literature review of Jet In Cross-Flow system

In this chapter, the concept of Jet in Cross-Flow (JICF) is introduced. The various similarity parameters involved in characterising such a configuration is discussed. A short bibliographic review of the different vortex structures that are formed due to the interaction of an injected jet and the mainstream is provided. Finally, the various factors affecting the film cooling performance and the methods to improve film cooling effectiveness found in the literature are discussed with focus on the auxiliary holes film cooling configuration.

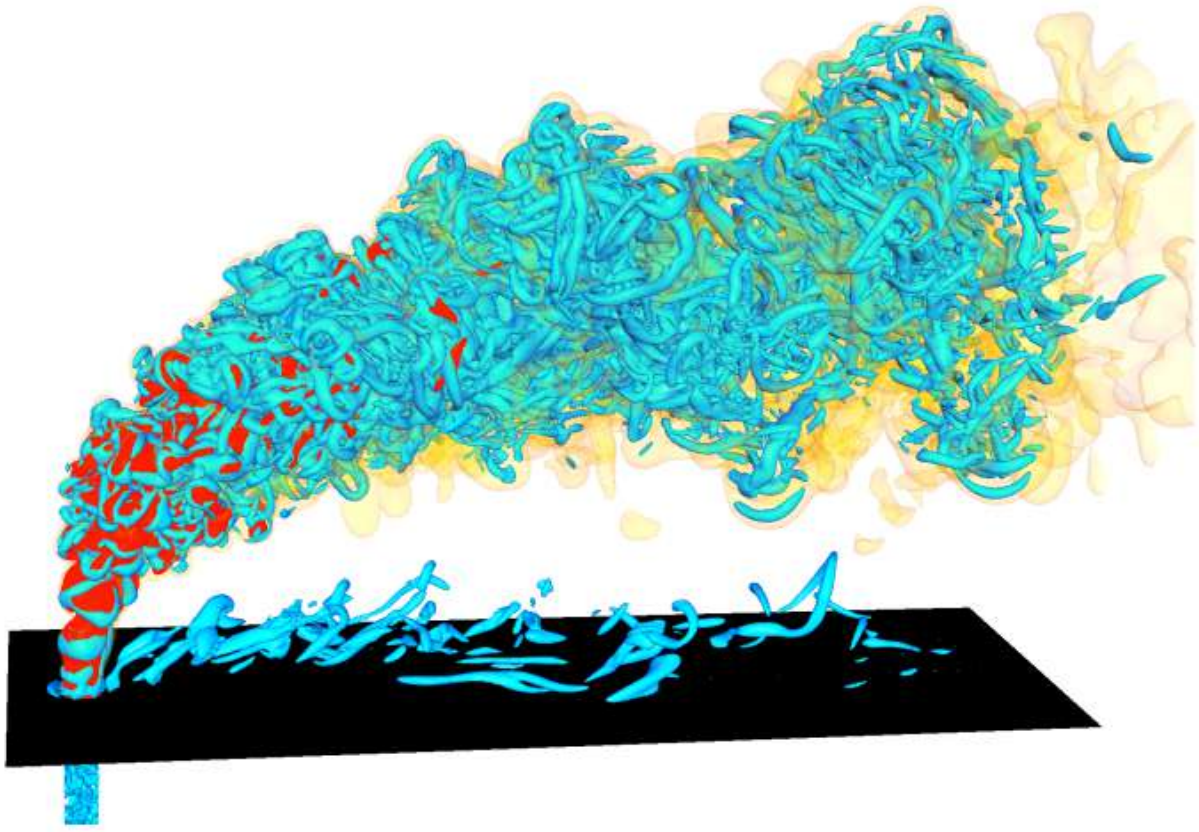

Figure 2.1: Instantaneous three-dimensional visualizations of the flow field in a perpendicular Jet in Cross-Flow arrangement. Ruiz *et al.* (2015)

Contents

2.1 Jet In Cross-Flow 8
2.1.1 JICF parameters and flow classification 8
2.1.2 Vortex systems in a JICF 10
2.2 Factors affecting film cooling performance 13
2.2.1 Blowing ratio 14
2.2.2 Mainstream turbulence 14
2.2.3 Injection angle 15
2.2.4 Hole shape 15
2.3 Anti-vortex film cooling configurations 15

2.1 Jet In Cross-Flow

Film cooling applications involve a phenomena called the Jet in cross flow (JICF) where a coolant jet is injected across a wall into a mainstream flow. Such a flow is observed in many other cases like a chimney or volcanic eruption too. The aerodynamic consequences due to the interaction of the jet with the cross-flow are many and it is important to understand the flow structures that evolve around the jet. In this section a brief explanation of the coherent structures formed due to the JICF is discussed. Depending on the velocity at which the jet is injected into the mainstream flow, different flow regimes are obtained, due to the trajectory of the jet. The basic idea of film cooling is to have a good film coverage over the surface of the turbine blade or the combustion chamber liner and hence, we need to define the regimes at which the flow stays close to the wall. Figure 2.2 shows a classical JICF arrangement.

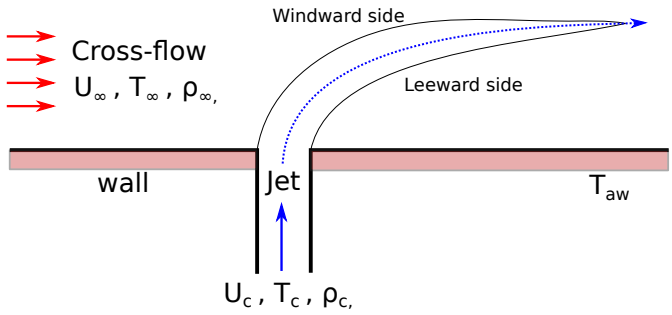

Figure 2.2: Arrangement of a Jet In Cross-Flow system.

2.1.1 JICF parameters and flow classification

The analytical models of the trajectory of a jet issuing perpendicularly from an orifice into a mainstream flow were proposed by Karagozian (1986), Hasselbrink & Mungal (2001) and Fearn & Weston (1974) to establish a relationship between the velocity of jet injection with respect to the crossflow and the trajectory of the injected jet. Karagozian (1986) proposes an analytical solution by following the trajectory of a jet issuing from an orifice as

$$\frac{y}{d} = \alpha r^{\beta} \left(\frac{x}{d}\right)^{\gamma} \tag{2.1}$$

where d is the diameter of the jet orifice. The constants are $\alpha = 0.527$, $\beta = 1.178$ and $\gamma = 0.314$. Here r is the velocity ratio, explained in more detail as follows.

Velocity ratio: It is defined as the ratio between the velocity of the mainstream flow to the velocity of the coolant jet. This parameter is the most important factor defining the flow regime in a JICF arrangement. Figure 2.3 shows the various flow regimes found in jet in crossflow. It can be seen that when the velocity of the injected flow is lower than that of the mainstream, the jet remains close to the wall. For regimes where r is between 1 and 2, the injected jet has enough momentum to penetrate into the mainstream but it is deflected back towards the wall. This process is called the jet lift-off and re-attachment. For higher velocity ratios of r greater than 2, the jet penetrates deeply into the mainstream.

$$r = \frac{U_c}{U_\infty} \tag{2.2}$$

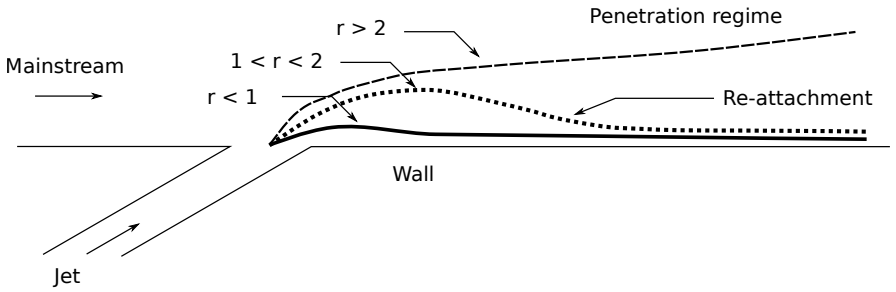

Figure 2.3: Illustration of the effect of velocity ratio on the jet trajectory

Blowing Ratio: It is defined as the ratio between the mass flux of the coolant to the mass flux of the mainstream flow. This parameter helps in determining flow regimes where there are differences in density and temperature between the mainstream and the injected flow as it takes density into account.

$$M = \frac{\rho_c U_c}{\rho_\infty U_\infty} \tag{2.3}$$

Momentum flux ratio: It is the ratio between the momentum flux of the coolant jet to the momentum flux of the mainstream flow. This parameter is useful where there are high temperature differences between injected and mainstream flow.

$$I = \sqrt{\frac{\rho_c U_c^2}{\rho_\infty U_\infty^2}} \tag{2.4}$$

Where the temperatures and the densities of the jet and cross-flow are the same, equations 2.3 and 2.4 reduce to 2.1.

Film cooling parameters

In film cooling applications, one of the most important parameters used to characterise the efficiency of a certain film cooling arrangement is the adiabatic film cooling effectiveness which can be written as

$$\eta = \frac{T_\infty - T_{aw}}{T_\infty - T_c} \tag{1.2}$$

where T_∞ is the temperature of the mainstream flow, T_{aw} is the temperature of the adiabatic wall with the film cooling applied and T_c is the temperature at which the jet is injected.

The main requirements of a film cooling system are to maintain the injected jet flow as close to the wall as possible and to reduce the turbulent mixing with the cross-flow. To achieve this, it is important to understand the various coherent structures in the JICF configuration as they adversely affect the film cooling process.

2.1.2 Vortex systems in a JICF

The appearance of complex unsteady vortex systems due to the interaction of a jet emanating from an orifice into a mainstream flow has been widely studied. Several classical studies of a transverse jet in cross flow have been made in the past by Fric & Roshko (1994), Andreopoulos & Rodi (1984), Mahesh (2013), Cortelezzi *et al.* (2001) Haven & Kurosaka (1997), Keffer & Baines (1963), Blanchard *et al.* (1999) and others. They studied cases where a cylindrical or rectangular jet ejected perpendicular to the base wall and the cross-flow or mainstream flow. Based on the similarity parameters discussed in the preceding section, the vortical structures can vary enormously. The understanding and manipulation of these structures are imperative as these unsteady structures can augment mixing of the jet with the cross-flow and eventually a higher heat transfer into the wall supporting the orifice of the injected jet. The interaction of the mainstream flow with the ejecting jet creates four main vortex systems as seen in the classic representation of a jet in cross-flow in figure 2.4 by New *et al.* (2006) are listed below.

- Horse-shoe vortex
- Wake vortices or standing vortices
- Shear layer vortices
- CRVP

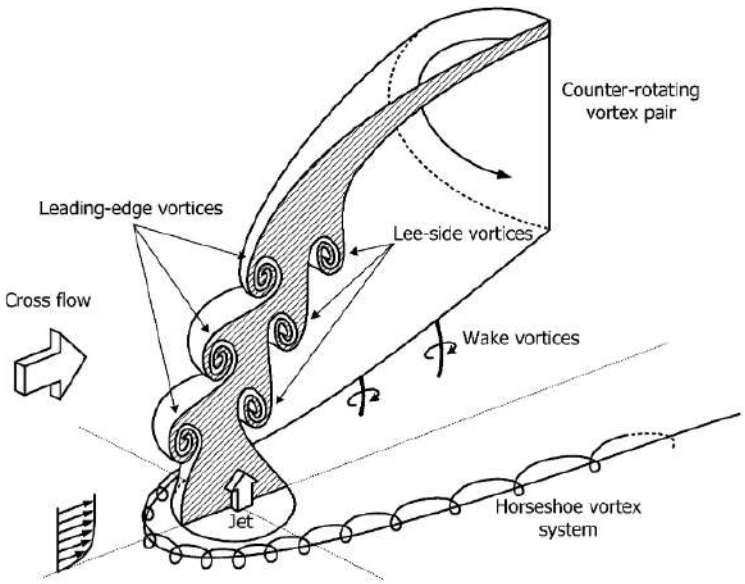

Figure 2.4: Representation of JICF with vortex configurations New *et al.* (2006)

Horse-shoe vortex

The formation of the horse shoe vortex is attributed to the adverse pressure gradient at the cross-flow boundary layer just ahead of the leading edge of the jet (figure 2.5). This causes a separation of the mainstream flow and a system of span-wise vortices around the jet. Depending on the velocity ratio r, it has been shown that wake region could be steady, periodic or coalescent. At low values of r and at low Re values, the flow remains steady. At higher values of r (r >2), the coalescent and periodic shedding is observed. Moreover there is a strong correlation between the unsteadiness of the wake region just downstream of the jet and the horse-shoe vortex as these vortices manipulate the standing vortices. Figure 2.5 shows the instantaneous streamline patterns of the steady regime by Kelso *et al.* (1996*a*) and on the right , a flow visualisation of the horse shoe vortex and the wake region behind a circular jet by Fric & Roshko (1994).

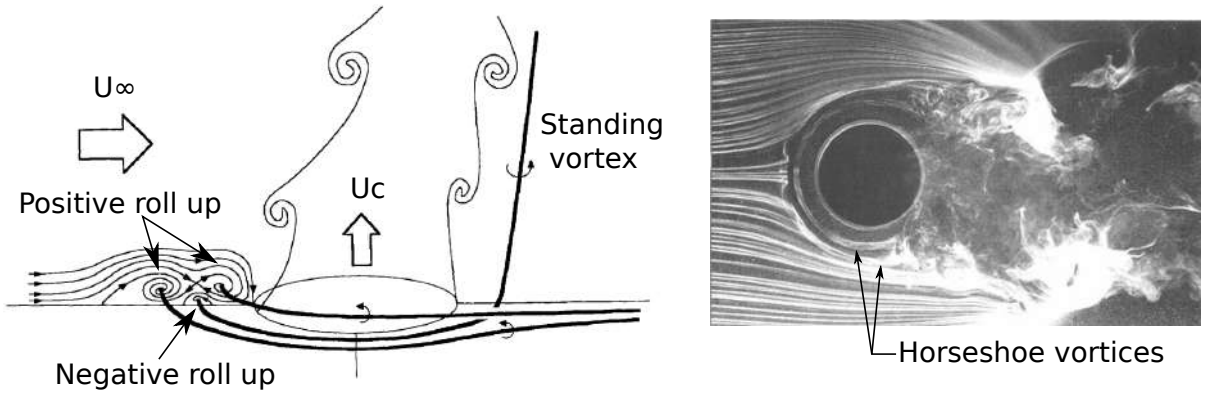

Figure 2.5: Trajectories of the horseshoe vortices at low Reynolds number Kelso *et al.* (1996*a*). Right: Horse shoe vortex and the ensuing wake region visualisation around a round transverse jet. The smoke is injected in the cross-flow boundary layer Fric & Roshko (1994)

Wake vortices or standing vortices

The standing vortices are a very interesting phenomena observed in the leeward side of the jet stream. These are finger-like structures seen to be arising from the wall up to the bottom edge of the jet. These 'tornado' vortices are attributed to the vorticity contained in the wake region (the region of recirculating flow immediately downstream of the jet) and also due to the possibility of vortex generation along the wall. The vortex is lifted up due to the wall normal vortex present just above the wall and the spiral structure is drawn to the wake structures as they pass above the wall (Kelso *et al.* (1996*a*)). Figure 2.6 shows the standing vortices along with the jet trajectory. As explained in the previous section, the presence of a vortex roll up upstream of the jet exit with a sign opposite to that of the boundary layer vortex gives rise to the wake vortex being pushed upwards towards the jet. Hence the instabilities of the horse-shoe vortex system have a profound effect on the location and strength of these vortices.

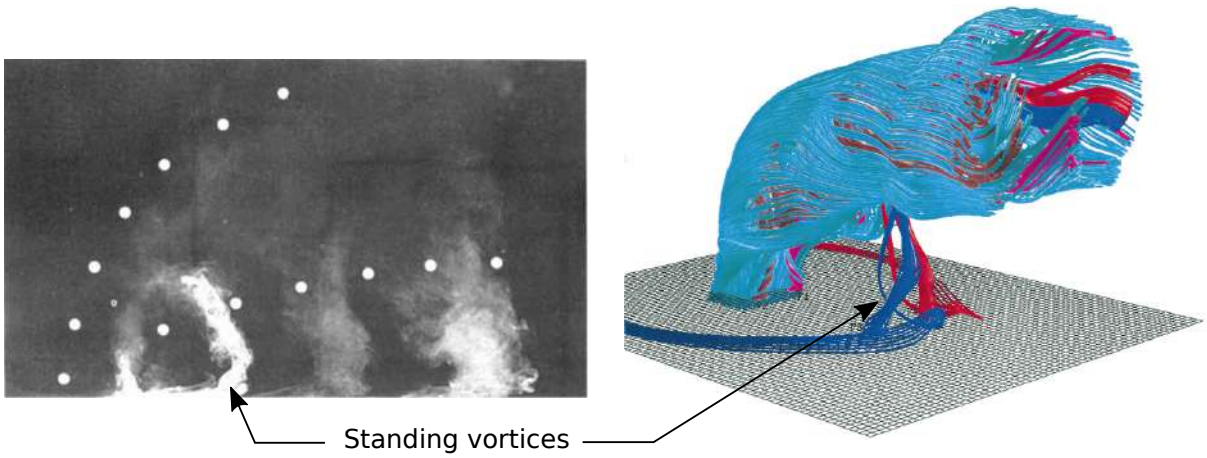

Figure 2.6: Side view of a jet in cross flow configuration with standing vortices clearly seen. The dots represent the trajectory of the jet at a velocity ratio VR=4 Fric & Roshko (1994). Right: Upright vortex formation from the channel floor shear layer, their lifting from the topological critical points Sau *et al.* (2004)

Jet shear layer vortices

The jet shear layer vortex system appears on the upper and lower sides of the jet stream as in figure 2.7. They are believed to originate due to the Kelvin-Helmholtz instabilities of the annular shear layer that separates from the edge of the jet orifice (Fric & Roshko (1994)). In fact, the differences in the velocities of the jet and the mainstream flow in magnitude and direction give rise to the Kelvin-Helmholtz instability and the eventual roll up of the jet and cross-flow shear

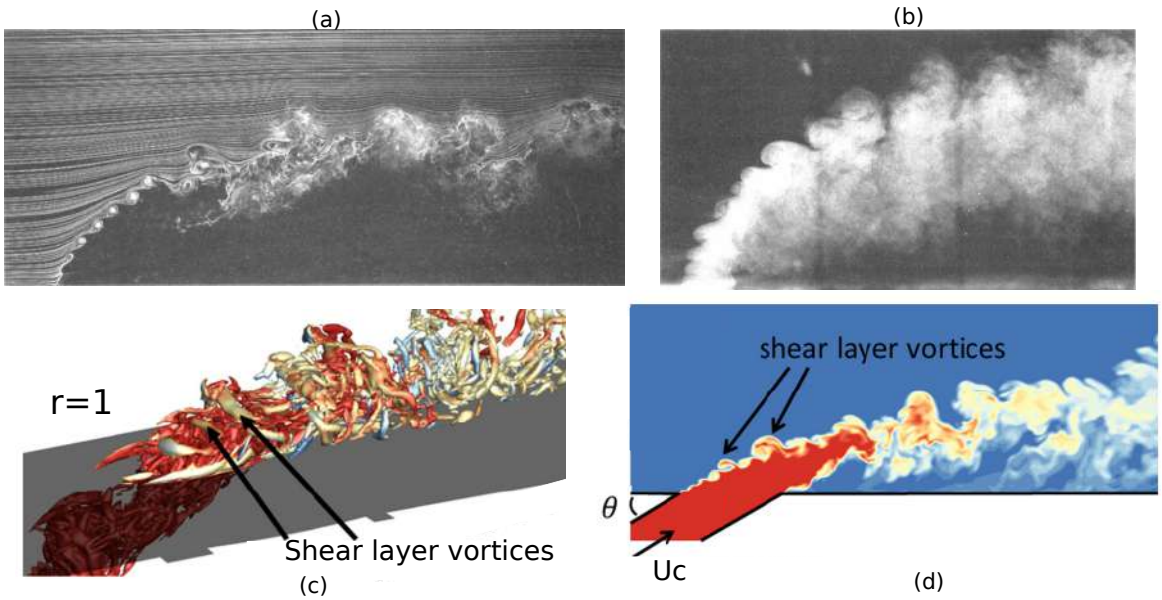

Figure 2.7: Left: Transverse jet shear-layer structure visualised by use of smoke injection in jet. Right: Transverse jet shear-layer structure visualised by use of smoke streaklines injection in the transverse flow Fric & Roshko (1994). Three dimensional vortex structures can be seen in the figures (c) and (d) based on LES simulations from Milani *et al.* (2020)

layer. Naturally, this phenomenon strongly depends on the flow parameters like the jet velocity and the mainstream velocity. LES and DNS simulations by Yuan *et al.* (1999), Kali *et al.* (2010), Sau *et al.* (2004) and Sau & Mahesh (2008) show the presence of windward and leeward vortices which are not related to each other. Stronger features of these shear layer vortices are found in the upstream side than on the downstream side due to the presence of a favourable pressure gradient in the upstream side. The jet shear layer is also suggested to be one of the causes for the formation of counter rotating vortex pair in the flow field.

Counter Rotating Vortex Pair

The Counter Rotating Vortex pair (CRVP hereon) is the most defining vortex system in a JICF arrangement. The CRVP as in figures 2.8(a)(b) is a pair of contra-rotating vortices that is present in the mean flow but difficult to identify in an instantaneous flow-field.

Numerous studies have focused on the origin and evolution of a CRVP system (Keffer & Baines (1963), Kamotani & Greber (1972), Pratte & Baines (1967), and Fearn & Weston (1974) Kelso *et al.* (1996*b*) and others). Despite this, there is no single consensus on the origins of the CRVP. However, there is certainty that as the jet emanates out of the hole, the mainstream boundary layer shears the edges of the jet. This causes the side-wise roll up of the jet shear layer leading to the formation of a vortex pair. The transverse jet is bent along the cross-flow direction and the CRVP is transported too. This causes the initial two dimensional roll up of the shear layer into a three dimensional vortex system along the axis of the jet as described by Muppidi (2006). Figure 2.9 (a)(b) shows the formation of a CRVP as per Kelso *et al.* (1996*b*) and validated by Cortelezzi *et al.* (2001). Kelso *et al.* (1996*b*) proposed that the plane of the upstream part becomes perpendicular to the mean trajectory of the jet due to the reorientation and folding of vortex rings. Lim *et al.* (2001) proposed that the side arms of the vortices in the lateral regions of the jet get aligned to the trajectory of the jet and eventually become the CRVP. In reality the various mechanisms discussed above could contribute to the increase in the intensity of the CRVP. The differences in the origin of the CRVP notwithstanding, one common consensus is that the CRVP is critical in a film cooling configuration as it has a direct effect on the adiabatic film cooling effectiveness. Due to the strong vorticity (ω_x),the mainstream flow is sucked into the jet stream all along the longitudinal axis of the flow and hence the film cooling effectiveness along the length of the test plate drastically reduces. The CRVP curls into a crescent shape and has the strongest vortex magnitude immediately at the

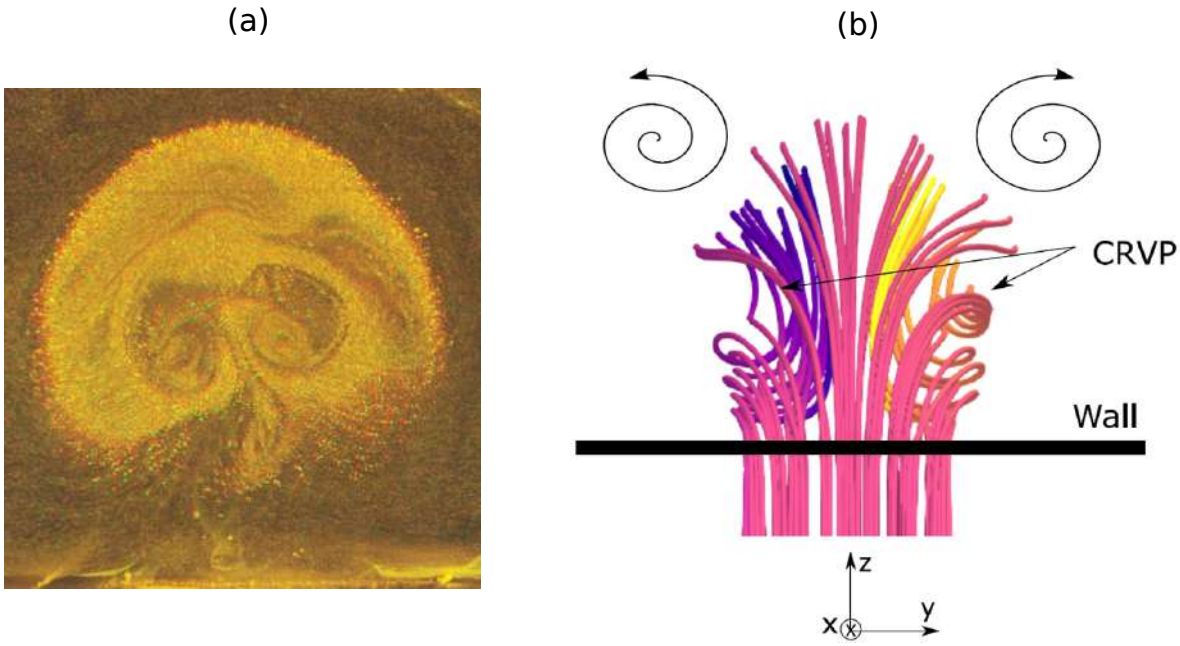

Figure 2.8: Visualisation of a Counter Rotating Vortex Pair by experiments by Gogineni *et al.* (1996) and numerically by an in-house RANS simulation

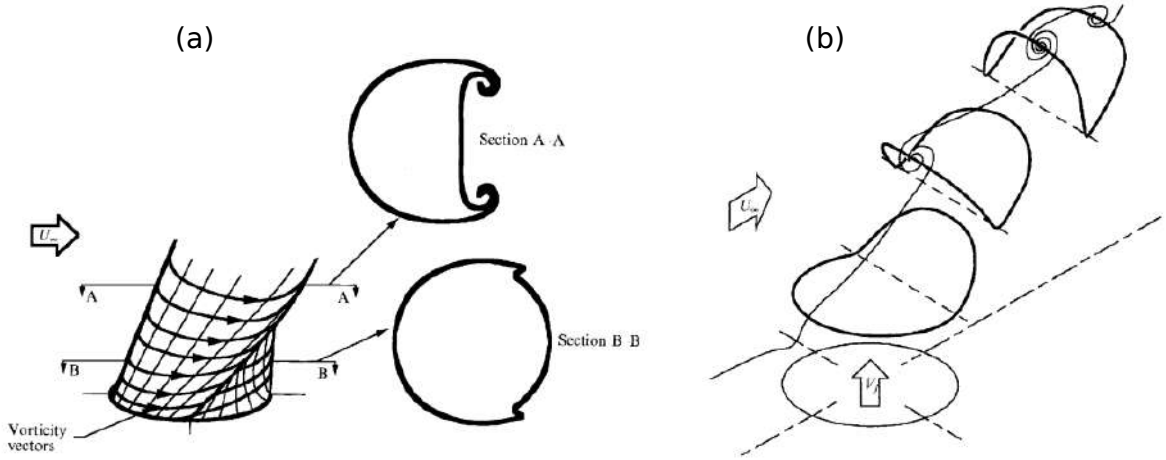

Figure 2.9: Origin of the CRVP as proposed by Kelso *et al.* (1996*a*). (a) the large-scale vortex ringlike roll-up and (b) the reorientation of the shear layer vorticity leading to the folding of the cylindrical vortex sheet

exit of the jet and its vortex strength diminishes as the flow evolves. However, the dimension or the size of the vortex increases and the CRVP continues to exist far from the hole.

2.2 Factors affecting film cooling performance

The various physical parameters of the cool jet injected and the mainstream hot flow affect the film cooling performance. In addition to this, the geometric parameters of the film cooling hole like the hole shape, injection angle, positioning of film cooling holes and surface smoothness all have a role in dictating the outcome of the film cooling efffectiveness of a particular system. Bogard & Thole (2006) summarised a list of factors affecting film cooling performance and a selected few are mentioned in detail.

2.2.1 Blowing ratio

As discussed in the previous section, the blowing ratio is an important factor deciding the trajectory of the film cooling jet. Jets with low blowing ratio tend to stay closer to the wall, meaning high film coverage. As the blowing ratio increases, the jets penetrate deep into the mainstream flow and hence the film cooling effectiveness on the wall remains poorly protected by the film. Sultan (2011) studied the effect of blowing ratio on the adiabatic film cooling effectiveness for a cylindrical hole geometry with an injection angle of 30°. From the figure 2.10, one can observe the above mentioned effect as the lateral and centerline evolution of the adiabatic film cooling effectiveness decreases with increase in blowing ratio.

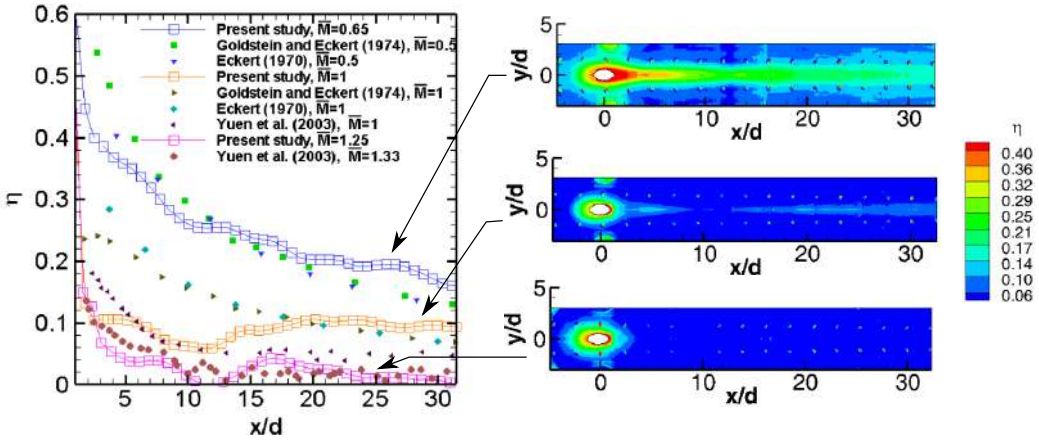

Figure 2.10: Adiabatic film cooling effectiveness of a single inclined cylindrical hole configuration at various blowing ratios by Sultan (2011).

2.2.2 Mainstream turbulence

For low blowing ratios, the effect of mainstream turbulence has an adverse impact on the adiabatic film cooling effectiveness. This can be related to the increased mixing of the mainstream flow with the film cooling jet, effectively increasing the temperature within the film. Studies by Mayhew *et al.* (2003) and Schmidt & Bogard (1996) at low blowing ratios have demonstrated the effect of freestream turbulence on the adiabatic film cooling effectiveness as in figure 2.11

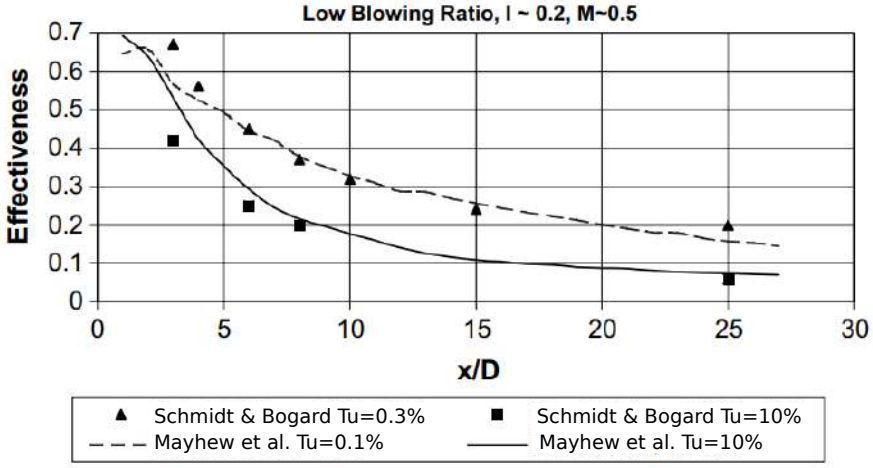

Figure 2.11: Results of the experimental study on the effect of freestream turbulence on the adiabatic film cooling effectiveness by Mayhew *et al.* (2003)

2.2.3 Injection angle

Upon changing the angle of injection (α) with respect to the streamwise flow, the film cooling characteristics have been found to be extensively influenced. As an example to demonstrate this effect, the results of the study by Yuen & Martinez-Botas (2003) are presented in the figure 2.12. They observed that a jet injected at an angle of 30° shows better film cooling performance in along the centerline and lateral directions than a jet injected at 60° or 90° angle. A jet injected perpendicularly at 90° showed the worst performances of all configurations. Hence, not surprisingly it is advantageous to have an low injection angle, preferably at 30°.

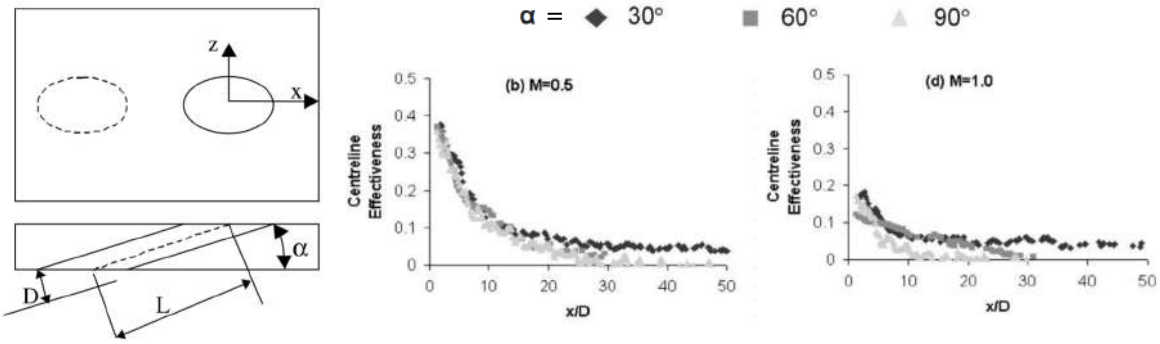

Figure 2.12: Results of the experiment obtained at different distances from the nozzle exit in the wall-normal direction showing the formation of a CRVP Yuen & Martinez-Botas (2003)

2.2.4 Hole shape

The use of shaped holes to improve the film cooling effectiveness has been widely studied. Adiabatic film cooling effectiveness for shaped holes as compared to a simple cylindrical hole have shown immense improvements. Gritsch *et al.* (1998) studied the fan shaped holes, Barigozzi *et al.* (2010) compared the laid back hole shape to the fan shape and cylindrical hole shape, Azzi & Jubran (2007) proposed a new hole shape called the converging slot-hole aiming for full coverage, Ramesh *et al.* (2016) proposed a new tripod hole shape and a trenched hole shape to produce anti-CRVP vortices were studied by Kalghatgi & Acharya (2015) to name a few of the innovative hole shapes. Figure 2.13 shows few selected types of holes shapes proposed by researchers. All these hole shaped were aimed to provide a better film cooling performances by reducing the mixing with the mainstream flow and showed improvements of over 50% over standard hole shapes.

2.3 Anti-vortex film cooling configurations

It is clear that the most important phenomenon in the jet in cross-flow configuration is the formation of the CRVP vortices. It is also seen that the CRVP vortices are detrimental to the film cooling effectiveness due to the entrapment of the freestream flow into the coolant flow, hence drastically reducing the coolant cover over the surface to be protected.

The academically studied film cooling configurations are seldom possible to be implemented in a real turbine. This is because the academic studies are conducted on film cooling holes that are orders of magnitude larger than the actual film cooling holes on the turbine blade which are of 0.5mm in diameter. These designs however promising are difficult to be machined into the turbine blade which are made of super-alloys and care must be taken to preserve thermal barrier coatings while drilling film cooling holes.

In this thesis, primitive cylindrical hole shape is used in the design of a novel film cooling configuration. With the advent of additive manufacturing techniques and improved machining processes, simple hole designs of very small sizes are possible. The high improvement in the film cooling effectiveness at high and low blowing ratios of the auxiliary hole configuration strongly merits implementation in production scale gas turbine blade fabrication, albeit improvement in manufacturing capabilities.

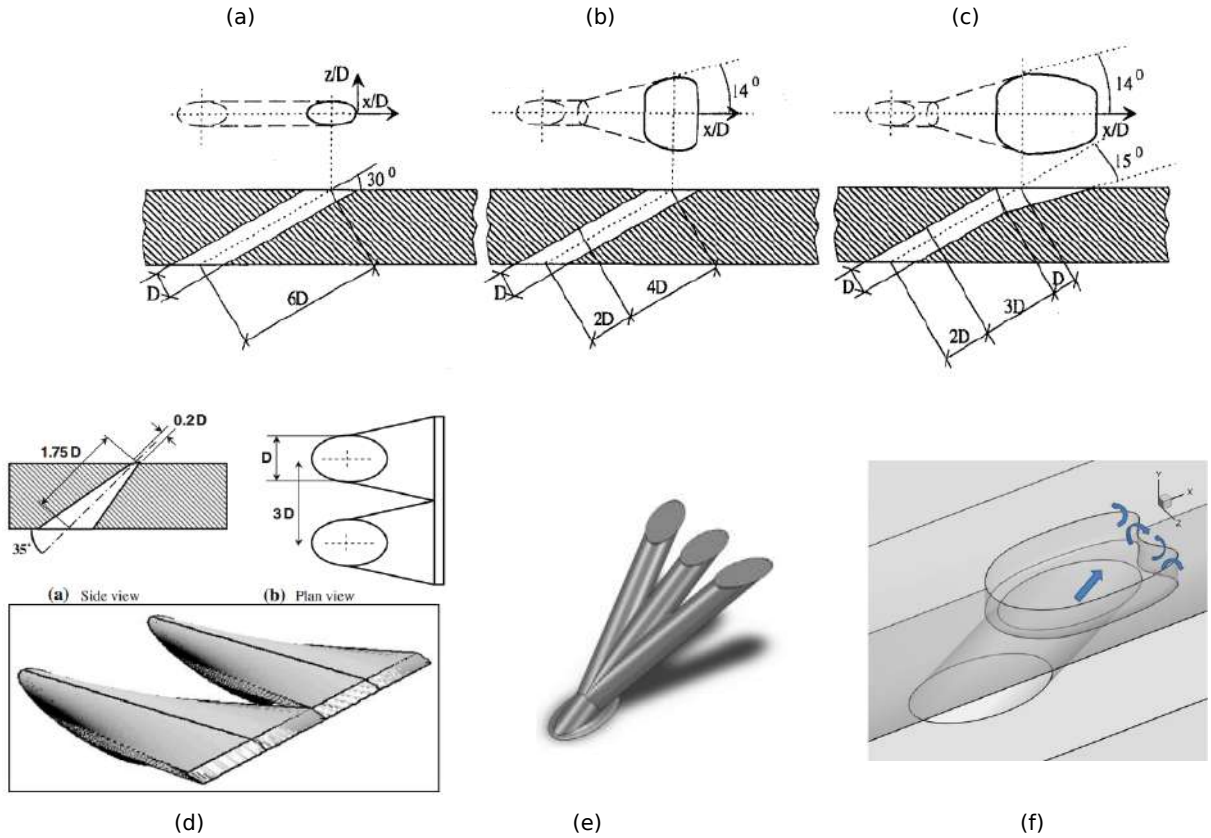

Figure 2.13: Film cooling hole configurations: (a) simple cylindrical hole (b) Fan shaped hole (c) Laid-back hole (d) Console hole (e) Tri-pod hole (f) Crater hole. Citations: Gritsch *et al.* (1998), Barigozzi *et al.* (2010), Azzi & Jubran (2007), Ramesh *et al.* (2016), Kalghatgi & Acharya (2015).

Heidmann & Ekkad (2008) put forward the possibility to add small holes near the main hole which are smaller in dimension. These smaller holes around the main hole could be in the upstream or downstream with respect to the main hole and they are called as 'auxiliary holes' or 'anti-vortex holes'. Figure 2.14 shows an example of the secondary hole system. In the figure, A represents the CRVP emanating from the small auxiliary holes which is smaller in intensity and B represents the CRVP formed from the jet arising out of the main hole. The resultant flow system due to the interaction of these vortices is complex and needs to be studied in detail.

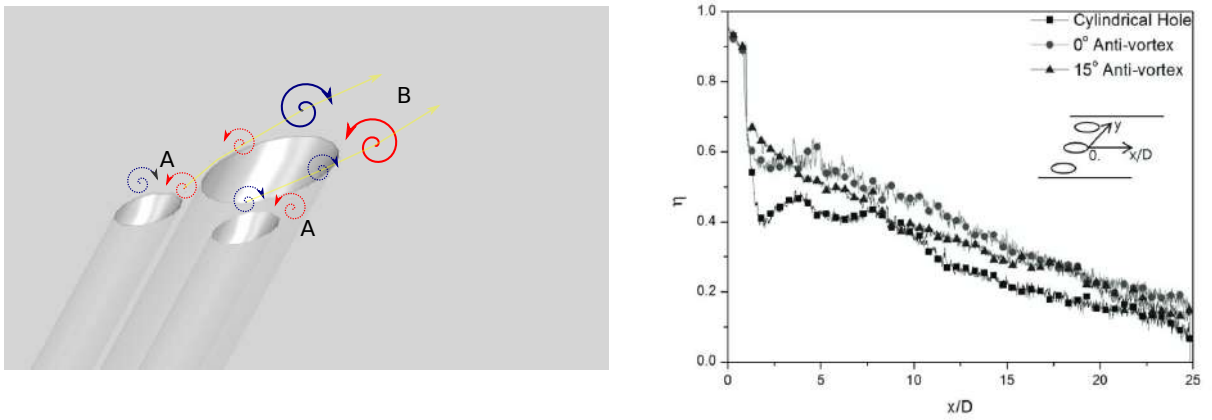

Figure 2.14: Left: Representation of an auxiliary hole configuration. Right: Adiabatic film cooling effectiveness of simple cylindrical hole and two streamwise injection angles for a configuration where auxiliary holes placed are along the lateral axis of the main hole by Park *et al.* (2014).

Various numerical studies were made on these configurations, Javadi *et al.* (2003) worked on the effect of the presence of two small holes downstream of the main hole , Park *et al.* (2017)

studied the effect of two small cylindrical holes in the aft and upstream positions with respect to the main hole while Ely et al. made a series of studies on the effect of the presence of auxiliary holes on the primary CRVP formed due to the main hole (Ely & Jubran (2008), Ely & Jubran (2009), Ely & Jubran (2010), Ely & Jubran (2012)). The film cooling effectiveness was seen to improve significantly for a range of blowing ratios in all the above stated works.

Experimental studies were made by Wu *et al.* (2016) at very low temperatures of 50°C in the mainstream flow and 33°C in the coolant flow and they studied the adiabatic film cooling effectiveness of few auxiliary hole configurations by the use of thermographic liquid crystals on a flat plate. They too showed experimentally the superiority of the auxiliary hole system.

Conclusion

Various parameters which determine the flow patterns in a JICF configuration have been discussed. A brief review of the factors affecting film cooling effectiveness have been described. It is identified that the CRVP is the most detrimental factor for film cooling and hence the optimisation of CRVP can lead to better film cooling effectiveness. So, there is a need to test auxiliary hole configurations, which are relatively easy to integrate into the turbine blade instead of complex shapes. It is also identified that there are no experimental studies made on the auxiliary hole configuration at higher temperatures and the use of novel measurement techniques to understand the vortex mechanisms better. In this thesis, a thorough investigation of the auxiliary hole configuration at a streamwise injection angle of 30° is made at relatively high temperature conditions (150°C) in order to analyse qualitatively and quantitatively the aero-thermal ramifications due to the presence of auxiliary holes experimentally and numerically. As a first step, a RANS study is conducted to study the influence of auxiliary holes position around the main hole on the film cooling performance which will be explained in Chapter 3.

Chapter 3

Auxiliary holes position optimisation: RANS study

In this chapter, RANS simulations are performed to optimise the spacial position of the auxiliary holes with respect to the main hole and to test the performance of two auxiliary holes configurations. The results are compared with the results obtained numerically and experimentally of a baseline case (simple cylindrical hole) from previous results of an in-house PhD thesis. A brief introduction is followed by a description of the geometry and numerical setup. Results on aerodynamic characteristics of the different systems are discussed and their implications on the thermal behaviour are highlighted.

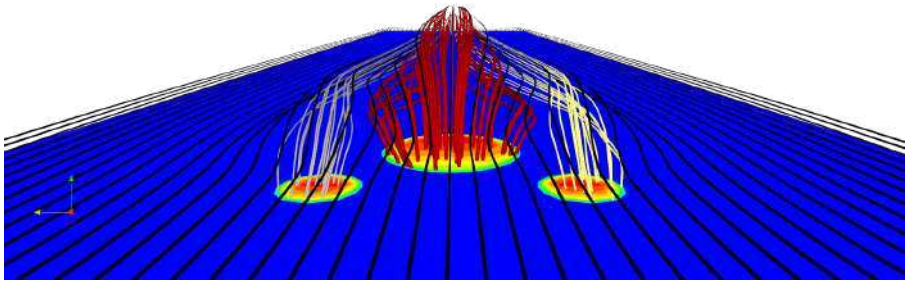

Figure 3.1: Flow visualisation of streamlines from auxiliary holes configuration seen from upstream location. (in-house simulation)

Contents

3.1 Introduction **20**
3.2 Numerical setup **22**
3.2.1 Geometry 22
3.2.2 Solver and Boundary conditions 22
3.2.3 Mesh Validation 23
3.3 Results **25**
3.3.1 Adiabatic Film Cooling Effectiveness 25
3.4 Heat transfer characteristics **26**
3.4.1 Adiabatic film cooling effectiveness 26
3.4.2 Heat transfer 28
3.5 Analysis of flow aerodynamics **33**
3.5.1 Vortex intensity 33

3.5.2 Streamlines analysis 35
3.5.3 Boundary layer characteristics 35
3.6 Review 37

3.1 Introduction

There is a need to optimise the number of geometrical cases studied experimentally as the cost involved in fabricating and running the test rig can be enormous. Hence time averaged RANS simulations have been realised so as to have a first optimisation of the hole shape and the location of the holes. As a part of a previous research project, the author conducted basic RANS studies on various film cooling configurations using StarCCM+ software. Few geometrical parameters are shown in figure 3.2. In the figure, α is the streamwise injection angle, D is the diameter of the hole, H and L are the lateral and longitudinal distance of auxiliary holes from the main hole.

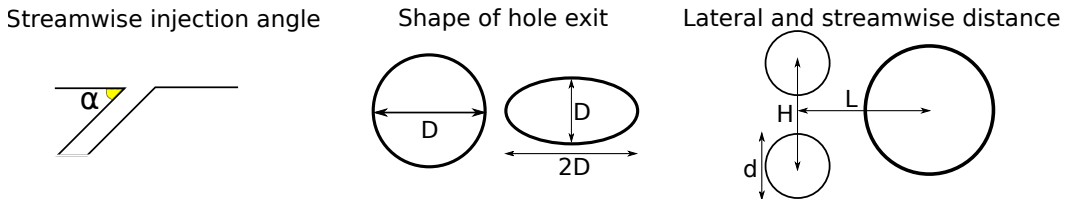

Figure 3.2: Geometrical parameters frequently used in film cooling studies.

The optimisation process was based on the Adiabatic film cooling effectiveness η.

$$\eta = \frac{T_{aw} - T_\infty}{T_c - T_\infty} \tag{3.1}$$

As a first step, the influence of injection angle on the adiabatic film cooling effectiveness η (refer eq.3.1) was studied by varying the injection angle (30°, 45°, 60°, 90°). It is inferred that it is beneficial to have a streamwise injection angle, preferably 30°, over other angles of injection. In total, 12 different parameters were analysed and it was determined that having an auxiliary hole upstream of a main hole is beneficial to the film cooling process. The blowing ratio 'M' (refer eq.7.2) and the shape of the hole exit also had a profound effect on the film cooling effectiveness.

$$M = \frac{\rho_c U_c}{\rho_\infty U_\infty} \tag{3.2}$$

To summarize, the following parameters were studied.

- Streamwise injection angle: 30°, 45°, 60°, 90°
- Longitudinal distance of auxiliary holes from main hole: 1D, 2D
- Hole arrangement: Single hole and auxiliary hole arrangement
- Blowing ratio: 0.65, 1, 1.25 (attachment, re-attachment, jet liftoff regimes)
- Wall conditions: Adiabatic and heat-flux

Figure 3.3 shows a sample simulation of a film cooling system with the presentation of (a) velocity contour, (b) temperature contour with wall heat flux (c) a sample mesh used.

With these initial CFD simulations (not presented here for brevity), it was concluded that having a streamwise injection angle of 30°, longitudinal distance H of 1D for the auxiliary holes position, and an elliptical hole exit were beneficial geometrical parameters for the film cooling process. Additionally, low blowing ratios showed higher adiabatic film cooling effectiveness than a high blowing ratio. This confirmed the results in the literature (Bunker (2005)).

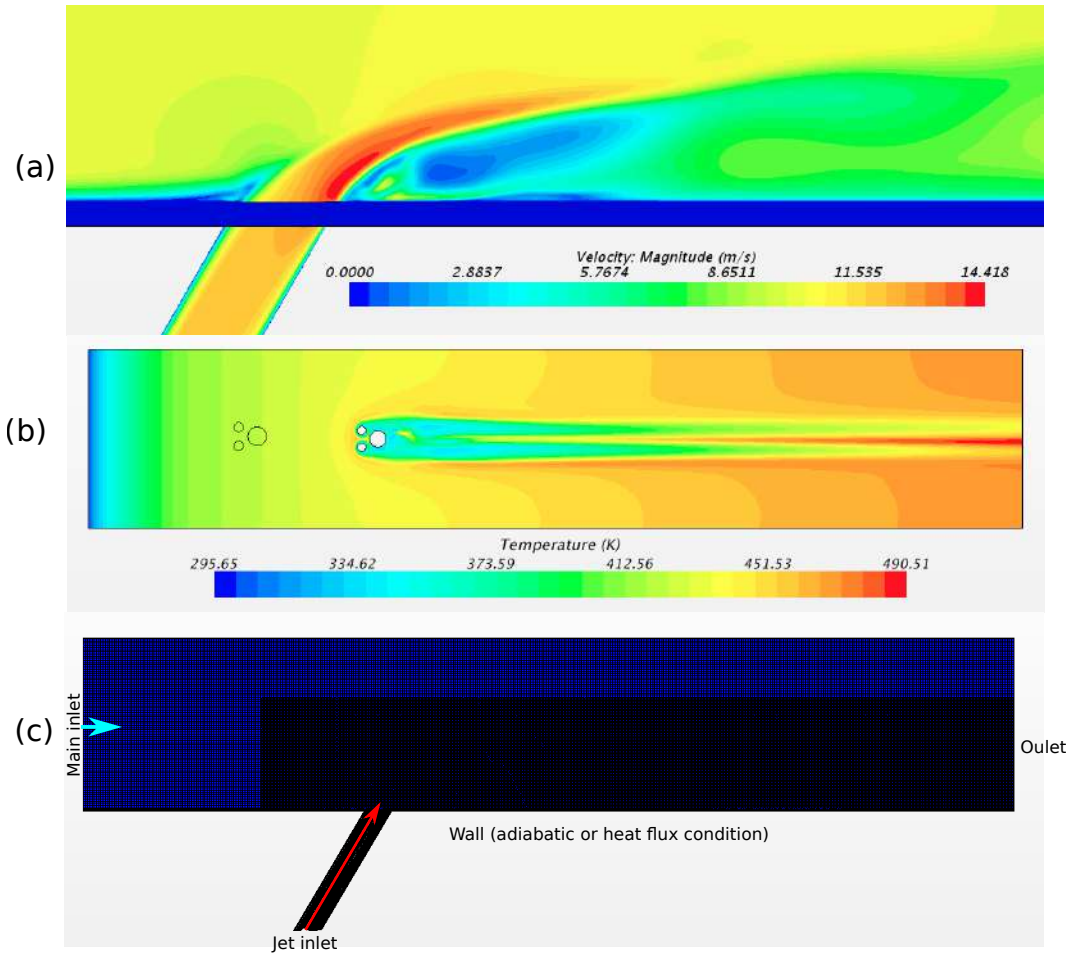

Figure 3.3: Film cooling study from a previous work. (a) Velocity contour, (b) Temperature contour, (c) mesh used in few of the cases are shown.

In this current RANS study, three geometric hole configurations (Single hole baseline and two auxiliary hole configurations) are tested at three different blowing ratios (M=0.65, 1, 1.25), one at each blowing regime (attached, lift-off and reattachment, and penetration regimes). Experimental studies on a single cylindrical hole were conducted by Sultan *et al.* (2011). The main objective of this previous experimental study was to compare the effect of bulk pulsations as compared to steady blowing on the film cooling performance. The experimental results from the steady cases will be used as a reference to compare and validate the procedure used to conduct the simulations.

Through this RANS study using OpenFOAM 7, a qualitative and quantitative analysis of a few time-averaged parameters judging the effectiveness of a film cooling system is performed

- Adiabatic film cooling effectiveness
- Mean vorticity evolution
- Heat transfer coefficient
- Net Heat Flux Reduction
- Flow visualisations

3.2 Numerical setup

3.2.1 Geometry

Due to the reasons mentioned in the introduction of this chapter, three different hole geometries are chosen to be studied in this chapter where two cases are auxiliary hole configurations and one is a standard cylindrical inclined hole (see Table 3.1).

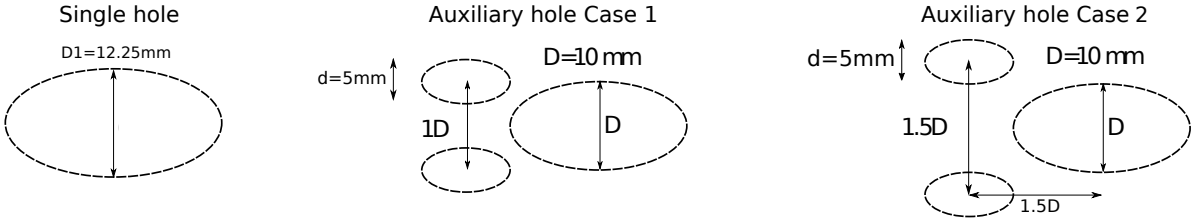

Figure 3.4: Geometrical representation of the three configurations tested.(not to scale)

A simple cylindrical hole of diameter D_1 of 12.25mm inclined at 30° with respect to the flow, and two auxiliary hole configuration cases are studied. The diameters of the main hole of the auxiliary hole configuration which is of 10mm and the smaller auxiliary holes of 5mm diameter upstream of the main hole as in figure 3.4 are chosen so as to have a similar area as of the simple cylindrical hole base case. It should be noted that due to this reason, the ensemble of auxiliary hole configuration has the same blowing ratio as the single hole case. The blowing ratio of the auxiliary holes are the same as that of the main hole as a velocity is imposed at the hole entry. The geometrical details are summarised in the table 3.1.

Table 3.1: Geometric parameters

Parameter	**Single hole**	**Aux. hole case 1**	**Aux. hole case 2**
Main hole Diameter	$D1$=12.25 [mm]	D=10 [mm]	D=10 [mm]
Aux. hole Diameter	-	d= 5 [mm]	d= 5 [mm]
Aux. hole lateral distance	-	H=10 [mm]	H=15 [mm]
Aux. hole longitudinal distance	-	L=15 [mm]	L=15 [mm]

Single cylindrical hole shape is chosen as a reference case due to the availability of experimental data to compare the CFD results with. The experimental study of Q.sultan et al Sultan *et al.* (2017) at steady blowing (without pulsation) are used for this purpose.

3.2.2 Solver and Boundary conditions

All the simulations in this study are RANS steady state simulations which were performed using openFoam 7. k-ω SST turbulence model has been used with second order equations to solve the pressure, velocity and turbulence terms. The three different hole configurations as discussed above have been tested at three blowing ratios namely, attached, lift-off and reattachment, and penetration regimes (M=0.65, M=1, M=1.25 respectively) under adiabatic wall conditions, and with a constant heat flux of 1512 W/m^2 imposed on the wall (similar to experimental base case). The heat flux case will be used to calculate the heat transfer coefficients, Net Heat Flux Reduction (NHFR) which are indicators of film cooling performance. A flat plate case with no holes is also analysed so as to calculate the heat transfer coefficient. A plenum is not used in this study as a feed to the coolant jets, as the length of the coolant channel is long enough to have a developed flow at the jet exit. The boundary conditions are mentioned in the table 3.2.

It has to be noted that the temperature at the inlet is lower (20°C) and the temperature of the injected 'coolant' jet is higher (40°C). These conditions are taken into account so as to compare the single hole results with those of experiments Sultan *et al.* (2011).

Since the problem is density-based and steady state, the rhoSimpleFoam solver with the Geometric agglomerated Algebraic MultiGrid preconditioner (GAMG) was used to solve the pressure term and Preconditioned bi-conjugate gradient (PBiCGStab) with DILU pre-conditioner for the U, k and omega terms.

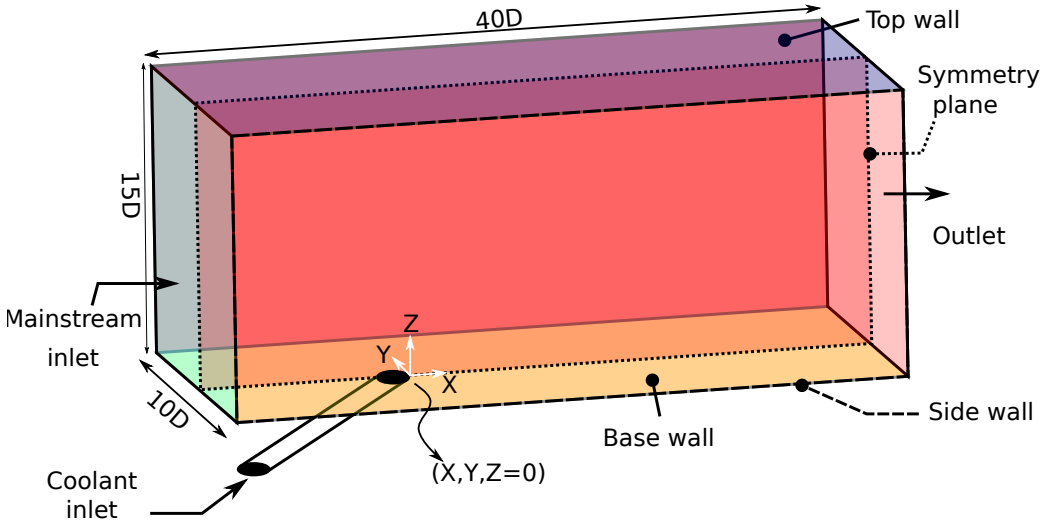

Figure 3.5: Illustration of the computational domain with the boundary conditions.

Table 3.2: Boundary conditions

Parameter	**Value**
Freestream velocity	10 [m/s]
Freestream temperature	20 [°C]
Freestream turbulence intensity	5%
Jet inlet velocity	6.9 , 10.7 , 13.4 [m/s]
Blowing ratio	0.65, 1, 1.25
Jet inlet temperature	40 [°C]
Outlet pressure [Pa]	101325
Wall heat flux [W]	Adiabatic or Heat flux (1512 W/m^2)
Wall roughness	Smooth

3.2.3 Mesh Validation

Since the geometry is symmetrical and the problem is steady state, it is possible to simulate half of the domain by imposing a symmetry boundary condition on the plane along the axis of the central hole (as shown in figure 3.5) to obtain similar results as in a full geometry case. This helps in reducing the number of mesh elements by two directly. In the current study, tetrahedral meshes were used in all the domain. As seen in figure 3.6, three regions (Coolant channel, near-hole region, and the region upto 3.5D away from the wall) have a refined mesh. A prism layer with 15 layers has a thickness of 2mm to capture the boundary layer flow field better. The mesh was generated using StarCCM+ mesher and the Table 3.3 provides data on the different meshes used. The wall Y+ values were less than 1 throughout the domain for all the cases including the highest blowing ratio case. To perform the mesh validation procedure, the single hole case at a blowing ratio M=1 is used.

The grid convergence index(GCI) as suggested by Roache (1998) is employed to determine the quality of the mesh used. Three different meshes are studied and a parameter is chosen to be analysed.

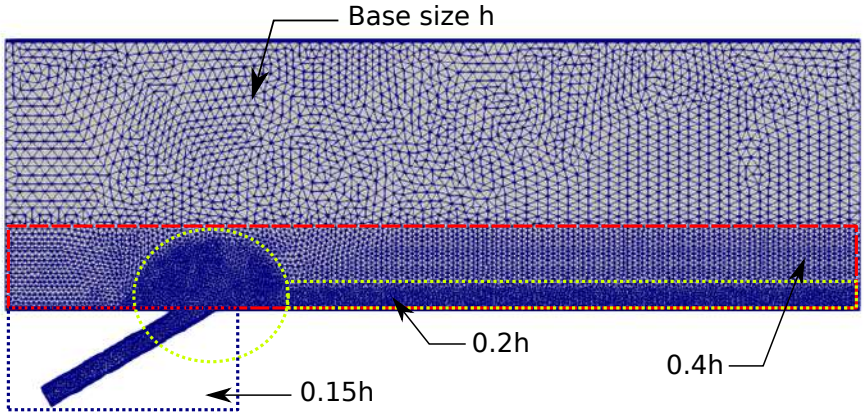

Figure 3.6: Side view of the mesh where the three refinement zones are clearly seen.

Table 3.3: Mesh statistics

Mesh	Cell size	Cells	Prism layers	f
1-Fine	4mm	4 million	15	0.158
2-Medium	6mm	2 million	15	0.155
3-Coarse	9mm	1 million	15	0.171

An adiabatic wall provides thermal information of the flow immediately above the wall. Hence, clear information of the 'cooling effect' of the injected jet can be derived using the adiabatic wall temperature distribution over the wall. The adiabatic film cooling effectiveness is defined as

$$\eta = \frac{T_{aw} - T_\infty}{T_c - T_\infty} \tag{3.1}$$

where T_{aw} is the adiabatic wall temperature, T_c is the injected jet temperature and T_∞ is the freestream temperature. The Richardson procedure for the GCI study is presented. The three meshes are defined as follows - Mesh 1 (Fine), Mesh 2 (Medium), Mesh 3 (Coarse). Considering f as the variable (adiabatic film effectiveness η), averaged values of this variable are f1, f2, f3 corresponding to the fine, medium and coarse meshes. The refinement ratio 'r' (not to be confused with velocity ratio) between the different meshes is 1.5 where r is defined as h_2/h_1 with h as the base size of each cell (not to be confused with the usual h used to denote heat transfer coefficient).

The order of convergence p is defined as

$$p = ln\left(\frac{f_3 - f_2}{f_2 - f_1}\right)/ln(r) \tag{3.3}$$

Richardson extrapolation to predict the value at h=0 is obtained by

$$f_{h=0} = f_1 + \frac{f_2 - f_1}{r^p - 1} \tag{3.4}$$

Using the known values, it is found that the Richardson extrapolation value is $f_{h=0}$= 0.15892. From this one could calculate the Grid convergence index for the two finest grids (Mesh 1 and 2). The GCI is given as

$$GCI = \frac{F_s|e|}{r^p - 1} \tag{3.5}$$

where e is the error between the two grids and F_s is an optional safety factor as 1.25 (recommended value for two or more grids studied).

This gives the result $GCI_{1,2}$= 0.73% which is well within the accepted range of 5% deviation from the Richardson extrapolation value $f_{h=0}$. In addition to this, one can see from figure 3.7 that the medium mesh is in accordance with the experimental values of Sultan (2011). Hence it can be concluded that the Mesh 2 is good enough to solve the current problem.

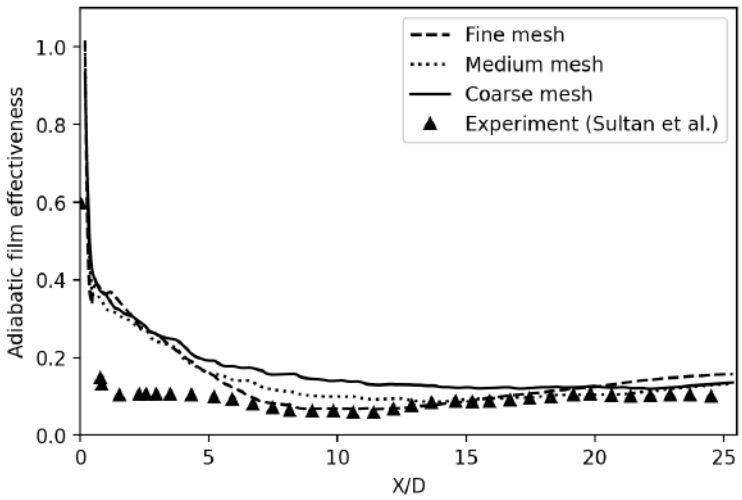

Figure 3.7: Centerline adiabatic film cooling effectiveness for single hole case at M=1 for the three meshes used in the GCI study.

3.3 Results

3.3.1 Adiabatic Film Cooling Effectiveness

As discussed in the above sections, the adiabatic film cooling effectiveness (AFCE) is the most frequently used parameter defining the effectiveness of a certain film cooling arrangement. A higher value of AFCE indicates a better wall thermal protection with an imposed adiabatic wall boundary condition.

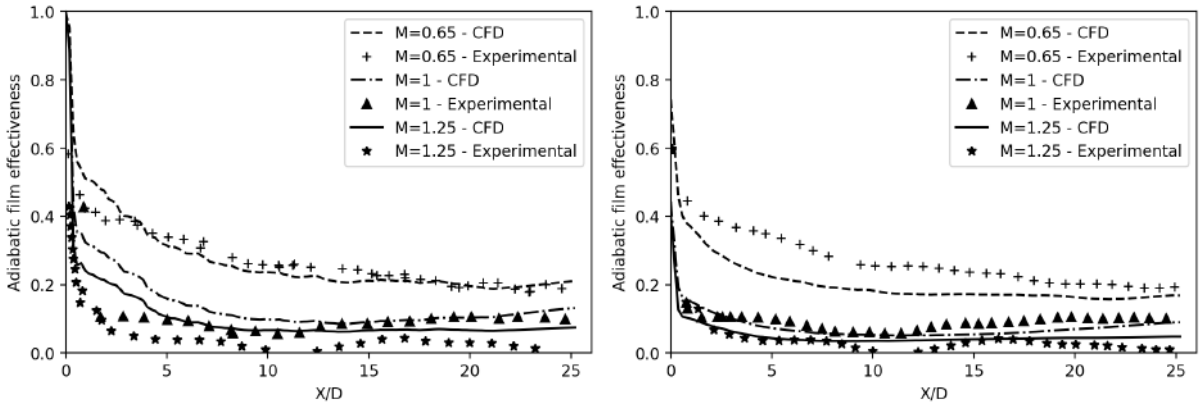

Figure 3.8: Comparison of numerical and experimental results: Evolution of centerline (left) and lateral AFCE (right) along the X-axis for various blowing ratios: M=0.65; M=1; M=1.25

The longitudinal centerline the adiabatic film cooling effectiveness (AFCE from now on) for the three blowing ratios is presented in the figure 3.8, with the single hole case solved numerically and a comparison with the baseline experimental single hole case values. The CFD simulations of the single hole case follow the results obtained experimentally, although there is a slight deviation close to the hole exit. This over estimation is expected from RANS simulations which tend to align the jet flow towards the central axis of the hole and hence a higher estimation of the AFCE. One other factor is that the experimental results could be influenced by the non-uniform heating around the hole exit in the study by Sultan *et al.* (2017).

The laterally averaged adiabatic film cooling effectiveness results are presented in the figure 3.8 (right) for the different hole configurations and blowing ratios. The AFCE values on the wall are averaged over a distance of (Y/D=0 to 1.5D) The CFD predictions of the single hole case follow the experimental values qualitatively despite a slight under prediction for the case with blowing

ratio M=0.65. Nevertheless, from these figures it can be safely assumed that the single hole case predictions are accurate enough to be compared with the auxiliary hole configurations, validating the mesh and the turbulence models used in this RANS simulation.

3.4 Heat transfer characteristics

Since the mesh and the solver are validated, the further sections, results obtained numerically alone will be discussed. The effects of the aerodynamic characteristics of the film cooling arrangement has a profound effect on the thermal characteristics of the wall. In this section, a few parameters are analysed concerning the thermal performance of the three hole systems (see figure 3.4).

3.4.1 Adiabatic film cooling effectiveness

The longitudinal centerline AFCE for the three blowing ratios is presented in the figure 3.9 (a-c), with the three configurations studied numerically. Both the auxiliary hole configurations show higher effectiveness than a simple cylindrical jet for all the blowing ratios. Table 3.4 summarizes the improvement in centerline adiabatic film cooling effectiveness of the case 1 and case 2 over the baseline case for M=0.65, 1 and 1.25. Here, the AFCE is averaged laterally at different X/D zones. In some regions, upto 265% increase in adiabatic film cooling effectiveness for case 2 is achieved. Case 2 performs better than Case 1 for all blowing ratios and in all regions.

The laterally averaged AFCE results are presented in the figure 3.9 (d-f) for the different hole configurations and blowing ratios. The AFCE values on the wall are averaged over a distance of (Y/D=0 to 1.5D). As seen in the centerline AFCE graphs, Auxiliary hole configuration case 2 provides the best protection in the lateral directions too.

Table 3.4: Percentage increase in centerline film cooling effectiveness compared to baseline case

Blowing ratio	Total domain		0<X/D<5		5<X/D<10	
	Case 1	**Case 2**	**Case 1**	**Case 2**	**Case 1**	**Case 2**
0.65	30%	61%	19%	59%	39%	71%
1	84%	149%	39%	110%	123%	198%
1.25	69%	184%	36%	134%	114%	265%

Figures 3.10 and 3.11 are the contour plots of the AFCE on the wall and the evolution of the fluid temperature at different planes. Analysing figure 3.10 representing the single hole case, one can observe that having a lower blowing ratio is beneficial so as to have a higher AFCE. This can be attributed to the fact that at low blowing ratios, the fluid emanating from the jet rests close to the wall as the energy in the jet is not enough to penetrate the cross-stream flow. At higher blowing ratios, the flow tends to lift off from the surface and penetrates into the free stream. For M=1, it can be seen that the flow temporarily detaches from the wall surface at X/D=3 but reattaches further downstream at X/D=10. This is due to the insufficient momentum of the jet to continue penetrating into the flow and is hence bent downwards towards the wall by the freestream. This phenomenon is seen in the experiments (Sultan (2011)) as well as numerical simulations ((a) and (b) in figure 3.10). At higher blowing ratios as in the case M=1.25, the flow has enough energy to penetrate deep into the freestream flow and mix at a height away from the wall.

Also in the figure 3.10, the second and the third rows show the AFCE contour for the Auxiliary holes configurations. Instantly, one can deduce that there is a stark augmentation of AFCE as compared to the single hole case. The lateral spread of the jet along the wall is predominantly higher and the fluid from the jet travels a longer distance from the hole exit along the wall surface.

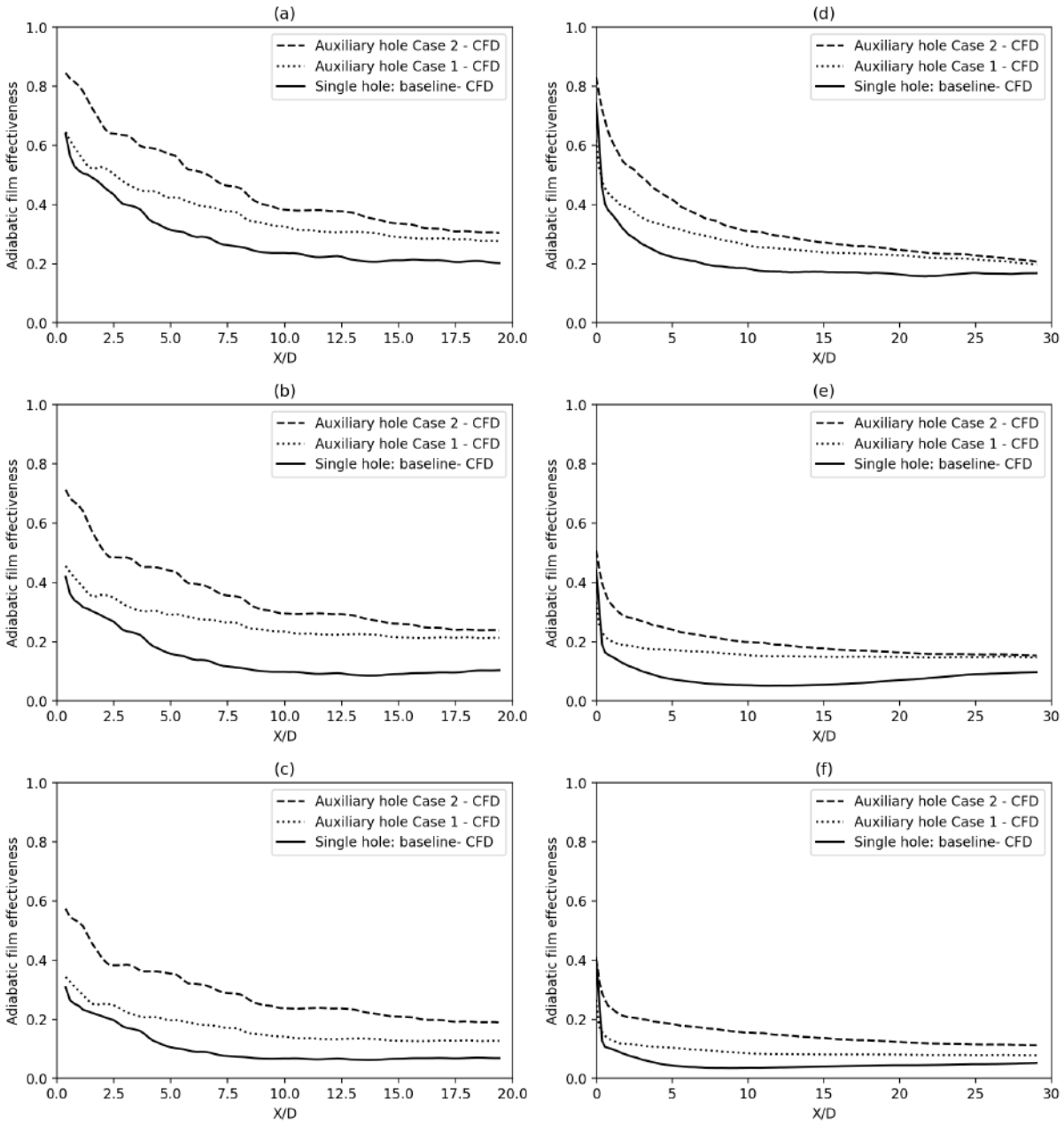

Figure 3.9: Evolution of centerline (a-c) and lateral AFCE (d-f) along the X-axis for various blowing ratios. (a,d) M=0.65; (b,e) M=1; (c,f) M=1.25

Similar to the baseline single hole case, having a lower blowing ratio is beneficial to the film cooling process.

Figure 3.11 shows the temperature evolution along different planes and the lateral distribution of the jet. This figure permits us to visualise the flow-field in three dimensions. The rows represent the different cases studied and moving along the columns show the effect of blowing ratio. To visualise the trajectory of the injected jet, the center plane of the non-dimensional fluid temperature θ is shown.

$$\theta = \frac{T - T_\infty}{T_c - T_\infty} \tag{3.6}$$

For a given configuration, as discussed before, the flow is either attached, or re-attached or penetrates into the mainstream. Also, for a given blowing ratio, the presence of two auxiliary holes seem to force the injected flow towards the wall. In all, the Case 2 configuration shows the best effectiveness, closely followed by Case 1 and the baseline case.

To complete the discussion on this area, figure 3.12 is presented to study jet trajectories. Figure 3.12 shows the contour plots of non-dimensional temperature θ. Here, (a-c) show temperature contours for M=0.65, (d-f) for M=1, (g-i) for M=1.25. Figures (j) and (k) show the near-hole area. For a given blowing ratio, it can again be confirmed that the injected flow remains closer to the wall for the auxiliary hole cases than the baseline case. Case 2 performs better than Case 1 in terms of injected flow remaining closer to the wall. The jet trajectories are traced in the figures (j) and (k) for the baseline case and auxiliary hole case 2 respectively for M=1.25. In figure (k), the trajectory of the baseline case is also shown to enumerate the differences between the two cases. It is obvious that despite having the same mass flow rate, Case 2 shows better coverage as the injected jet stays low and closer to the wall.

3.4.2 Heat transfer

In the previous section, an adiabatic wall boundary condition was imposed. In order to study the heat transfer characteristics, the adiabatic wall boundary condition to a constant wall heat flux can give better insights due to the possibility to calculate the local and spatial average heat transfer coefficient. A lower heat transfer coefficient indicates a lower heat transfer into the wall. The heat transfer coefficient for a constant wall heat flux q applied to the wall can be calculated as

$$h = \left(\frac{q}{T_w - T_{aw}} \right) \tag{3.7}$$

The parameter driving the heat transfer here is the difference between the wall temperature and a reference temperature, in this case the adiabatic wall temperature previously calculated. In order to calculate the heat transfer coefficient, further simulations were carried out with a constant wall heat flux of 1512 W/m^2 imposed on the wall containing the film cooling hole as in the experimental case of Sultan *et al.* (2017).

It is insufficient to consider only the adiabatic film cooling effectiveness and the heat transfer coefficient locally on the wall to determine the effectiveness of the cooling setup. This is because of the fact that injecting a fluid into the freestream alters the flow significantly by augmentation of turbulence and hence it could be detrimental to the heat transfer into the wall. In order to quantify the net improvement due to film cooling, a parameter called the Net Heat Flux Reduction is used.

$$NHFR = 1 - \frac{h}{h_0} \left(1 - \frac{\phi}{\eta} \right) \tag{3.8}$$

Where ϕ is the normalised surface temperature of the wall with the imposed constant heat flux condition and it is given by the relation

$$\phi = \frac{T_w - T_c}{T_\infty - T_c} \tag{3.9}$$

Generally, a value of 0.6 is assumed for this parameter and is used for the calculations. (Bogard & Thole (2006))

In figures 3.13 (a)-(c), the evolution of centerline NHFR values along X-direction are presented for the three film cooling configurations. It can be observed that the Auxiliary hole: Case 2 performs the best among all the cases in the near and mid downstream locations. Far from the hole, there are few differences between the Case 1 and Case 2 auxiliary hole configurations. Figures (d)-(f) highlight the NHFR values averaged laterally over a distance of 1.5D from the center of the hole. Although the laterally averaged AFCE values show a good effectiveness just downstream of the hole, it can be seen from the figure 3.13 (e) and (f) that the NHFR could be even negative at some regions for the single hole case. The superiority of both the auxiliary hole cases is established from this figure as for all the blowing ratios, the NHFR values are higher than the single hole case. Again, the Case 2 performs the best.

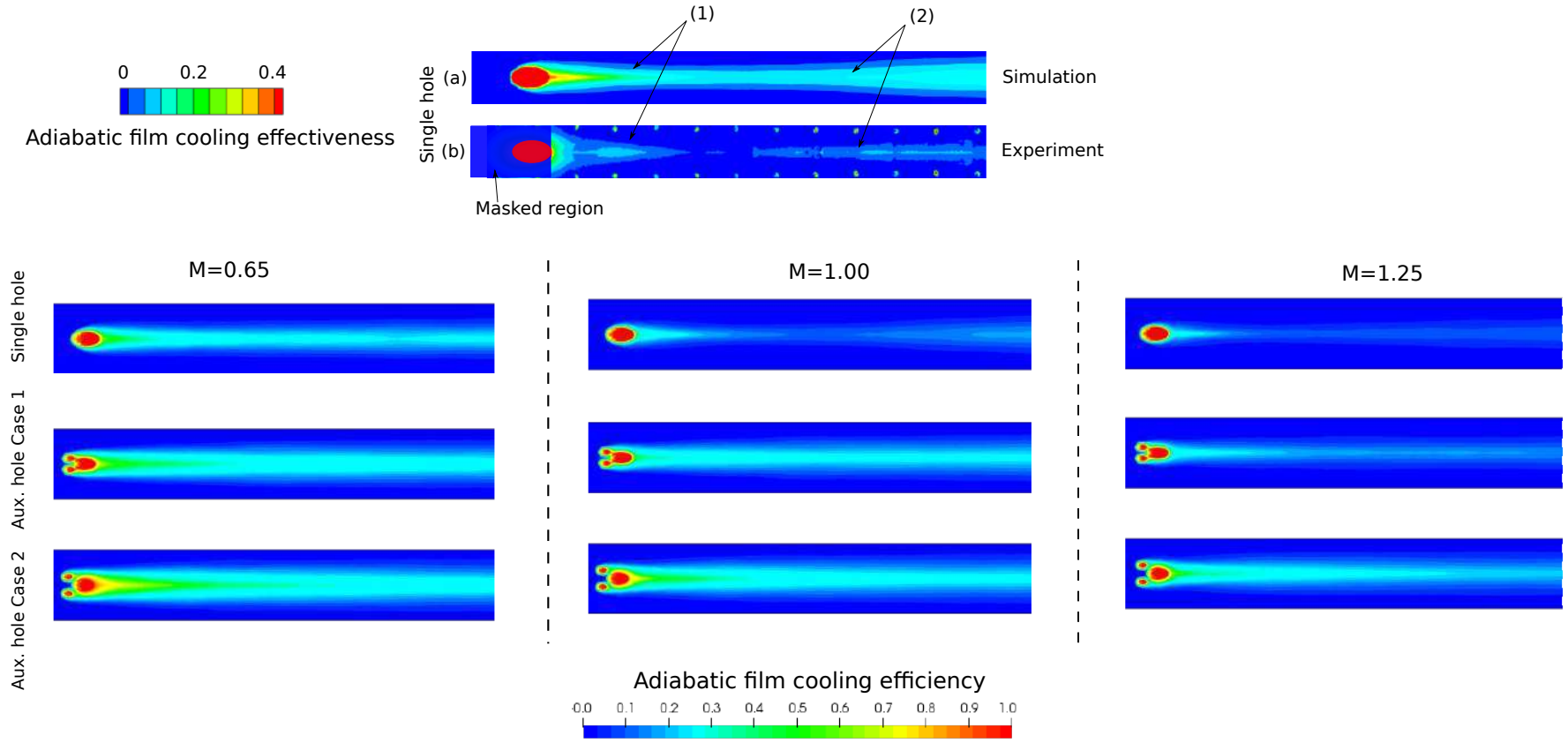

Figure 3.10: Top view of adiabatic film cooling effectiveness contours along the streamwise direction for the three configurations at different blowing ratios

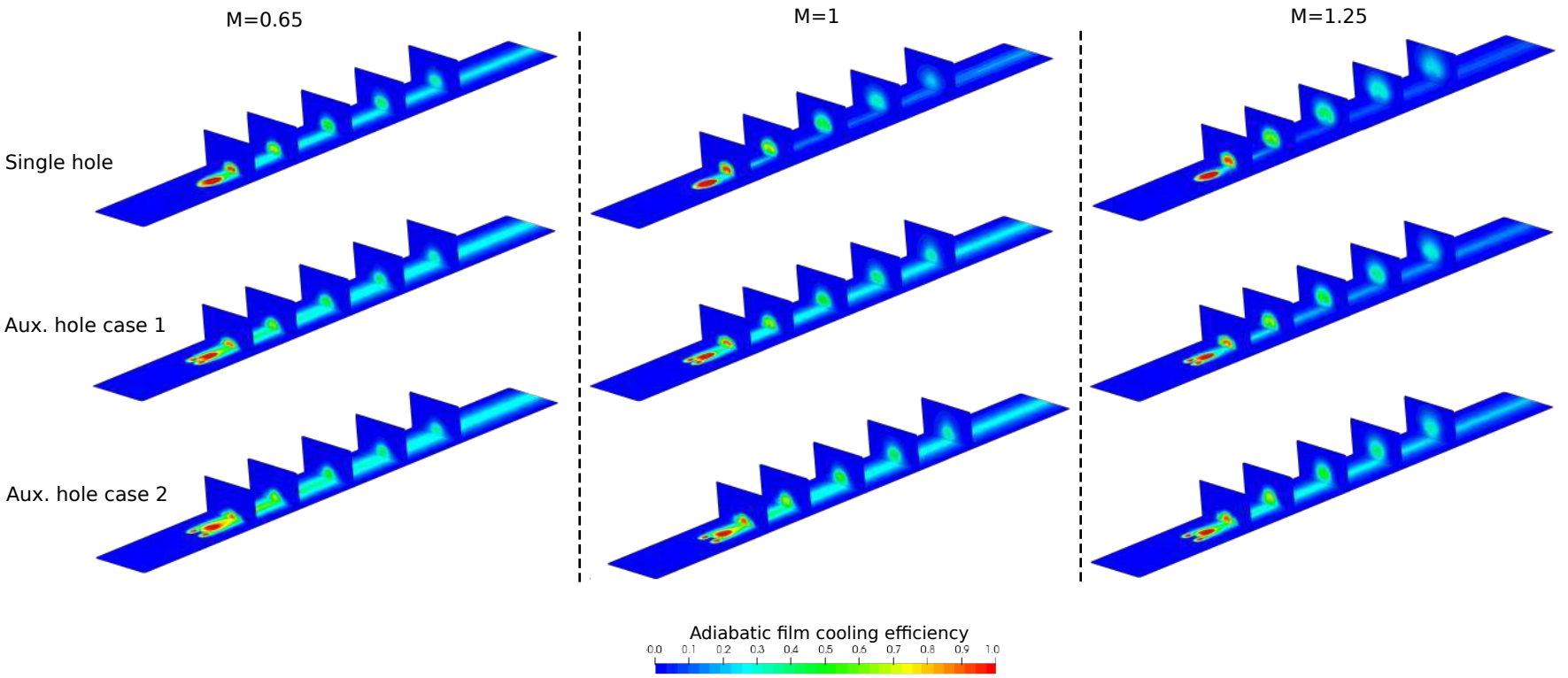

Figure 3.11: Evolution of adiabatic film cooling effectiveness along the streamwise direction for the three configurations at different blowing ratios. Note: the planes perpendicular to the stream show non-dimensional temperature θ.

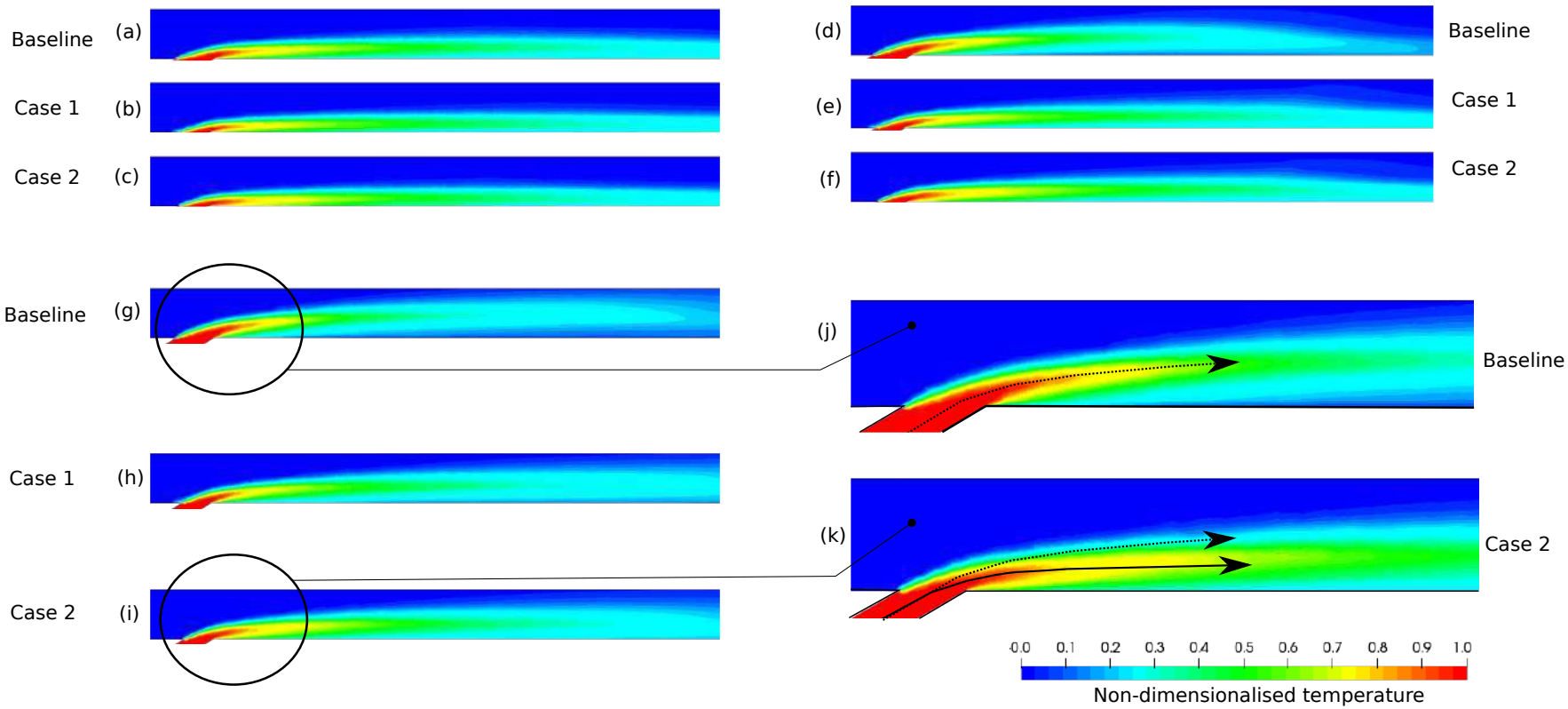

Figure 3.12: Temperature field along the symmetry plane for the various film cooling configurations at different blowing ratios : M=0.65 (a-c); M=1 (d-f); M=1.25 (g-i). Figures (j) and (k) are a zoom of (g) and (i) to highlight the jet trajectories of the single hole and Auxiliary hole Case 2.

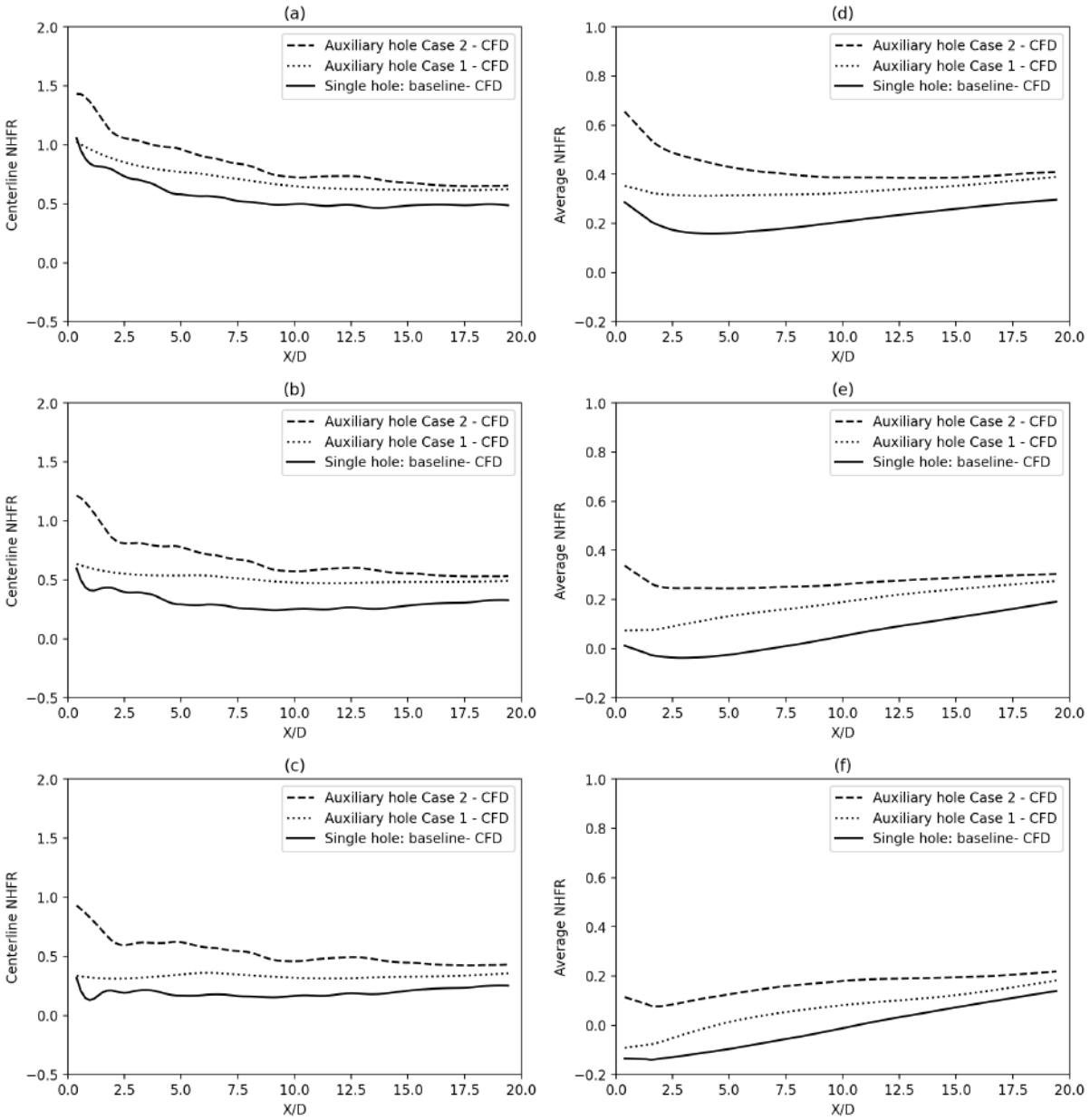

Figure 3.13: Evolution of centerline (a-c) and laterally averaged NHFR (d-f) values along the longitudinal axis (X-axis) for various blowing ratios. (a,d) M=0.65 (b,e) M=1 (c,f) M=1.25

3.5 Analysis of flow aerodynamics

As explained in Chapter 2, the counter rotating vortex pair (CRVP) is the biggest detrimental factor for film cooling process. The quest to reduce the intensity of this vortex system and its height is the reason to study the auxiliary hole arrangement. In this section, the vortex intensities, boundary layer and streamlines close to the wall are analysed. In order to facilitate easy understanding of the figures, the case 1 auxiliary hole is omitted from discussion. It is also clear from the previous section that the case 2 performs better than the case 1.

3.5.1 Vortex intensity

The interaction of the freestream with the jet causes shear along the outer edges of the jet which eventually form into the CRVP structure. Measure of the maximum vorticity intensity (refer eq. 3.10) at different locations highlights the position of the CRVP from the wall. An upstream front view of the CRVP formation in the single hole case at a blowing ratio of 0.65 is seen in the figure 3.14

Vorticity defined as the curl of the velocity is an indicator of the presence of large structures in the fluid flow.

$$\omega = \nabla \times U \tag{3.10}$$

$$\text{vortex intensity} = \sqrt{\omega_x^2 + \omega_y^2 + \omega_z^2}$$

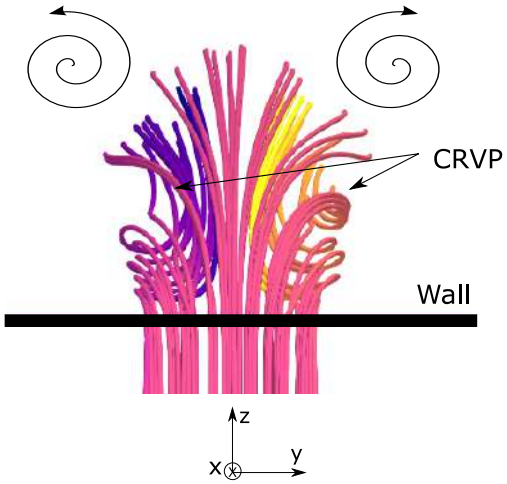

Figure 3.14: Upstream view of CRVP formation at the hole exit in a single hole case from RANS simulations for M=1.25

A lower CRVP height and intensity in the jet emanating from the hole means less entrainment of the freestream into the jet axis and hence the jet is able to travel longer distances due to reduced mixing.

Figure 3.15 with the black lines shows the locations where the laterally averaged vortex intensities are measured. Laterally averaged vortex intensities (Y/D = 0 to 1.5) at various height locations are plotted in figure 3.16 (a)-(c) (along Z/D=0.5) and figure 3.16 (d)-(f) (along Z/D=1).

From figure 3.16 (a) there is not much difference in the vortex intensity or the location since the flow is attached to the wall for all the three hole arrangements. However at higher blowing ratios, it can be seen that the auxiliary hole arrangement fares better than the single hole case as seen in (b) and (c).

At a higher location from the wall (Z/D=1) as in figure 3.16 (d)-(f), the auxiliary hole configuration demonstrates a clear reduction in vortex intensity. The locations of the peak of the vortex intensities are at a position delayed downstream (X-direction), indicating that the CRVP stays closer to the wall in the auxiliary hole cases.

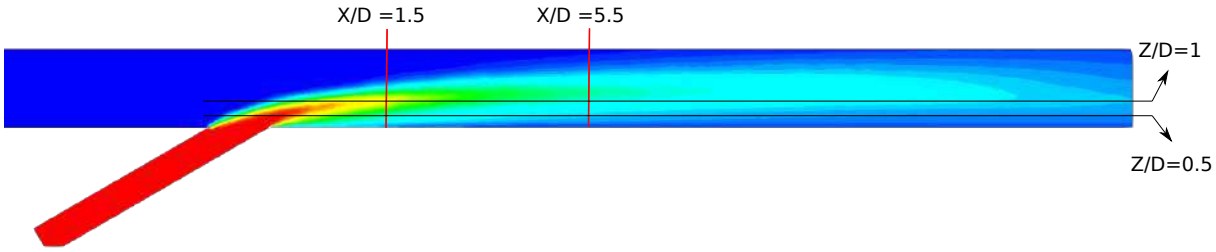

Figure 3.15: Contour plot of the temperature profile for the single hole case at M=1 showing the various locations used for the vortex intensity measurements (Z/D=0.5,1) and the boundary layer study locations (X/D=1.5,5.5)

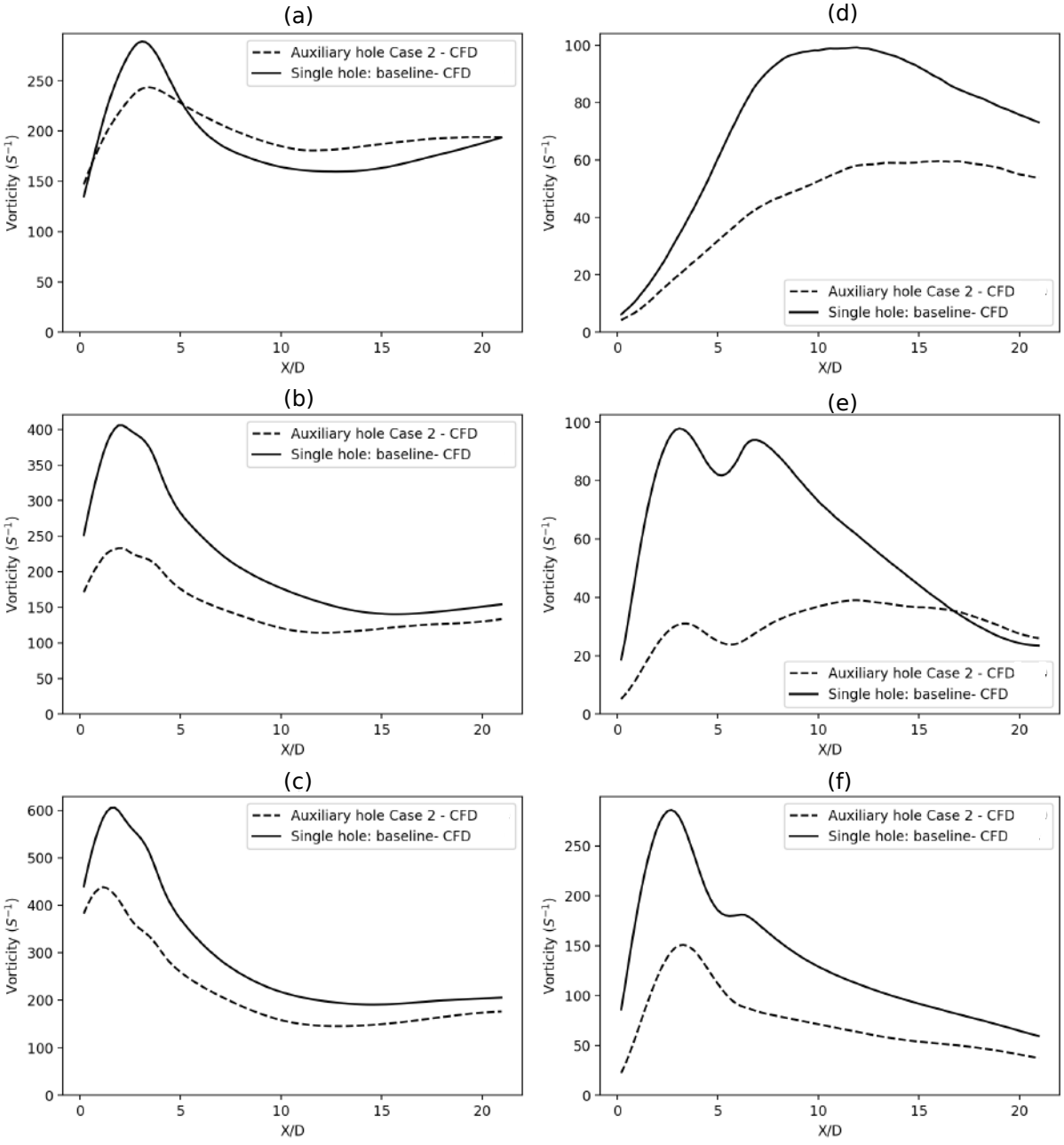

Figure 3.16: Evolution of laterally averaged vortex intensities along the longitudinal axis (X-axis) at a height of Z/D=0.5 (a,b,c) and Z/D=1 (d,e,f) for various blowing ratios. (a,d) M=0.65; (b,e) M=1; (c,f) M=1.25.

3.5.2 Streamlines analysis

A short analysis of the streamlines from the freestream and the jet emanating from the film cooling hole is discussed in this section. Figure 3.17 provides light on why the jet flow in the auxiliary hole stays close to the wall. From the figures (a)-(d) representing the single hole case, it can be observed that the injected jet is raised up due to the momentum of the jet. Additionally, from figure (d) it can be seen that the freestream intrudes into the jet axis quickly, due to the low pressure area at the hole exit. Since there is nothing to protect the lateral areas below the exiting jet, this process happens easily. However from figures (e-i), it is evident that the freestream is prevented effectively from interacting with the main hole jet along the sides due to the presence of the smaller auxiliary holes. Since shear along the sides of the jet is the predominant factor in creating the CRVP, the effective prevention of freestream jet from accessing the sides of the main hole jet reduces the intensity of the CRVP. In addition to this, the auxiliary holes protect the main hole jet from the freestream streamlines trying to enter the axis of the jet further downstream as seen in (i). This is the reason for enhanced lateral spread of the jet. Finally, the clockwise rotating vortex part of the auxiliary hole is closer to the anti-clockwise rotating part of the main hole CRVP (vice-versa for the clockwise rotating part of the main hole CRVP) and hence the intensity of the main hole CRVP is diminished as compared to a simple cylindrical jet. These are confirmed with the previous discussion on vortex intensity.

3.5.3 Boundary layer characteristics

In order to cover all the angles possible to ascertain that the auxiliary hole configuration has better features than a simple hole case, the aero and thermal boundary layer thickness distribution is also analysed. The aim of the film cooling process is to control the boundary layer characteristics better so as to protect the wall surface. In addition to analysing the velocity boundary layer, temperature data close to the wall is an excellent indicator whether the flow is predominantly from the jet or freestream. Figure 3.15 with the red lines shows the locations where the boundary layer properties are measured.

In the figures 3.18 (a-f), the non-dimensional velocity boundary layer (U/U_∞) is superimposed on the normalised temperature profile at various X/D locations along the centerline (see figure 3.15). The scale on the y-axis is the vertical location of the points from the wall and a log-scale is used to highlight the points close to the wall clearly. The experimental data shown in the graph is obtained from Sultan (2011), where point measurements of velocity were made using PIV.

The normalised film temperature is given as

$$\theta = \frac{T - T_\infty}{T_c - T_\infty} \tag{3.6}$$

Note: if $\theta = 0, T = T_\infty \rightarrow$ For small values of θ, flow dominated by mainstream flow
if $\theta = 1, T = T_c \rightarrow$ For high values of θ, flow dominated by injected flow

The boundary layer can be analysed as a function of the downstream location and as a function of blowing ratio.

At a location close to the hole exit (X/D=1.5), the form of the boundary layer remains the same for all the hole configurations for a given jet injection velocity. However, figures (b) and (c), demonstrate that the peak of the velocity is at a higher Z/D location for the single hole case compared to Auxiliary hole: Case 2, showing higher penetration of the single hole case jet into the freestream. Moreover, the temperature very close to the wall is significantly higher for the Auxiliary hole: Case 2 than the base line case, implying a higher injected flow coverage over the wall surface.

Further downstream , mixing of the freestream with the jet causes the film temperature to be lower and also the velocity of the jet is closer to the freestream velocity. For X/D=5.5, the non-dimensional temperatures closer to the wall are lower indicating a reduction in the adiabatic film cooling effectiveness. Moreover, the maximum velocity in the boundary layer which tends to be closer to the free stream velocity reinforces the idea of heavy mixing between mainstream and injected jet flows.

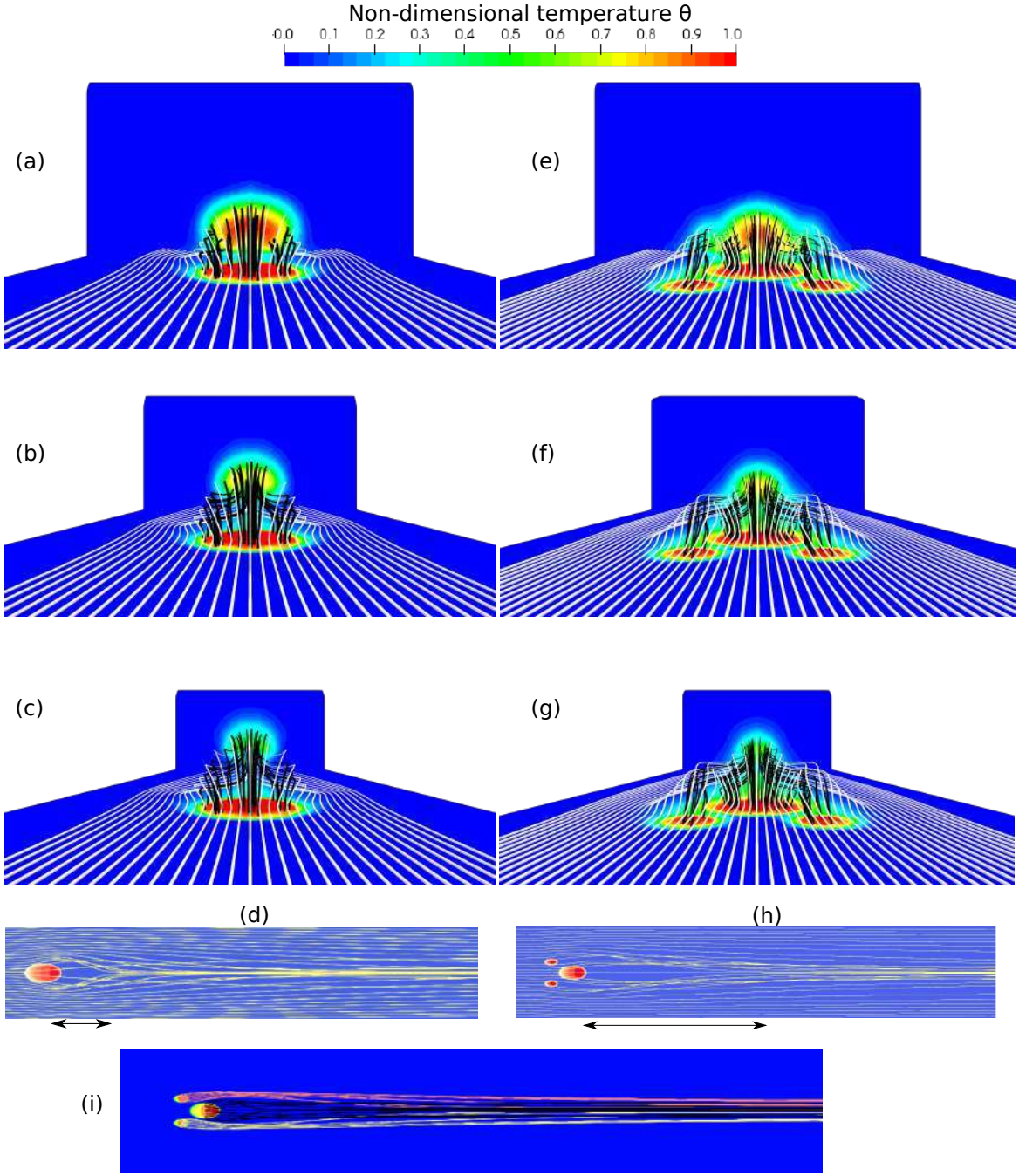

Figure 3.17: Visualisation des lignes de courant du courant libre et du jet pour le cas de trou unique (a-d) et le cas de trou auxiliaire 2 (e-i) à différents plans :(a,e) X/D=1; (b, f) X/D=3; (c,g) X/D=5 avec les contours de température sur les plans. Les figures (d) et (h) montrent la vue de dessus des lignes de courant libres près de la paroi, et (i) les lignes de courant du jet injecté dans la configuration du trou auxiliaire 2.

Considering the effect of blowing ratio, it can be seen that higher the blowing ratio, starker is the difference in the profiles of the single hole case and the auxiliary hole system. The auxiliary hole outperforms the single hole configuration for all blowing ratios studied. The dimensionless film temperature is higher and the vertical location of the film remains lower compared to the single hole case for any given blowing ratio.

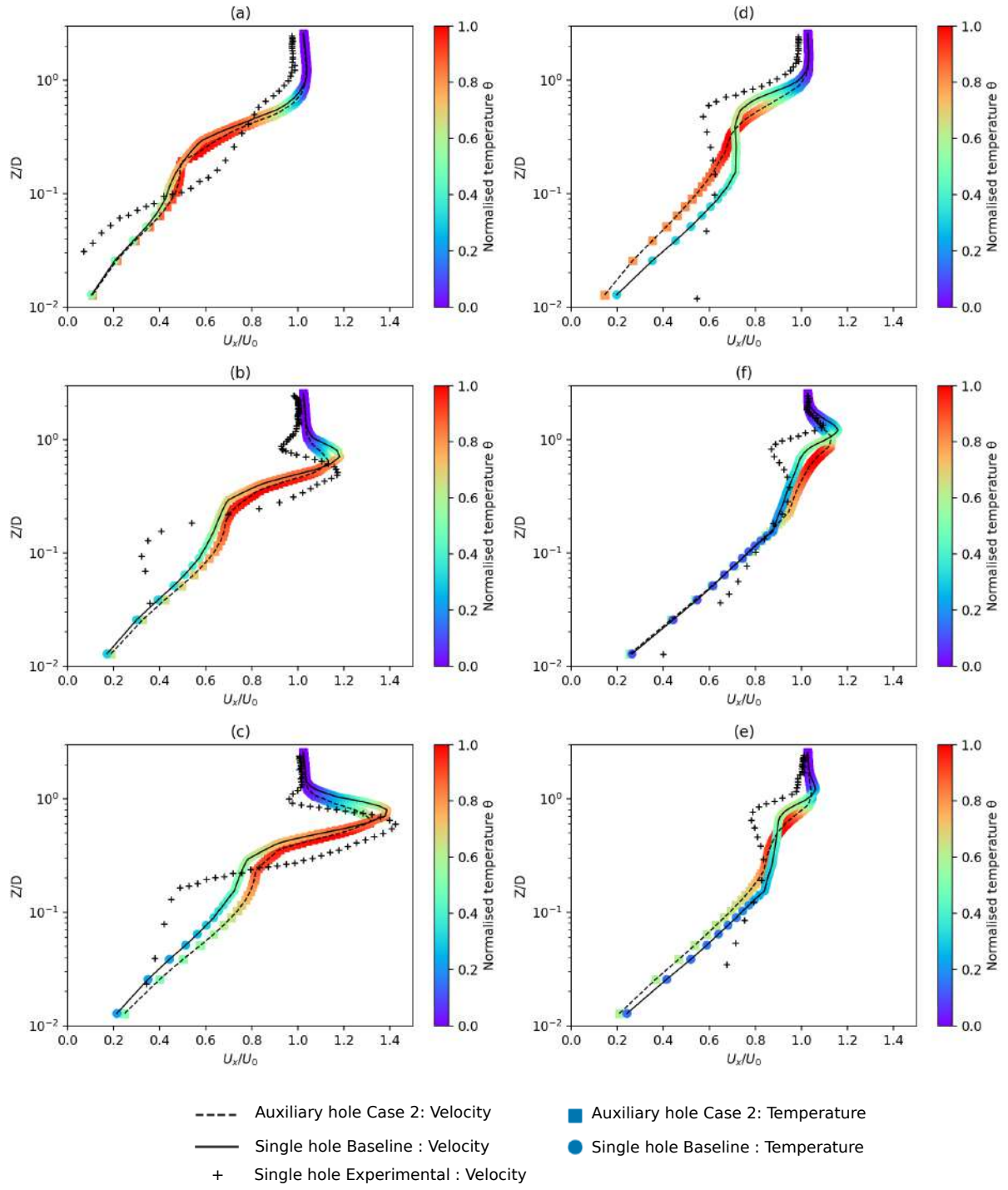

Figure 3.18: Evolution of non-dimensional velocity boundary layer at X/D=1.5 (a,b,c) and X/D=5.5 (d,e,f) for various blowing ratios: (a,d) M=0.65; (b,e) M=1; (c,f) M=1.25. The corresponding evolution of the normalised temperature is also marked by colored dots to represent the jet and freestream fluids. Higher value indicates higher presence of injected jet.

3.6 Review

In this chapter, three film cooling hole configurations have been analysed for their thermal and aerodynamics characteristics, in order to find the optimal spatial positioning of auxiliary holes. In combination with the adiabatic film cooling effectiveness results and the heat transfer coefficients obtained, the Net Heat Flux Reduction was computed to compare the film cooling improvements due to the auxiliary hole system. The results of a baseline case with a simple inclined cylindrical

hole were benchmarked with those of existing experimental results.

- The presence of auxiliary holes immensely improve the adiabatic film cooling effectiveness on the wall surface. Improvements upwards of 30% as compared to the simple hole system.
- The location of the auxiliary holes plays an important role as significant changes in the Net Heat Flux Reduction quantities are found for auxiliary holes placed closer or farther away from each other.
- In some cases the Net Heat Flux Reduction was found to be 2 times higher for the Auxiliary hole: Case 2 arrangement than a single hole case.
- Study of the thermal and velocity boundary layers proved that the auxiliary hole jet remains closer to the wall compared to the single hole case.
- The anti-CRVP vortices from the auxiliary holes help in significantly reducing the strength of the vortices

Conclusion
It can be concluded that from the preliminary RANS study, Case 2 Auxiliary hole configuration shows a better performance than Case 1 and hence further analyses will be done on this configuration. With this RANS analysis, one can conclude on the dimension and the position of the film cooling modules to be tested experimentally and to have an overall idea of the results to expect. Hence this configuration will be used on the BATH test rig for experimental film cooling analysis. Moreover, as mentioned before, a novel fluid flow temperature measurement technique has been developed in the framework of this thesis. In Chapter 4, the development of ZnO phosphor thermometry to measure instantaneous 2-D flow temperature is discussed.

Note: A part of this RANS study was presented and published in an international conference (HEFAT 2021).

Chapter 4

Novel thermometry technique: Phosphor thermometry

This chapter focuses on phosphor thermometry to measure 2-D instantaneous and mean temperature flow fields. The notions of the phosphor working principles are introduced. Phosphor properties and the ways to perform temperature calibration are explained. The main content of this chapter is the study of zinc oxide phosphor for various properties, discussion of the various methods explored to implement temperature calibration and a procedural description of two-color spectral intensity ratio method. The validation of this method is done using a Rayleigh-Benard natural convection test case.

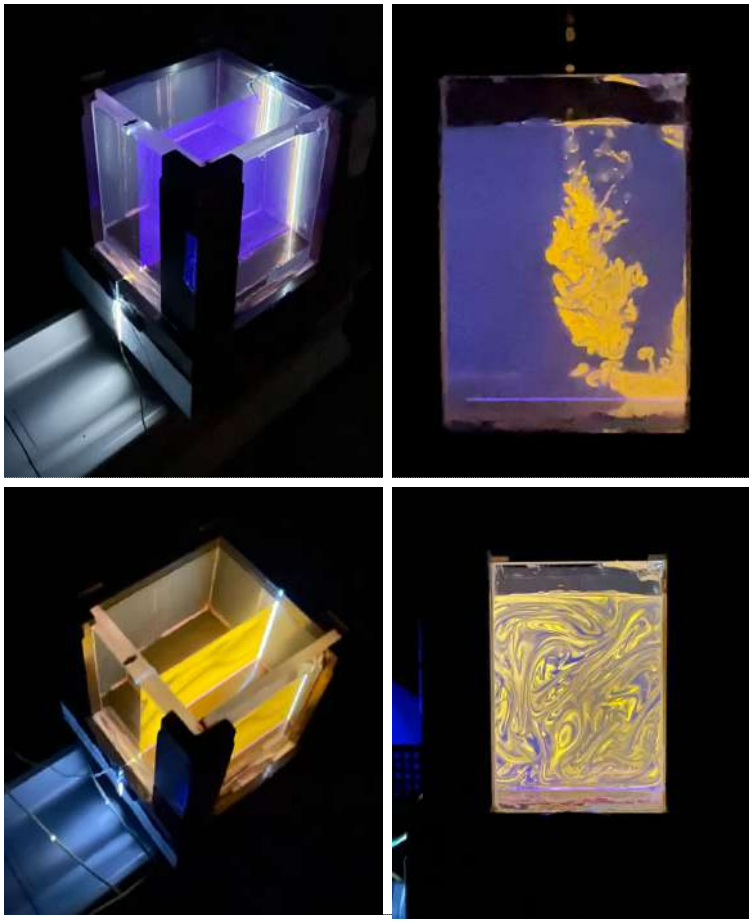

Figure 4.1: Metrology studies at Institut P': Real time emission of ZnO particles in water (phosphorescence) mixed with rhodamine-B (fluorescence), upon excitation with a 266nm laser. (In-house experiments)

Contents

4.1 Need for Phosphor thermometry 40
4.2 Phosphors - working principles 41
4.2.1 Basic overview and definitions 41
4.2.2 Working mechanism 42
4.2.3 Factors affecting precision in phosphor thermometry 43
4.2.4 Phosphor thermometry techniques 45
4.2.5 Phosphor types 48
4.3 ZnO properties 49
4.3.1 Liquid phase 49
4.3.2 Gas phase 50
4.4 Experimental setup 51
4.5 Study of ZnO phosphor properties 52
4.6 Spectral properties of ZnO 53
4.6.1 Effect of ZnO temperature 54
4.6.2 Effect of ZnO concentration 54
4.6.3 Effect of laser fluence 55
4.6.4 Luminescence decay properties 56
4.6.5 Exploration of a novel technique 59
4.7 Development of two-color spectral intensity ratio method 60
4.7.1 Image acquisition 62
4.7.2 Calibration procedure 62
4.7.3 Validation and accuracy 66
4.8 Application: Raleigh-Bénard convection 67

4.1 Need for Phosphor thermometry

The common practice to measure flow temperatures currently are intrusive methods like the use of thermocouples or resistance thermometers. These are usually inserted into a flow by means of a probe to make point measurements. However, there are disadvantages of such a technique. Single point measurements are complicated to make 1D measurements and are impractical for 2D measurements in addition to being intrusive and altering flow properties.

In order to overcome this problem, non-intrusive techniques like Raman spectroscopy, Laser Induced Fluorescence or Phosphorescence (LIF or LIP) have gained interest. As a first at Institut P', one of the Laser Induced Phosphorescence technique called the Phosphor Thermometry to map instantaneous and time-averaged 2-D temperature fields in complex turbulent flows is developed in as a part of this thesis. The elements of phosphor thermometry developed to meet the goals of this thesis are listed below.

- In-house PIV software using python for spectral intensity ratio image matching
- In-house Spectral Intensity ratio calibration code using python
- Setup of a single camera system to perform phosphor thermometry
- Design of a calibration cell to test the code and technique
- Use of developed calibration procedure on film cooling applications to obtain 2-D temperature fields.

4.2 Phosphors - working principles

In order to maximise the exploitation of phosphor properties to determine temperature, there is a need to understand basic working principles of phosphors.

4.2.1 Basic overview and definitions

A few definitions are often used to describe phosphors and is helpful in understanding the physical processes involved.
Phosphor A material which when excited with an incident radiation emits light even after the excitation source is cut-off. The duration of this radiance can be of the order of nanoseconds to several hours. Luminescence is the phenomena when a material absorbs incident energy which eventually gets excited to a higher state of energy and upon de-excitation the material returns to its original state with the emission of light causing it to glow. Shigeo Shionoya (2006)
Electronic state: The energy level of an electron can be classified as valence state or ground state, and a conduction band where the electrons with liberty to move freely. A forbidden band of energy level exists between the two states which is the band gap. A certain amount of energy is needed to excite the electrons from the ground state to the excitons which are the various energy levels in the conduction band. This is usually done by a laser source of suitable wavelength depending on the phosphor.
Host material: Host material in a phosphor is a solid crystal or matrix which is transparent and has an efficient way of absorbing, transmitting light.
Dopant: The host material is doped in small proportions with impurities called activators which act as luminescence centers. These are the active centers where the electronic transitions happen between the various electronic levels facilitating emission of light.
Excitation band: The range of wavelengths across which a phosphor can be excited to a higher energy level.
Emission band: The spectrum of wavelengths at which the de-exciting phosphor emits light. Usually there is a single dominant wavelength with high intensity and several other wavelengths with lower intensities. This emission band has a temperature dependent waveform.
Decay time: It is defined as the time required for the intensity of the emission to decrease 99% of its initial intensity. Thermographic phosphors have temperature dependant emission of light intensity and emission spectrum upon excitation through a light source, typically a LASER, which makes them highly suitable for thermometry applications.
Sensitizers: These are passive elements that help in improving the transmission of incident radiation to the activators that are weak and hence act as a catalyst to improve the intensity of the emission. A representation of the working of the sensitizers is show in Figure 4.2. The excitation energy from the Laser strikes the sensitizer which pass on the energy to nearby activators and hence enhancing the phosphorescence process.

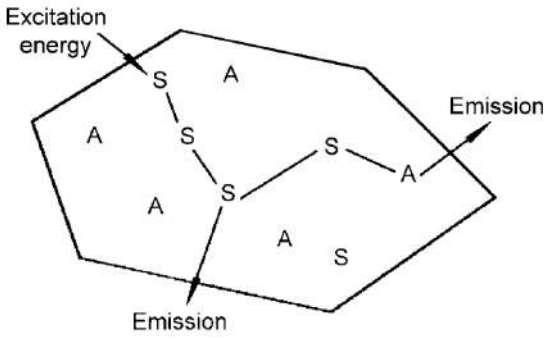

Figure 4.2: Schematic representation of the absorption and emission processes in a phosphor with Activators(A) and sensitizers(S)

4.2.2 Working mechanism

The excitation radiation from a source like laser passes through the host material and reaches the activator or dopant. The radiation excites the electrons in the activator to higher energy levels. Since the conduction band is an unstable zone, the electron returns to its ground state by the release of radiation or non-radiative energy like heat.
Jablonski diagram (Figure 4.3) shows the various transition processes between the different energy states of an electron. Here the state S refers to singlet state and T refers to a triple state. Radiation is emitted during the transition between a triplet state and the ground state. A preferred characteristic of the phosphor is to have minimal de-excitation through non-radiative quenching processes in order to maximize the intensity of the emitted light.

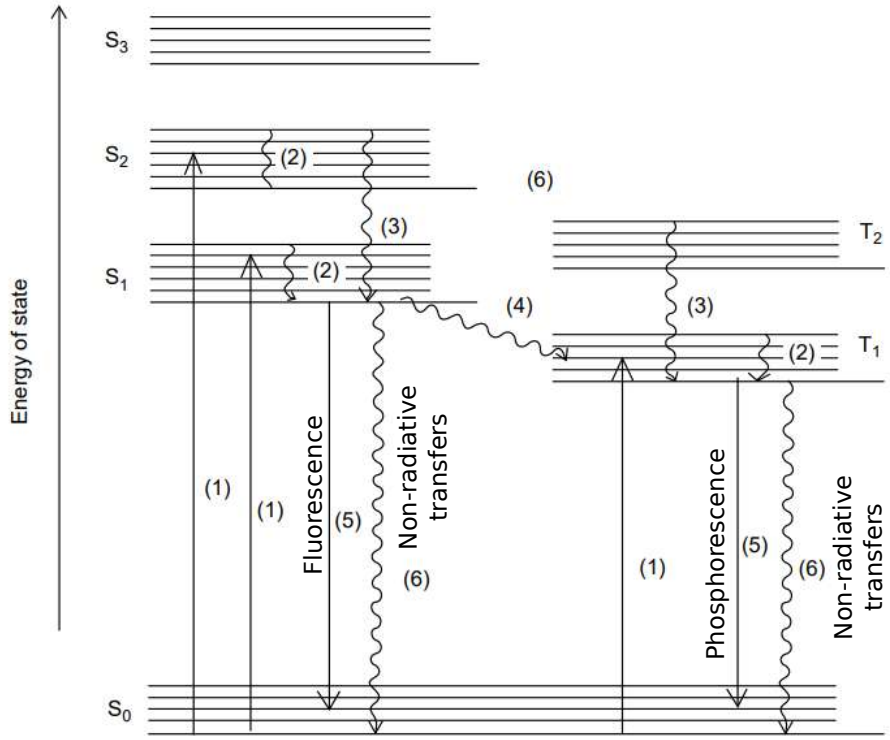

Figure 4.3: The Jablonski diagram to represent the transitions between the energy states of an electron. (1) light absorption, (2) vibrational relaxation, (3) internal conversion (IC), (4) intersystem crossing (ISC), (5) radiative transition, and (6) non-radiative transition Shigeo Shionoya (2006)

The phosphor particles absorb the incident radiation I_0 and get excited to higher temporary energy states.They return to the lower energy states by emission of radiation, and for the purpose of phosphor thermometry, phosphors with emission in the visible spectrum are preferred. The number of photons emitted upon excitation by a laser depends on various factors like temperature of the working fluid T, the local concentration χ of particles, the laser sheet intensity I_0 working at wavelength λ_0 and the inherent emission property of the phosphor used σ. The emission intensity I is given by the expression:

$$I(\lambda, x, y, z) \approx \underbrace{I_0(\lambda_0, x, y, z)}_{(1)} \underbrace{\sigma(\lambda_0, T)}_{(2)} \underbrace{exp(\chi(x, y, z)d)}_{(3)} \underbrace{\chi(x, y, z)}_{(4)} \tag{4.1}$$

In the above equation the emission intensity hence depends on (1) laser wavelength and intensity, (2) phosphor characteristics, (3) the local absorption due to Beer-Lambert effect and (4) local concentration of phosphor particles. In addition to these parameters, factors like detector efficiency, the transitivity of optics and the direction at which the radiation is emitted upon excitation also play a role on the detected emission intensity.

4.2.3 Factors affecting precision in phosphor thermometry

Concentration quenching

With very low levels of activator concentration, the signal intensity is less than optimum.The intensity of emission increases with increase in activator concentration upto a certain limit. After this limit, the emission intensity drastically reduces and the phenomena is called as concentration quenching which can happen due to dissipation of emission energy due to cross-relaxation or formation of quenching centers due to aggregation of the activators. One another reason is that due to resonance, the excitation energy can reach the impurities or killers (Fe or Ni etc) or the crystal surface which act as quenching centers. (Shigeo Shionoya (2006) Yang *et al.* (2002) Dexter & Schulman (1954))

Impurities

The presence of impurities especially by Fe,Ni and Co ions are immensely detrimental to the luminescence intensity of the phosphor emission. Zinc phosphors have shown to be susceptible to the " killer effect" (impurity ions absorb or divert energy and 'kill' the luminescent properties of the phosphor) due to these elements.(Abou Nada *et al.* (2016), Tabei *et al.* (1975)). The active centers dissipate more non-radiative energy than normal with the presence of impurities as this energy is passed on to the impurities. It is important to make sure that the phosphor used in phosphor thermometry to have high purity levels (more than 99%).

Temperature

It is widely known that an increase in temperature can lead to quicker decay times and reduction in the intensity of the emission radiation. Phosphors have a " ceiling temperature" after which the intensity of emission becomes too low for the detector. The quantum yield of phosphorescence ϕ_p is a ratio of the emitted and absorbed photons and it is a good measure to characterise a phosphor. If O_r is the radiative transition rate and O_{nr} is the non-radiative transition rate,

$$\Phi_p = \frac{O_r}{O_r + O_{nr}} \tag{4.2}$$

The higher the temperature, higher are the vibrational and rotational motions of the atoms which is a factor promoting the non-radiative transfers. Hence phosphors are limited to their working temperatures. The effect of temperature is more pronounced for surface measurements as high temperatures affect the binders too.

Application

Some phosphors are easily soluble in binders and hence make them suitable for surface temperature measurements. The bonding techniques cannot be arbitrary as they need to be properly cured so that they do not degrade when used at very high temperatures. There are phosphors that work well in liquid phase measurements and are stable when used in water or other solutions too. Hence the right type of phosphor needs to be chosen for a given application. Care must be taken for agglomerates so as to avoid increased response times.

Detector

Since phosphor thermometry relies on quantification of the photon emission, detector errors tend to be a crucial factor while choosing the thermometry strategy. Temporal methods like decay time or rise time method require high speed cameras to capture the decay curve of the emission. Spectral methods require higher gain due to the use of filters which cause reduction in the captured signal intensity. In addition to this, care must be taken to reduce the noise and background interference to improve accuracy in measurements. Detector-induced distortions due to detector saturation can results in a biasing of the temperature results obtained. Detectors operating in a saturation

mode can severely distort the generated waveform leading to false decay time and consequently to false temperature.

Thickness of phosphor layer

Studies have shown that applying a layer of more than 20μm can be intrusive to the flow and also cause errors in measuring the actual temperature of the surface (Knappe *et al.* (2013)). A thick layer can cause gradients to be developed within the layer and is highly undesirable. This is however irrelevant to the current study as the focus is on using phosphor particles to study 2-D temperature fields in fluids. To summarize, some of the factors affecting phosphorescence and their description are given in the table 4.1.

Table 4.1: Summary of the various factors affecting phosphorescence.

Factor	Short description
Intrinsic factors	
Dopant Concentration	Low levels of dopant concentration may yield low emission output. At the same time a high dopant concentration may lead to dissipation of energy amongst the impurities leading to quenching of luminescence intensity.
Saturation effects	Subjecting the phosphor to high laser fluence may lead to saturation of the light output. There are evidences that high Laser fluence can even alter the emission spectrum characteristics (spectral distribution).
Impuritites	Even at very low levels impurities can be detrimental to luminescence intensity output. Fe and Ni are some examples of strong inhibitors of luminescence saturators.
Sensitizers	Addition of sensitizers could improve the emission yield as the sensitizers help in directing excitation energy to the activators.
Thermal Quenching	The working temperatures of phosphors can affect their emission properties immensely. Thermal quenching happens due to different mechanisms like cross-over and thermal ionization mechanisms. Many phosphors tend to decrease emission at high temperatures due to non-radiative transitions between various energy states.
Experimental conditions	
Pressure	Application of very high levels of pressure alters the spectral and temporal emission properties of phosphors. However, the order of magnitude is GPa.
Layer thickness	For surface measurements, the thickness of the layer should be less than 20 μm to be non-intrusive. Higher thickness can alter the thermal properties of the surface on which it is applied with misleading results. This property does not concern the activities of this thesis.
Seeding density	A uniform distribution with right seeding density is favoured for simultaneous measurements of velocity and temperature. High concentration can lead to beer-lambert absorption and detrimental for PIV.
Response time	Particle sizes need to be carefully chosen to ensure that they adapt to the flow quickly while also making sure that enough intensity of light is emitted from the particle upon excitation.

Presence of foreign substances	Soot or oil lubricants can have a quenching effect on decay time of a phosphor. This is one of the biggest problems and in order to reduce complexity, film cooling studies in this current study are made without using combustion.

Instrumentation and post-processing

Detector errors	Minimal camera noise is desired. High amplification or gain causes increase in salt and pepper noise.
Background interference	Experiments need to be conducted in dark environment and avoid reflections from metallic surfaces to reduce background noise
Laser fluence	For efficient excitation, a stable laser fluence with minimal changes in laser energy is necessary.
Calibration errors	Use of suitable calibration fitting curves with sufficient number of data points. Erroneous data from thermocouple can also influence the results
Excitation source	Phosphors are excited at certain wavelengths with suitable energy to excite electrons from ground state to conduction band

4.2.4 Phosphor thermometry techniques

The two main methods to exploit the temperature dependence of phosphors are the spectral and temporal methods. Spectral method is based on the variation of emission properties in terms of emission spectrum upon change in temperature. The temporal method on the other hand, depends on the change in emission properties of the thermographic phosphor with respect to time after excitation.

Spectral Method

The spectroscopic distribution of some thermographic phosphors varies with the change in temperature that the phosphor experiences as seen in figure 4.4. Two approaches can be used to use the temperature dependence of the emission spectrum

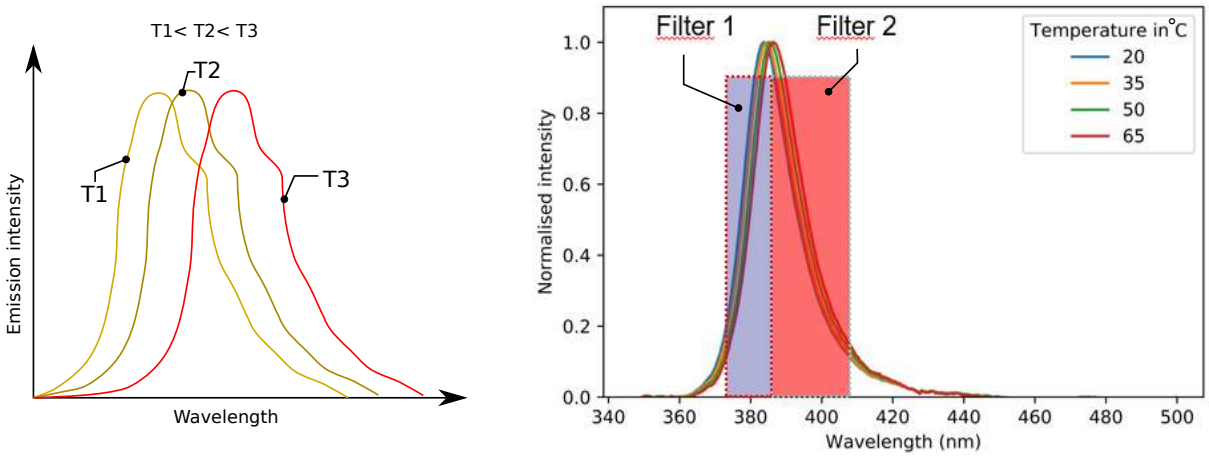

Figure 4.4: Working principle of Spectral intensity ratio method. As the temperature increases, the emission spectrum moves towards longer wavelengths.

- Integration of the entire spectrum: By this method, the amount of signal collected is the entirety of the emission, so there is no loss due to the use of bandwidth filters. However, since this method is based on the ratio of the emission intensity at different temperatures, local variation of laser fluence can heavily impact results.

- Spectral intensity ratio method: By observing the phosphor emission through two different wavelength bandwidths by use of filters, the division of the two filtered images can be effectively used to calibrate temperatures (Refer figure 4.5). However, due to the use of filters, the collection of the emission signal is drastically reduced and some times necessitates the need for an intensified camera.

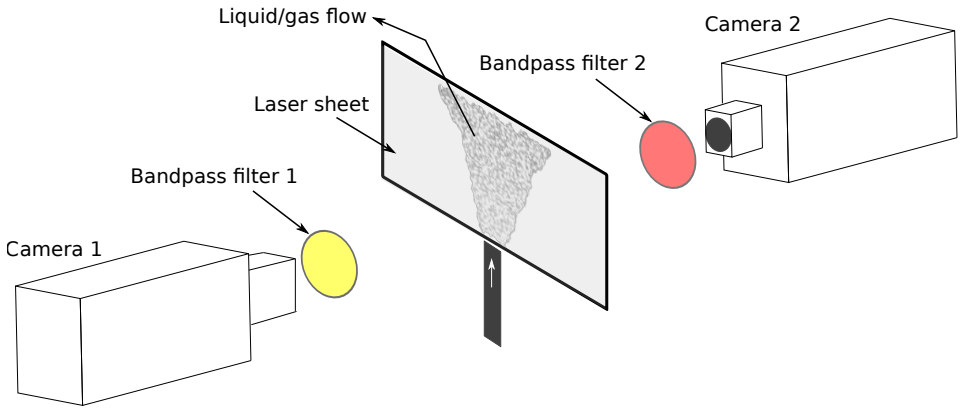

Figure 4.5: Spectral intensity ratio method: A typical experimental setup.

As the spectroscopic distribution changes, the relative intensity of some of the emission bands varies in relation to one another. By collecting the emission intensity of each of the two bands by means of a 2-D detector, such as an ICCD camera, the intensity ratio at a specific temperature can be obtained. By changing the temperature of the phosphor, full temperature calibration of this ratio can be achieved.

From eq. 4.1 it can be seen that the emission dependence on the laser wavelength, local Beer-Lambert absorption and the local concentration of the particles can be eliminated, if the intensity of emission emitted by a phosphor particle at different wavelengths can be divided by one another.

$$\frac{S_{\lambda 1}}{S_{\lambda 2}} = \frac{\sigma(\lambda_0, T_1)}{\sigma(\lambda_0, T_2)} \tag{4.3}$$

From eq. 4.3, it can be seen that by such a division, the intensity ratio value depends only on the temperature of the phosphor and the excitation source wavelength.

There are several setup configurations that can be used to determine temperatures by use of the intensity ratio method. The first of these involves use of two cameras, each equipped with an interference filter that transmits one of the bands of the emitted radiation and blocks the others. This configuration requires spatial matching of the two detectors in order to obtain an accurate two-dimensional temperature map. The second configuration utilizes a stereoscope fitted to a single camera which enables the projection of the spectral intensity of each band onto a single detector chip. Stereoscopes can suffer from radiation cross-talk which can affect the accuracy of the temperature determination obtained though.

The calibration procedure starts with the acquisition of the intensity images of the two spectral bands that have been pre-selected by the user. Then, the images are subjected to background subtraction and to de-warping process to adjust image distortions. After this the division of the two intensity maps results in the intensity ratio distribution corresponding to the temperature distribution of the object. The intensity ratio distribution obtained is then transformed into temperature values by use of a calibration polynomial to convert the ratios obtained.

Temporal Methods

The lifetime of the phosphorescence usually decreases with increase in temperature depending on the phosphorus material. Figure 4.6 shows the emission decay with time which follows the equation

$$I = I_0 exp\left(\frac{-t}{\tau}\right) \tag{4.4}$$

where I_0 is the initial emission intensity, t is time and τ is the lifetime of the phosphorescence. τ is the amount of time after which the emission intensity has decreased to 1/100 of the initial emission I_0.

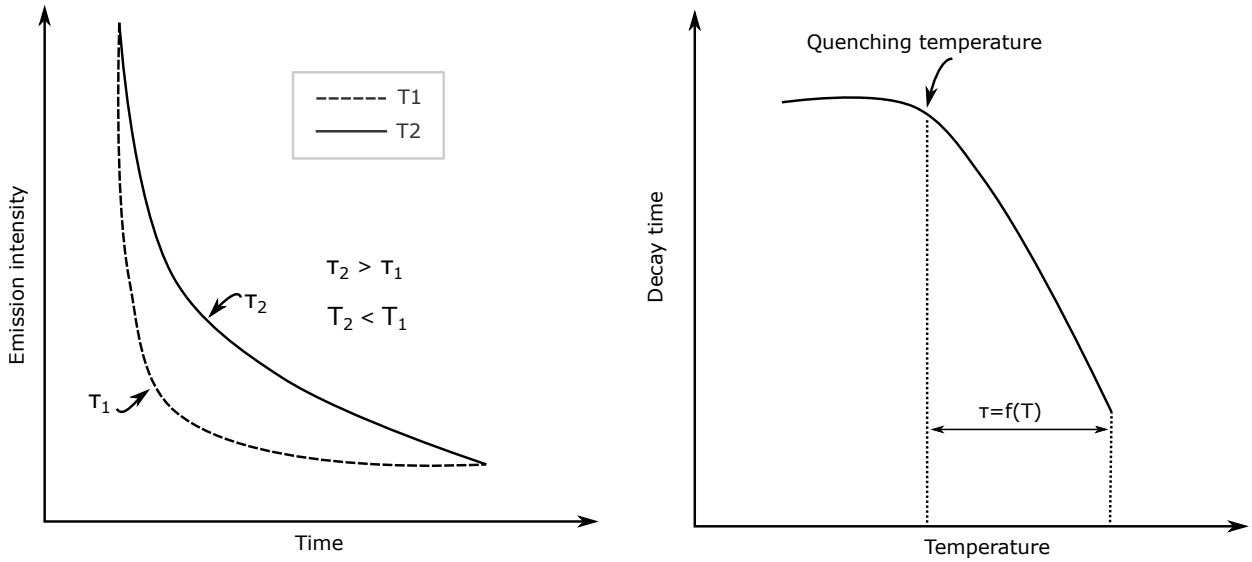

Figure 4.6: Working principle of decay time method. The lifetime becomes shorter when the temperature increases.

The decay time method requires a high speed camera to capture the emission from the phosphor particle at high frame rates. This is one of the biggest disadvantages of this method. However, with the availability of suitable equipment, very precise measurements can be made using the decay time method. This method maybe more suitable for phosphors with the life times of the order of few hundred micro seconds to milliseconds.

Choice of method

The spectral ratio method is capable of providing 2D temperature information regarding surfaces with a high degree of spatial resolution. The accuracy and precision of this method is however considered to be less than that of the decay time method due to the difference between the intensity ratio and the decay time parameters in terms of the magnitude of temperature sensitivity. Thermographic phosphors decay times usually exhibit a change of 2-3 orders of magnitude as function of a few hundred degrees of change in temperature. In comparison, the intensity ratio typically displays a change of only one order of magnitude for the same degree of temperature change. Moreover, the intensity ratio method is susceptible to detector-induced non-linearities that can severely bias the object temperatures obtained. It has also been shown that the intensity ratio method is sensitive to the positioning of the detector that can result in about a 25 K temperature bias Lee *et al.* (2016). This indicates the necessity of in-situ calibrations so as to minimize the error induced by difference in the position of the detector between calibration and experimentation. Some other drawbacks of this method are the requirement for two cameras and the image corrections required for to adjust the angle in which the cameras are placed. If a beam splitter is used, there is a possibility to have low intensity of light being captured. There are solutions to overcome this problem by using a fly-wheel with filters of selected bandwidths that spin around at high speeds in order to capture a series of images.

Despite these problems, solutions are sought after to develop the spectral intensity ratio method due to its simplicity in post-processing and cost-effectiveness as it eliminates the use of several cameras as in the case of decay-time method. In the present study, a device called 'Optosplit' is used to split the incident light emission into two paths that captured using the same camera after passing through two filters, hence the need for just one camera instead of two. This also eliminates the above mentioned problems related to alignment.

4.2.5 Phosphor types

Each phosphor has its own intrinsic properties, operation temperatures and limits. A short list of phosphors used for thermometry in fluids is provided in the Table 4.2. (Note: IR - Spectral Intensity Ratio method and LT -Life Time method or decay time method.)

Table 4.2: Phosphor types and applications

No	Phosphor	τ	Laser excitation (nm)	Spectral emission (nm)	Temperature (K)	Strategy
1	$Mg_4FGeO_6 : Mn^{4+}$	3ms	266,355,385	632-657	700-1050	IR,LT
2	$La_2O_2S : EU^{3+}$	12 μs	355,337	512	300-600	LT,IR
3	$Y_3Al_5O_{12} : Dy^{3+}$	1ms	355	458/497	400-1700	LT,IR
4	$Y_2O_3 : EU^{3+}$	1ms	266,355,532	512,538,624	300-900	LT
5	BAM: EU^{2+}	1 μs	355,375,266,376	460	300-900	LT,IR
6	**ZnO: Zn**	<1ns	355,266	389,510	300-500	IR
7	$Y_2O_2S : Er^{3+}, Yb^{3+}$	50 μs	980	500-540/540-575	300-600	LT,IR
8	YAG: Pr^{3+}	190 μs	266	484/610	300-750	IR
9	ZnO:Ga	<1ns	355	386	300-600	IR
10	$YVO_4 : EU^{3+}$	300 μs	355	535-592/618-620	650-930	IR,LT

The choice of phosphor is usually dictated by the range of temperatures at which the experiments are conducted. However, in order to cover a large temperature interval several different phosphors may be used. During the development phase of phosphor thermometry, there is a need to do a lot of experiments and hence the need to spend a lot of phosphor particles. From all the different phosphors mentioned in the table 4.2, ZnO is the most accessible phosphor and lowest in cost. Therefore, zinc oxide is chosen as the phosphor conduct 2-D phosphor thermometry in this study. The properties of ZnO are enumerated in detail in the following sections.

References to the phosphors mentioned in the table 4.2 are provided below.
[1]- Omrane *et al.* (2004*a*), Brübach *et al.* (2006), Omrane *et al.* (2008) Someya *et al.* (2012), Kim *et al.* (2017)
[2]- Omrane *et al.* (2004*a*), Omrane *et al.* (2004*b*), Omrane *et al.* (2004*c*), Armfield *et al.* (1997)
[3]-Abram *et al.* (2015), Abram *et al.* (2016), Särner *et al.* (2008), Fan *et al.* (2017)
[4]-Hasegawa *et al.* (2007), Hasegawa *et al.* (2008), Lawrence *et al.* (2013), Jenkins *et al.* (2008), Jordan & Rothamer (2013), Takada *et al.* (2009), Jovicic *et al.* (2014), Hertle *et al.* (2017)
[5]-Lawrence *et al.* (2013), Fond *et al.* (2012), Fond *et al.* (2015), Lee *et al.* (2016), Yin *et al.* (2017), Zentgraf *et al.* (2017), Abram *et al.* (2013)
[6]-Schreivogel *et al.* (2016), Ojo *et al.* (2015), Ojo *et al.* (2017), Van Lipzig *et al.* (2013), Takada *et al.* (2009), Lindén *et al.* (2009)
[7]-Rothamer & Jordan (2012)
[8]-Jordan & Rothamer (2013), Neal *et al.* (2013), Witkowski *et al.* (2013)
[9]-Tan *et al.* (2013), Tan *et al.* (2014)
[10]-Yokomori *et al.* (2015)

4.3 ZnO properties

In the present study, due to its easy availability, cost and its properties, ZnO has been chosen to carry out calibration process and validate the post-processing programs built in-house. Zinc oxide (ZnO) or zinc doped zinc oxide (ZnO:Zn) is a natural phosphor due to the oxygen vacancies caused by the reduction process. This is responsible for the emission of ZnO phosphors. The thermal dependence of the ZnO phosphors have previously been explored for possibilities to perform a new type of thermometry, which is the phosphor thermometry. Several studies have been conducted on ZnO phosphorescence notably by, Fan *et al.* (2017) who were able to make simultaneous measurements of velocity and temperature using ZnO thermographic phosphors in a heated jet, Dragomirov *et al.* (2018) carried out temperature measurements in a solid phase, Frattina (2019) demonstrated in his thesis that the ZnO based phosphors could be used in lower temperatures to provide high accuracy results in air and also used the technique to analyse engine temperatures in an internal combustion engine. Abram et al. conducted a series of thermographic phosphor experiments in air (Abram *et al.* (2015)) and in water (Abram *et al.* (2016)) to study the various factors affecting the ZnO phosphorescence. As a reminder of the methods possible to conduct phosphor thermometry to determine temperatures, figure 4.7 summarises the possible techniques currently in use.

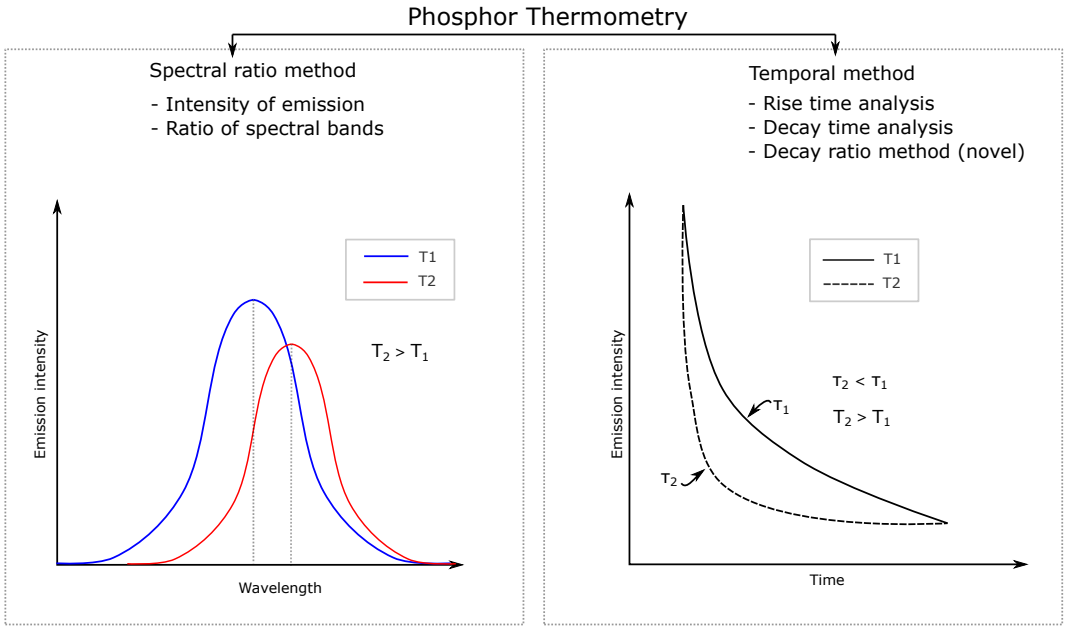

Figure 4.7: Methods to perform phosphor thermometry by exploiting the spectral and temporal emission dependence on temperature.

4.3.1 Liquid phase

The knowledge of ZnO properties in water is important from the point of view of this thesis, as numerous spectral and temporal properties and an initial calibration process is conducted by the use of ZnO particles suspended in water. This is done due to the easy design of a simple test cell and to avoid particle extraction and collection mechanisms required for calibration processes in gaseous phase. Additionally, studying properties of ZnO in a wind tunnel will require enormous amount of ZnO. Hence, the validation of a calibration process to conduct ZnO phosphor thermometry is performed in water as medium. In this thesis, ZnO particles have been mixed with water to perform the phosphor thermometry calibration process. The validated calibration process has been introduced to study film cooling temperature flow fields (ZnO in gaseous flows).

The spectral intensity ratio method has been carried out in water by Abram *et al.* (2016) and they have shown that the emission spectrum has a strong dependence on the temperature. It is important to note that a 266nm laser was used to avoid the Raman interference that was seen with

a 355nm laser during their experiments. Figure 4.8 shows the emission spectrum of ZnO particles at 23°C using 266 and 355 nm excitation, and 355 nm excitation at 95°C. One can observe a strong red shift (movement of the emission spectrum towards longer wavelength) which can be exploited to produce accurate results of temperature fields. In the liquid phase, the ZnO particles have very quick decay rates in emission (in the order of very few nanoseconds due to increased collisions at the molecular level) and hence it is not possible to perform decay time measurements due to camera limitations. Despite this, a short study is conducted to determine the feasibility of this method in the framework of this thesis (section 4.4.4).

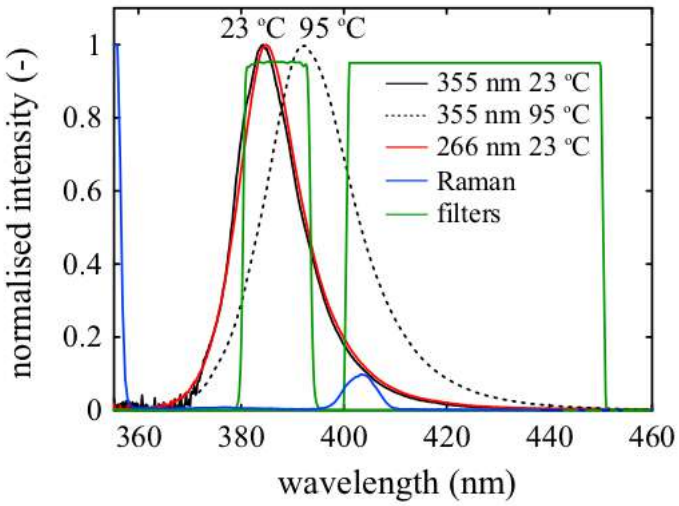

Figure 4.8: Emission spectrum of ZnO particles at 23°C using 266nm and 355 nm excitation, and 355 nm excitation at 95°C (Abram *et al.* (2016)).

4.3.2 Gas phase

The properties of ZnO in air were analysed by Abram *et al.* (2015) and Frattina (2019). ZnO particles were characterised as tracers for temperature imaging in fluid flows. Spectroscopic measurements of ZnO particles with no deliberately added dopants show that there is a strong red-shift of the edge luminescence with temperature that can be used for sensitive thermometry. In gas

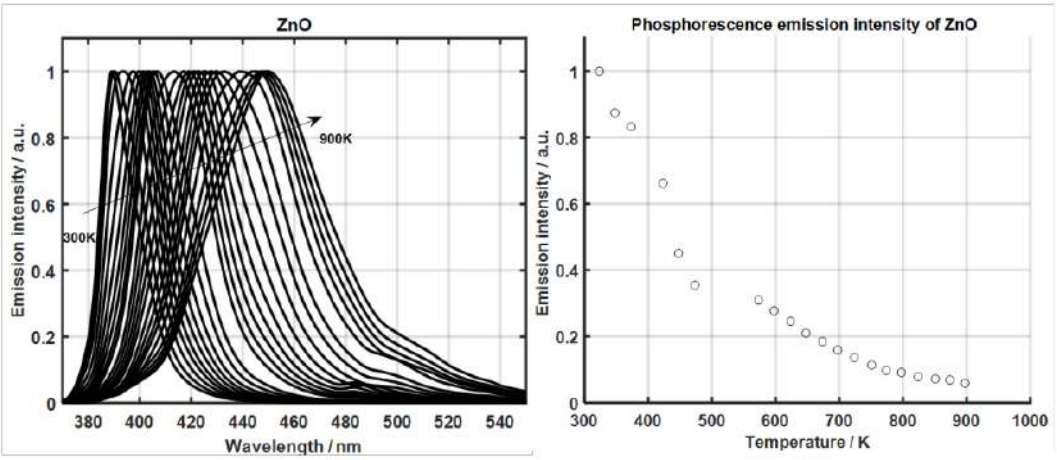

Figure 4.9: Temperature dependence of the normalized ZnO:Zn emissions. Left: spectra obtained at different temperatures normalized at each spectrum maximum value. Right: Normalised emission intensity for various temperatures Frattina (2019)

phase measurements, direct comparison with BAM:Eu phosphor particles indicates similar signal levels per particle and the intensity ratio calibration showed significantly improved temperature

sensitivity of ZnO. At room temperature a threefold gain in temperature precision can be achieved for the same particle number density, laser fluence, luminescence collection and spatial resolution. Figure 4.9 shows the temperature dependence of the normalized ZnO:Zn emissions. The spectra (left figure) obtained at different temperatures normalized at each spectrum maximum value. It is seen that up to a temperature of about 450°C, there is a good emission level by ZnO.

Objectives pertaining to current work

The temporal and spectral properties of an excited phosphor particle can be exploited to construct a temperature field. In this chapter, the various properties of ZnO phosphor are studied for its spectral and temporal properties. Precisely, the aim of this part of the thesis is to put in place a reliable calibration methodology either for the spectral or temporal method, so that the process can be used for any phosphor thermometry application. Due to its simplicity and cost-effectiveness, the entire process is made in water.

4.4 Experimental setup

A Rayleigh-Bénard convection cell made out of copper, with cubic dimensions of 77 mm, was designed on the basis of Valori (2018) presented in Figure 4.10. The bottom wall of the cell is heated by the heating plate of a magnetic stirrer (LLG Unistirrer 3), the power of which is regulated electronically. The upper plate consists of a water circulation circuit and the temperature of the top plate is controlled using a cryostat (Huber CC-410wl). Two type K thermocouples are used to monitor and regulate the temperatures of the lower and upper walls. The side walls are made of 2 UV transparent glass, and two other walls made of PVC. In all the experiments, the fluid medium is water and is constantly stirred by a magnetic stirrer to maintain a uniform temperature during the calibration process. Another important utility of the stirrer is to prevent the settling of particles with time and maintaining a more uniform concentration in all the cavity during the measurements. Schematic representation and the actual experimental setup is shown in figure 4.11.

The metrology equipment consists of a double cavity laser (DANTEC PIV Laser Spectra physics)

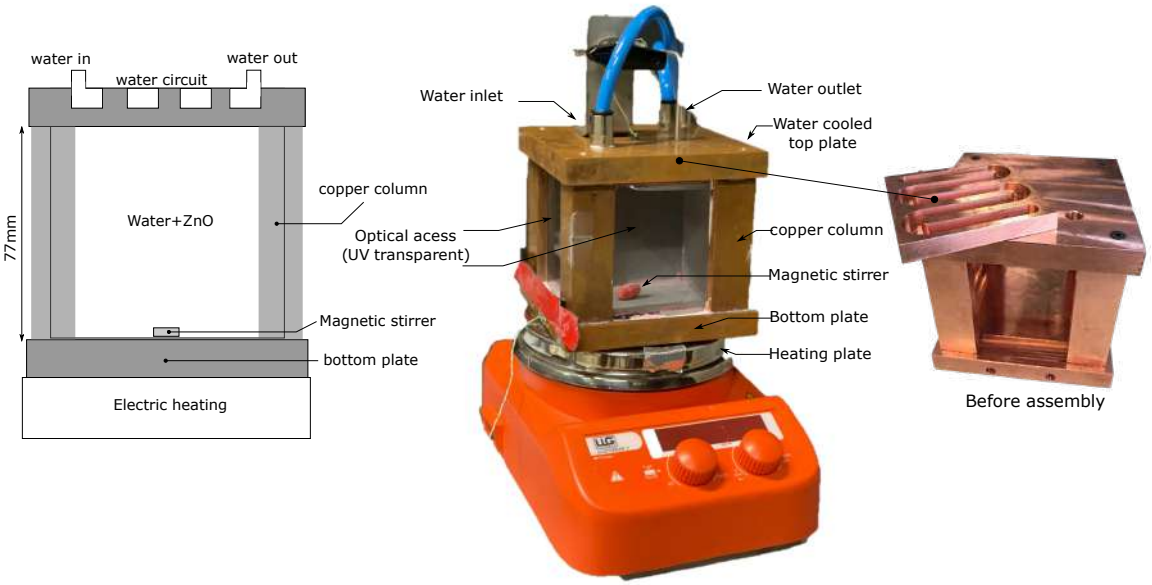

Figure 4.10: Schematic representation of the test cell and actual image of the test cell.

which acts as an excitation source emission wavelength at 266nm. The maximum power delivered by the laser is 30mJ and the laser operates at a frequency of 10Hz. Sheet optics are used to transform the laser beam into a laser sheet which has a thickness of 0.5mm. The objective of this

part of the thesis is to investigate the possibility of using a single camera for performing phosphor thermometry. Regarding the camera specifications, they will be introduced at the appropriate sections to have better relevance.

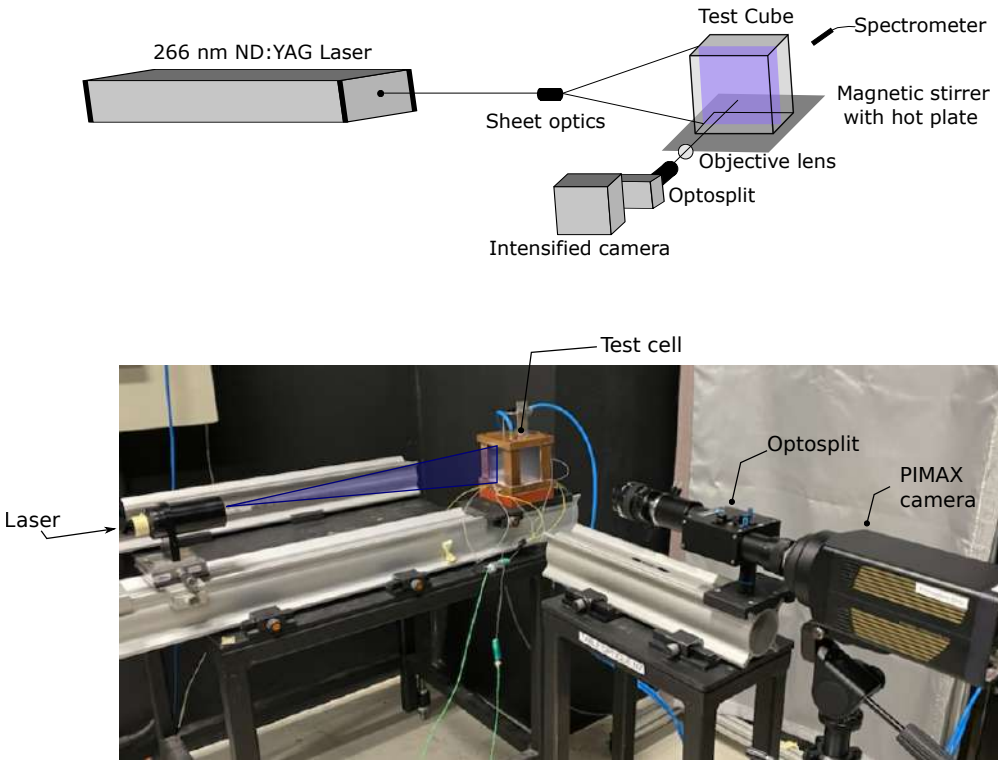

Figure 4.11: Schematic representation of the experimental setup with various components used.

4.5 Study of ZnO phosphor properties

Extensive spectrometer tests (Ocean Optics (USB 2000) spectrometer) were done to analyse the spectral properties of ZnO phosphor emission. A sample emission spectrum and an image of the ZnO emission upon excitation with a 266nm laser is shown in figure 4.12 Their dependence on temperature of working fluid, laser energy and concentration of ZnO were analysed. In the current study, laboratory grade zinc oxide particles from Sigma-Aldrich (96479) and Chem-lab (CL00.2627) with a purity greater than 99.9% have been used, effectively eliminating the impurities problem.

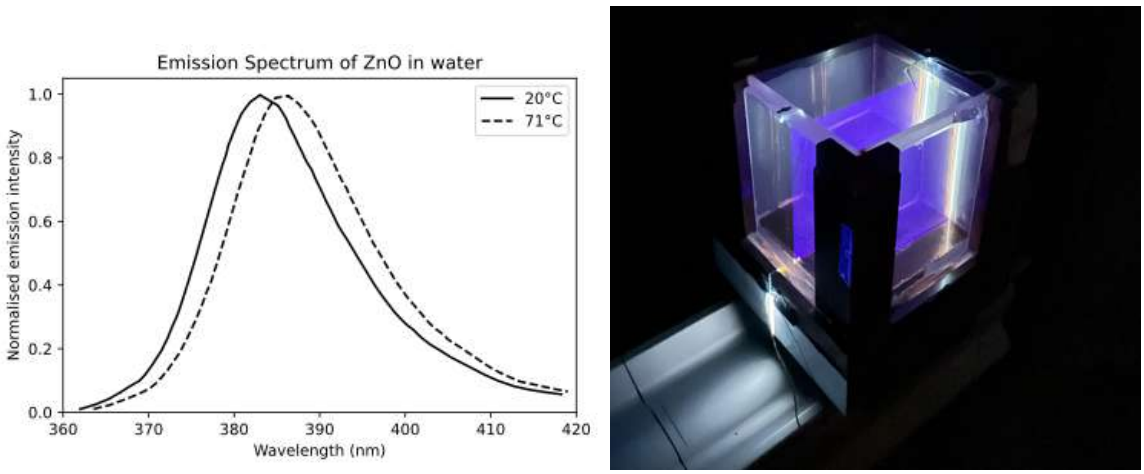

Figure 4.12: Emission spectrum of ZnO in water at two different temperatures and an image of the emission as seen visually is shown on the right.

Table 4.3: ZnO particle parameters made by Mie analysis

Parameter	Value
Refraction Index of Particles	1.989
Absorbtion Index of particles	0.01
Dispersing Medium	Water
Refraction index of dispersing medium	1.33
Diffusion model	Mie
Weighted residuals	0.35%
Laser Obscuration	4.94%
Span = (D90 – D10)/D50	4.175

Physical properties

The zinc oxide particles (Chem-lab CL00.2627) were tested for their properties by granulometry. A Malvern diffusion analysis of the ZnO particles suspended in water showed that the volumic diameter of the particles was found to be of the order of 1-10 μm. It should be noted that due to agglomerations, some particles could exceed 20 μm, however, the percentage of this population is too low and can be neglected. The particle size distribution and other properties are shown in the table 4.3. The volume density distribution by Mie analysis is shown in figure 4.13.

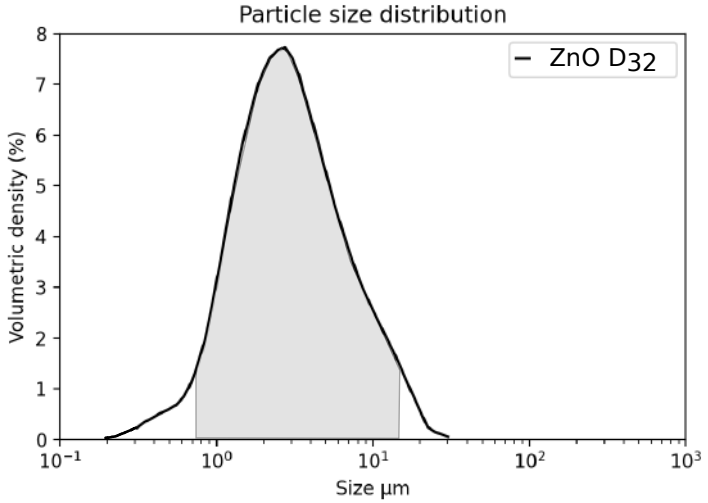

Figure 4.13: Particle size distribution of the selected lot of ZnO particles made by Malvern analysis.

4.6 Spectral properties of ZnO

In this section, the dependence of the emission spectrum on various parameters like temperature, particle concentration and laser fluence are analysed. A spectrometer by Ocean Optics (USB 2000) with a sensitivity from 300nm to 1000nm was used to study the spectral properties. The signal integration time was set at 10 seconds and the raw data is exported to an acquisition PC for each test case. In the next sections, since the raw data is noisy, a moving average filter (Savitzky-Golay filter) was applied to smoothen the data to improve readability. The noise is seen as the emission duration is of the order of nanoseconds and the total integration time was 10 seconds with laser excitation at 10Hz with a duration of 10ns.

4.6.1 Effect of ZnO temperature

The temperature of the water Zno mixture at a constant concentration and laser fluence was studied. The tests were conducted at 20°C, 35°C, 50°C and 65°C at a constant concentration of 0.1g/L with a laser pulse energy of 16.8 mJ. In the figure 4.14, (a) shows the raw data and the filtered data, (b) shows the actual emission intensity with respect to emission wavelength (c) shows the decrease in the peak emission intensity with increase in temperature. The emission values are normalised with that of 20°C, (d) highlights the spectral variation of the emission with changes in temperature. Here the emission intensity values for each temperature are normalised with their respective maximum emission intensity.

- There is a strong spectral shift towards the red spectrum on increasing the temperature
- The intensity of the emission decreases with increase in temperature.
- The decrease in intensity is related to thermal quenching effect where non-radiative transitions increase with temperature.

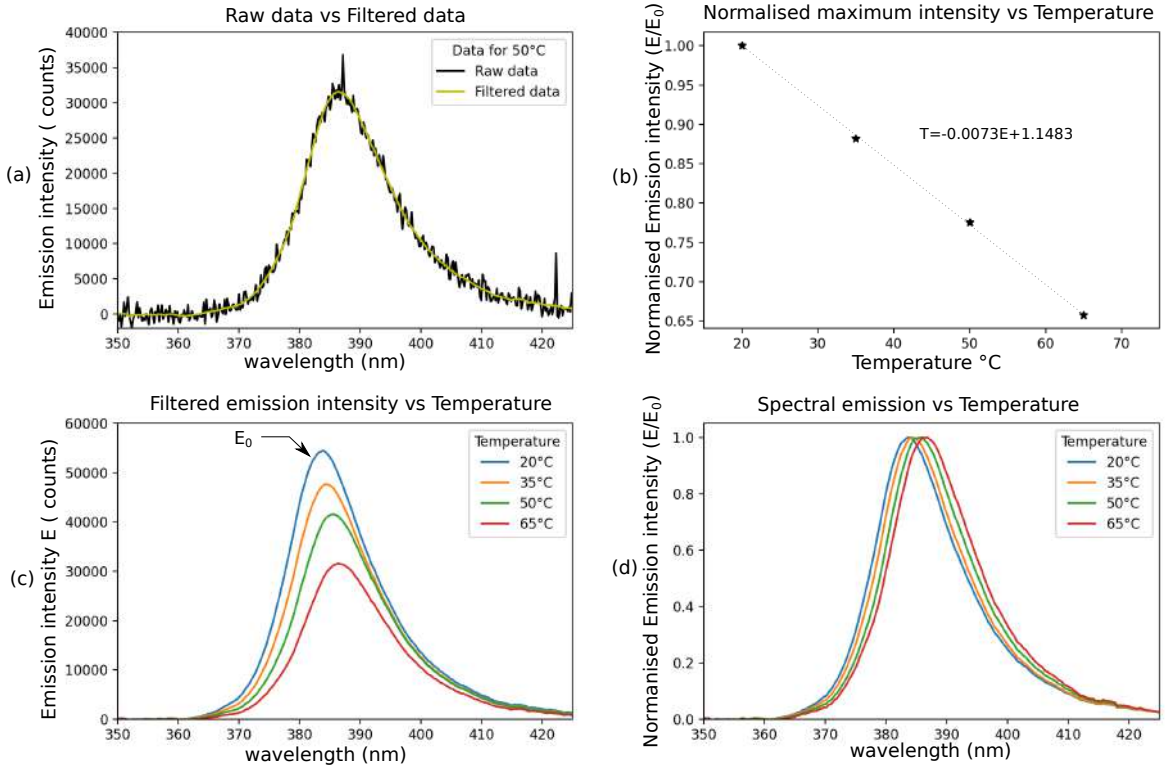

Figure 4.14: Spectral and emission intensity dependence with respect to temperature of ZnO and water mixture.

4.6.2 Effect of ZnO concentration

In a series of experiments, the effect of concentration of ZnO in water was studied. The ZnO powder was measured using a highly precise balance with an accuracy of 0.1mg. A solution of 1g/L was diluted as required to get the different concentration solutions and hence by this process, the errors in concentration are reduced. It can be seen that the increase in concentration increases the emission intensity output for a constant temperature (20°C) and constant laser fluence (16.8mJ). The variation in the emission intensity and spectral properties are shown in figure 4.15 where(a) shows the raw data and the filtered data, (b) shows the actual emission intensity with respect to emission wavelength (c) shows the decrease in the peak emission intensity with increase in temperature.

By increasing the concentration by two times, the emission intensity increases twice. However, this data is a point measurement and must be interpreted carefully concerning 2-D phosphor thermometry. As the concentration increases, there is an increase in Beer-Lambert absorption in the direction of the laser and also the absorption of emitted light by other out of plane ZnO particles in the perpendicular direction where the emission light is collected by a camera. This causes a clear distinction between a linear and non-linear emission intensity response to changes in concentration. This is shown in the figure 4.15 (c). Hence, a very low ZnO concentration of 0.01g/L was chosen for the 2D spectral intensity ratio method and the resulting mixture is observed to be clear as if it was purely water. Previous studies as in Abram *et al.* (2016) were also performed with very low concentrations too.

The emission values are normalised with that of 20°C, (d) highlights the spectral variation of the emission with changes in temperature. Here the emission intensity values for each temperature are normalised with their respective maximum emission intensity. As expected, the increase in the concentration does not alter the spectral properties of ZnO emission as the peak of the emission intensity remains at the same emission wavelength irrespective of temperature (slight variations in the other zones could be linked to the filtering used to smoothen the curves).

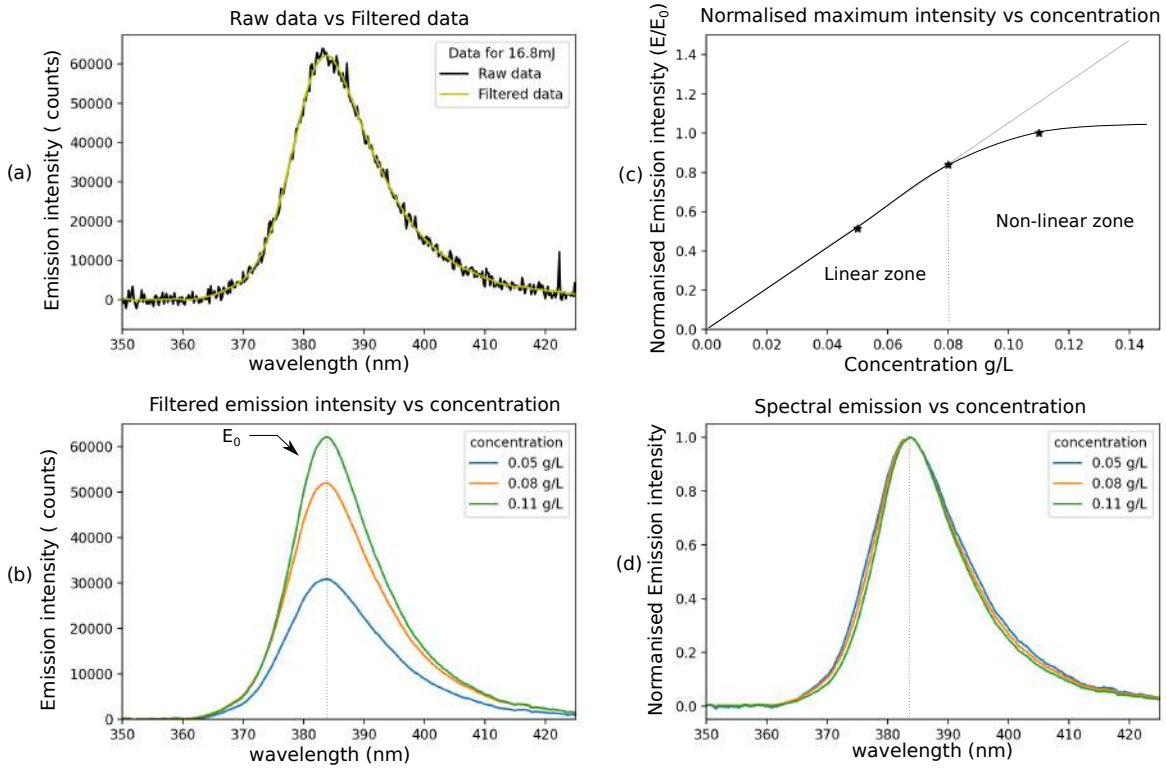

Figure 4.15: Spectral and emission intensity dependence with respect to concentration of ZnO phosphor in water.

4.6.3 Effect of laser fluence

There is a need to optimise the laser intensity used in excitation of the laser. The emission intensity dependence on the laser fluence is seen in the figure 4.16 where (a) shows the raw data and the filtered data, (b) shows the actual emission intensity with respect to emission wavelength (c) shows the decrease in the peak emission intensity with increase in temperature. The emission values are normalised with that of 20°C, (d) highlights the spectral variation of the emission with changes in temperature. Here the emission intensity values for each temperature are normalised with their respective maximum emission intensity.

By increasing the laser fluence by two times, there is an increase of 35% in the emission intensity of the ZnO Phosphor. The trend is linear up to a certain point after which the increase in laser fluence has a non-linear effect on the emission intensity due to saturation effect. This is

a phenomenon where the addition of laser excitation energy can no longer excite more electrons as the maximum number of electrons that can be excited in the valence bond of the phosphor has reached an upper limit. From figure 4.16(d) it can also be seen that the change in laser fluence has no effect on the spectral emission properties (a slight deviation is seen in the curve for 7.8mj, which can be linked to non-homogeneous temperature and/or the change in temperature during the measurement) The laser used in this study had stability problems and the average laser energy over a period of time are shown here. The average fluctuation was found to be of the order of 8-10% depending on the laser energy used.

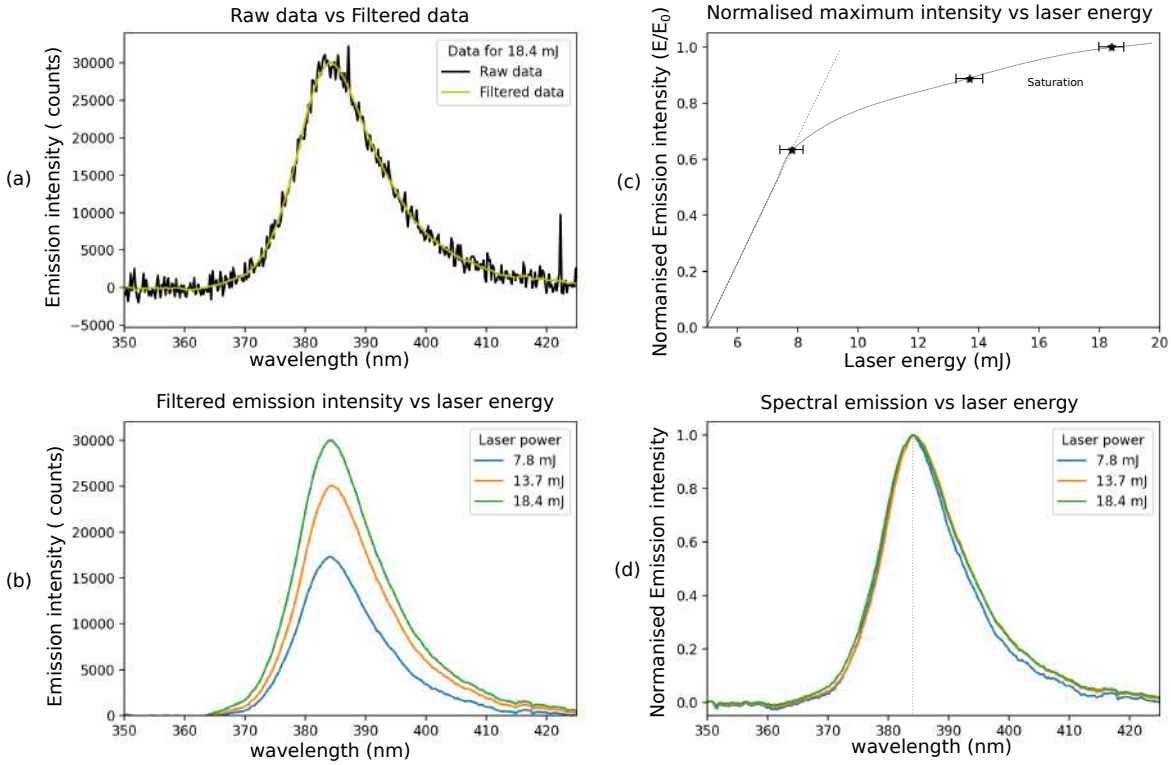

Figure 4.16: Spectral and emission intensity dependence with respect to total laser energy (measured before the laser sheet generator).

4.6.4 Luminescence decay properties

The emission decay properties of ZnO phosphor were studied in detail to identify potential methods to exploit the temperature dependency of emission decay time. In this study, an intensified camera ANDOR iStar sCMOS camera is used as a detector. The specific model of the camera with 5.5 megapixel (2560*2160) is equiped with a P46 phosphor photocathode which allows the camera to operate at optical gating widths of less than 2ns. This camera also has a high spectral sensitivity in the 300-700nm range (See figure 4.17), thus one can be sure that the ZnO emission in the 380nm range is fully captured. There are many advantages of using such a camera as this camera operates with gating widths possible in the nanosecond range and hence analysis to check the decay time of the ZnO particles is feasible. It must be noted that for each temperature case used for calibration, 100 images were acquired, subtracted with background image and averaged before working on them. Two approaches were used to test the emission decay properties. As a first step, the gating width was set at 2ns starting at the same time as the laser pulse (T_0) as shown in figure 4.18(a). Then, the camera gating was set at $T_0 + \delta T$ where δT is the delay from the moment when the laser pulse happens. The delay was progressively added with 2ns at each step from δT= 0ns to 100ns. This is illustrated in the figure 4.18. This procedure was done so as to determine the exact moment when the emission starts to take place. It was determined that about 18ns-20ns, the emission intensity starts to increase.

In another study, the camera was triggered at the same time as the laser pulse but this time, the

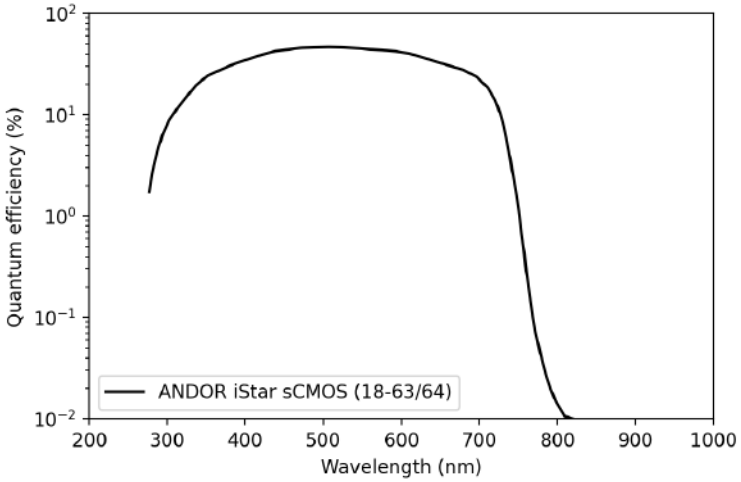

Figure 4.17: Quantum Efficiency Curves for Gen 3 Image Intensifiers for the ANDOR iStar sCMOS camera.

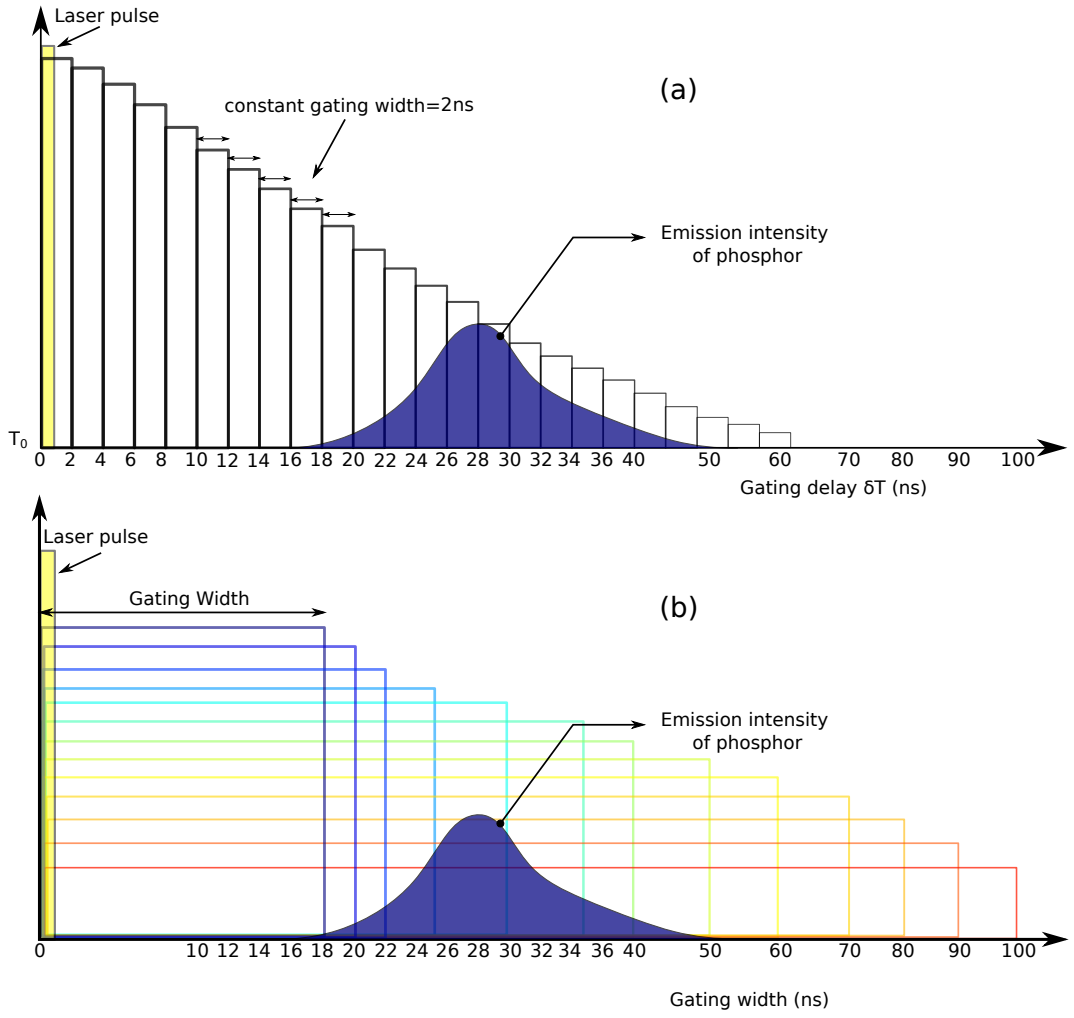

Figure 4.18: (a) Timing diagram for a constant gating width of 2ns and variable delay (δt) introduced before camera aperture (b) Timing diagram for a variable gating width and constant delay (δt) before camera aperture. T_0 is the instant at which the laser pulse is fired.

camera integration time (gating width) was varied from 2ns to 100ns incrementally. The procedure is shown in figure 4.18(b). The results of this study are shown in the figure 4.19. In this figure,

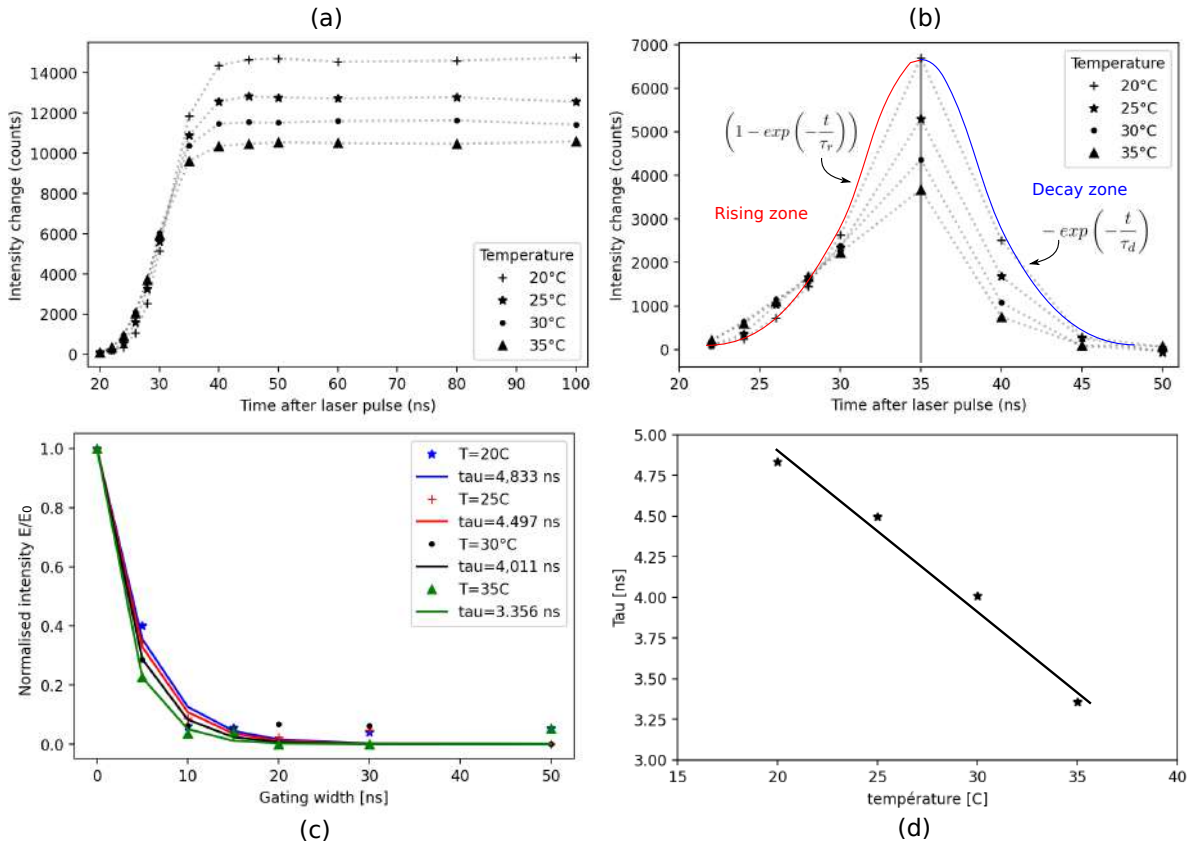

Figure 4.19: (a) Total emission intensity (I)vs time after laser pulse (b) Change in emission intensity (E) vs time after laser pulse. (c) Normalised emission intensity in the decaying arm of the emission vs camera gating width. (d) Evolution of the time constant τ vs temperature.

- (a) shows the variation of emission intensity with respect to camera integration time. It can be seen that the emission process occurs between 20ns to 45ns after the laser pulse. This delay of 20ns could also be due to the BNC cables used to connect the camera and the other devices, inducing some transmission delay. 10m cables were used to connecting the instruments and the length of the cable was the same for all measurements. The constant emission intensity for integration times between 45ns to 100ns shows that the emission process has already ended at 45ns. Additionally, the mean intensity of the emission decreases with increase in temperature. The emission intensity at a given time 't' can be modelled by exponential functions as:

$$I(t) = \begin{cases} \left(1 - exp\left(-\frac{t}{\tau_r}\right)\right) & \text{for rising arm} \\ -exp\left(-\frac{t}{\tau_d}\right) & \text{for decaying arm} \end{cases}$$

  Where τ_r is the rise time constant and τ_d is the decay time constant for a given temperature.

- (b) shows the change in emission intensity with change in time interval $(I(T_n) - I(T_{n-1}))$. One can observe that the maximum change happens around 35ns after the laser pulse. After this time, the emission intensity start to drop and at about 50ns, there are no more emissions.

- (c) shows the evolution of normalised intensity change (E/E_0) where E is the change in the emission intensity $(I(T_n) - I(T_{n-1}))$, and E_0 is the maximum value of $(I(T_n) - I(T_{n-1})$ for a given temperature. This is done so as to demonstrate a 'decaying exponential' of the form

  where τ is a time constant, showing the rapidity with which the emission decays. (Note: this is not the life time of the phosphor).

- (d) shows the effect of temperature on τ. This figure reinforces the previous bibliographic studies mentioned in section 4.2.2 that the emission decay time decreases with increase in temperature due to faster interstate electronic transfers.

From these above inferences, one can highlight that if there are enough cameras available to record the emission with various integration times, the decay time method can be helpful in measuring temperature. Even by working with the mean of 100 images in our current study, one can achieve a precision of 0.01ns/°C change in temperature.

4.6.5 Exploration of a novel technique

A new method is also explored with the aim to reduce the number of detectors required. Figure 4.20 shows the principle of this technique where the intensity ratio of two images, with different gating widths to measure temperature. Taking as an example of a sample study as in figure 4.20, a reference gating width of 30ns is chosen (this can be different obviously). The emission intensity at this reference gating width is 'I_{30ns}'. By dividing the emission intensity for gating widths over 40ns by the reference emission intensity, the ratio remains the constant for a given temperature as seen in (b). The ratio can be given as

$$R_{(\Delta t)} = \frac{I(30ns + \Delta t) - I(30ns)}{I(30ns)} \tag{4.5}$$

By averaging these ratio values for various Δt between 10ns and 50ns (for example), a plot can be for the evolution of this ratio as a function of temperature as in figure (c). Immediately one can see that this method has a better sensitivity to temperature than the cumbersome and expensive decay-time method discussed earlier.

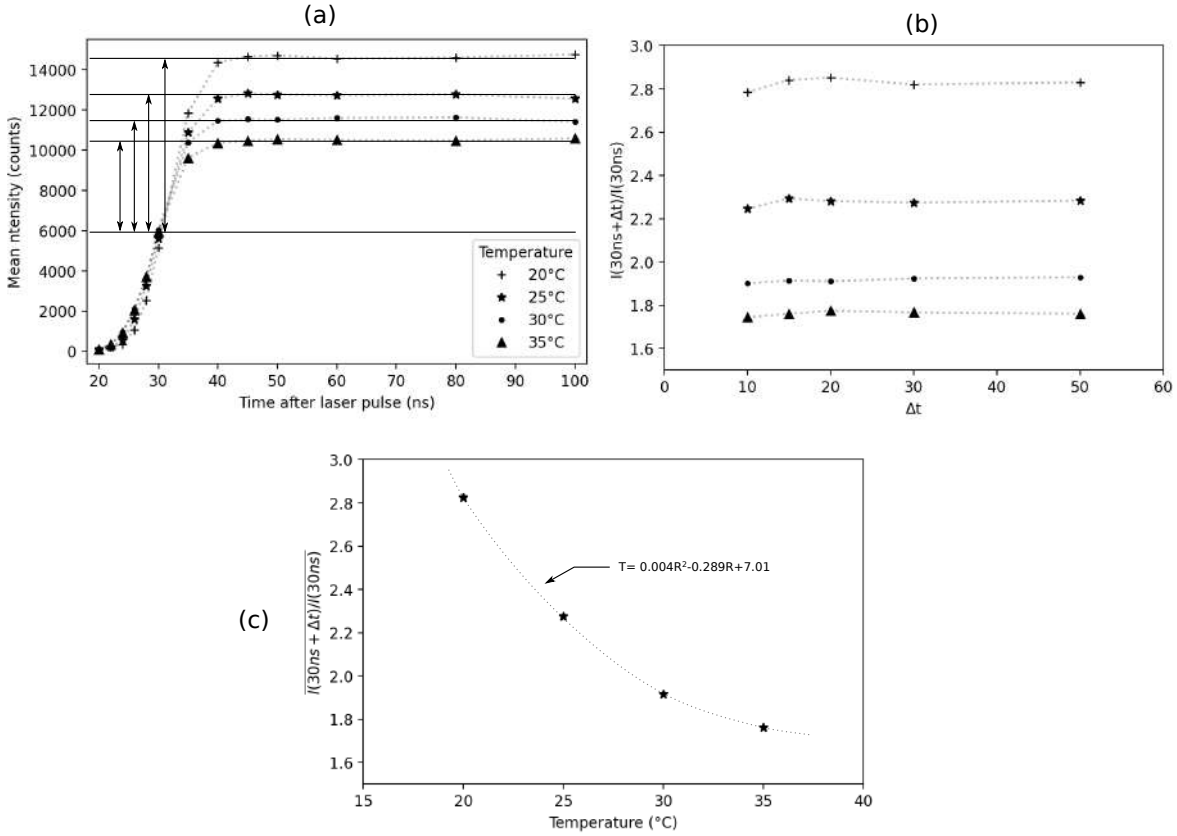

Figure 4.20: (a) Total emission intensity (I) vs time after laser pulse for various temperatures (b) Emission intensity ratio for various temperatures (see text for explantion) (c) calibration curve for the proposed decay-rise time ratio method: Normalised emission intensity vs temperature.

By using two cameras focused on the same region of interest and having two gating widths (one in the rising part of emission and one in the decaying part of the emission) as in figure 4.21 , this method is promising to perform highly accurate phosphor thermometry.

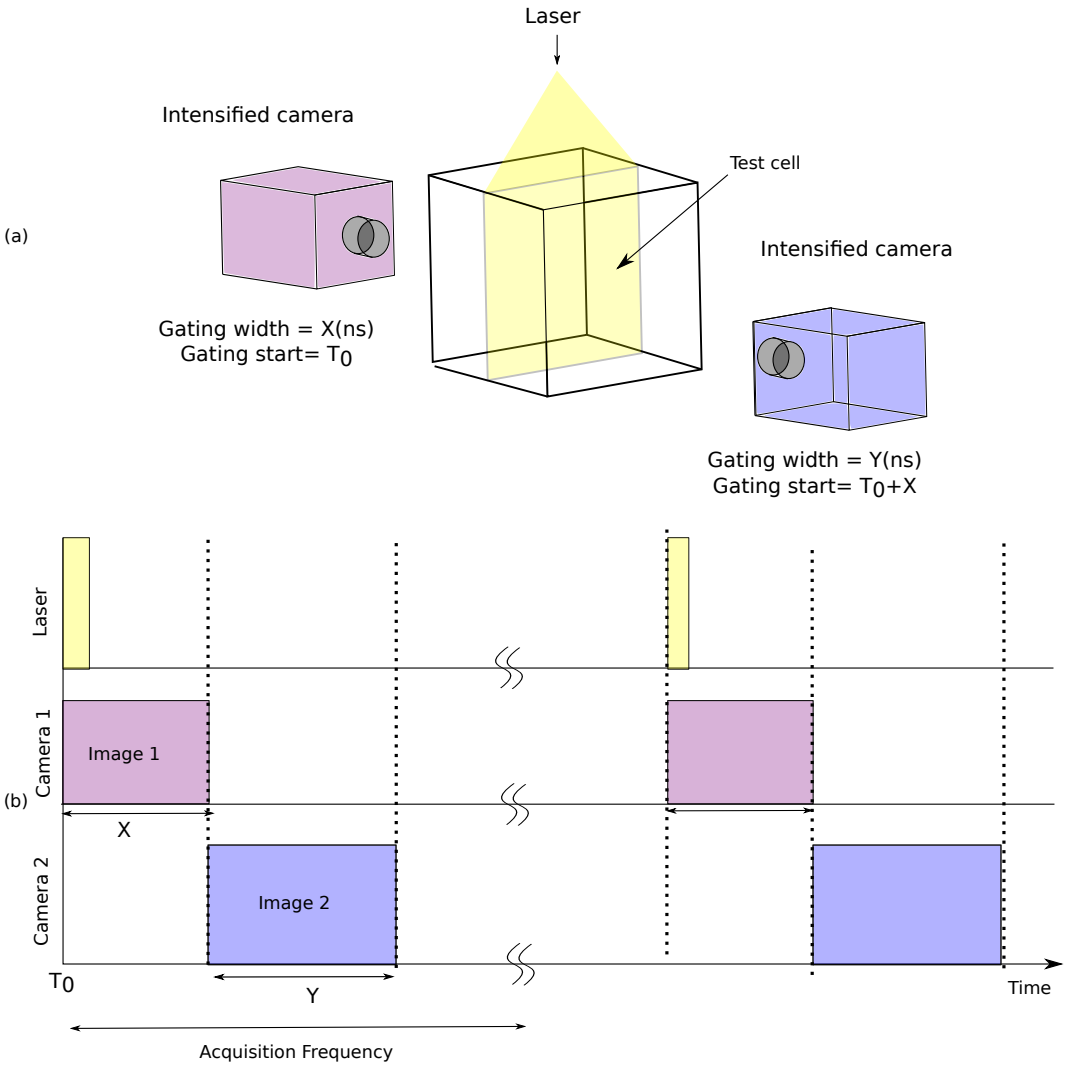

Figure 4.21: (a) Representative image of an imaginary setup for the proposed decay-rise time ratio method (b) Timing diagram for the laser and cameras for the proposed method.

However, even this method requires a minimum of two cameras that have very short gating widths in the order of few nanoseconds, as with a single camera, the time required to capture emission at incredibly short intervals using a single camera is impossible (frame 1 at 0 to 30ns and immediately frame 2 at 30 ns to 100ns). In the current thesis, the lack of an identical intensified camera is a constraint to explore this method further. Hence, it was decided to implement a spectral method called spectral intensity ratio.

4.7 Development of two-color spectral intensity ratio method

In this section, the procedure used to perform the spectral intensity ratio method is described. As demonstrated in the section 4.5.2, the spectral emission of ZnO changes with temperature and hence, it can be exploited to map 2-D flow temperatures. By division of images obtained by through filtering using appropriate filter bands, intensity ratio maps can be obtained, which can eventually be used to convert it to temperature fields. In short the expression for the intensity ratio R for excitation wavelength λ_0 and temperature T, is given as

$$R_\lambda = \frac{\sigma(\lambda_0, T_1)}{\sigma(\lambda_0, T_2)} \tag{4.6}$$

Concerning the experimental arrangement for this study, every equipment (Test cell, laser and optics, temperature regulation, thermocouples to monitor temperature etc.) used is the same, except for the camera and a device called optosplit. For the emission decay properties, ANDOR iSTAR camera was used. However, due to material constraints, the author is forced to work with another intensified camera Princeton PIMAX2. This camera has features inferior to the ANDOR camera, but sufficient enough to carry out calibration process in the Rayleigh-Benard cell.

The PIMAX2 camera works at 5Hz, and has a maximum resolution of 1024 x 1024 pixels. It also equipped with an intensifier 'Gen II' with gain variable between 0 and 255. This is controllable with a software with an accuracy of the order of 0.1ns close to the gating width. When a fluorescence photon is captured by the camera, it has a certain probability to be converted into an electron at the photocathode. It is then multiplied by the matrix of microchannels, which acts as an electron multiplier. Depending on the gain, the voltage applied between the photocathode and the microchannel plate varies and determines the amount of electrons that will then hit the phosphor screen. Upon contact with the phosphor sensor, electrons are converted into photons, and the resulting light signal is greatly enhanced than that reaches the photocathode. These photons are then guided by optical fiber to the CCD sensor, which will, for its part, convert the optical signal into 16-bit levels (65,535 levels). The camera is also sensitive between 120-400nm, enabling to work with ZnO phosphor emissions.
However, the low quantum efficiency (<15%) implies the need to have significant incident radiation

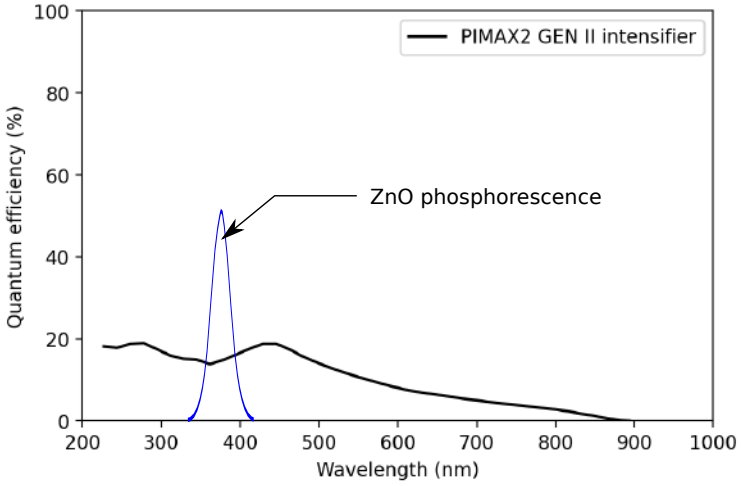

Figure 4.22: Quantum efficiency of Princeton camera with the superposition of the emission spectrum of ZnO phosphor.

(Figure 4.22). In addition, ICCD technology has some disadvantages: since each pixel is intensified individually, the response can vary from one to another. Moreover, it turns out that the levels recorded by the CCD sensor are not directly proportional to the intensity measured and that the gain also influences the final image. In the current study, the maximum recorded levels (camera counts) was of the order of 2000 counts and the gain applied was 150. This is chosen so that the response of the camera is in the linear region and hence eliminates the need to perform non-linear corrections.

The spectral intensity ratio method is based on exploiting the temperature dependence of the emission spectrum. To this end, an Optosplit II device is used to split the emitted radiation into two paths which are eventually passed through two different bandpass filters and recombined to produce two images on the same camera. A raw image of such an operation is shown in the figure 4.25. The two bandpass filters were chosen based on an iterative method to obtain the best calibration curve slope by using the data obtained from the spectrometry tests and taking the manufacturer's product range. The filters chosen are i)370-380nm and ii)395-410nm (ET380x and ET402-15x by Chroma). It must be noted that although the camera used may be sensitive around 370nm, boro-silicate glass components may be a hindrance in the transmission of emitted radiation. Care must be taken to choose the right components including the necessary modifications

of the components like mirrors, lenses and other optics in the Optosplit unit to ensure high signal collection in the camera.

4.7.1 Image acquisition

The first step is the acquisition of images by setting up the camera, laser and Digital Delay and Pulse Generator operate synchronised. The timing diagram is shown in the figure 4.23. It can be seen from this figure that the laser operates at 10Hz and the laser pulse width is 10ns. Upon excitation, it is seen that the ZnO emission is almost spontaneous of the order of 20ns (as explained in the section 4.5.4). In order to capture the entire emission, the camera is triggered along with the laser and the gating width is set at 200ns. Also, the camera is physically limited to work at 5Hz. Hence, the emissions are captured for every alternate laser pulse and one out of every two laser pulses are used to capture the emission by the camera.

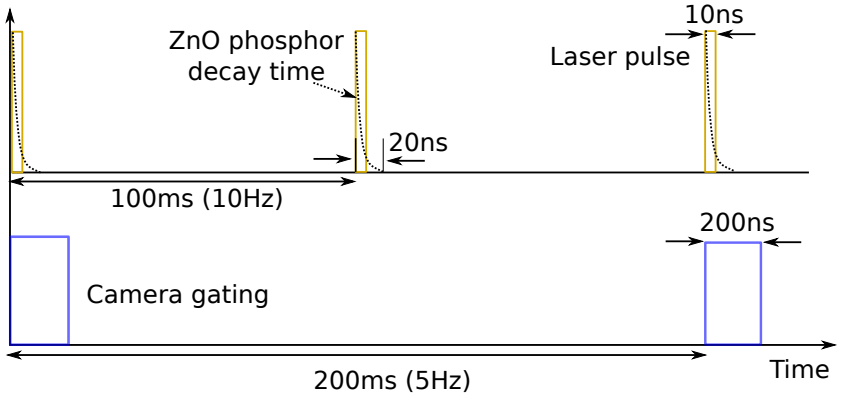

Figure 4.23: Timing diagram for the laser fire and camera gating.

Since the camera is an intensified camera, a gain is applied to multiply the detected signal, albeit an increase in noise. For this reason, a Gaussian filter is necessary to smoothen the image. A study was made to determine the right balance between the intensification (gain) applied to the camera to increase the luminosity of the particles and while keeping the noise generated low. Figure 4.24 shows the standard deviation in percentage as a function of the Gaussian filtering applied and as a function of gain applied to the camera intensifier. During this study, the camera was focused on a target zone and care was taken to have the same image intensity for each case so as to have a correct comparison between the different cases. The figure highlights the independence of the standard deviation with respect to the size of the Gaussian filtering applied for values more than 7x7 pixels. Eventually, a Gaussian filter (7x7 pixels) is applied to smoothen the images acquired with a gain of 150 to get the best compromise in the succeeding experiments. Hence to summarise, the choice of measurement technique is finalised (a) Princeton PIMAX2 camera with an integration time of 200ns at a gain of 150, 7x7 Gaussian filtering, 100 images to work on mean images (b) Dantec Spectra physics laser working at 266nm providing a laser pulse energy of 16.8mJ, (c) ZnO mixed in water with a concentration of 0.01g/L.

For each test case, 100 images are obtained so as to be statistically convergent when working with mean values. Thanks to the use of optosplit device, each of these 100 images contains two filtered images of the area in focus (test cell). A raw image is shown in the figure 4.25. From hereon, the image filtered through filter 1 and filter 2 will be called as Image A and Image B respectively.

4.7.2 Calibration procedure

A calibration procedure is required to be set in place so as to robustly perform temperature measurements irrespective of the application used. For this reason, an in-house code is developed in the framework of this thesis to perform PIV and phosphor thermometry simultaneously. Due to camera constraints (impossibility of the camera to work in PIV mode), the procedure for PIV is described but it is not used to perform simultaneous velocity and temperature measurements.

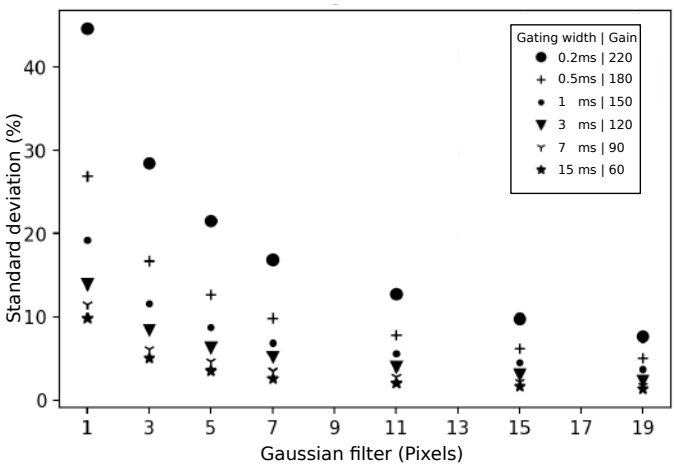

Figure 4.24: Percentage standard deviation as a function of gating width/ intensification and Gaussian filtering. Note: In all cases, the image intensity was kept at a constant level so as to be comparable between different cases.

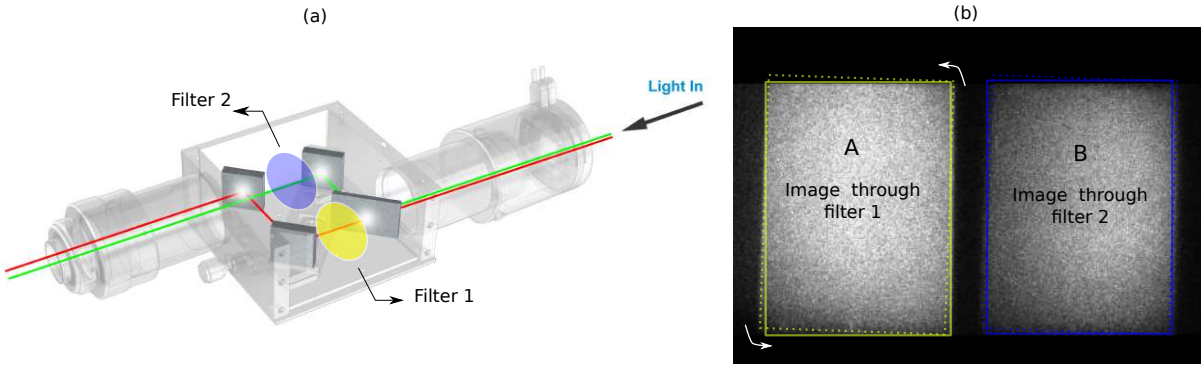

Figure 4.25: (a) Working of Optosplit. (b) Example of a raw image containing two filtered images.

However, the code is used for image identification and corner matching to execute spectral intensity ratio phosphor thermometry. Further, an image processing code to implement intensity ratio method is developed. The entire calibration process is described below.

In all more than 50 experiments were conducted to understand and master the calibration process better. Here, one such calibration is chosen as an example to explain the process. Eight calibration points are chosen between 20°C and 50°C and the magnetic stirrer is switched on for all the cases so as to obtain a uniform temperature inside the test cell. It must be noted that in all the test cases, a central zone of 50mm by 35mm was chosen to do the calibration so as to prevent light reflections from the top and the bottom walls and the presence of columns on the sides prevents capturing the entire width of the cell as seen in figure 4.10. Figure 4.26 shows the overall view of the calibration procedure with various steps to perform the spectral intensity ratio method. These steps will be elaborated in the proceeding sections.

Image matching by PIV

The image matching of the zones of images A and B is done by using a PIV code developed using Python 3. To know the right pixel to cm scaling, the PIV matching is done by the use of a 'calibration image' where a solid plate with dots printed in a pattern is used as region of interest.

The PIV code is developed by following the books by Adrian & Westerweel (2011) and Raffel *et al.* (2018). The PIV code is provided in Appendix B. The functionalities of the code are many and some are listed here.

- Choice of Region Of Interest (ROI) in the image.

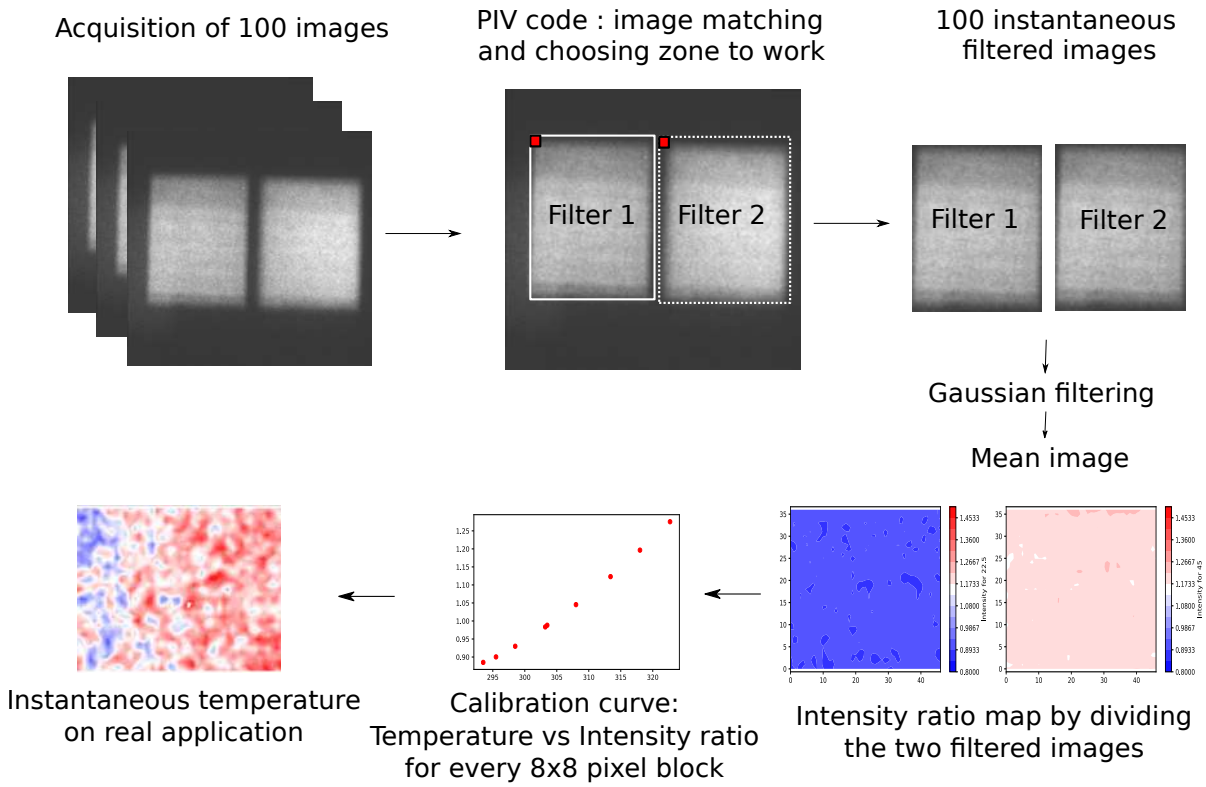

Figure 4.26: Image showing the various processes involved in the calibration procedure.

- Option to choose Window size/ Interrogation window
- Automatic cross-correlation to find matching locations for the two PIV images (Peak locking).
- Sub-pixel estimation
- Spurious vectors filter and replacement with a weighted average mean vector
- Display of vectors in the form of 2D plots. Different variables like velocity, rotation etc. can be plotted

The end result of using this code is perfect matching of the zones of images A and B.

Pre-processing of images

The step following image acquisition is the procedure to do image corrections like rotation and de-warping before working on the two filtered images A and B. Figure 4.25 shows the raw images before (dotted line) and after rotation (solid line). This correction is necessary to obtain the right matching of the corners of image A and B. Using the PIV code mentioned in the previous text, the exact zones of A and B are already found. Now, there is an option to choose the working area (ROI) and the images are cropped to right dimensions. All the 100 'A' and 'B' images are stored separately and subtracted with the background image.
ZnO particles suspended in water tend to be discrete particles and hence there are zones in the images where there are no particles. In order to work only on the zones where there are particles, a pixel by pixel verification on each of the 100 images of each calibration temperature is done to make sure that the intensity of the emission is more than a cut-off limit, effectively identifying if there is a particle or not. The procedure is shown in figure 4.27. For every pixel of the images A and B, this procedure is done and the mean is calculated assuring that the mean includes only zones with particles. The mean images for each calibration temperature is stored separately. The intensity ratio calibration will be performed on the averaged images.

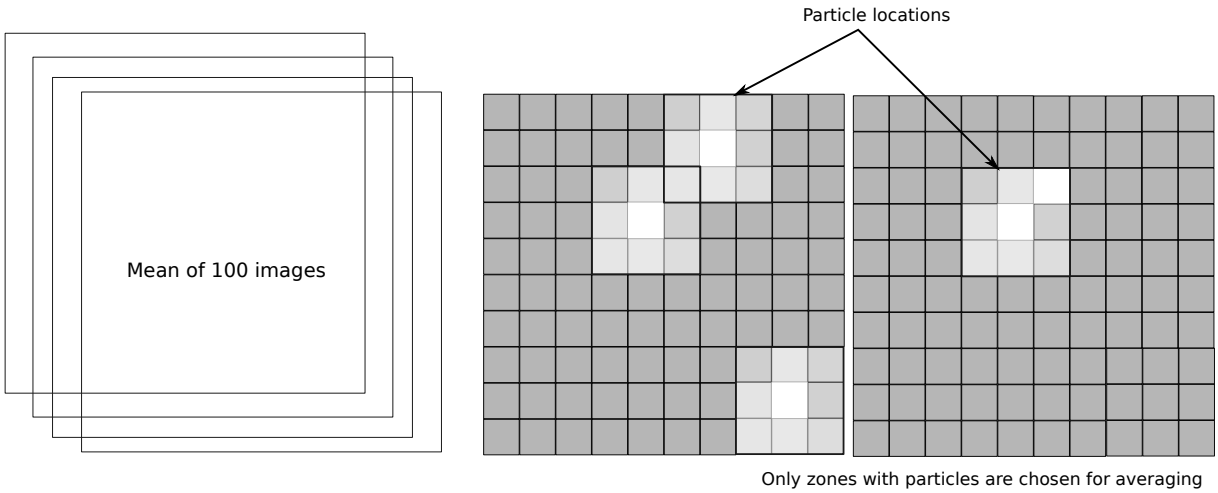

Figure 4.27: Representation of the averaging process. The zones with the particles are alone considered for obtaining the mean image.

Obtaining calibration curves

The mean A and B images for each temperature are then processed in a separate function to obtain the intensity ratios for each calibration temperature and obtaining a calibration curve.

$$T(i,j) = kR^2_{\lambda(i,j)} + lR_{\lambda(i,j)} + m \tag{4.7}$$

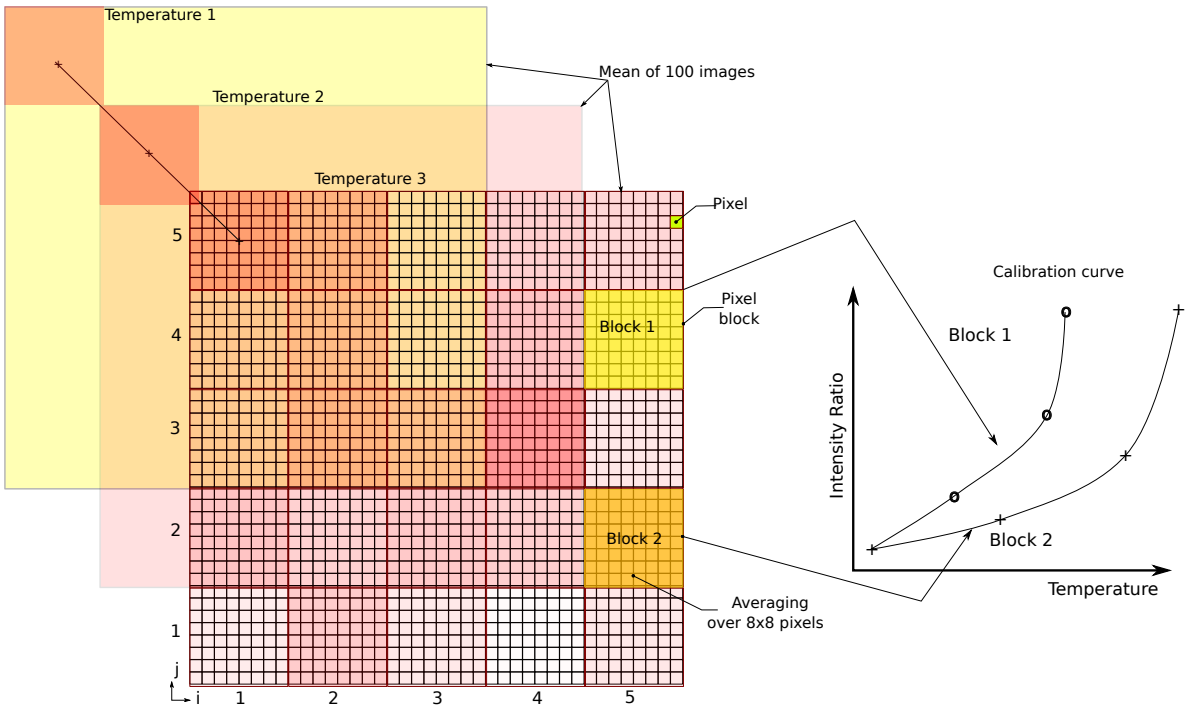

Figure 4.28: Representation of the 'block averaging' process. Each block has its own temperature vs intensity ratio calibration curve following 4.7.

In all, if I_A and I_B are the corrected intensities of the mean images A and B (through filter 1 and filter 2), the rationing process can be summarised by the expression

$$R_\lambda = \frac{I_A}{I_B} = f(T) \tag{4.8}$$

$$I_A = \left(\frac{\overline{Iimg_i} - \overline{Iimg_{BG}}}{\overline{Iimg_{ref}} - \overline{Img_{BG}}} \right) ImgA_{(\lambda_1,T)}$$

$$I_B = \left(\frac{\overline{Iimg_i} - \overline{Iimg_{BG}}}{\overline{Iimg_{ref}} - \overline{Iimg_{BG}}} \right) ImgB_{(\lambda_2,T)}$$

Here T is the temperature, λ is the bandwidth of the filter used (As explained in section 4.7: λ_1=370-380nm , λ_2=395-410nm) $Iimg_{BG}$ is the background image, $Iimg_{ref}$ is a reference image chosen at a certain temperature (20°C for example) and $Iimg_i$ is the image at temperature T. In addition to the (nxn) pixel block averaging, the intensity ratio map of every calibration temperature was divided by that of a reference temperature at 20°C to normalise values. Hence through these two processes, the effect of varying local laser intensity in the calibration cell is eliminated.

Computing temperatures

Now that each of the nxn pixel block has a calibration curve, these can be used to calculate the temperature of a zone if intensity values are known. For example, if the procedure described in the above sections are followed to obtain an intensity ratio map for a certain flow field, this intensity ratio contour can be converted to temperature by inserting intensity ratio values into eq. 4.7. Figure 4.26 shows the entire calibration procedure and the determination of temperature.

4.7.3 Validation and accuracy

The calibration curves obtained are then tested on known test cases as in figure 5.17 to validate the results. The top and the bottom plates are maintained at the same temperature for sufficiently long periods so as to make sure that the temperature does not vary during the acquisition. The magnetic stirrer is switched on so as to have a uniform temperature in the test cell. In addition to the two thermocouples in the top and the bottom plates, a third thermocouple monitors the water temperature inside the cavity. From figure 5.17, the uniformity in the 2-D temperature field inside the cavity can be observed clearly. In addition to this, the temperature distribution plots show the high accuracy of this technique. For example, 90% of the field had an accuracy of 0.5°C for the case where the temperature was maintained at 40.4°C. This is in the order of the accuracy of the thermocouples used to monitor the temperature of the bottom and top plates. In all the cases, the maximum deviation from the mean temperature was 1.2°C. The average deviation of the average temperature in the entire zone was of the order of 0.2°C.

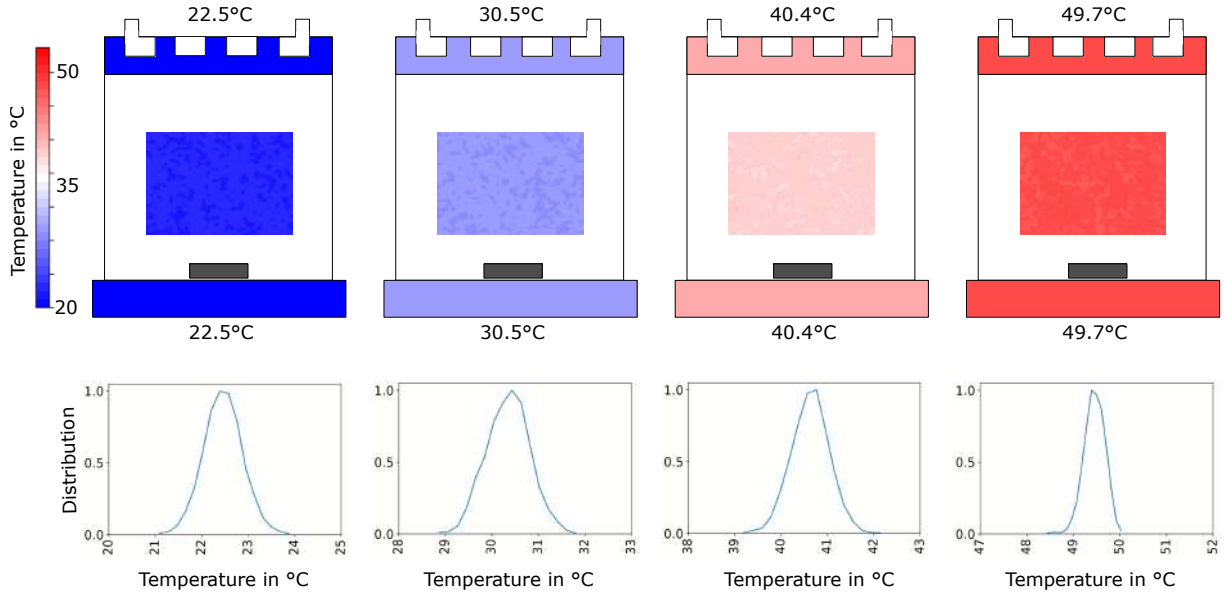

Figure 4.29: Validation of the calibration process by testing the process at constant temperature cases at various temperatures. A frequency distribution of temperature for the entire calibration zone is shown below each case.

4.8 Application: Raleigh-Bénard convection

In this section, an application of the ZnO thermometry in liquid is discussed. The same setup is used to conduct Rayleigh-Benard natural convection. This phenomenon is a classic example of natural convection occurring in a fluid initially at rest between a hot bottom plate and a cold top plate. Rayleigh suggested that the instability generates a recirculation flow when the Rayleigh number Ra is greater than a certain critical value (Ra=1708). Where g is the acceleration due to gravity, β is the thermal expansion coefficient , T the temperature difference between top and bottom walls, L is the characteristic length (distance between the walls), ν the kinematic viscosity and α is the thermal diffusivity, the Rayleigh number Ra_L for the given characteristic length L is given as

$$Ra_L = GrPr = \frac{g\beta\Delta TL^3}{\nu\alpha} \tag{4.9}$$

Here, upon heating the bottom plate and cooling the top plate at a constant temperature, density differences of the water in the lower and higher regions give rise to natural convection. The most important parameter deciding the form and manner of mixing within the cavity is the Rayleigh number as discussed above. In this study, a Rayleigh number of 7x10^7 is studied with a temperature difference of 10 °C between the top and the bottom plate.

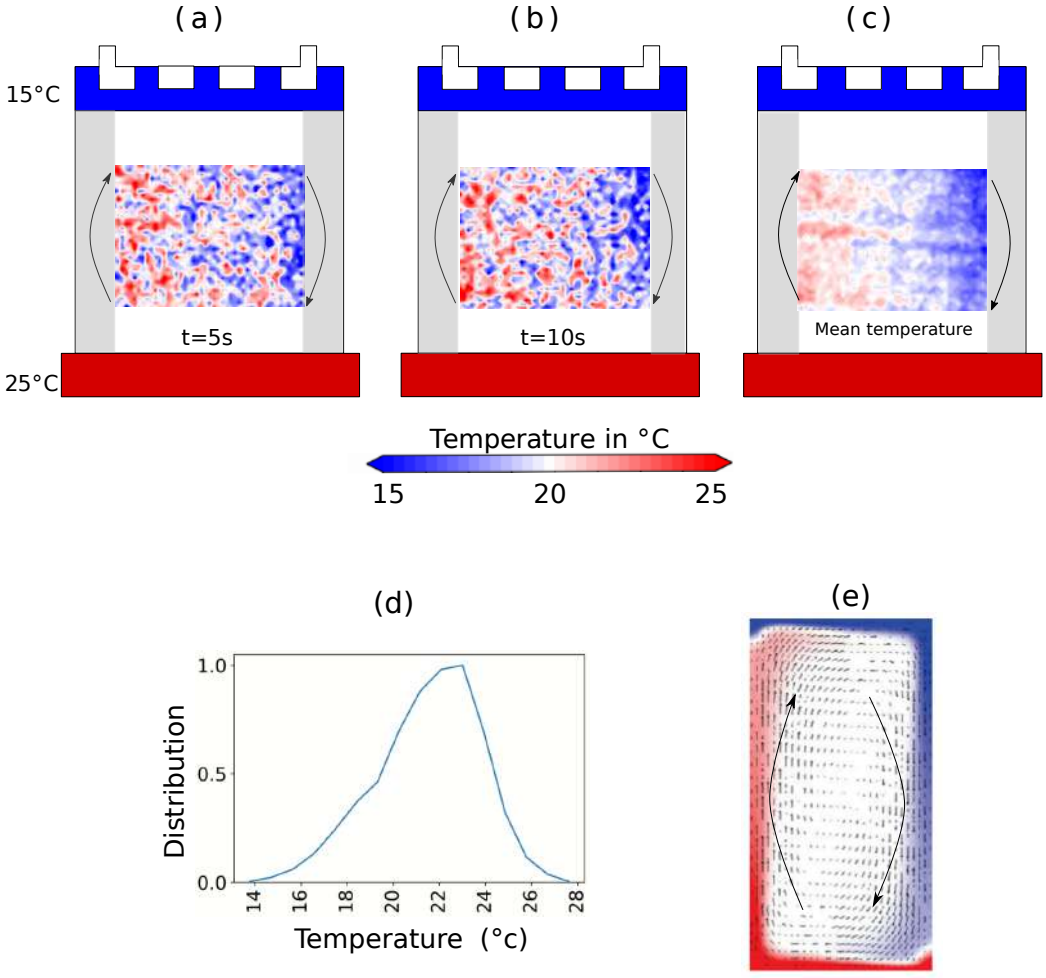

Figure 4.30: Instantaneous temperature fields at 5s (a) and 10s (b). Mean temperature field and the corresponding temperature distribution is seen in (c) and (d) respectively. (e) Mean temperature field with superimposed velocity vectors: adapted from Silano *et al.* (2010)

The experiments were conducted at the same time as the calibration with similar conditions of

concentration of particles and laser intensity. In this case, however, the magnetic stirrer is removed during the experiments. A single circulation in the anti-clockwise direction is observed and this is comparable to the previous work of Silano *et al.* (2010). In addition to this, thermal plumes are seen to raise above from the bottom wall and these are clearly visible in the instantaneous temperature field as shown in figure 4.30. The average temperature field shows a warm column on the right and a cold column on the left validating the measurement technique. Moreover, the temperature distribution of the mean flow field contains temperatures between 16°C and 24°C which is the range of temperature expected from this problem. The mean temperature in the zone considered was 21.0°C. It must also be noted that the calibration points chosen to do the calibration curve were between 20°C and 50°C. The temperatures for the present Rayleigh-Benard case were chosen on purpose to check the accuracy of this method outside the calibration curve (15°C on the top plate) and the results have obtained are accurate enough to safely validate the performance of this technique.

Conclusion

In this chapter, phosphor thermometry has been introduced. The various properties of ZnO phosphor have been analysed. Different calibration techniques were explored and it was decided that for the current thesis, use of spectral intensity ratio method is the best choice. A detailed calibration procedure has been described for this method and validated using a natural convection test case. The entire process with the validated calibration code to perform spectral intensity ratio phosphor thermometry can be translated to study film cooling experimentally. In the next chapter, the film cooling analysis of the auxiliary hole configuration and a single hole configuration is discussed. ZnO phosphor thermometry is employed so as to determine the 2-D temperature flow field in gaseous medium with an in-situ calibration done for the gaseous working phase.

Chapter 5

Analysis of film cooling using Experimental methods

This chapter deals with the experimental analysis of film cooling. Auxiliary hole configuration and single cylindrical hole configuration are tested on the BATH test rig. The description of the innovative BATH test rig is provided. As the test bench has been used for the first time, the characterisation of the flow in the test section is performed to study the velocity and thermal profiles. Eventually, film cooling configurations are tested using the spectral intensity ratio phosphor thermometry as described in Chapter 4 to visualise 2-D temperature fields.

Figure 5.1: Aerial view of the PROMETEE platform (PROgramme et Moyens d'Essais pour les Transports, l'Énergie et l'Environnement) at Poitiers.

Contents

5.1 Concept of BATH 70
5.2 Description of BATH Test rig 71
5.2.1 Test facility components 71
5.2.2 Seeding system 75
5.3 Calibration of BATH test rig 79
5.3.1 Presentation of measurement techniques used for calibration purposes . . 79
5.3.2 Working points of BATH test rig 81
5.3.3 RANS simulations: effect of step 85
5.4 Film cooling: 2-D temperature measurements 86
5.4.1 Film cooling geometry 87
5.4.2 Film cooling: Boundary conditions 87
5.4.3 Experimental setup 88
5.4.4 Calibration 91
5.4.5 Results: 2-D temperature fields 91

5.1 Concept of BATH

Banc Aero-THermique (BATH) is a new test rig developed at the PROMETEE platform shown in figure 5.2. Most studies of flows are tested currently wind tunnels that operate at cold temperatures for aerodynamic analysis in a controlled environment or using combustion for high temperature studies but at non-homogeneous and steady conditions. Some of the test benches have the possibility to combine the two characteristics but at much lower temperatures and pressure as compared to a real aero-engine. The BATH test rig aims to bridge the gap and to provide an innovative solution to test components at very high temperature (1200°C) and pressure (10 Bar) in steady state conditions. The test rig is brand new and was first commissioned in 2019 and hence extensive calibration of the working points of the test rig were carried out in the framework of this thesis too. This chapter sheds light on the various components and the working of this test rig.

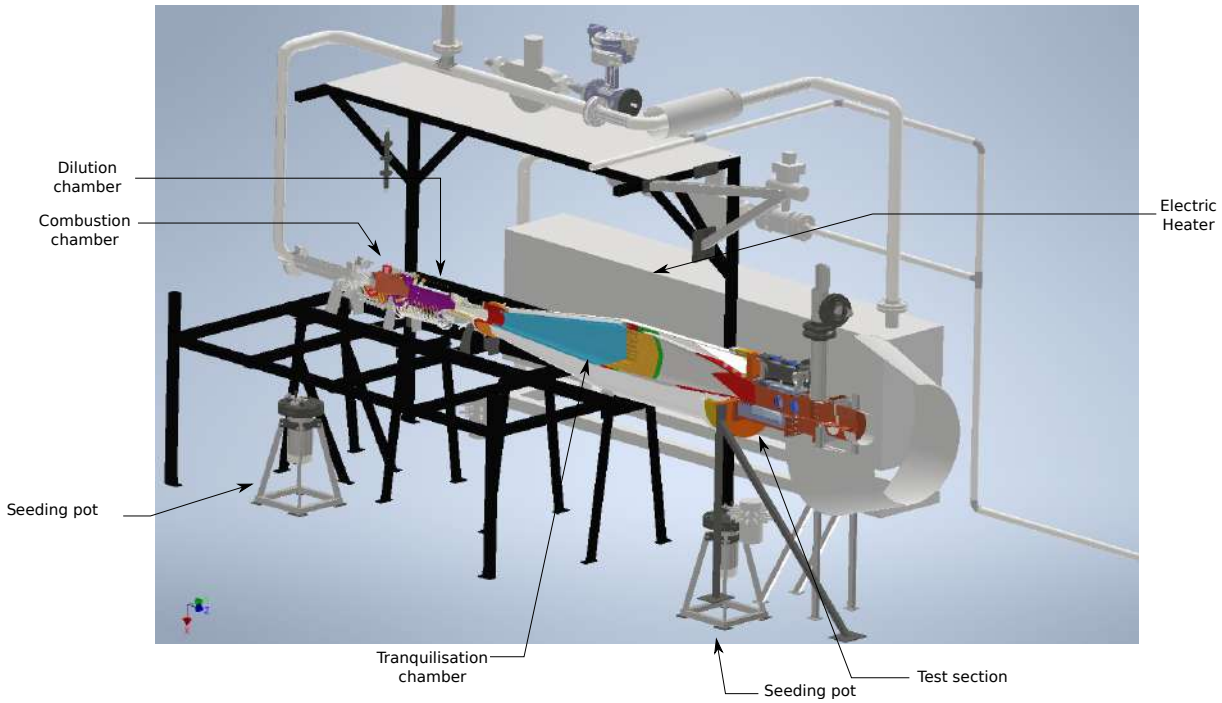

Figure 5.2: BATH test rig: CAD view

5.2 Description of BATH Test rig

The BATH test bench is an open circuit wind tunnel which aims to recreate the flow and temperature conditions found in aero engines within a test section. Air from a compressor tank is electrically heated before controlled air-kerosene combustion which raises the temperature of the air to extreme temperatures. It consists of a premix chamber where kerosene is injected and vaporized into an air flow, a combustion chamber fitted with a spark plug, a two-stage dilution chamber where a flow of fresh air is added, a sonic-throat which ensures a constant flow in the test section and a convergent-divergent chamber which dampens the turbulence of the flow. Moreover, this also helps in increasing the pressure in the combustion chamber and a lower pressure in the test section at high mass flow rates. An adjustable neck at the test section outlet makes it possible to adjust the pressure in the test section. At the outlet of the test channel, the flow is taken up by an extractor which expels the flow outside the building. This flow is diluted with the air from the test hall and is cooled by spraying water. An important aspect of the test bench is the fully automated system with a control room. During the course of the experiments, there are no physical contacts with the test bench as all the parameters are monitored remotely.

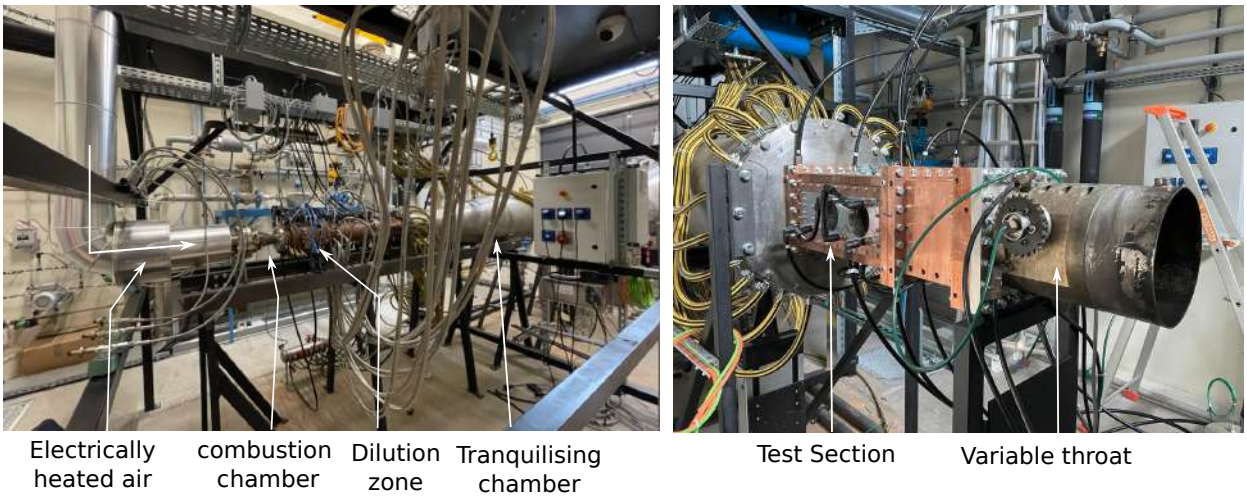

Figure 5.3: BATH test rig: assembled view of premix and combustion zone, dilution and expansion chambers.

5.2.1 Test facility components

The BATH test rig has numerous essential components. The main components of the test rig are shown in figure 5.4. These components are explained in the sections below.

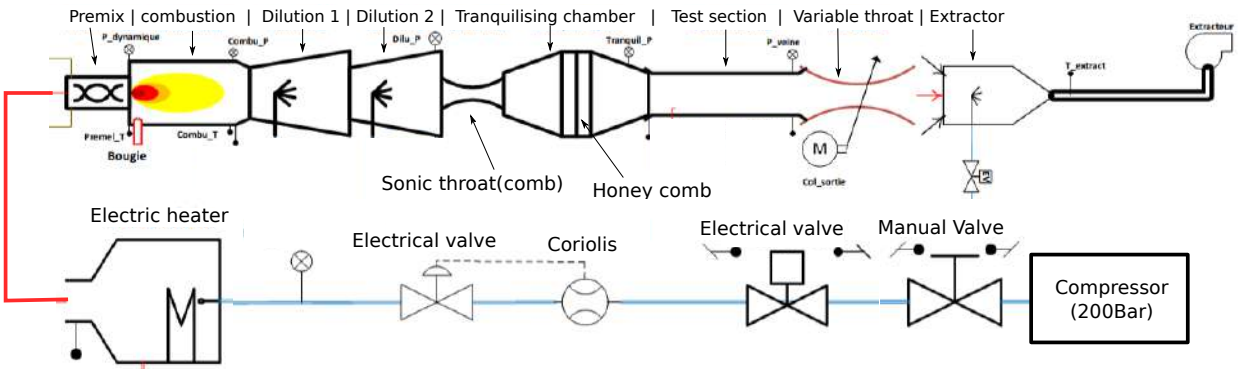

Figure 5.4: Schematic view of the Bath test rig components

Compressed air feed

The first component of the BATH test rig is the compressor that operates at 200 bars of pressure. The compressed air is stored in a metallic tank and feeds the air to the test rig at 40 bars of pressure through two pressure regulators. A series of valves and security valves are attached to the main line of the air feed so as to reduce the pressure to lower operable levels. A coriolis mass flow meter is attached to this line to observe the flow rate in kg/s. It is to be noted that all the supply tubes are made to withstand a pressure of 40 bars as a safety precaution. An electronically controlled regulation valve is attached to the main air line to vary the pressure and mass flow rate required by the experiments.

Electric heater

An electric heater shown in figure 5.5 is used to heat the cold air before entering the combustion chamber. The heater operates at 287 kW of power and is capable of functioning between 20 to 500°C. The heater can work at low velocities from 1m/s to 77 m/s and a pressure range of 1 to 15 bar. The presence of the electric heater allows us to operate the test bench at lower temperatures too, without the need to use combustion. Moreover, the combustion process is stable without interruptions when the air is pre-heated to about 80°C.

Figure 5.5: Picture of the electric heater system.

Premix chamber

The premix chamber seen in figure 5.6 is the first zone of the combustion chamber where the air is mixed with kerosene and is vaporised in this zone. The air entering the premix zone arrives axially and through the use of to co-axial swirlers, the air is set into swirling motion. Upon injection of the kerosene through injectors that operate at 80 Bar pressure, the fine droplets of kerosene become vaporised immediately. The injectors are placed radially just after the first swirler and each of the 6 injectors can be operated individually.

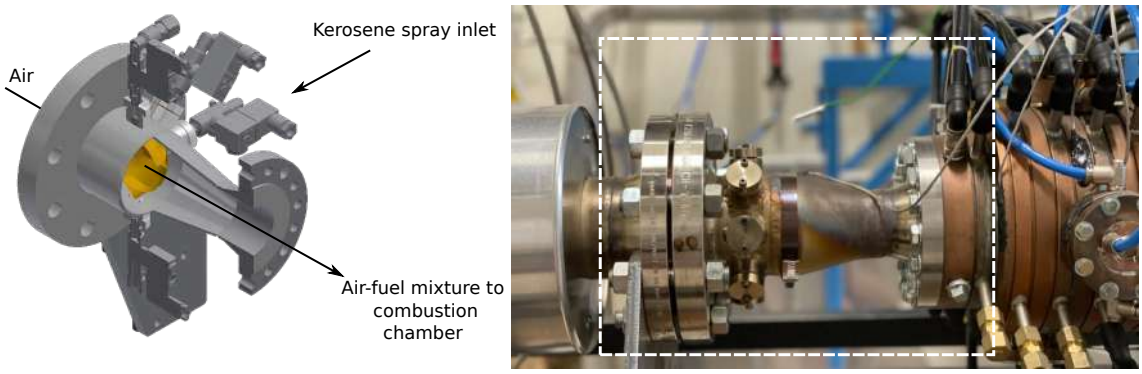

Figure 5.6: CAD view of the premix chamber with the injectors. Right picture shows the actual view of the pre-mix chamber

Combustion chamber

The combustion chamber as in figure 5.7 is of the type 'Lean Pre-mixed Pre-vaporised' or LPP. Lean refers to the air-fuel mixture ratio where less than stoichiometric levels of fuel is used. Pre-mixed refers to the mixing of the fuel and the air before entering the combustion chamber. The pre-vaporised configuration is a technique where the fuel in liquid form completely vaporises and mixes with the air before the combustion actually takes place.

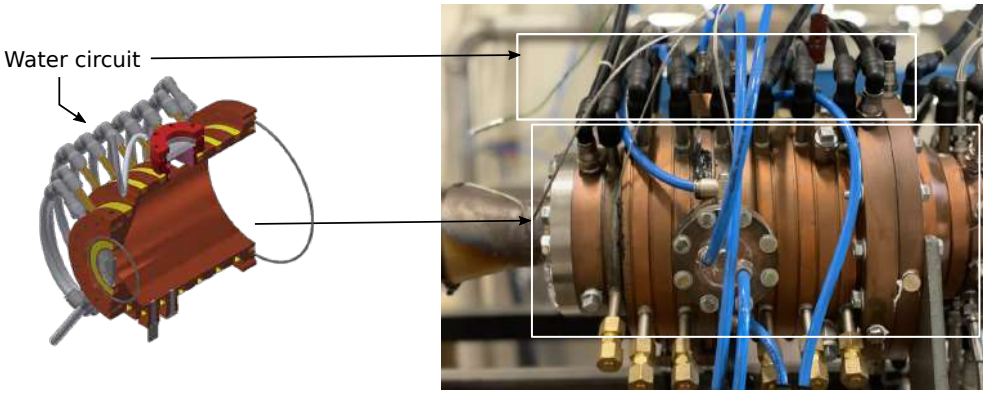

Figure 5.7: CAD view of the combustion chamber. Right picture shows the actual view of the combustion chamber

Primary reaction zone

Just after the second swirler, the air-kerosene mixture enters the combustion chamber and here, the ignitors are present which ignite the flow. In theory, temperatures of up to 1900°C can be achieved. However, the material constraints restrict the temperatures to lower levels. In real gas turbine applications lean burn combustion is preferred due to the low emission of soot and NOx and the flame temperatures remain in the range where the material can withstand the temperatures. At the beginning of the combustion chamber, the temperature is about 1700°C which gradually reduces to about 1600°C at the exit. The walls of the combustion chamber are maintained at about 750°C thanks to the water cooling circuit.

Dilution zone

The hot mixture after combustion is further added with air through two dilution zones. This helps in reducing the temperature to the required level in the test section and also to maintain the wall temperature at acceptable levels in the test bench. Just the exit of the dilution zone is the sonic throat which ensures a constant flow in the test section without fluctuations. An important

function of the dilution zone is also that the seeding in the primary flow is added through the first dilution. The description of the seeding chamber will be discussed in more detail. The air introduced into the dilution zone is fed radially through many tubes attached. Figure 5.8 shows the actual dilution chamber and a CAD view.

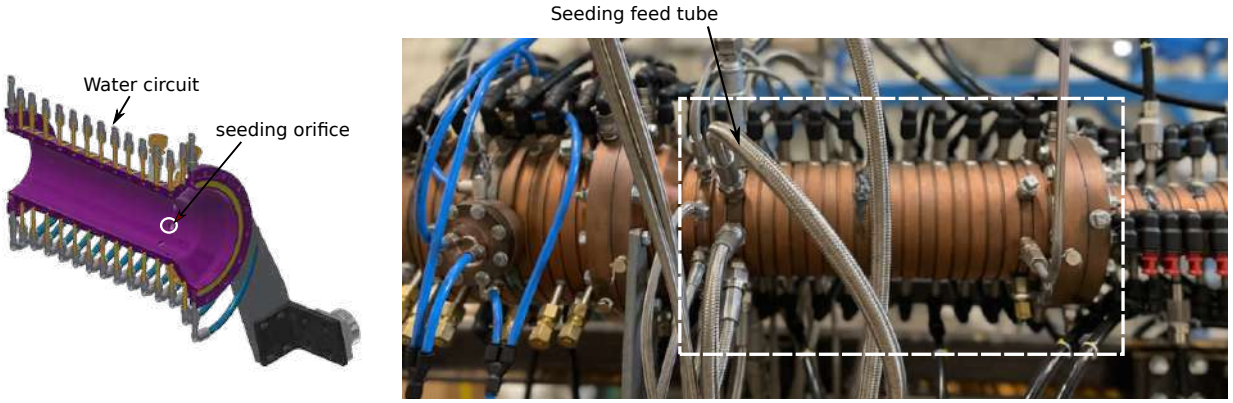

Figure 5.8: CAD view of the dilution zone. Right picture shows the actual view of the pre-mix chamber

Tranquillising chamber

The burnt gases exiting the combustion chamber are quite turbulent. In order to perform meaningful experiments specifically in the same operating conditions as in a real aero-engine, this high turbulence has to be reduced. Hence the hot gases are passed through a diverging converging section. In this zone, a honey-comb made with ceramic material and which can withstand very high temperatures is used to reduce the turbulence intensity of the flow. At the exit of the chamber, hot-wire measurements have shown a turbulence intensity of 5-9%.

Test section

The test section as shown in figure 5.9 is the zone where the film cooling configurations are tested. The exit of the tranquillising chamber leads to the test section. The test section is made of cupronickel material and is water cooled. At the top side of the test section, the film cooling plate to be analysed is fixed. The holes of the test plate are fed from a pressurised chamber. This chamber also consists of a window which permits the use of an IR camera to study the heat transfer into the plate.

At the bottom side of the test section, an access is provided to illuminate with a laser sheet. Each of the window accesses are water cooled around the edges in order to support the high temperatures.

On one side of the test section, two circular windows are present in order to have a clear view of the zone of interest and to observe the particles illuminated by the laser. On the other side, a metallic plate with plain surface is used. All the inside surfaces of the test section are completely smooth and the effect of having protrusions within the flow was also analysed numerically which showed very less influence on the film cooling zone even in the presence of a 'step' where the optical access are located. The results are presented in the section 5.3.3.

The dimensions of the test section are 45cmx16cmx16cm (length x width x height). The test section is highly modular and the film cooling modules or the optical access windows can be mounted on any of the four walls of the test section.

Exhaust

An extractor is present at the exit of the sonic throat to collect the burnt gases. An extraction fan removes the air from the experimental room and releases it to the exterior. A spray of water is used to cool the metallic part (aluminum) of the extractor. The extractor is capable of extracting about $40m^3$ of air per second.

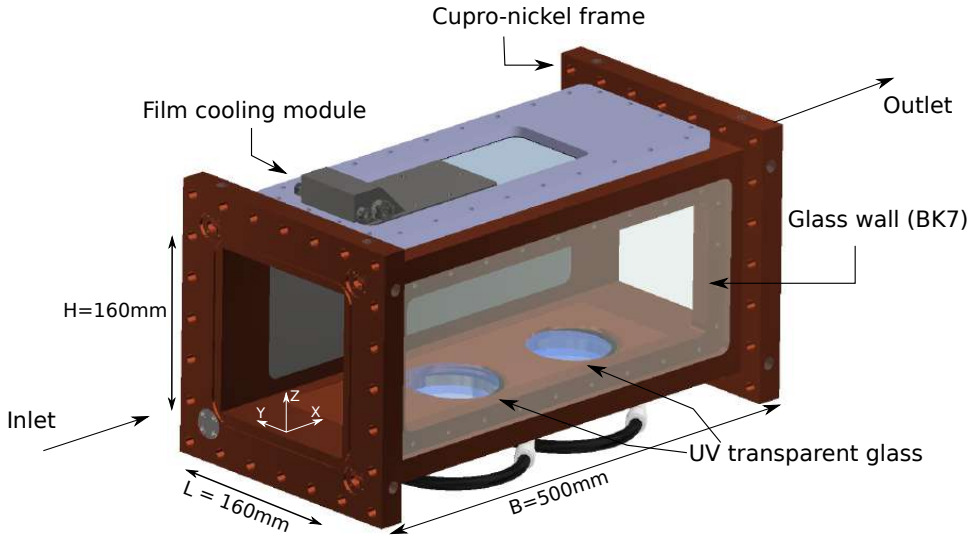

Figure 5.9: Illustration of the modular test section with the various features.

Water Circuit

The combustion chamber, tranquillising chamber, test section are the regions in contact with very high temperatures and are required to be cooled. A water circuit is used to cool the walls of these zones. The three zones are cooled individually with three different circuits of water. The water passes through a heat exchanger in order to release the heat energy acquired by the water before continuing in the cycle. At every section of the test bench, the temperature and pressure are monitored. Based on the need, the mass flow rate of in the water circuit is adjusted in the particular section (for example, the combustion chamber).

5.2.2 Seeding system

Seeding pot

Two identical seeding pots are used to seed the primary and secondary flows with particles. The seeding pots as seen in figure 5.10 have an internal volume of about 3 litres. The seeding pot is air tight thanks to locking lid at the top which has two orifices. One of the orifices is used to inject air into the seeding chamber via an electrically controlled valve (marked EV in the figure). This allows the user to switch on the seeding only when required. The mass flow into the seeding chamber is controlled by an electronic mass flow meter and and electronically controlled valve to adjust the flow rate. A long cane with 4 perpendicular tubes help in releasing the air along the circumference of the seeding pot. This agitates the particles and a form of cyclone is created inside the seeding chamber, thus mixing the air well with the particles. Finally, the air with the seeding particles exits the chamber via the second orifice. A flexible tube connects the seeding chamber to the dilution zone. The second seeding pot is connected to the film cooling module.

The seeding system is seen in figure 5.10 which can be filled with common seeding particles like SiO_2 or phosphor particles like ZnO. The final design of the seeding pot was conceived after many iterations and modifications of the air feed tube. The design changes were arduous and essential as compacting of the ZnO and SiO_2 particles hindered smooth seeding process in the initial designs. Additionally, a bypass valve was also added to regulate the amount of air passing through the seeding chamber as seen in figure 5.11. This helps in optimising the seeding density in the main flow. Despite these modifications, the seeding of ZnO is tricky and the best working conditions were obtained for a mainstream mass flow rate of 300g/s.

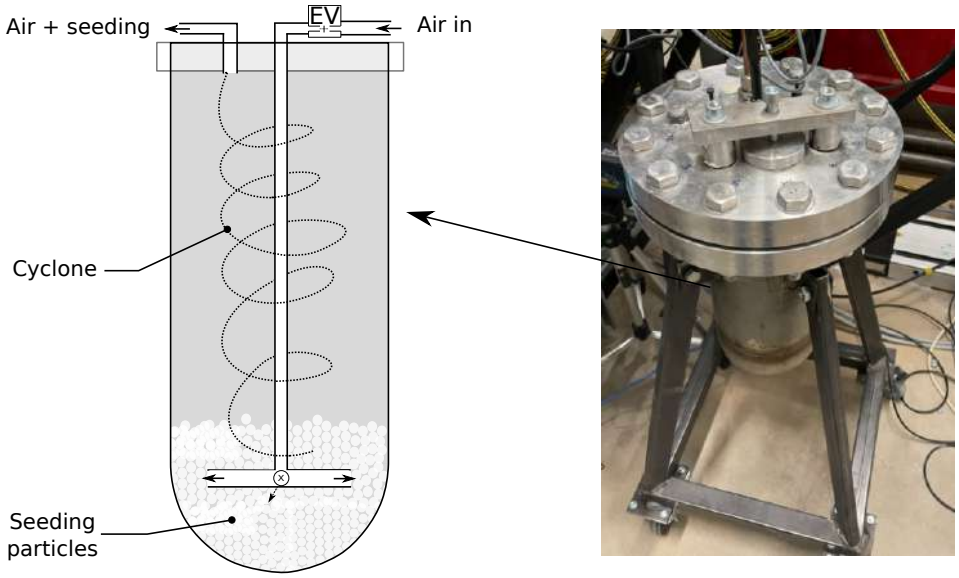

Figure 5.10: Picture showing the seeding chamber with supports.

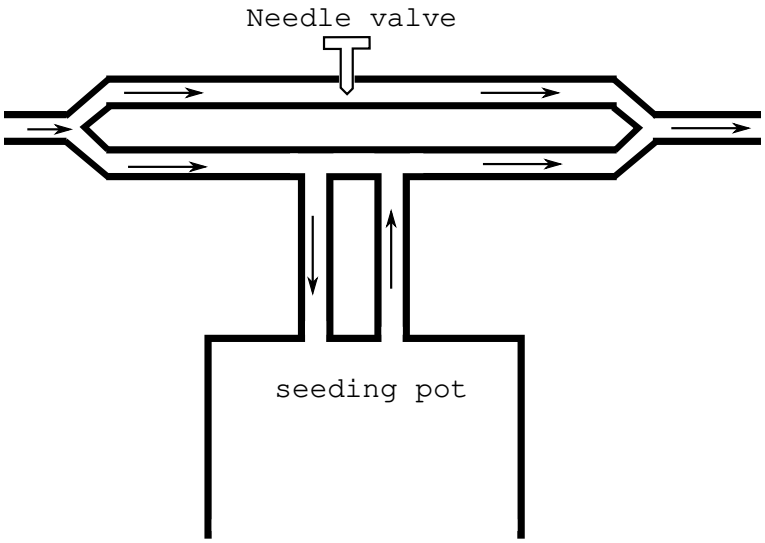

Figure 5.11: Illustration of the bypass system.

Choice of seeding particle size

While choosing the particle to conduct phosphor thermometry , it is imperative to choose the right size of the particle. A too small particle will emit too low intense light upon decay and a too large particle will have a high response time with respect to velocity and temperature and this will cause a wrong estimate of the flow properties. The derivation of the velocity and temperature response times are described in this section.

Velocity response time

The equation of motion for a spherical particle in a gas is given by the expression 5.1 which itself is derived from the BBO equation (Basset (1887), Boussinesq (1885), Oseen (1927)). Here u_f is the fluid velocity, ρ_f is the fluid density, u_p is the particle velocity, C_D is the particle drag coefficient, D_p is the particle diameter.

$$m_p \frac{du_p}{dt} = \frac{1}{2} C_D \frac{\pi D_p^2}{4} \rho_f (u_f - u_p)|u_f - u_p| \tag{5.1}$$

The relative particle Reynolds number can be expressed as follows

$$Re_p = \frac{|u_f - u_p| D_p \rho_f}{\mu_f} \tag{5.2}$$

Here μ_f is the fluid dynamic viscosity.
Dividing the expression 5.1 by the particle mass given as

$$m_p = \rho_p \frac{4}{3} \pi \frac{D_p^3}{8} \tag{5.3}$$

Expression 5.1 becomes

$$\frac{du_p}{dt} = \frac{18\mu_f}{\rho_p D_p^2} \frac{C_D Re_p}{24} (u_f - u_p) \tag{5.4}$$

When the factor $\frac{C_D Re_p}{24}$ approaches unity (Stokes flow), the other factor $\frac{18\mu_f}{\rho_p D_p^2}$ has a dimension of s^{-1} and it is called as the velocity response time τ_v

$$\tau_v = \frac{\rho_p D_p^2}{18\mu_f} \tag{5.5}$$

Replacing these terms in equation 5.4, one can obtain a more simplified equation as

$$\frac{du_p}{dt} = \frac{1}{\tau_v} (u_f - u_p) \tag{5.6}$$

By imposing constant u_f and an initial particle velocity of u_p as at rest (zero velocity) gives us the solution

$$u_p = \left(1 - exp\left(\frac{-t}{\tau_v}\right)\right) .u_f \tag{5.7}$$

One can see that upon imposing initial conditions to (5.7), as u_p=0 at t=0 , and $t = \tau_v$ gives u_p=0.632 u_f. Hence, τ_v is the time required for the particle to obtain 63.2% of the free stream velocity from rest.

Thermal response time

Similar to velocity response time, we can derive an expression to obtain the thermal response time τ_T. This is a measure of the time taken by a particle to respond to temperature changes in its surroundings. For a spherical particle considering uniform temperature in the entirety of its volume, one can write the heat balance equation with negligible radiative heat transfer as

$$m_p c_p \frac{dT_p}{dt} = Nu\pi k_p D_p (Tf - Tp) \tag{5.8}$$

where Nu is the Nusselt number, c_p is the specific heat of the particle material and k_p is the thermal conductivity of the material. Where h is the heat transfer coefficient of the continuous phase (fluid), dividing through by the particle mass and specific heat gives

$$\frac{dT_p}{dt} = \frac{Nu}{2} \frac{12k_p}{\rho_p c_p D_p^2} (T_f - T_p) \tag{5.9}$$

For low Reynolds number Nu/2 tends to unity. The other factor can be grouped as the thermal response time τ_T

$$\tau_T = \frac{\rho_p c_P D_p^2}{12k_p} \tag{5.10}$$

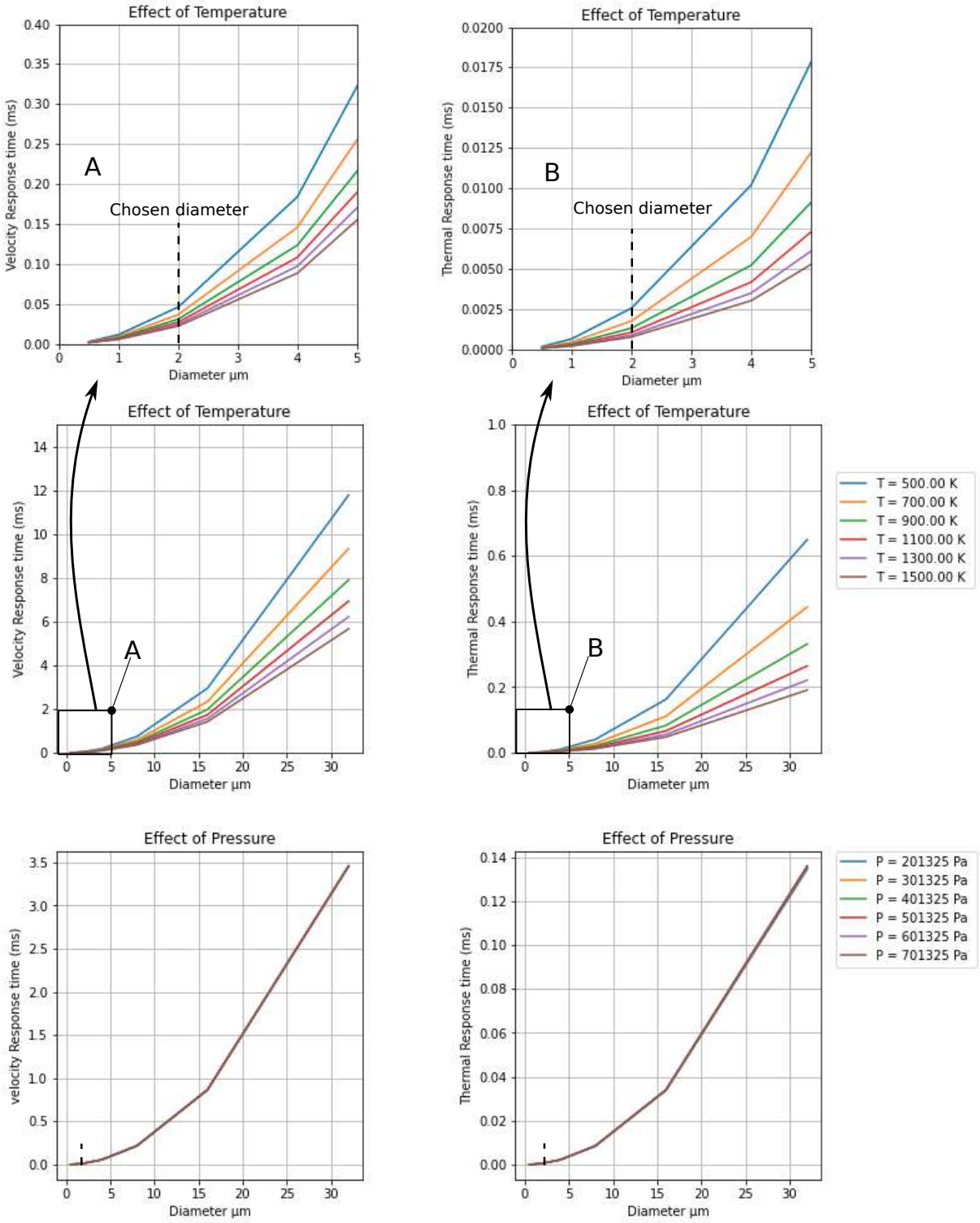

Figure 5.12: Evolution of velocity and thermal response time with respect to temperature and pressure for different particle sizes. Figures A and B are a zoom for the particle sizes less than 5 μm

The convective heat transfer coefficient can be written in the form

$$h = \frac{Nu_{mean}\lambda_f}{L_c} \tag{5.11}$$

where
For a spherical particle, the mean nusselt number can be given as

$$Nu_{mean} = 2 + (Nu_{lam}^2 + Nu_{turb}^2) \tag{5.12}$$

The laminar and turbulent Nusselt numbers are defined as

$$Nu_{lam} = Re^{1/2} + Pr^{1/2} \tag{5.13}$$

$$Nu_{turb} = \frac{0.037Re^{0}.8Pr}{1 + 2.443Re^{-0.1}(Pr^{2/3} - 1)} \tag{5.14}$$

where Re = $\frac{uD}{\nu}$ and Pr = $\frac{\nu}{a}$. For the calculations, velocity= 0.632u is used to calculate the Reynolds number used in the thermal response time.

Based on these above expressions, a simple python code is used to visualise the effect of particle size, pressure and temperature on the velocity and thermal response times.

Figure 5.12 shows the effect of temperature and pressure on the velocity and thermal response time. As the particle size grows, there is an increase in the velocity and thermal response time. This effect is more pronounced at lower temperatures (500k). As temperature increases, the response times decrease. But there is no visible change in the evolution of response times due to changes in pressure. In the present study, particles of a diameter of the order of 2μm are used and their velocity and thermal response times are 40μs and 2.5μs respectively as seen in figure 5.12.

5.3 Calibration of BATH test rig

The BATH test rig having been constructed recently, there is a need to test its performance. In the frame of this thesis, extensive tests were also conducted to calibrate the test bench. The following are the measurement systems used in the calibration process.

5.3.1 Presentation of measurement techniques used for calibration purposes

Triple probe measurements

Three probes were mounted on an automated displacement test bench as shown in figure 5.13.

- **Pressure sensors**: The pitot tube measures the static and dynamic pressures of the fluid at one point in the pipe. The flow rate can be determined from the difference between the static and dynamic pressures, which is the velocity head of the fluid flow. Hence, two probes (pitot tube to measure total pressure and static port to determine static pressure) were used to calculate flow velocity. The range of measurable pressures was 0Pa to 2500Pa with an uncertainty of 5Pa.

- **Thermocouple (Type K)**: The basic principle of K type thermocouple temperature measurement is that two conductors of different components form a closed loop. When there is a temperature gradient at both ends, there will be a current passing through the loop. This current is proportional to the temperature in the flow. The thermocouple has an accuracy of $\pm$ 0.5K and an uncertainty of 0.5%

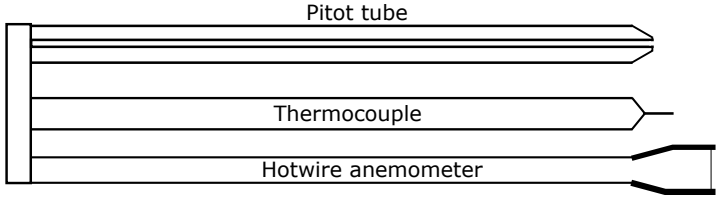

Figure 5.13: Illustration of the the triple probes used to calibrate the test bench.

Hot wire anemometer

Constant Temperature Anemometry (CTA), also known as Thermal Anemometry, is a technique for the measurement of turbulence in gas and liquid flows using hot-wire or hot-film probes inserted into the flow. CTA is particularly suitable for the measurement of flows with very fast fluctuations at a point (high turbulence) and the study of flow micro-structures, where there is a need to resolve small flow eddies down to the order of tenths of a millimeter. A pre-calibrated hot wire anemometer from Dantec systems was used in this calibration process. The acquisitions were made for 10s at a frequency of 20kHz, with a low pass filter at 10kHz. The King's law (see Perry (1982)) is used for the calibration of the hot-wire with the velocity values from the pitot tube as the reference.

Figure 5.14 shows the grid of points where the velocity and temperature measurements were conducted with the use of these probes.

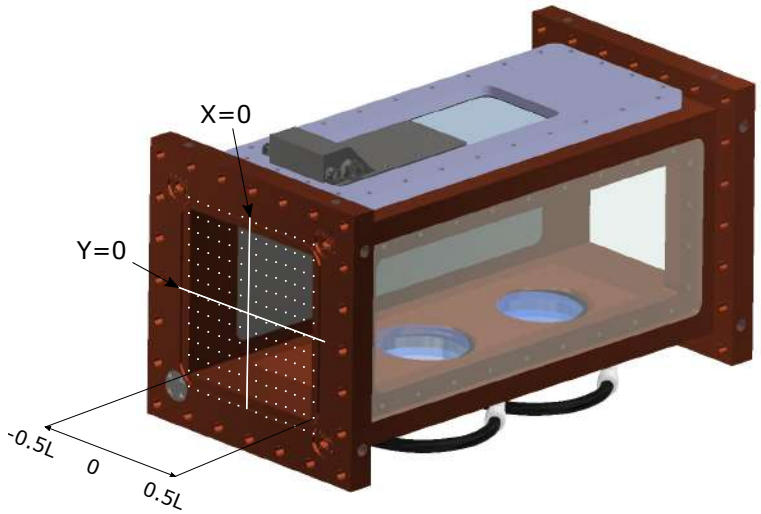

Figure 5.14: CAD representation of the test section with the locations where triple probe measurements were conducted. L=16cm here.

PIV

Particle Image Velocimetry (PIV) is a semi-intrusive technique to measure an instantaneous flow field. In this technique, seeding particles are added to the flow and by tracing their path, a velocity field can be established. The particles are illuminated by a light source like a laser and the light scattered by the seeding particles are collected by a camera of the type CCD or CMOS at two consecutive instances (at least 2 images are need at short intervals). The images obtained by this method are divided into smaller interrogation zones and by using auto-correlation or cross-correlation, the displacement of the seeding particles with respect to time can be calculated. By recording a series of images over a period of time, these instantaneous velocity fields can yield a mean flow field by averaging techniques. An extensive review was made by Raffel *et al.* (2018) regarding PIV techniques in the past decades. A typical PIV setup is shown in figure 5.15.

In order to perform a short PIV study, the following components were used.

- A LaVision Imager pro X 4M camera whose characteristics are
  - Type of CCD sensor
  - Sensor size 16.7 x 16.1 mm^2
  - Single pixel size 7.4 x 7.4 μm^2
  - Resolution 2048 x 2048 pixels
  - Speed at full resolution 4fps
  - Minimum inter-frame time 300 ns
- A Nikon AF Nikkon 28mm 1:2.8 lens

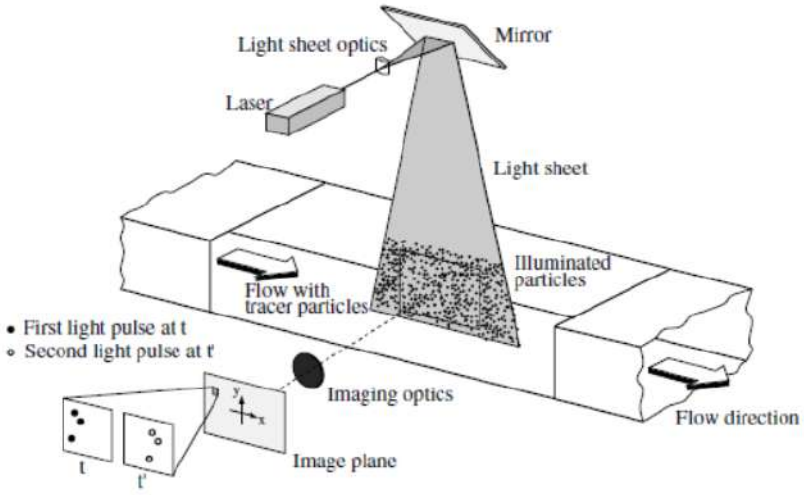

Figure 5.15: Illustration of a classical PIV setup. Raffel *et al.* (2018)

- New Wave Solo III-15 laser whose characteristics are
  - Solid type Nd-YAG
  - Useful wavelength 532 nm
  - Nominal power 2 x 50 mJ at 135 μs
  - Beam diameter $<$ 3.5 mm
  - Pulse duration 3 to 5 ns
  - Frequency range 0 - 15 Hz
- Seeding: Seeding pot is connected upstream of the tranquillising chamber containing solid particles of hydrophobic fumed SiO2 (Aerosil R-972) with a mean D_{32} of 1μm.
- LaVision HighSpeed Controller synchronization system
- Davis 8 acquisition software from LaVision

  In order to acquire the velocity fields, the configuration of the measuring instruments is as follows, the laser and the camera are positioned at 90° to each other in order to have the least possible distortion. The distance between the camera and the laser sheet is about 30cm in order to visualize the flow velocity as close as possible to the wall due to the constraint caused by the presence of optical window. Figure 5.16 shows this configuration.

5.3.2 Working points of BATH test rig

In all the following sections a brief summary of few working points of the test bench are highlighted. Mass flow rate was varied from 100g/s to 1500g/s with a step of 100g/s. The corresponding velocity and Reynolds number are shown in the table 5.1. In order to simplify the presentation of results, the cases with 500g/s and 1000g/s for 20°C and 150°C (using the electric heater alone) are shown in the figure 5.17 (a) at the horizontal centerline of the test section (Y=0 in the figure 5.14). Additionally a velocity contour at the entry of the test section for a mass flow rate of 500g/s at 20°C in the figure 5.18 is shown. The velocity in the corners of the test section are seen to be higher than at the center of the test section although the variation between the extremity and the center is less than 3%. From the same figure it can be observed that the velocity boundary layer shape evolves with increase in mass flow rate.

Figure 5.17 (b) shows the horizontal centerline temperature profiles. It can be observed that the temperature at the entry of the test section at these points are exactly as required: at 20°C and 150°C. This is possible thanks to the automated PID controller that manages the power of the electric heater.

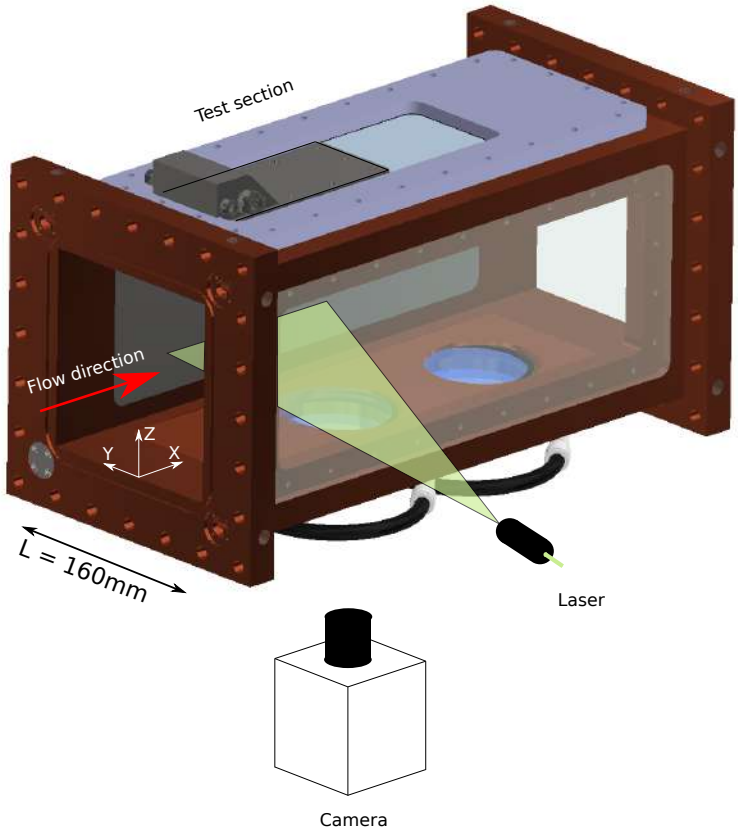

Figure 5.16: Illustation of the PIV setup. A 532nm laser is used to generate the green laser sheet.

Table 5.1: Working points of the Bath test bench. (only few points are shown for better readability). Here Re_L is the Reynolds number for the test bench with a characteristic length L=160mm (width of the test section) and Re_d is the Reynolds number corresponding to the film cooling configuration with characteristic length d=12.25mm.

Mass flow rate (g/s)	U (m/s)	T (°C)	Re_L	Re_d
100	5	150	34000	2600
200	9	150	69000	5300
300	14	150	100000	7900
500	23	150	170000	13100
1000	47	150	340000	26400
1500	70	150	510000	40000

Turbulence intensity

Hot wire anemometry measurements at various locations at the entry of the test section showed an average turbulence intensity of 7-11% depending on the mass flow rate. Upon addition of a honeycomb ceramic structure in the tranquillising chamber, the turbulence dips down to 6-8% depending on the mass flow rate (see figure 5.19(a)). Acquisitions were made at a frequency of 20kHz. A Power Spectral Density (PSD) plot of the data obtained showed a peak at 6kHz and 12kHz (Position 1). The peak at 6kHz disappeared when the displacement system was placed outside the zone where the test bench was fixed (Position 2). The peak at 12kHz can arise due to the use of high voltage electrical devices like displacement bench, acquisition systems and the systems used to pilot the test bench remotely. Upon moving some of the devices, the intensity of this peak also reduced drastically. An example of a PSD is shown in figure 5.19(b).

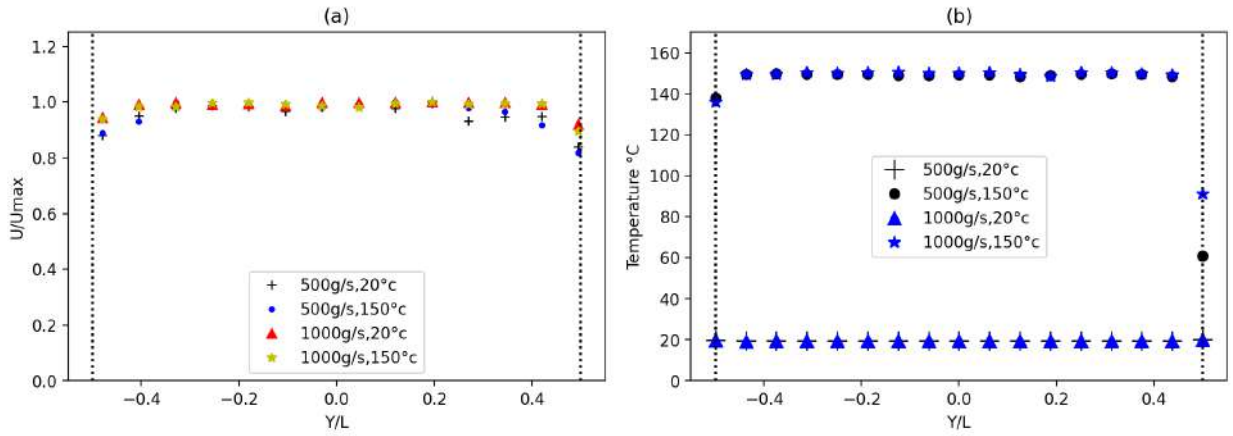

Figure 5.17: (a) Velocity profile and (b) Temperature profile at the horizontal centerline for a mass flow rate of 500g/s and 1000g/s at 20°C and 150°C at the entry of the test section. Vertical dotted lines denote the extremities of the test section dimension.

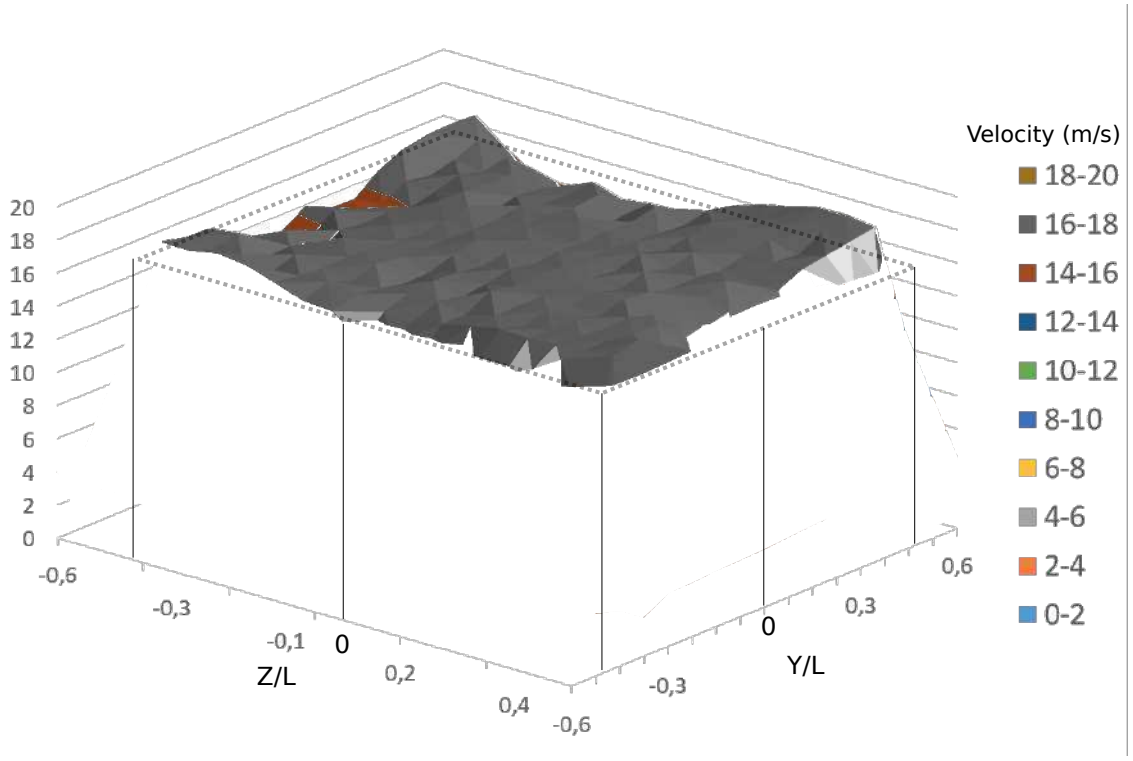

Figure 5.18: Velocity contour at the entry of test section for a mass flow rate of 500g/s at 20°C. Vertical dotted lines denote the extremities of the test section dimension.

PIV measurements

From the PIV measurements, the boundary layer thickness and the visualisation of the velocity field is possible. It must be noted that a ultra-absorptive tape (Metal velvet-Acktar) was fixed to the wall where the laser strikes perpendicularly to avoid high reflections from the wall, which is detrimental to the study of the boundary layer. Figure 5.20 shows the results of one of the measurements conducted at 500g/s at 20°C. The velocity profile and the turbulence intensity at X=100mm and Z=80mm is shown in the figures (a) and (b) while figure (c) shows the 2D velocity map. From this figure, it can be observed that the mean velocity of the flow is 17.2 m/s and the mean turbulence is 9.2%. This is the case measured with the honeycomb in place. The difference in turbulence levels between the hot-wire measurements and the PIV could arise due to the damage occurred to the honeycomb section during tests with the combustion process. The boundary layer thickness for this case was determined to be 11mm from the wall. However, the

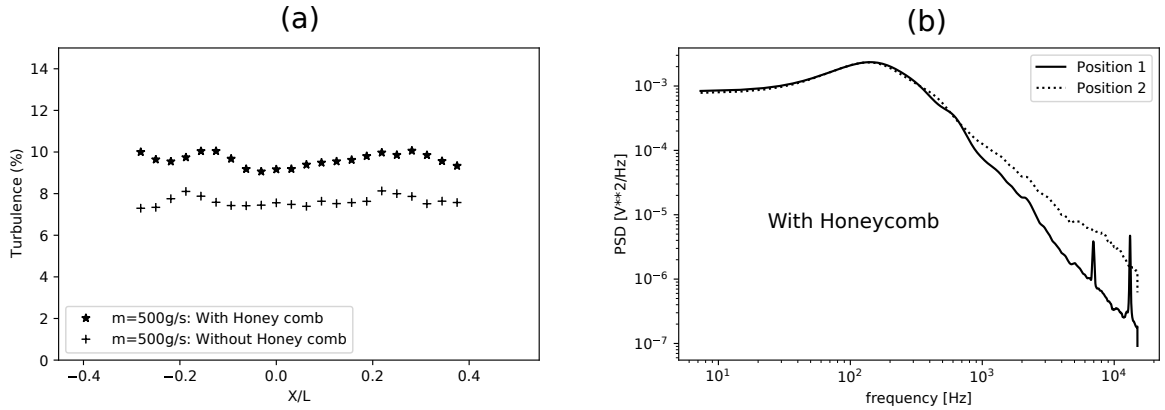

Figure 5.19: Left: Turbulence intensity evolution for Y=0 at 500g/s and 20°C. Right: PSD at the central point of the test section at 500g/s and 20°C.

accuracy of the results were affected due to seeding problems as the initial design of the seeding pot sent unstable packets of seeding particles into the main flow. Hence, the period during which the measurements were possible were limited to a few seconds. Nevertheless, the results from this study are comparable to those of hot-wire anemometry and the pitot-static tubes. Additionally, the mean flow field in the entire zone away from the boundary layer shows a constant flow field which is highly desirable.

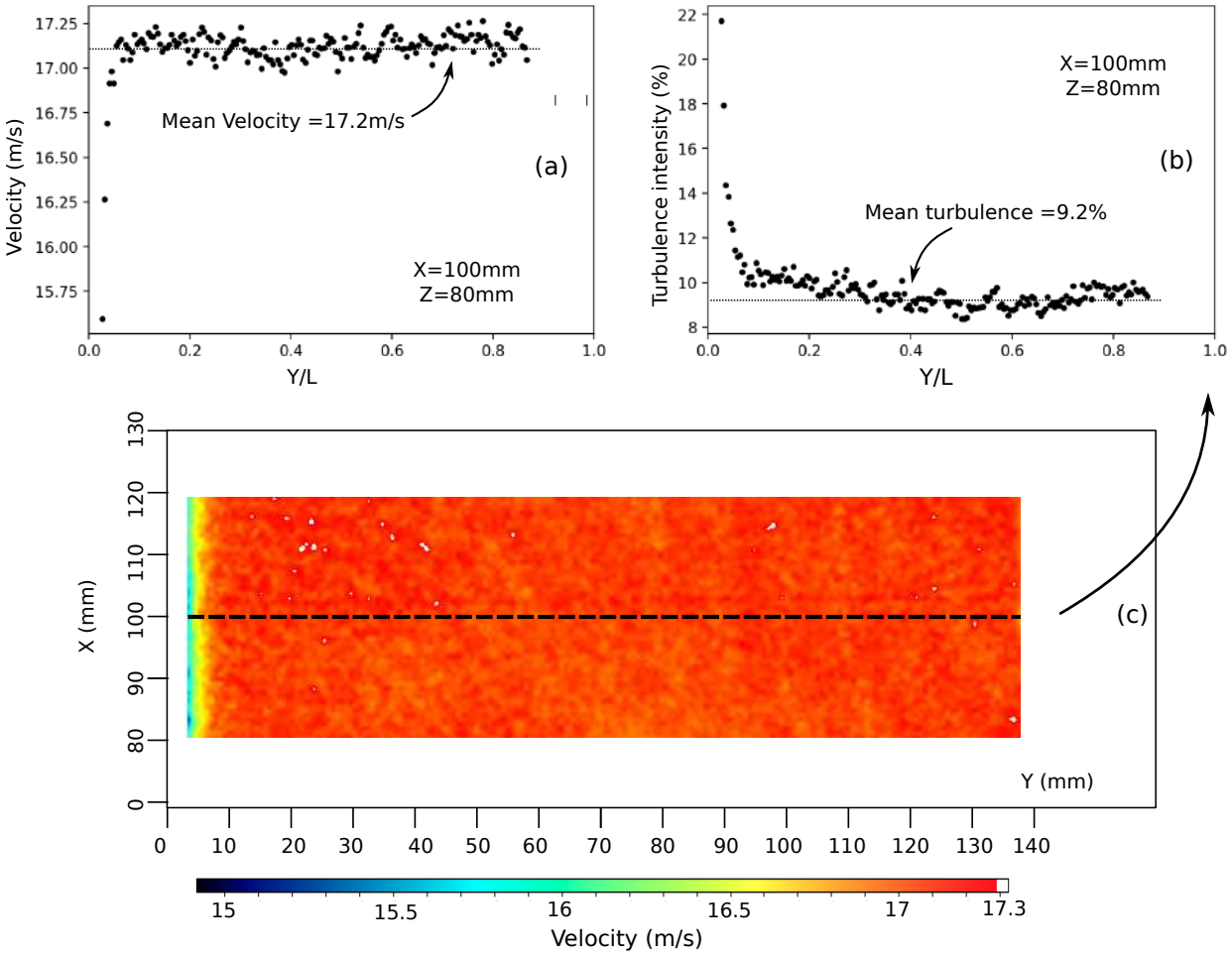

Figure 5.20: (a) velocity profile along the Y direction at X=30

In all about 200 calibration test cases were conducted changing the mass flow rate in the test section, flow temperature, measurement techniques and position of the probes. A summary of the

obtained results for a mass flow rate of 500g/s and 20°C using various measurement techniques are presented in the table 5.2. With this, the homogeneity of the velocity and the temperature flow field are assured and hence the test bench is validated.

Table 5.2: Mean velocity values at the center of the test section (Y/D=0) for a mass flow rate of 500g/s in the test section

Measurement type	Velocity(m/s)	Turbulence intensity
Theoretical	16.2	-
RANS	16.6	-
Pressure sensor	16.6	-
Hot-wire	15.8	7.8%
PIV	17.1	9.2 %

5.3.3 RANS simulations: effect of step

Two types of glasses were used to provide optical access in the test section. The first type was a flat disc of 1cm thickness which produced a step of 2mm in the test section and the second type was a glass with a 'shoulder' making the glass level with the floor of the test section. In order

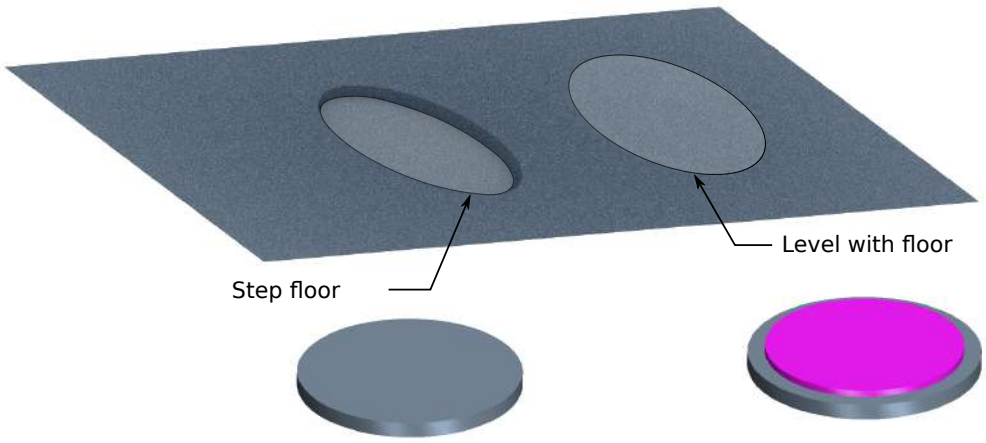

Figure 5.21: Representation of the test section with and without a step

to quantify the effect of having a step, RANS simulations were performed for the case with and without a step. Figure 5.21 shows the difference in the two cases.

The geometry chosen has the exact dimensions as the test section at BATH. This is shown in figure 5.22 along with the imposed boundary conditions.

StarCCM+ was used to numerically analyse the problem with k-ω SST turbulence model for RANS simulations. 15 prismatic layers ensured that the wall y+ remained less than 1 in all the domain. Inlet conditions were set as mass flow rate inlet with 500g/s at 20°C. The center plane velocity results are shown in figure 5.23. One can observe obvious differences in velocity in the zone near the bottom wall having the glasses (with or without step). However, in the current study, the zone of interest lies in the wall opposite to the optical access as this is the region where the film cooling modules will be installed. Visually, there are no differences in the velocity field in the area near the top wall. All along the top wall (5mm from the wall), the changes in the velocity field were limited to a maximum value of 0.1% between the two cases. Hence one can conclude that the presence or absence of the small step due to the glasses providing optical access for the flow visualisation do not pose any problems in the velocity flow field.

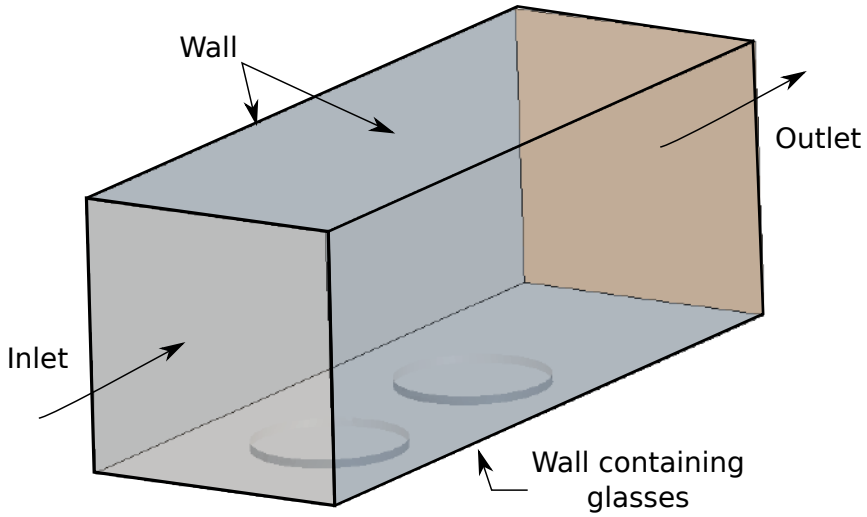

Figure 5.22: Representation of the geometry used for the RANS simulations with boundary conditions

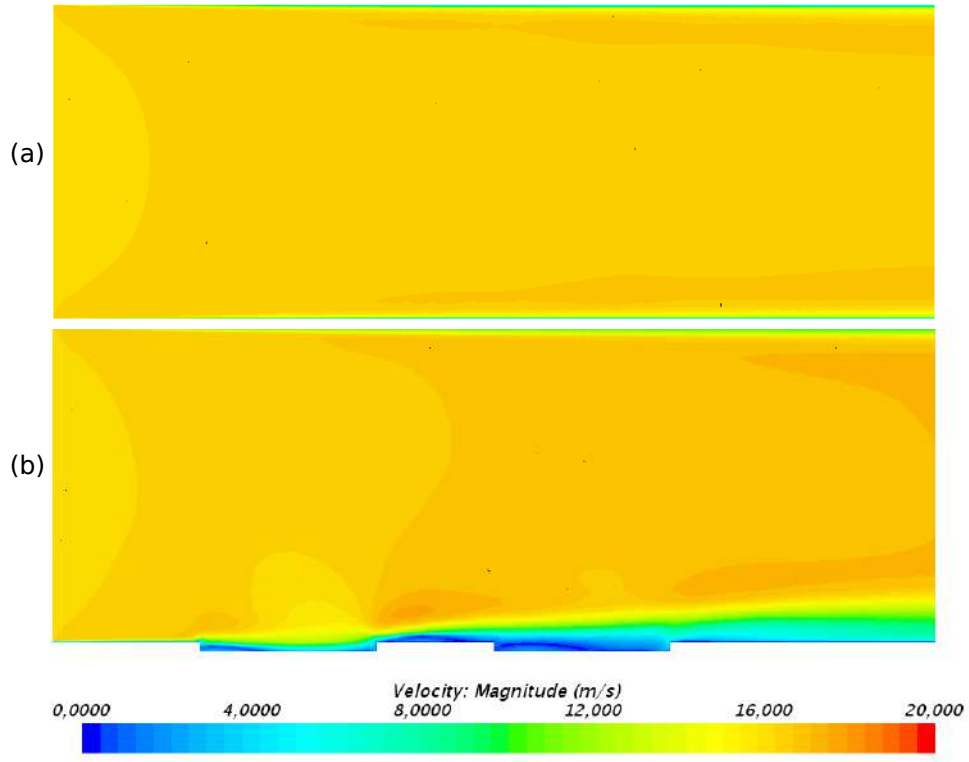

Figure 5.23: Velocity flow field analysed numerically using RANS simulations: (a) without and (b) with presence of a step.

5.4 Film cooling: 2-D temperature measurements

As the parameters of the test section have been analysed, it is possible to move on to film cooling measurements. The experimental objective of the thesis, is to test the ZnO phosphor thermometry technique to obtain 2-D instantaneous and mean temperature fields for film cooling configurations. To achieve this, an extensive setup was mounted and various tests were conducted to perform the spectral intensity ratio phosphor thermometry. The procedure and the results are analysed in detail in the following sections.

5.4.1 Film cooling geometry

In this section, the film configurations are described. In order to have preliminary verification that the proposed auxiliary hole configurations have better flow characteristics, a case with cylindrical hole is used as a reference. Table 5.3 shows the various geometrical characteristics of the three configurations studied. Figure 5.24 is a representation of the film cooling module. It must be

Table 5.3: Geometric parameters

Parameter	**Single hole**	**Aux. hole case 1**	**Aux. hole case 2**
Main hole Diameter	$D1$=12.25 [mm]	D=10 [mm]	D=10 [mm]
Aux. hole Diameter	-	d= 5 [mm]	d= 5 [mm]
Aux. hole lateral distance	-	H=10 [mm]	H=15 [mm]
Aux. hole longitudinal distance	-	L=15 [mm]	L=15 [mm]

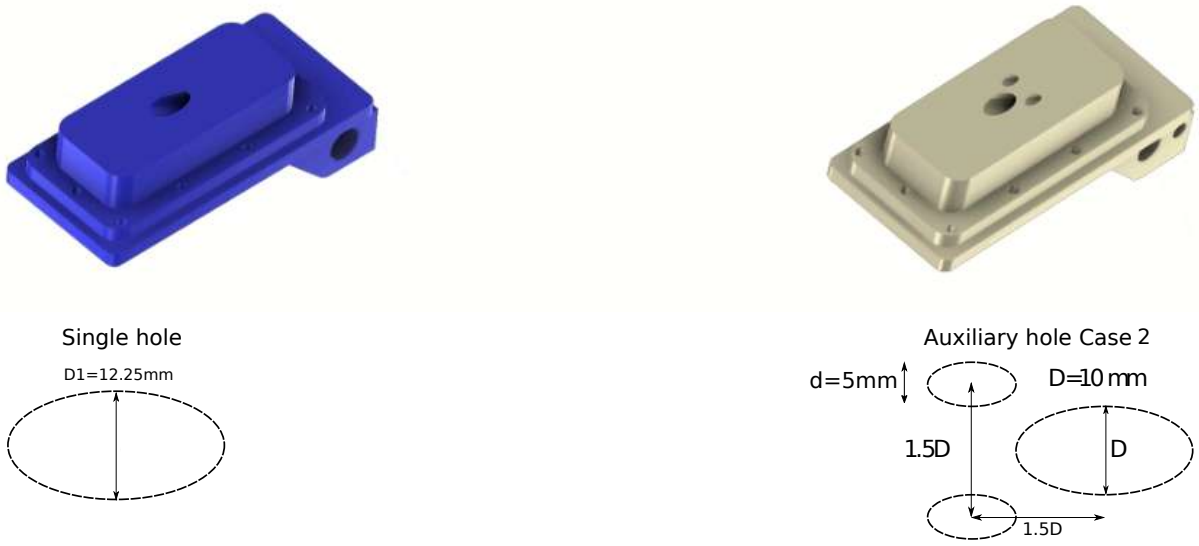

Figure 5.24: Illustration of the film cooling modules used in this thesis and their corresponding hole shape from the top view is shown below each module with geometrical parameters.

noted that although experiments are conducted at relatively lower temperatures (150°C in the mainstream flow) in this thesis, the test bench is capable of performing film cooling analysis at very high temperatures of the order of 1500°C at 10 bars of pressure. This is the reason for the film cooling modules and the other surfaces to have a thick wall.

5.4.2 Film cooling: Boundary conditions

Care was taken to ensure that the injected jet mass flow rate in the three configurations remain the same, as the surface area S of the holes are equal for the three configurations. If ρ_c and u_c represent the density and the velocity of the coolant jet, the injected mass flow rate of the jet is given by

$$\dot{m}_c = \rho_c S u_c \tag{5.15}$$

When the mass flow rate is maintained constant, and for different configurations with the same surface area, one can observe that the velocity u_c remains the same. Hence the blowing ration M is the same for the three geometric film cooling arrangements. A constant mass flow rate into the film cooling inlet is achieved by the use of a orifice tube tube with an orifice of 2mm diameter before attaching it to the seeding pot. The pressure at the entry of the orifice tube can be adjusted by an adjustable pressure regulator and hence the mass flow through the orifice tube can be regulated.

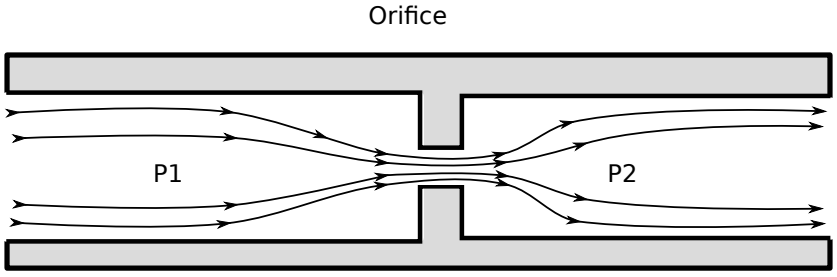

Figure 5.25: Schematic representation of the working of an orifice tube.

Choking of the orifice throat is obtained by using a differential pressure P_1/P_2 >2. Hence the test section which is at a pressure of 1.02 bars (P_2) at a flow rate of 300g/s requires a pressure of 2.4 bars at least upstream of the orifice tube. Using upstream pressure P1, upstream pressure T_0 and throat area S, where; γ =1.4, r=287 J/(kg°C)

$$\dot{m}_c = \frac{P_1 S}{\sqrt{T_0}} \left(\frac{\sqrt{\gamma/r}}{\left(1 + \frac{\gamma-1}{2}\right)^{\frac{\gamma+1}{2(\gamma-1)}}} \right) \tag{5.16}$$

Figure 5.26 shows the evolution of the mass flow rate through the orifice with increase in the absolute applied pressure upstream of the orifice tube.

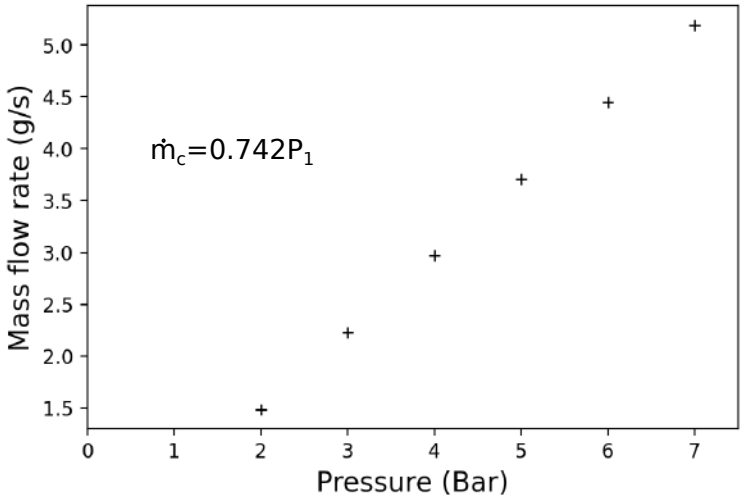

Figure 5.26: Calibration curve for the 2mm orifice

In the current thesis, a blowing ratio M=3 has been studied. The reason for this is the high jet penetration which makes the visualisation of the 2-D temperature field all along the jet trajectory achievable. Additionally, the coherent structures are amplified and helps in better identification and quantification. A summary of all the boundary conditions are presented in the table 5.4.

5.4.3 Experimental setup

The requirements of the experimental setup in this part of the study is quite similar to the setup described in Chapter 4. An overview of the various components necessary to acquire the images are described in this section.

Excitation source: Laser

A Quantel Q-smart 850 laser was used as the laser for the PIV analysis. The laser works at a constant frequency of 10 Hz and has a high power of 850mJ when working at 1032nm. The pulse duration is about 6ns. Using crystals, the incident 1032nm laser pulse can be converted to various

Table 5.4: Boundary conditions

Parameter	Cross-flow	Jet
Mass flow	310g/s	4.45g/s
Temperature	150°C	20°C
Density	0.83kg/m^3	1.32kg/m^3
Pressure	1.2Bar	1.2Bar
Velocity (theoretical)	12.8m/s	27.5m/s
Blowing ratio 'M'	3	
Density ratio	1.45	

harmonics to 532nm (2ω), 355nm (3ω), 266nm (4ω). However, there is a loss of energy during each conversion and hence when the laser works at 266nm, the pulse energy falls to 100mJ. However, this energy is sufficient enough to perform phosphor thermometry. The advantage of using the Quantel laser over the Spectra physics laser used to calibrate the ZnO phosphorescence in water is the highly stable laser pulses obtained over a sustained period of time and a higher laser pulse energy.

Camera

Various cameras were tried in order to perform ZnO phosphor thermometry in air. It was decided after many futile efforts to use the ANDOR iStar sCMOS camera due to the advantage of an intensifier and the short gating widths possible with this camera. Although this is the same type

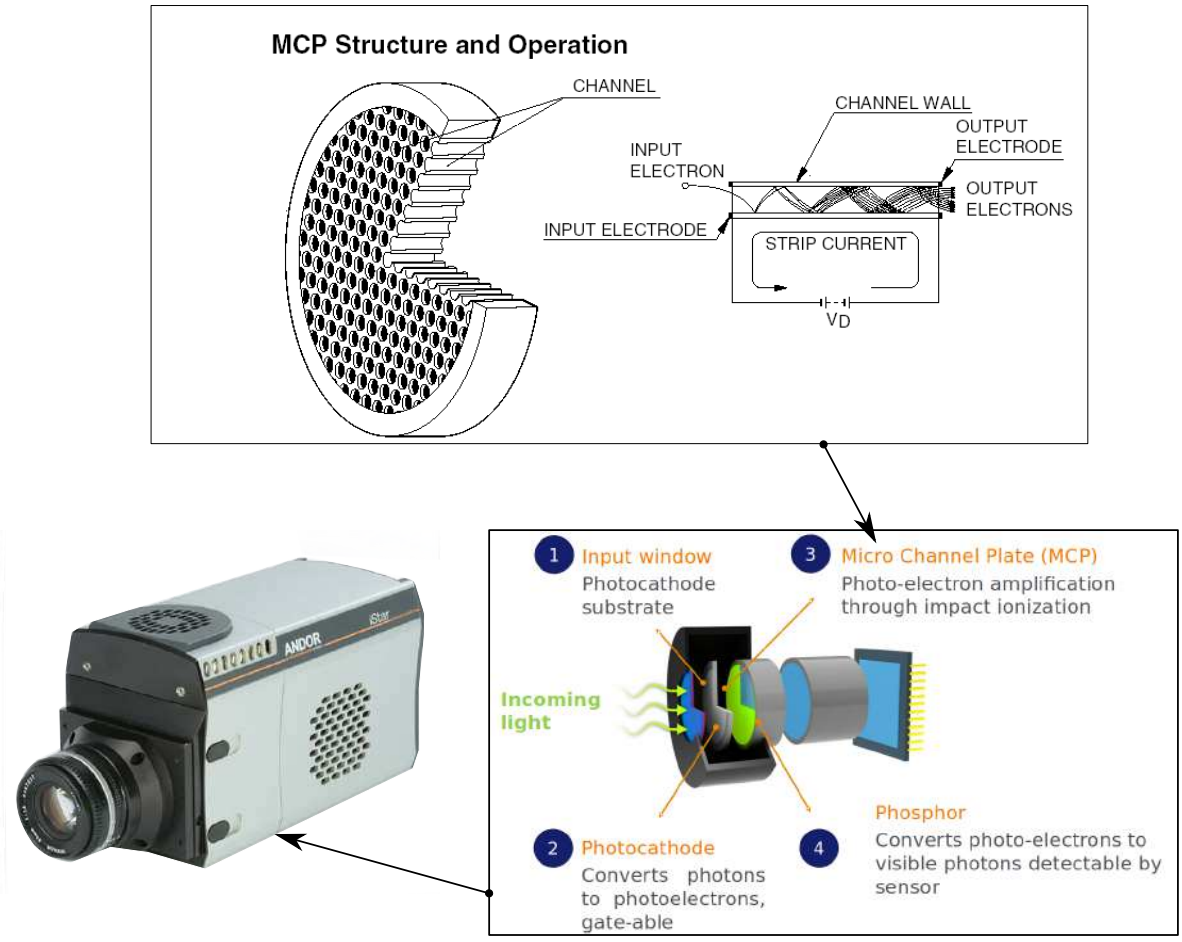

Figure 5.27: Andor iStar sCMOS camera: Depiction of various parts in the intensifier and the functioning of Micro Channel Plate.

camera used in section 4.6.4 and 4.6.5 to study the luminescence decay properties of ZnO, a P43 phosphor is used in this current study due to availability. The drawback of using such a phosphor with the same gating width (of the order of few nanoseconds) is the longer time required by the phosphor in the camera sensor to decay which severely affects the capabilities to perform PIV. However, the objective of this study is to use phosphor thermometry to visualise flow fields and hence it is adequate for this study.

Figure 5.27 shows the camera with various parts used in the intensifier. The incoming light photons strike the photocathode which produces photoelectrons. The number of photoelectrons are amplified by a multi cathode plate (MCP) before reaching the phosphor plate that converts these photoelectrons into photons dectectable by the sensor (CMOS). This procedure highly amplifies the incoming light signal. The specificity of the this camera is the high linearity between the amplification gain applied to the MCP and the signal response on the sensor.

Optics

Figure 5.28 shows the arrangement of the various components related to the image acquisition. Owing to the difficulty to placing the laser beneath the test section, relay mirrors are used to reflect the 266nm laser beam up to the laser sheet generator placed directly below the test section. A laser sheet generator is used to create the laser sheet of thickness which is less than 0.5mm at the entrance of the test section's optical access.

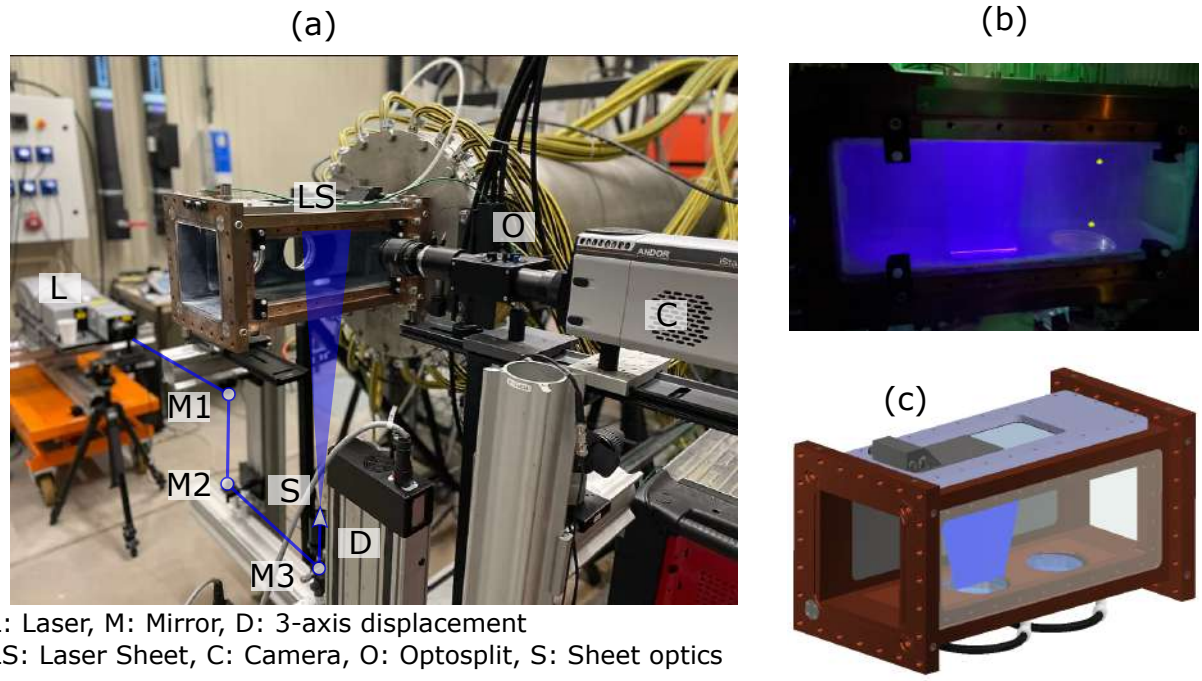

Figure 5.28: (a)Illustration of the PIV/ phosphor thermometry setup. (b) Actual image of the inside of the test section during the phosphor thermometry image acquisition. (c) CAD illustration of the laser path in the test section

A thin laser sheet helps in eliminating three dimensional particle effects as the flow in the current configuration (film cooling) is very much three dimensional. As can be observed, an Optosplit II device whose working was explained in Chapter 4 is used in front of the camera so as to be able to perform the spectral intensity ratio method using a single camera. To recollect, the Optosplit as shown in the figure 5.29 is used to separate incident emission radiation form the ZnO into two paths, with each passing through a bandpass filter. After passing through the filters, these two paths are 're-paralleled' to form two images of the same region of interest on the same image frame. This is the same process as explained in Chapter 4. The choice of filters, objective lenses used are mentioned in the table 5.5. A larger bandwidth for the filters was selected than the previous studies to allow more incident light on the camera.

Table 5.5: Lens and filters used

Part	Brand	Model	Characteristics
Objective lens	Nikon	AF Nikkor 28mm f/2.8D	Minimum aperture f/2.8
Bandpass filter	Chroma	ET395/25x	(395/25nm)
Bandpass filter	Chroma	AT425/50x	(425/50nm)

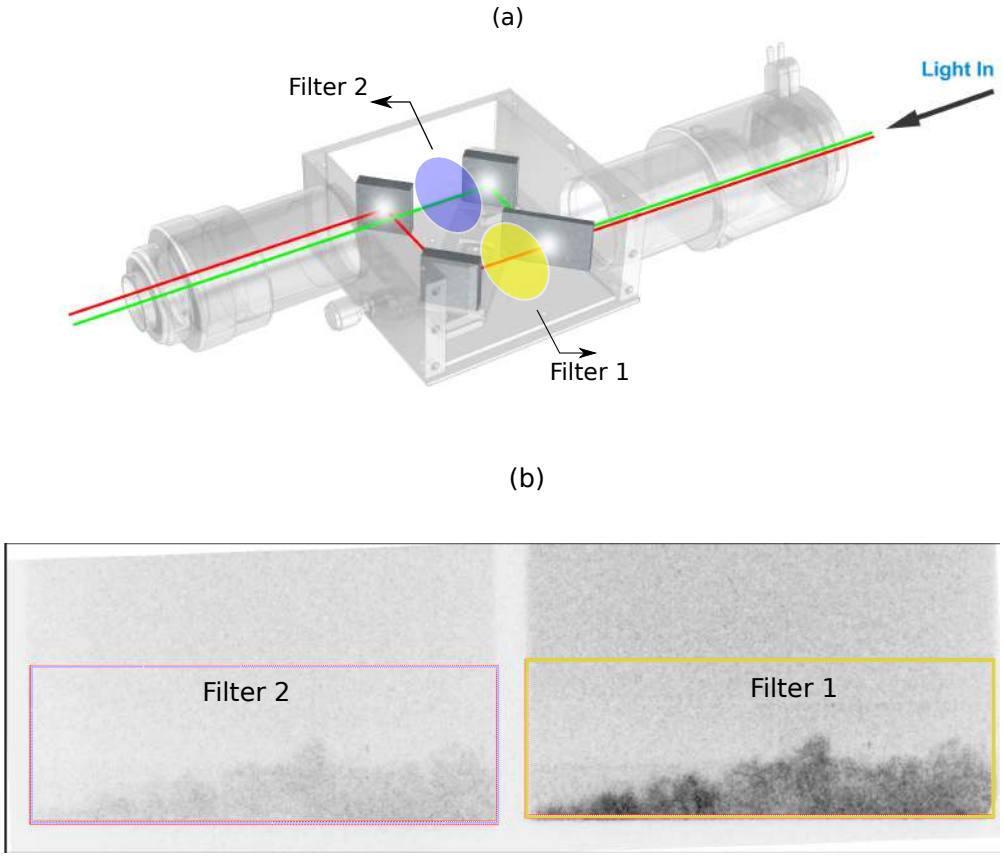

Figure 5.29: (a) Schematic representation of the working of optosplit device. (b) Raw image obtained on the ANDOR camera with two filtered images of the ZnO emission obtained during film cooling experiments.

5.4.4 Calibration

The calibration procedure is the same as described in Chapter 4 except for the fact that the range of temperatures investigated is larger. At least 7 calibration points were chosen to obtain the intensity ratio vs temperature calibration curve as shown in the figure 5.30. The images acquired were applied with a moving Gaussian filter (3x3 pixels) and binned (5x5 pixels) using python code developed in-house. The high resolution of the ANDOR camera permits us to capture the nuances of the instantaneous flow field despite these averaging processes. For each calibration point and ensuing film cooling study case, 150 images were obtained by capturing images at 10Hz and with a gating width of 200ns and camera gain of 2000.

5.4.5 Results: 2-D temperature fields

In this section, the 2-D non-dimensional temperature (θ) fields obtained from the film cooling experiments are discussed.

$$\theta = \frac{T_\infty - T}{T_\infty - T_c} \tag{5.17}$$

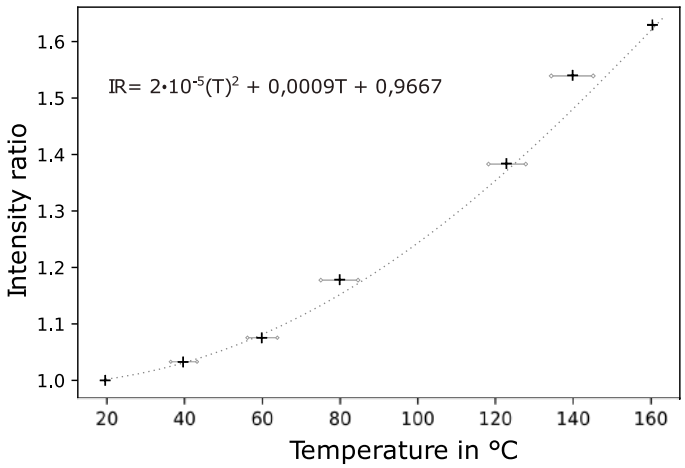

Figure 5.30: Intensity ratio vs temperature calibration curve for the ZnO phosphor in air.

In all the three configurations were tested at a blowing ratio of 3 owing to the simplicity in capturing the flow field far away from the wall. This is preferred as the ZnO particle deposition on the walls can cause bright zones just above the wall which lead to non-physical results. Low blowing ratio flows are restricted to short heights over the wall and hence limit the visualisation.

In this section, the results are presented for the baseline case (single hole case) and the auxiliary hole case 2 which showed better adiabatic film cooling effectiveness from RANS simulations in Chapter 3. Figure 5.31 shows the locations where the measurements were obtained in the Y-direction. The different planes along the Y-direction are analysed so as to get a better view of the lateral spread of the film cooling jet.

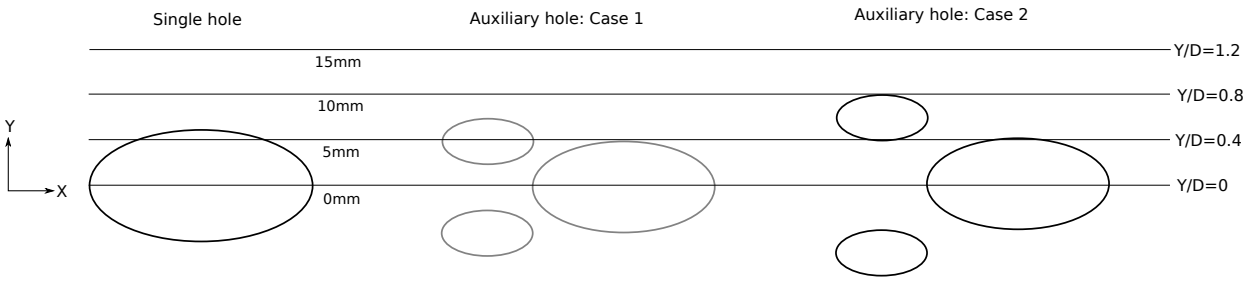

Figure 5.31: The locations of the XZ plane in the lateral direction where 2-D phosphor thermometry was conducted.

Figures 5.32, 5.33, 5.34 show the 2-D non-dimensional temperature fields for the single hole case at Y/D=0, Y/D=0.4, Y/D=0.8 respectively. The regions marked in blue indicate the presence of jet flow and the regions marked in red indicate mainstream flow and any color in between highlights the mixing between the jet and mainstream flows.

In figure 5.32, (a) shows the mean flow field and (b-d) show the instantaneous flow field obtained at different instances at Y=0 (centerline). The mean flow field are obtained by simply averaging the instantaneous images. From 5.32(a), one can clearly observe the trajectory of the film cooling jet as well as the prominent θ contours. The jet penetrates into the mainstream flow and has enough momentum to remain detached from the wall. In 5.32 (b), (c), (d) the instantaneous images help in identifying the jet-shear layer vortices in the top and the bottom areas of the jet. Additionally, it can be seen that the jet initially penetrates into the mainstream and later becomes unstable upon interaction with the main flow and 'packets' of cold air mix with the mainstream further downstream. Further analysis is provided in Chapter 6 in conjunction with unsteady LES simulations.

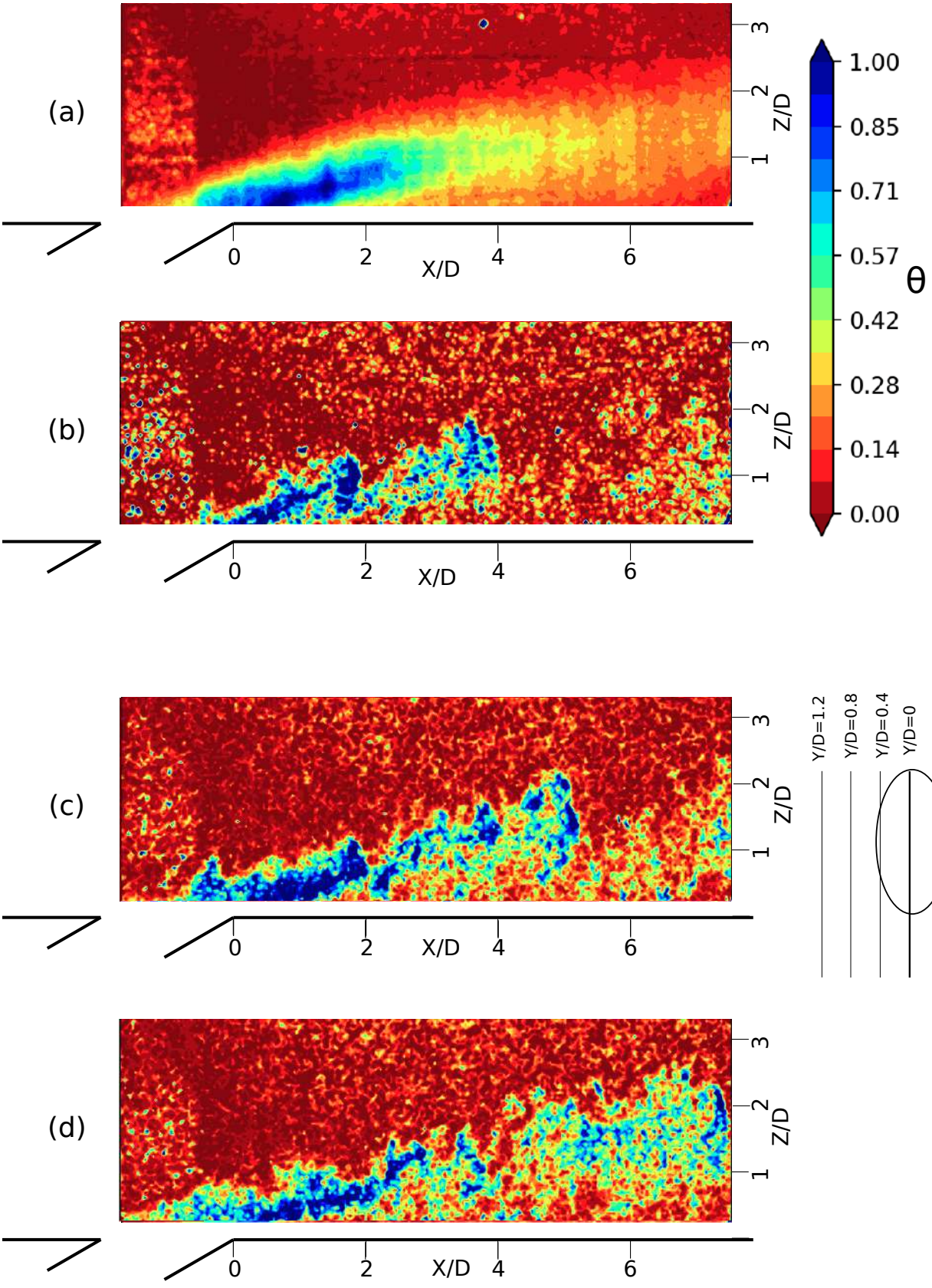

Figure 5.32: Phosphor thermometry: Non-dimensional temperature contours for M=3 for single hole case at Y/D=0. (a) Mean flow field. (b-d) instantaneous flow fields at different instances.

Similarly, in figure 5.33, (a) shows the mean flow field and (b-d) show the instantaneous flow field obtained at different instances at Y/D=0.4. It can be noticed that the strength of the jet core is reduced as compared to the case Y/D=0. The instantaneous flow fields show the wavy motion of the jet, which mixes with the mainstream all along the direction of the flow.

Figure 5.33(a) shows the mean flow field and (b-d) show the instantaneous flow field obtained at different instances at Y/D=0.8. The mean flow field (figure (a)), highlights the fact that at the outer edge of the film cooling hole, the high shear and mixing with the main flow starts much earlier leading to the reduced film presence. The instantaneous snapshots of the flow field show very few packets of film cooling jet in the mainstream flow showing the edges of the Kelvin-Helmholtz vortices.

At Y/D=1.2 as seen in the figure 5.35, no jet flow was found in the mainstream close to the hole exit upto X/D=3. The lateral spreading happens downstream of this region and very small streaks of the jet flow can be seen. This practically indicates the end of the influence of jet flow in the lateral direction. There is no point in making measurements further in the lateral directions.

The auxiliary hole case 2 presents interesting 2-D temperature contour results. Figures 5.36-5.39 show the non-dimensional temperature contour at various lateral locations as discussed earlier. (a) shows the mean flow field and (b-d) show the instantaneous flow field obtained at different instances.

Figure 5.36 shows the non-dimensional temperature contour at Y/D=0 (centerline). The first observation of figure 5.36 (a) highlights the tendency of the jet flow to be closer towards the wall than that of the single hole case (refer figure 5.32 (a)). Similar to the single hole case, the jet flow throws out packets of cold air that mix with the main flow further downstream. The intensity of the mixing and the corresponding vortex intensities and velocities can be visualised by LES numerical analyses.

Figure 5.37 shows the most interesting results with the presence of a secondary streak above the main hole jet. This streak could arise due to the presence of the auxiliary holes upstream of the main hole. The flow from the auxiliary hole in this case essentially reduces the shear experienced by the jet due to contact with the main flow. At Y/D=0.4, there is an increased jet presence in the flow field, due to the effect of the auxiliary holes. From the instantaneous images (b-d) one can also observe that the jet travels longer distance before dissipation into the main flow as compared to the single hole case.

Figure 5.38 shows the contour plots for non-dimensional temperature at Y/D=0.8. The jet-shear layer vortices or the tornado vortices can be very clearly identified from the instantaneous snapshots. Additionally, the mean flow field highlights improved jet presence as compared to the single hole case as seen in the figure 5.34.

Similar to the trends seen at other Y locations, θ contours show that the auxiliary hole case 2 presents jet flow even at locations X/D<2 which was unseen in the single hole case at similar Y location. Hence the Auxiliary hole configuration definitely has better lateral spread characteristics than the single hole case.

In all it is evident that the visualisation of the temperature flow field using phosphor thermometry is highly beneficial to the better understand of the film cooling process as it allows comparison between different film cooling configurations, and identification of coherent structures. Moreover, in Chapter 6 the validation of LES simulations is done through comparisons of the results presented in the above section.

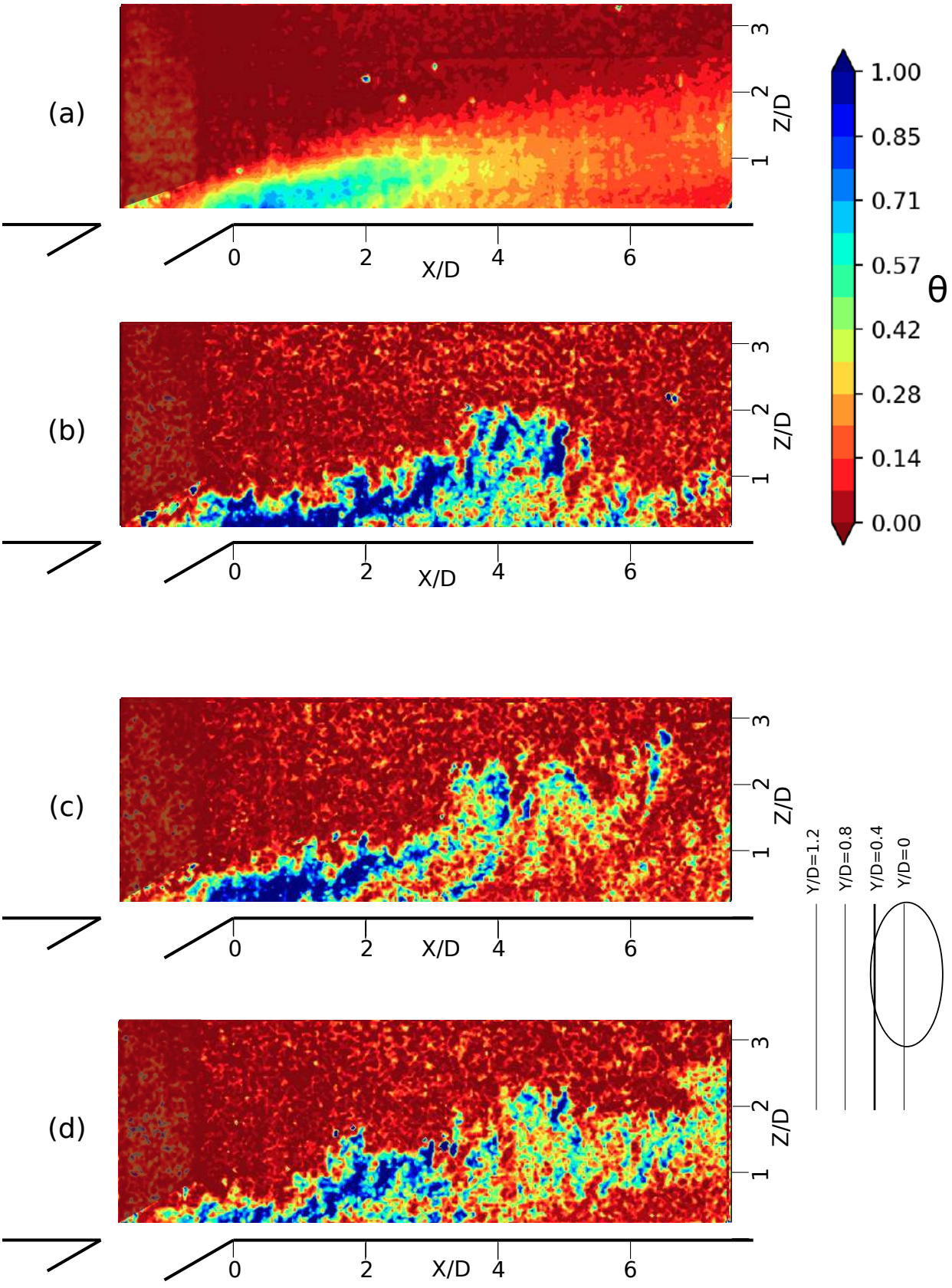

Figure 5.33: Phosphor thermometry: Non-dimensional temperature contours for M=3 for single hole case at Y/D=0.4. (a) Mean flow field. (b-d) instantaneous flow fields at different instances.

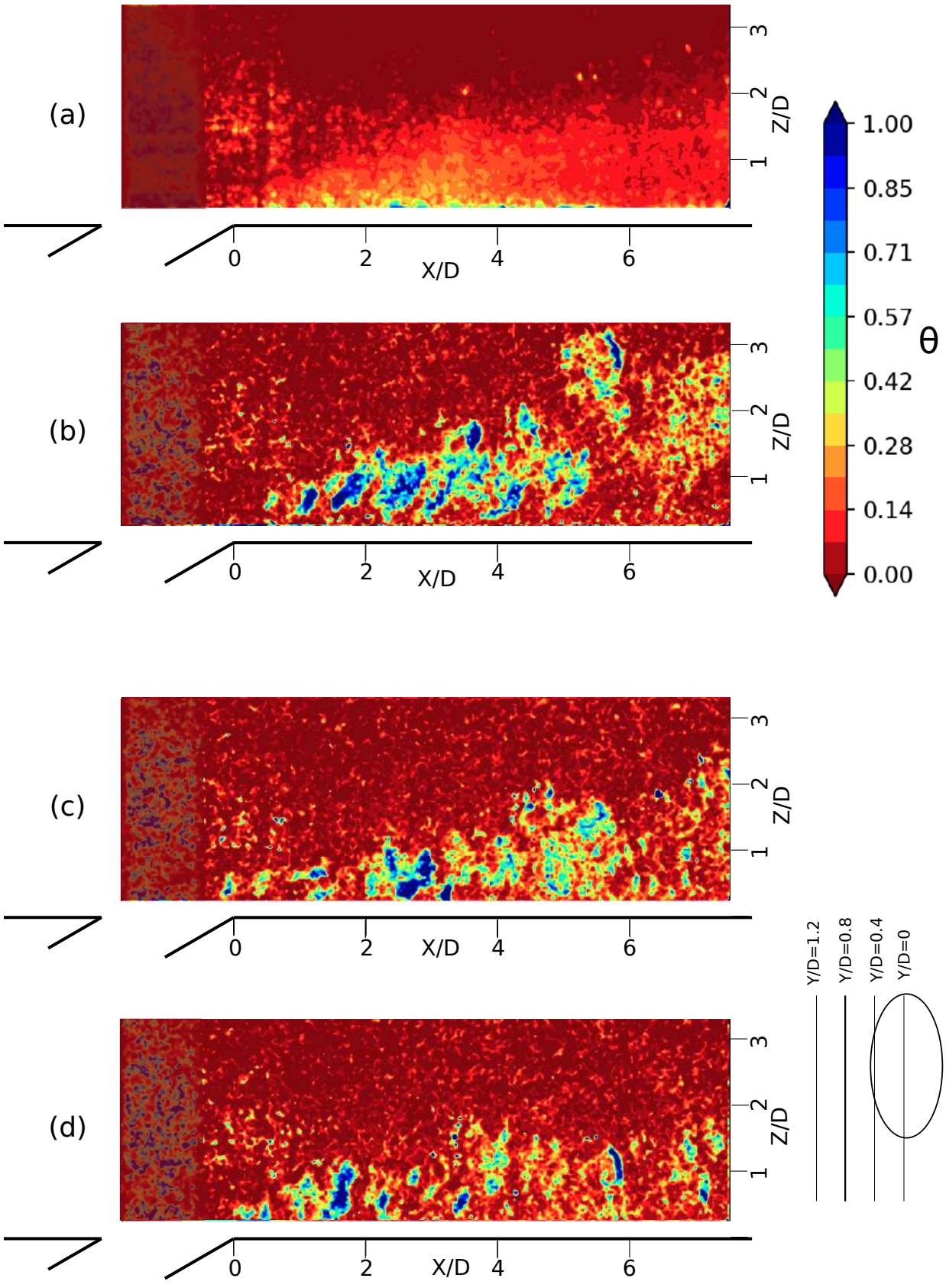

Figure 5.34: Phosphor thermometry: Non-dimensional temperature contours for M=3 for single hole case at Y/D=0.8. (a) Mean flow field. (b-d) instantaneous flow fields at different instances.

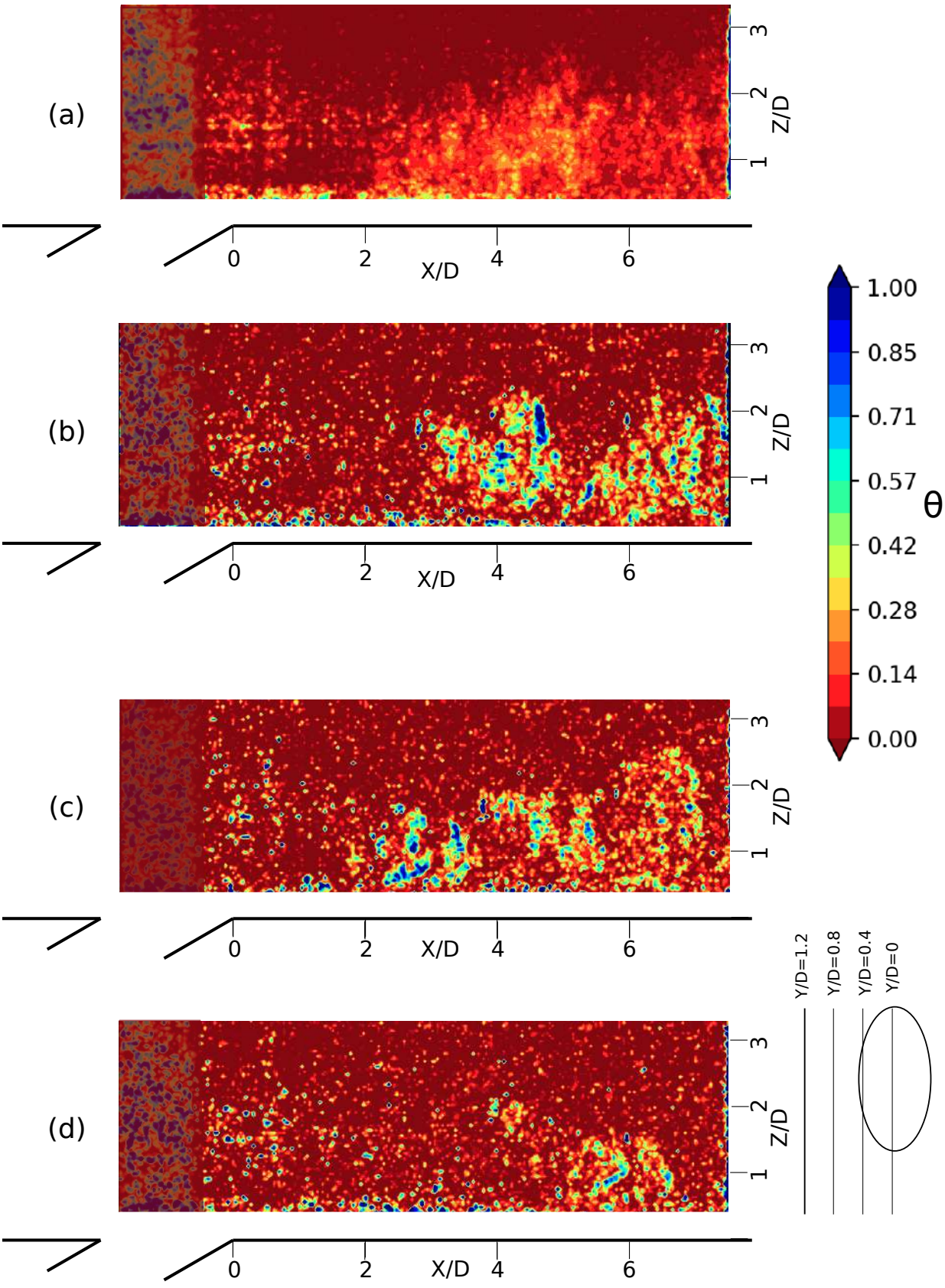

Figure 5.35: Phosphor thermometry: Non-dimensional temperature contours for M=3 for single hole case at Y/D=1.2. (a) Mean flow field. (b-d) instantaneous flow fields at different instances.

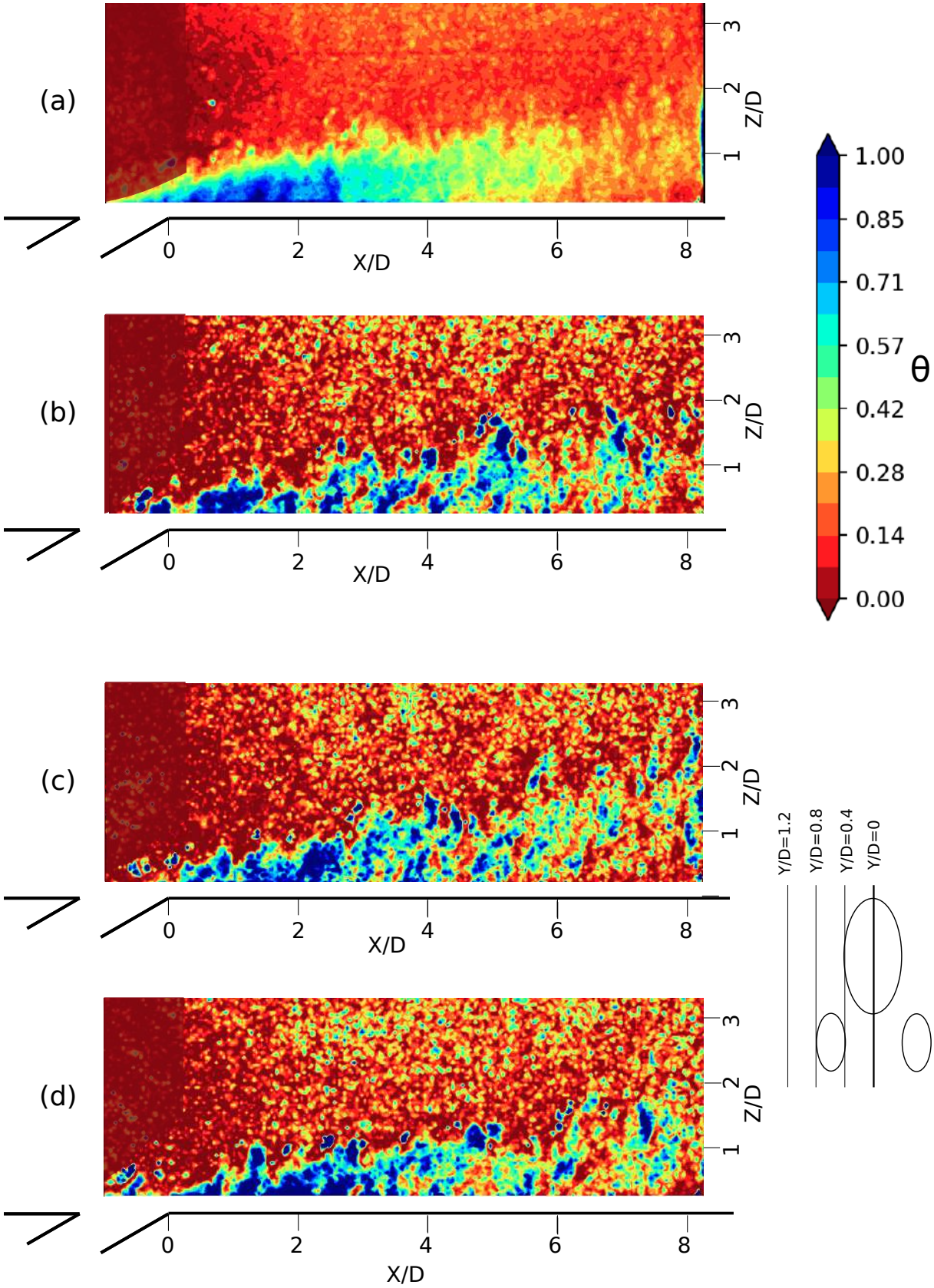

Figure 5.36: Phosphor thermometry: Non-dimensional temperature contours for M=3 for Auxiliary hole case 2 at Y/D=0. (a) Mean flow field. (b-d) instantaneous flow fields at different instances.

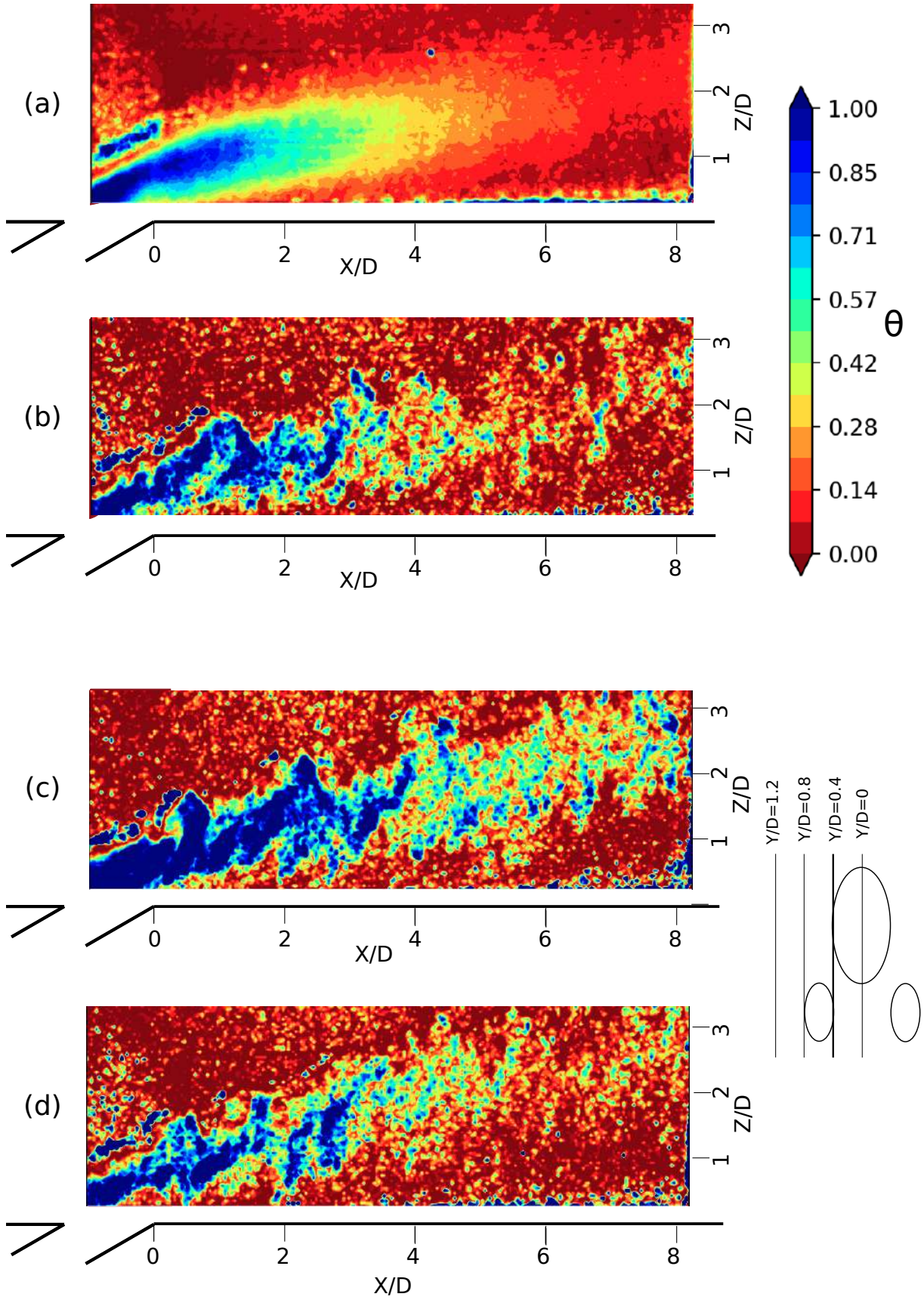

Figure 5.37: Phosphor thermometry: Non-dimensional temperature contours for M=3 for Auxiliary hole case 2 at Y/D=0.4. (a) Mean flow field. (b-d) instantaneous flow fields at different instances.

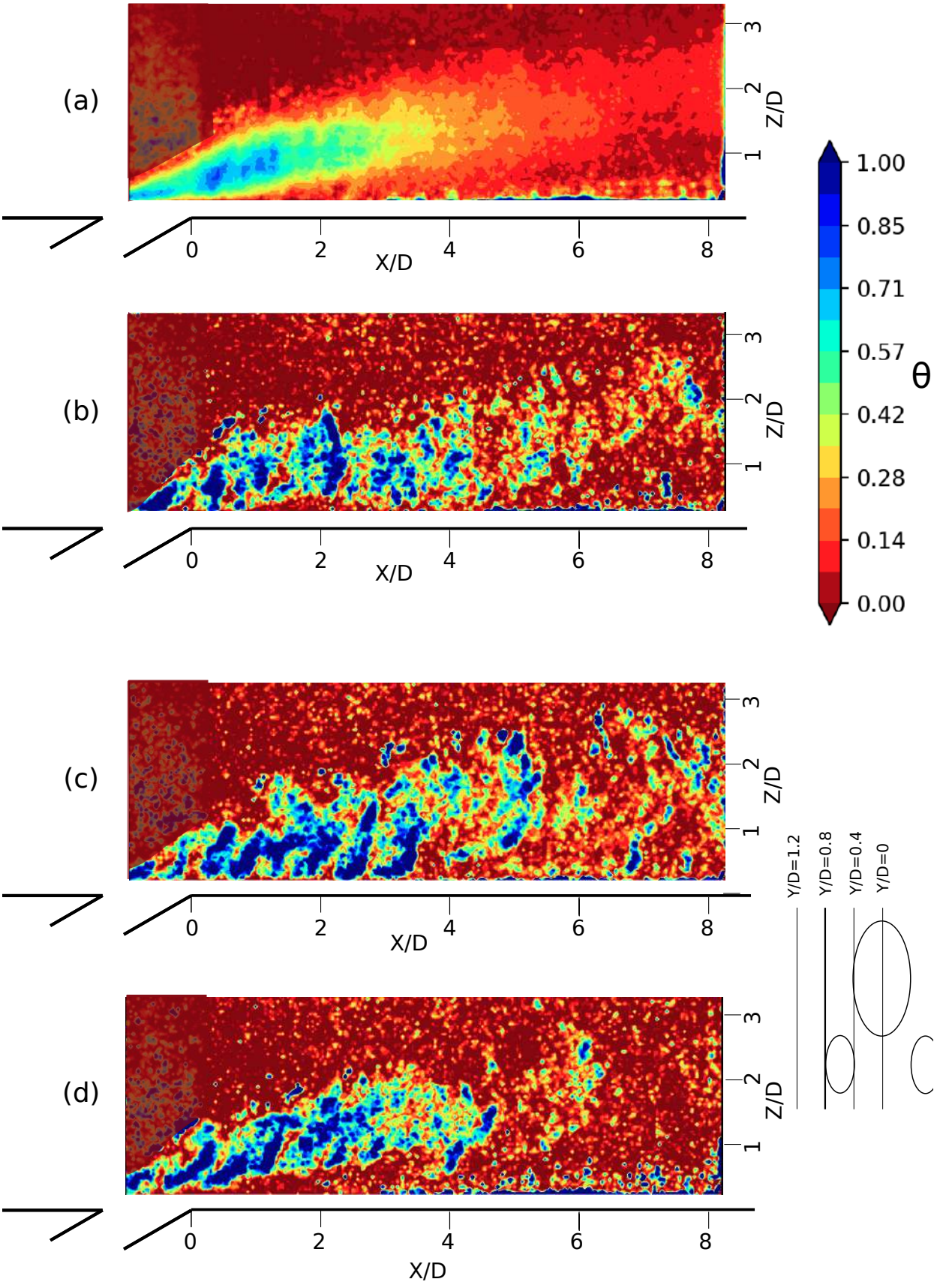

Figure 5.38: Phosphor thermometry: Non-dimensional temperature contours for M=3 for Auxiliary hole case 2 at Y/D=0.8. (a) Mean flow field. (b-d) instantaneous flow fields at different instances.

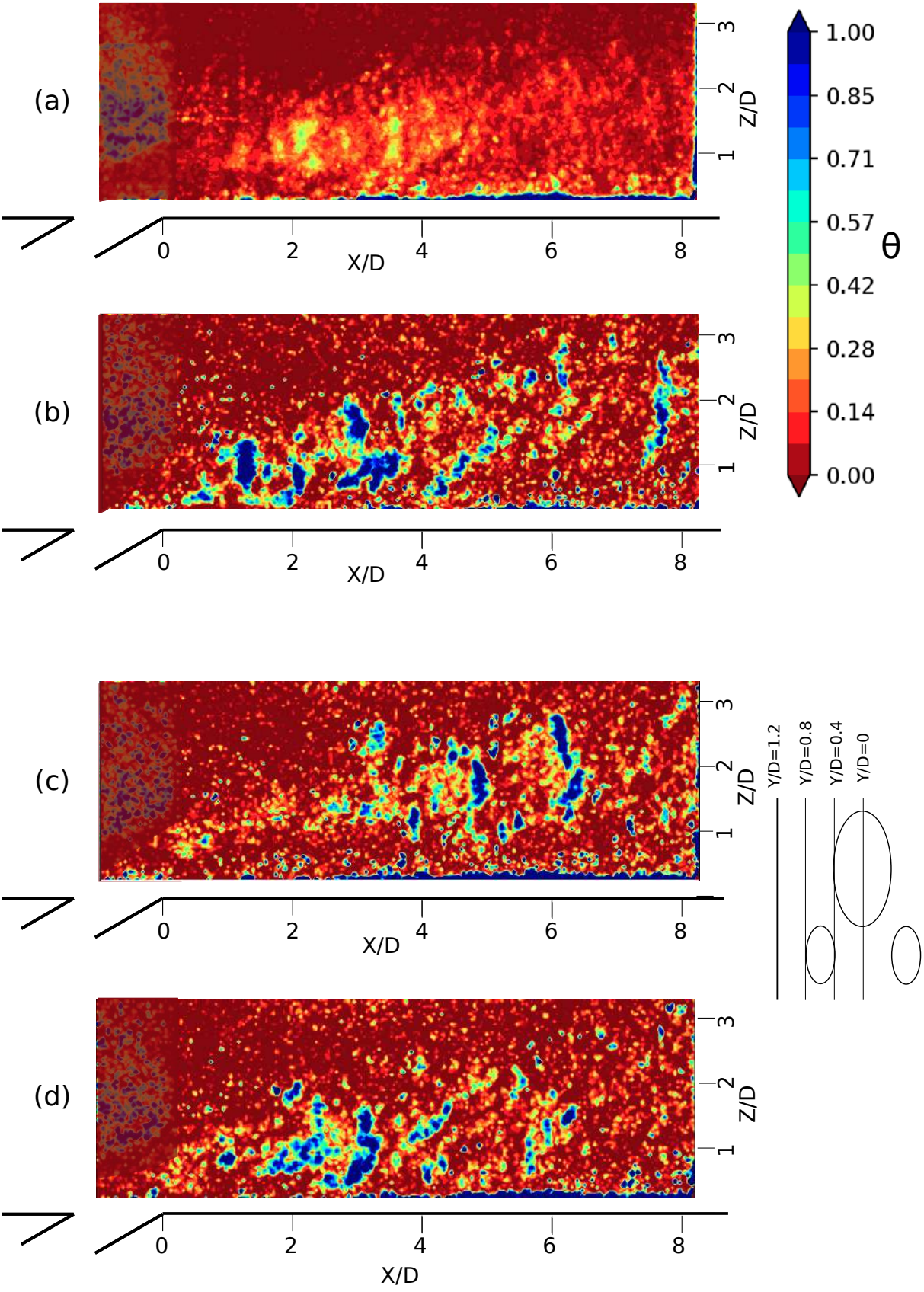

Figure 5.39: Phosphor thermometry: Non-dimensional temperature contours for M=3 for Auxiliary hole case 2 at Y/D=1.2. (a) Mean flow field. (b-d) instantaneous flow fields at different instances.

Conclusion

In this chapter, the new BATH test rig has been described. The calibration of the test rig for its flow properties have shown stable operating conditions for sustained periods of time. Flow velocity analysis was conducted using Pitot-static tube, hot-wire anemometer, Particle Image velocimetry (PIV) to characterize the flow. Once validated, the ZnO phosphor thermometry was successfully implemented to study film cooling configurations. Two dimensional temperature contours were provided for three geometric film cooling arrangements. The results highlight the temperature flow features which can be linked to various coherent structures in the injected jet flow. These results permit a detailed analysis and comparison with Large Eddy Simulations of the film cooling configurations to understand the physics of auxiliary hole film cooling configuration better.

Chapter 6

Large Eddy Simulations and discussion of results

In this chapter, the unsteady numerical analysis of film cooling configurations are described. The procedure followed to perform Large Eddy Simulations (LES) is detailed and various results related to film cooling are presented. The results obtained experimentally are compared with those obtained using unsteady numerical simulations and are analysed. The overall aim of this chapter to validate the LES simulations with experimental data and describe an understanding of the film cooling process in the auxiliary hole configuration.

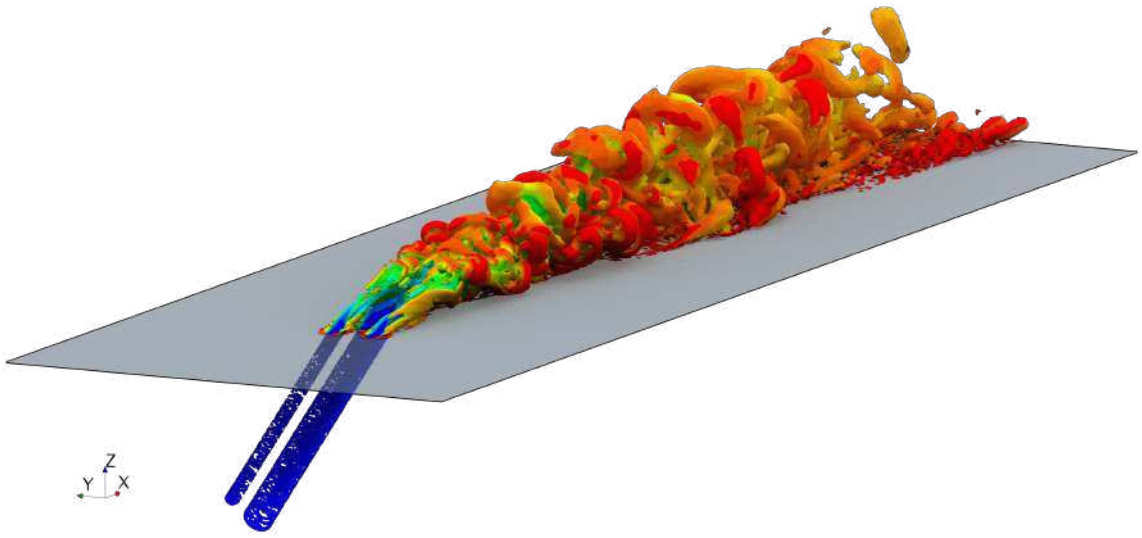

Figure 6.1: Iso-contours of Q-criterion colored with local temperature values. (in-house simulations)

Contents

6.1 Large Eddy simulations 104
6.1.1 Geometry and boundary conditions 104
6.1.2 Solver and Mesh sizing 105
6.2 Results 106
6.3 Discussion of flow physics 110

6.1 Large Eddy simulations

The use of Large Eddy Simulations facilitates unsteady analysis of the film cooling problem. An implication of Kolmogorov's theory of self similarity is that the large eddies of the flow are dependant on the geometry while the smaller scales more universal. In fact, since most of the energy in the flow is contained in the large vortices, resolution of these large eddies and modelling isotropic small vortices is the best compromise between a highly resolved flow and acceptable use of computational resources. In this study, parallel processed LES simulations were conducted using 48 core PC with 64GB RAM. Various parameters like the non-dimensional temperature Θ, adiabatic wall effectiveness, vortex features, Q-criterion and the velocity flow fields are analysed (The parameters as in Chapter 3). Simulations are conducted at blowing ratio M=3. The choice of blowing ratio has been made due to easier visualisation of the coherent structures and the adiabatic film effectiveness is very low for simple hole cases due to jet penetration. Through the auxiliary hole configuration, achieving higher film effectiveness at this blowing ratio implies much better performance at lower blowing ratios too.

6.1.1 Geometry and boundary conditions

The geometry of the current problem is chosen to be as close as possible to the experimental film cooling case. The length of the domain is 500mm while the breadth and the height are fixed to be 160mm. Cold air is injected through a supply tube inclined at 30° towards the streamwise flow. The geometry is shown in the figure 6.2.

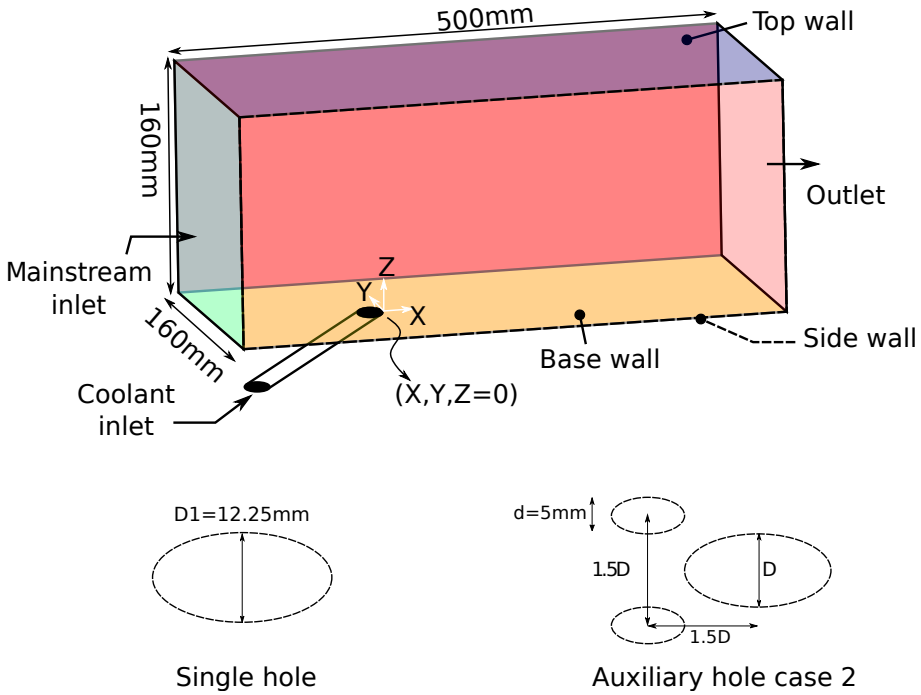

Figure 6.2: Geometrical representation of the domain. The two geometric hole configurations are shown at the bottom.

The turbulence length scale is fixed at 12.25mm due to the baseline single hole case diameter. An adiabatic wall condition is preferred as it is simple to analyse the adiabatic film cooling effectiveness. The boundary conditions are mentioned in the table 6.1.

Table 6.1: Boundary conditions used for the LES simulations

Parameter	Cross-flow	Jet
Mass flow	310g/s	4.45g/s and 1.44g/s
Temperature	150°C	20°C
Density	0.83kg/m^3	1.32kg/m^3
Turbulence intensity	7%	7%
Turbulence length scale	12.25mm	12.25mm
Blowing ratio 'M'		3
Density ratio		1.45

6.1.2 Solver and Mesh sizing

All the numerical computations were carried out using StarCCM+ software (including geometry modeling, meshing, solving, and post-processing). Polyhedral mesh elements are used as they provide a balanced solution for complex mesh generation problems. They are relatively easy and efficient to build, requiring no more surface preparation than the equivalent tetrahedral mesh. They also contain approximately five times fewer cells than a tetrahedral mesh for a given starting surface.

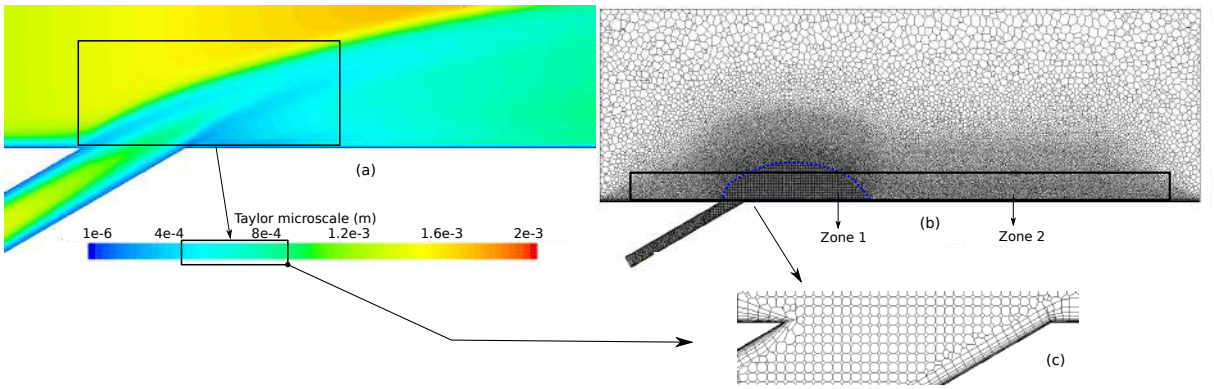

Figure 6.3: (a) Determination of Taylor length scale from RANS simulation. (b) View of the mesh with 2 refinement zones. (c) Close-up view of the coolant exit region showing prism layers

In order to determine the right cell sizing to provide accurate results, the Taylor microscale was first computed using RANS simulations run on a coarse mesh with 1.5 million elements. The Taylor microscale is the intermediate length scale which lies at the dissipation region end of the inertial sub-range within the turbulence spectrum at which fluid viscosity significantly affects the dynamics of turbulent eddies in the flow. In other words, viscosity does not affect the length scales larger than the Taylor length scale strongly. Hence mesh elements of the order of this length scale is beneficial for the LES simulation to be acceptably accurate Addad *et al.* (2008). Upon determination of the zones where mesh refinements were required, two refinement zones were defined (zone 1 and zone 2 in figure 6.3). Maximum cell size in the zone 1 was fixed at 0.6mm and 1mm in zone 2. In all, the mesh contained 5.2 million elements for the single hole case and 5.8 million cells for the auxiliary hole case 2 configuration. At a blowing ratio of M=3, the wall Y+ remained less than 1 throughout the domain.

To initialise the LES simulations, a RANS simulation was run on the same LES mesh. k-ω SST turbulence model was used with the same boundary conditions as in the LES case. WALE subgrid scale model (Nicoud & Ducros (1999)) is used to model the subgrid scale viscosity. The advantage of the WALE model is that it does not require any form of near-wall damping as it automatically

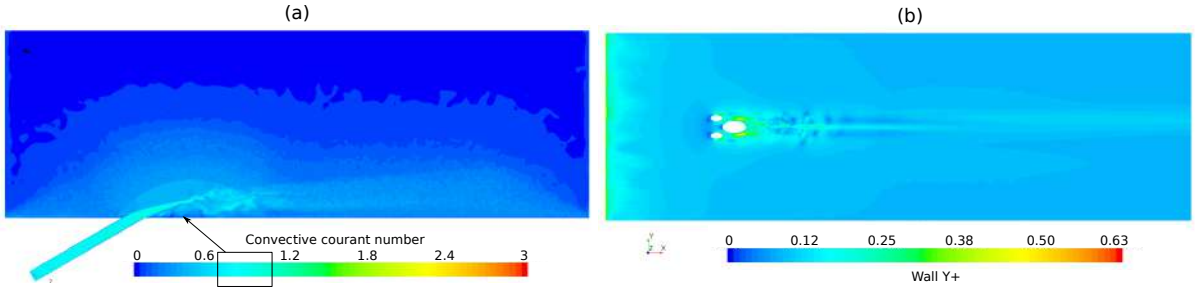

Figure 6.4: (a) Convective Courant number distribution (b) Wall Y+ distribution on the base wall.

gives accurate scaling at walls. Implicit unsteady scheme with second order temporal discretisation is used to improve accuracy. A convergence criteria called the Convective Courant Number is given as $\frac{vdt}{dx}$ (where v is the velocity, dt is the time step, dx is the cell size). The time step was set at 10^{-5}s for which the Convective Courant Number remained less than 1 throughout the domain, ensuring convergence. Figure 6.4 shows the Convective Courant Number in the central plane and the wall Y+ distribution on the base wall. In all, each simulation took about 5000 CPU hours for simulating 0.05s amounting to 3 complete flushes for the M=3 case.

6.2 Results

The discussion of the results obtained numerically and experimentally are presented in this section. This section begins with a comparison of the results obtained by experiments, LES and RANS simulations for a blowing ratio of M=3.

Mean temperature flow field

The mean non-dimensional temperature (Θ) flow field visualisation is presented in the figures 6.5-6.7 obtained by using phosphor thermometry, LES simulations and RANS simulations (which were used to initialize the LES simulations). LES simulations have a closer similarity to the experimental cases as compared to the RANS simulations. It should be noted that the experimental cases are an average of a limited number of acquisitions (100) as compared to the LES simulations with thousands of instances used for the averaging process. Despite this, there is a good qualitative accordance between these two visualisations.

$$\Theta = \frac{T_\infty - T}{T_\infty - T_c} \tag{6.1}$$

Figure 6.5 shows the non-dimensional temperature contour for Y=0 (central symmetry plane). Figures (a) and (b) are obtained through experiments using phosphor thermometry, figures (c) and (d) are obtained using LES simulations, while figures (e) and (f) are obtained from RANS simulations. Also, (a), (c) and (e) correspond to the single hole case while figures (b), (d) and (f) correspond to the auxiliary hole case 2 configuration.

From the presented figures, the trajectory of the jet and the effectiveness of the film close to the all in the single and auxiliary hole cases can be visualised. The trajectory of the single hole case is much further away (1.5D away from the wall at X/D=4) from the wall as compared to the auxiliary hole case (0.7D away from the wall at X/D=4). The flow field in the region X/D<4 highlights the increased Θ close to the wall for the auxiliary hole case.

Figure 6.6 shows the non-dimensional temperature contour in the XZ plane at Y/D=0.4 in the lateral direction.

Very interesting remarks can be made from the figure 6.6. The single hole case shows decreased Θ values as compared to the case with Y/D=0. The mean Θ distribution is comparable between the experimental (a) and LES results (c) for the single hole case but the RANS simulation case (e) tends to over-estimate Θ values. On the other hand, all the three auxiliary hole cases (b, d, f) show very similar qualitative properties. The most prominent feature of all is the appearance of a cold streak emanating from the auxiliary hole, which is present just above the cold streak of the

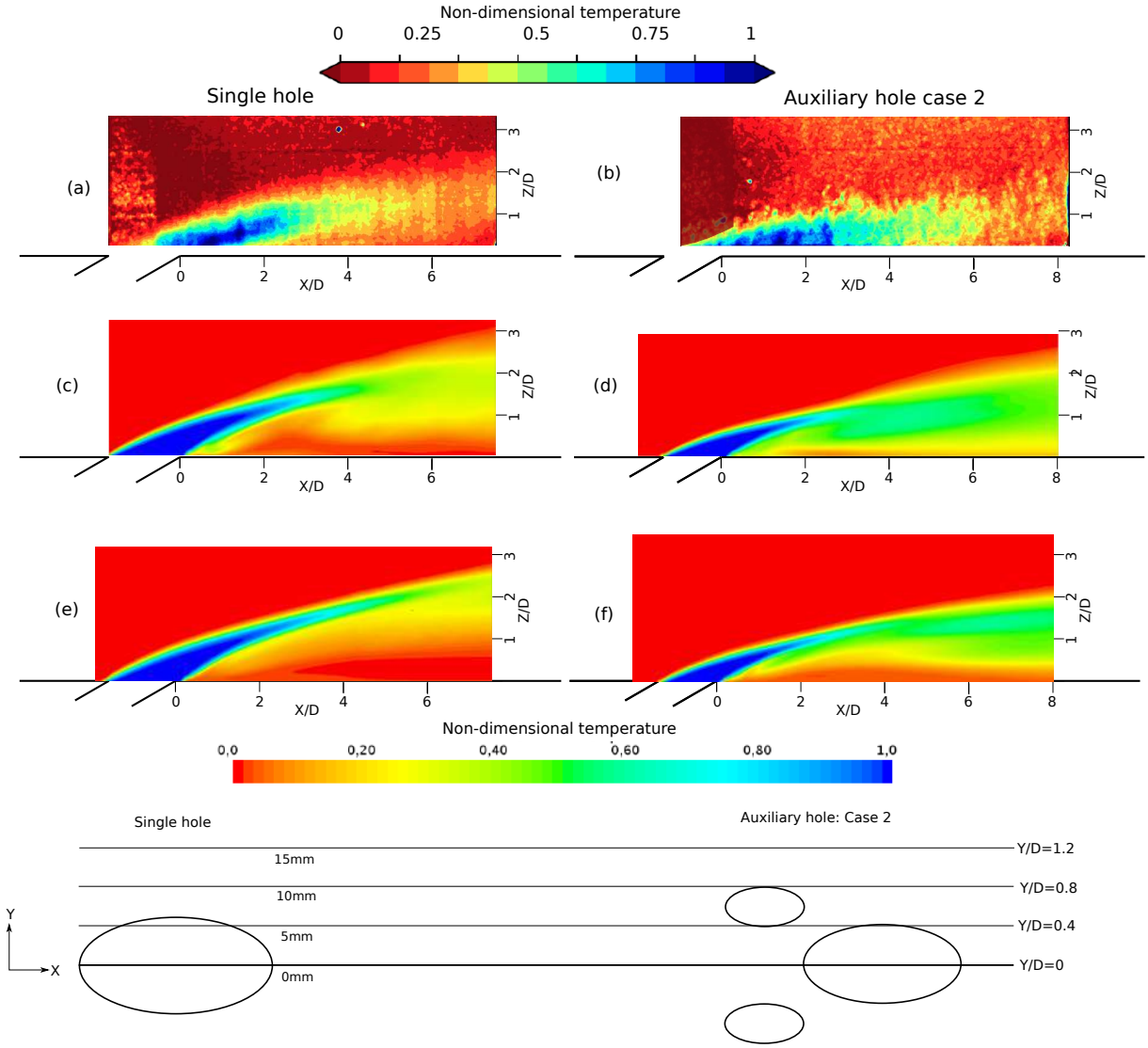

Figure 6.5: Mean non-dimensional 2-D temperature contours in the XZ plane at **Y/D=0** for the single hole configuration (a, c, e) and the auxiliary hole configuration (b, d, f). The figures (a) and (b) are obtained using phosphor thermometry, (c) and (d) are obtained through LES simulations, (e) and (f) are obtained using RANS simulations.

main hole jet. This can qualitatively confirm the validity of the LES simulations due to conformity with the RANS and experimental results . The RANS simulation predict that the combined jets from the auxiliary holes and the main hole penetrate deeper into the flow as compared to the LES or experimental cases.

Figure 6.7 shows the non-dimensional temperature contour in the XZ plane at Y/D=0.8 in the lateral direction.

The region at the hole exit of the single hole case has no presence of the injected cold jet. The presence of the jet flow is prominent in the region 2<X/D<4 where the expanding jet appears in the region away from the central axis of the jet. The LES case shows higher cold jet presence in the plane at Y/D=0.8 than that of the RANS case. A study by Harrison & Bogard (2008) has shown that the RANS turbulence modelling tends to have an adiabatic film cooling effectiveness over-prediction in the regions closer to the central axis of the jet while the models under-predict the adiabatic film cooling effectiveness in the lateral directions as compared to experimental values. This shows that the RANS models tend to gather the jet flow closer to the central axis of the hole. The auxiliary hole case presents a different story compared to the single hole case. There is a much higher cold jet presence in the hole exit region compared to the single hole case, thanks to the presence of the laterally displaced auxiliary holes. Again, the flow tends to the closer towards

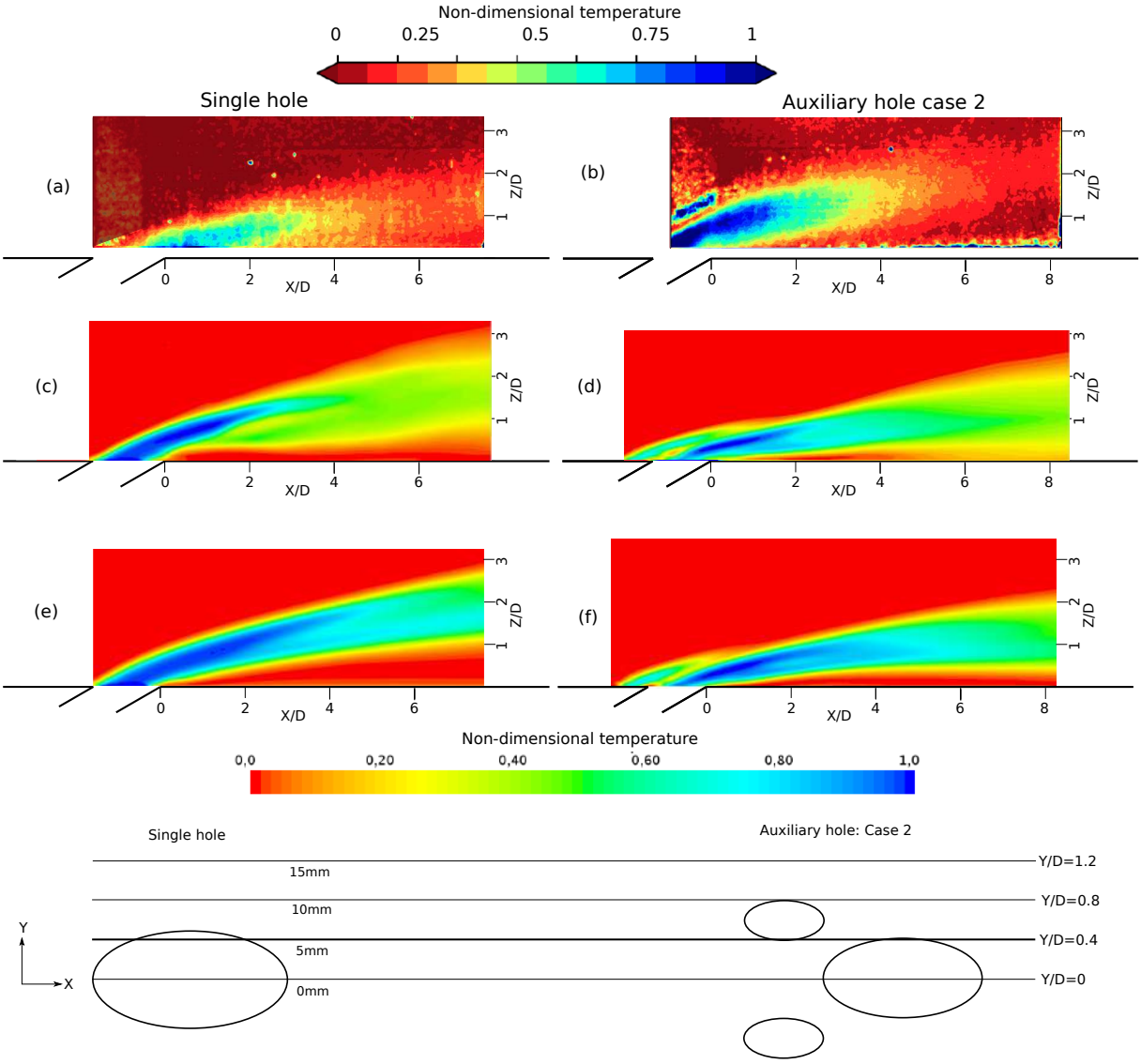

Figure 6.6: Mean non-dimensional 2-D temperature contours in the XZ plane at **Y/D=0.4** for the single hole configuration (a, c, e) and the auxiliary hole configuration (b, d, f). The figures (a) and (b) are obtained using phosphor thermometry, (c) and (d) are obtained through LES simulations, (e) and (f) are obtained using RANS simulations.

the wall deeming higher adiabatic film effectiveness on the wall.

Adiabatic film cooling effectiveness

Looking at figure 6.8 (a) and (b) which presents the centerline and lateral adiabatic film cooling effectiveness respectively, it is clear that the auxiliary hole arrangement outperforms the single hole case at high blowing ratio (M=3). This trend is seen throughout the longitudinal direction downstream of the hole exit. Due to the high momentum of the issuing jet, there is a dip in the centerline and laterally averaged adiabatic film cooling effectiveness at locations X/D<5. However, due to intense mixing with the crossflow and partial reattachment, there is an improvement in the η values at locations X/D>5.

Additionally, figure 6.9 shows the adiabatic film cooling effectiveness contour for the single hole and the auxiliary hole cases. The protection around the hole downstream of the hole is seen to have favourable lateral and longitudinal spread in the auxiliary hole case as compared to the single hole case.

With this, one can conclude some key aspects from all the obtained temperature field results so far.

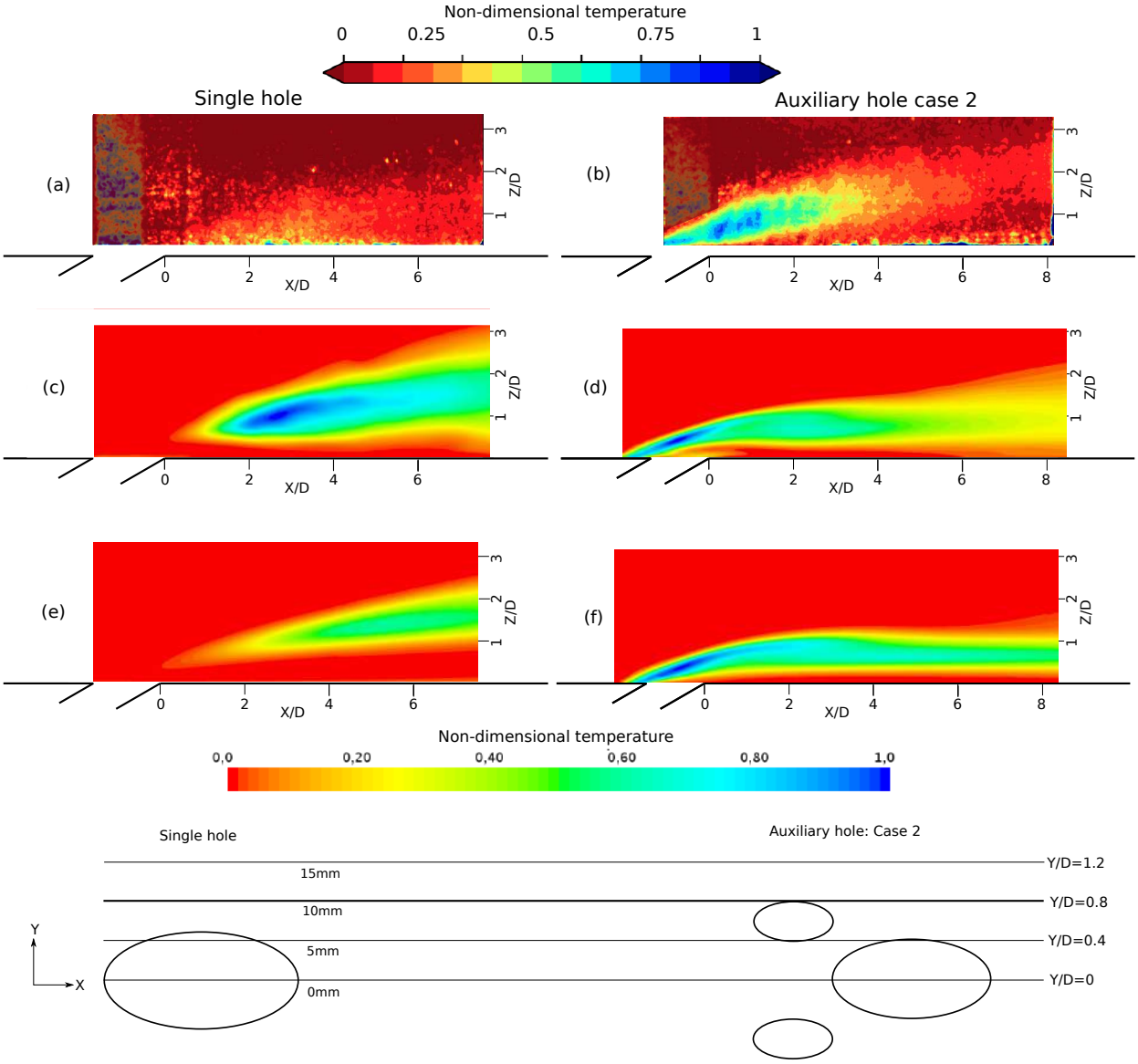

Figure 6.7: Mean non-dimensional 2-D temperature contours in the XZ plane at **Y/D=0.8** for the single hole configuration (a, c, e) and the auxiliary hole configuration (b, d, f). The figures (a) and (b) are obtained using phosphor thermometry, (c) and (d) are obtained through LES simulations, (e) and (f) are obtained using RANS simulations.

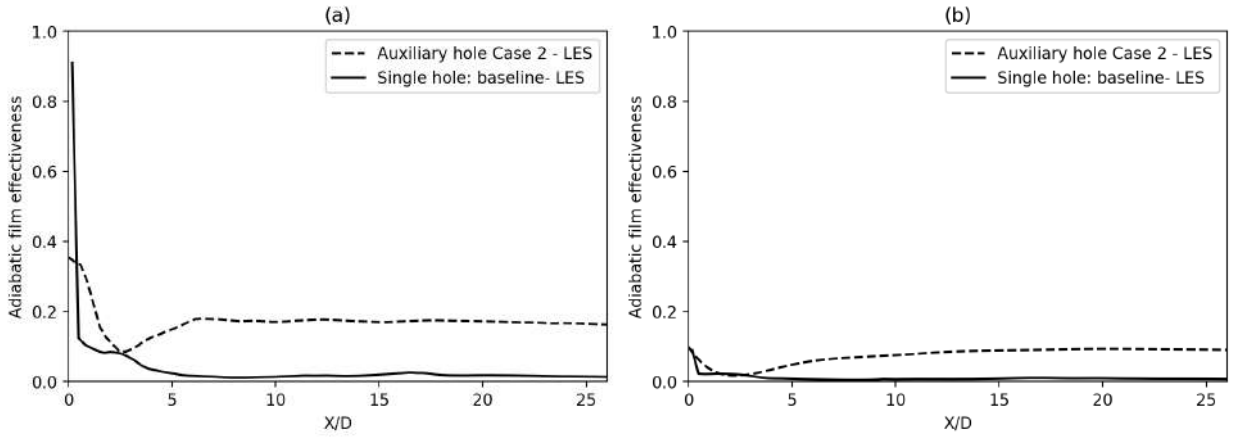

Figure 6.8: Adiabatic film cooling effectiveness evolution for M=3.

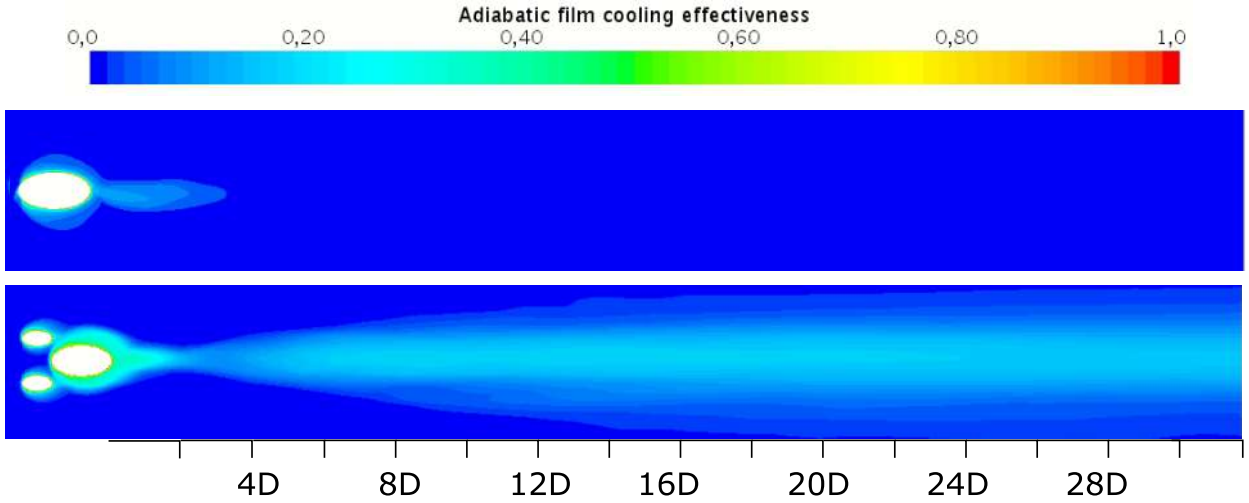

Figure 6.9: Adiabatic film cooling effectiveness contours for M=3. Top: Single hole, bottom: Auxiliary hole case 2

- Single hole case presents a higher jet penetration into the main flow as compared to the auxiliary hole case. Hence, on the first look, the auxiliary hole case tends to have better film cooling features.
- RANS simulations over-predict the cold jet presence in the regions along the longitudinal axis of the jet and under-predict in the lateral zones.

In this section, it was seen that the auxiliary hole configuration performs better than the single hole system in terms of the non-dimensional temperature flow visualisations through experiments and numerical analyses. However, the better flow features of the auxiliary hole system is the consequence of a reason. There is a need to identify the cause of this effect and hence in the next section, a qualitative and quantitative analysis of the velocity, vorticity and temperature fields are discussed to understand the auxiliary hole configuration better.

6.3 Discussion of flow physics

In this section, the physical phenomena occurring in the auxiliary hole configuration and the single hole configuration are discussed. RANS simulations cannot present instantaneous flow visualisations. However, LES simulations provide instantaneous flow data and can provide intricate details regarding coherent flow structures.

Instantaneous temperature flow field

The instantaneous non-dimensional temperature (Θ) flow field visualisation is presented in the figures 6.10-6.12. Figures (a) and (b) are obtained through experiments using phosphor thermometry and figures (c) and (d) are obtained using LES simulations. Also, (a) and (c) correspond to the single hole case while figures (b) and (d) correspond to the auxiliary hole case 2 configuration. Figure 6.10 shows the non-dimensional temperature contour for Y=0 (central symmetry plane).

Comparing the single hole case and auxiliary hole case, one can observe that the jet in the single hole case tends to penetrate into the crossflow deeper than the auxiliary hole configuration which stays closer to the wall. Additionally, the jet-shear vortices in the windward and leeward side of the jet found in the experimental case are comparable to the numerical results. As previously mentioned, a Θ value of 1 means purely cold injected jet, 0 represents purely hot crossflow, 0.5 refers to zones with perfect mixing between the crossflow and injected jet. The initial roll up of the top side jet shear layer induces strong mixing at a distance of 2-4 diameters away from the hole exit (values of Θ around 0.5). The standing vortices are also clearly seen as marked with arrows. The zone under the ejecting jet is found to have Θ values less than 0.3 indicating the predominant

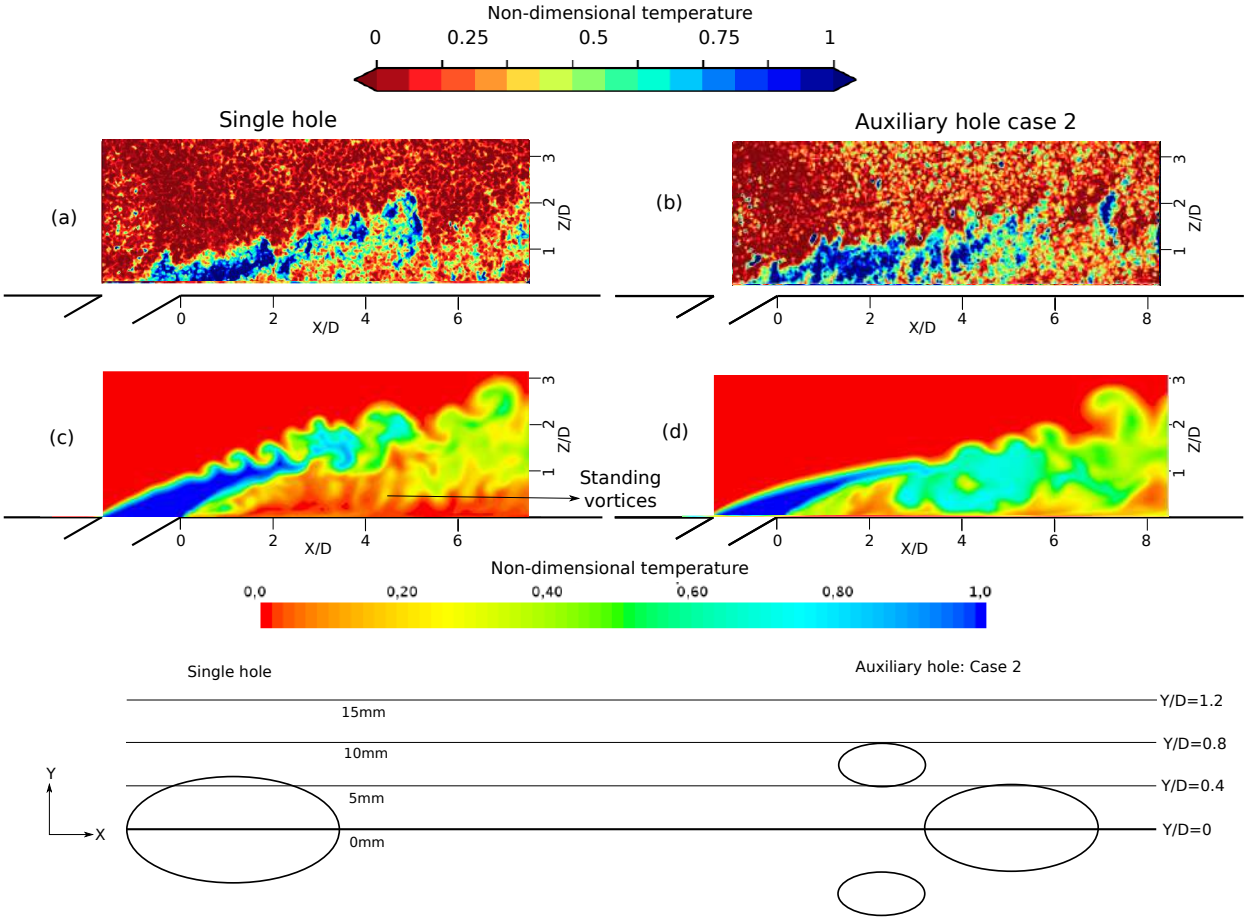

Figure 6.10: Instantaneous non-dimensional 2-D temperature contours in the XZ plane at **Y/D=0** for the single hole configuration (a and c) and the auxiliary hole configuration (b and d). The figures (a) and (b) are experimentally obtained using phosphor thermometry and (c) and (d) are obtained through LES simulations.

presence of crossflow closer to the wall. In the auxiliary hole case, the Kelvin-Helmholtz roll up is not present, consequently periodic coherent structures are absent. The mixing between the main flow and the jet happens further downstream at about 4-6 diameters away from the hole exit. However, the extended zone with Θ values around 0.6 indicate an addition of cold jet into the plane due to the auxiliary hole jet. It is also to be noted that Θ values less than 0.2 in the zone close to the wall at 1.5>X/D<2.5 indicate side-wise ingestion of crossflow due to horse-shoe vortices.

Figure 6.11 shows the non-dimensional temperature contour in the XZ plane at Y/D=0.4 in the lateral direction.

Figure (a) presents similar flow features as seen in the case Y/D=0. However, the zone close to the wall has Θ values around 0 indicating that the crossflow has been absorbed into the flow. This is the region below the CRVP structure and hence has high absorption of the crossflow under the jet. In the case of auxiliary hole, the auxiliary hole configuration presents a jet flow closer to the wall and in addition to this, the Θ values remain higher in the jet trajectory than that of the single hole. An interesting feature that can be observed in figures (b) and (d) is the presence of the auxiliary hole jet markedly seen just above the main hole jet. The zone marked 1 and 2 highlight this feature.

Figure 6.12 shows the non-dimensional temperature contour in the XZ plane at Y/D=0.8 in the lateral direction.

Comparisons of figures (a) and (c) show good similarities between the LES and experimental results. Close to the jet exit, the jet is non existent as the lateral spread is not quick enough to cover this zone. Further downstream, due to the expansion of the jet in the lateral directions, the jet flow appears as discontinuous streaks (due to Kelvin-Helmholtz instabilities). The auxiliary

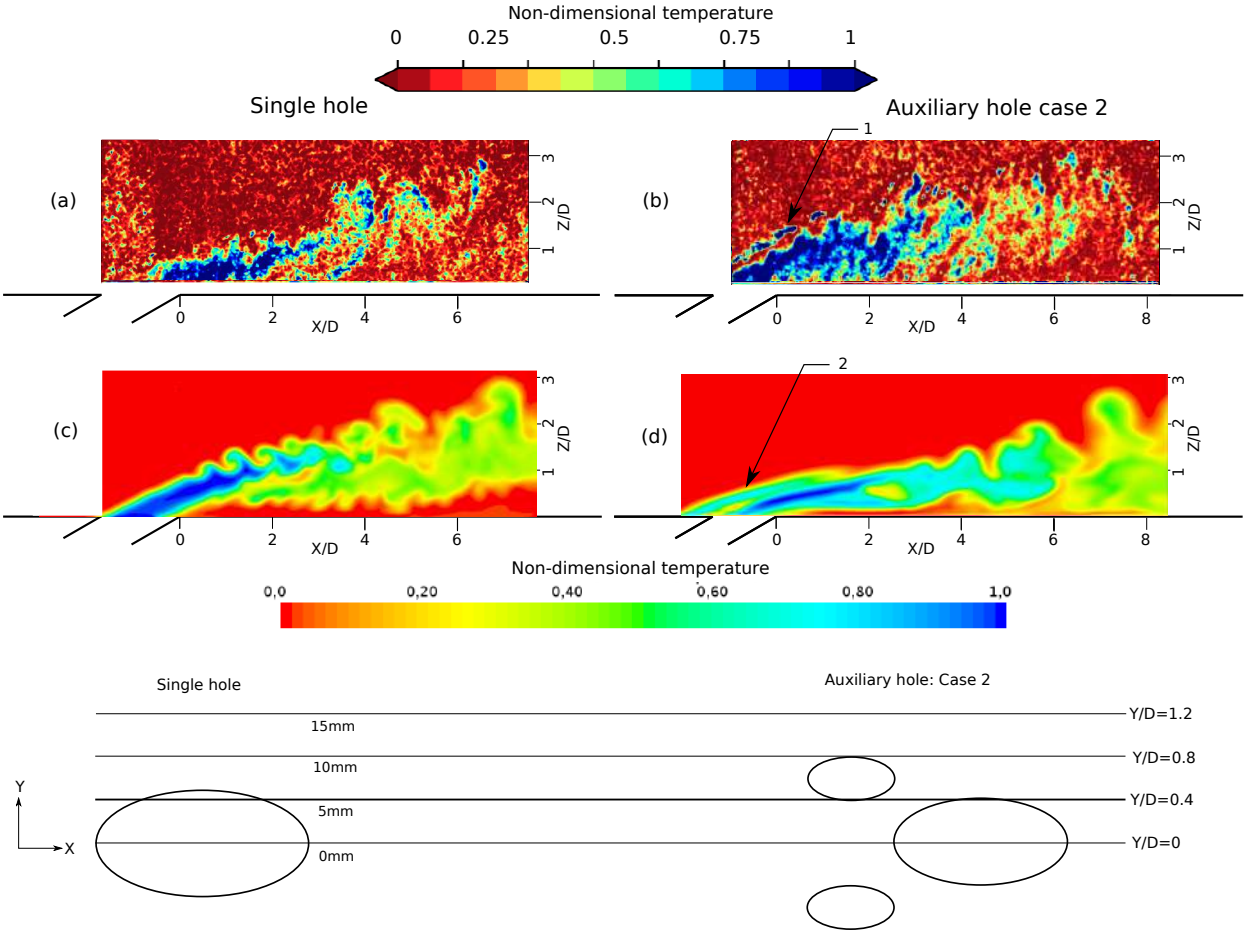

Figure 6.11: Instantaneous non-dimensional 2-D temperature contours in the XZ plane at **Y/D=0.4** for the single hole configuration (a and c) and the auxiliary hole configuration (b and d). the figures (a) and (b) are obtained using phosphor thermometry and (c) and (d) are obtained through LES simulations.

hole configuration presents a different scenario. Due to the presence of supporting auxiliary holes, the protection in the lateral direction is higher than that of the single hole case. As in previous cases, there is a good accordance in the qualitative features between the experimental and LES simulations as can be seen in (b) and (d).

Experimental and LES simulations have great accordance with each other qualitatively and hence validate each other. Instantaneous flow fields have shown that the 2-D phosphor thermometry is accurate as it captures the instabilities like the jet-shear layer vortices and also the presence of the cold jet in intricate and difficult to identify zones.

Velocity and vortex field

The mean velocity contour for the single hole and auxiliary hole configuration is presented in the figure 6.13. The central XZ plane (Y=0) is shown in this figure. As discussed previously, the jet from the single hole configuration penetrates deeper (Z/D=2 at X/D=6) into the flow compared to the flow from the main hole of the auxiliary hole configuration (Z/D=1 at X/D=6). Not only is the jet trajectory closer to the wall, but also the higher velocity downstream shows higher cold injected jet presence. This is not very explanatory to understand the mixing zones. Hence in figure 6.14, the variance of temperature, velocity (magnitude) and the i, j, k components of the velocity are presented. The variances are normalised as follows

$$Temperature : T_{norm} = \frac{T_\infty - T_c}{T_\infty - \sqrt{Variance}}$$

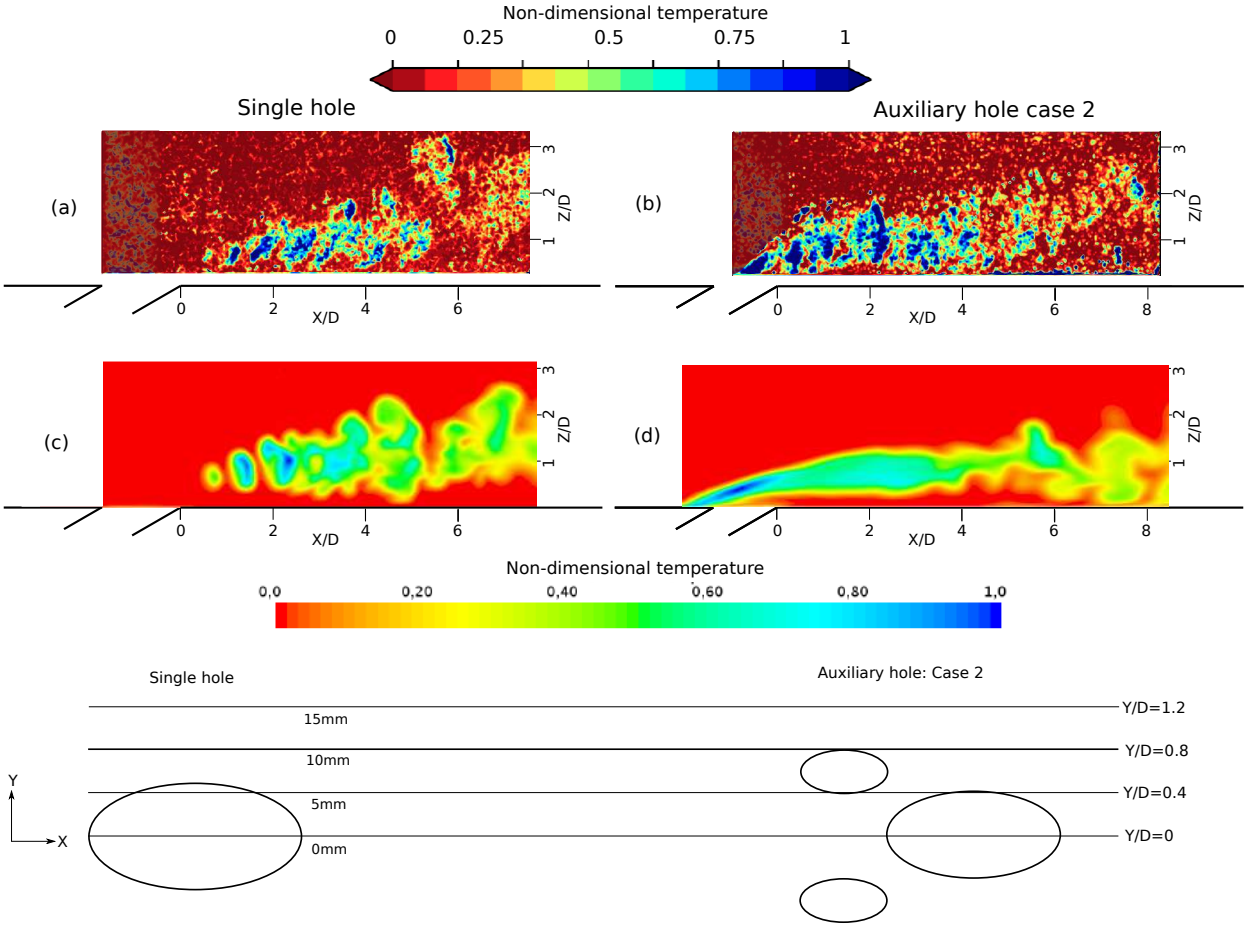

Figure 6.12: Instantaneous non-dimensional 2-D temperature contours in the XZ plane at **Y/D=0.8** for the single hole configuration (a and c) and the auxiliary hole configuration (b and d). The figures (a) and (b) are obtained using phosphor thermometry and (c) and (d) are obtained through LES simulations.

$$Velocity : V_{norm} = \frac{\sqrt{Variance}}{V_{max}}$$

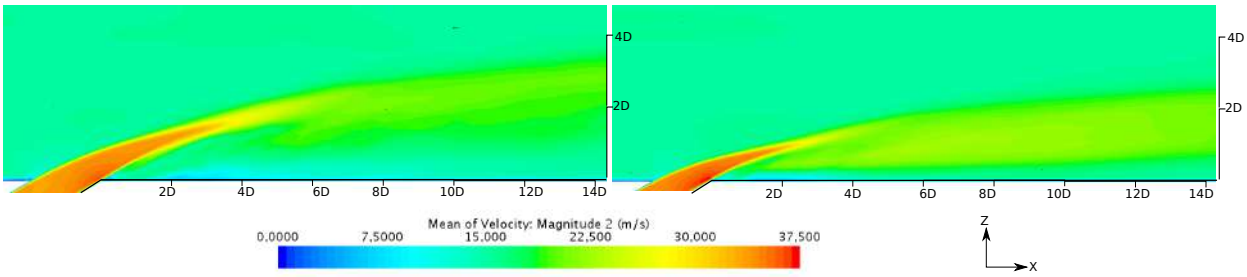

Figure 6.13: Mean velocity contour in the central plane (Y/D=0) for the single hole case (left) and the auxiliary hole configuration (right).

Figures (a, c, e, g, i) present the variance contours for the single hole case and (b, d , f, h , j) present variance contours for the auxiliary hole configuration. The presentation of the variance in velocity and temperature is useful to determine the zones where there are strong fluctuations in temperature and zones with high mixing between the cold jet and the hot main flow. From the figures (a, c) and (b,d) one can understand that there is a strong correlation between the fluctuations in temperature and velocity. The zones where there is a variation in the velocity (magnitude and i, j, k components) are an indicator of the wake region behind the jet. The comparison of (c) and (d) shows that fluctuations in velocity for the single hole case is along the jet-shear layer of the injected jet while for the auxiliary hole case, there are fluctuations in the

near wall region downstream of the hole exit in addition to the jet shear layer vortices. A similar trend is also seen in (a) and (b) showing the variation of temperature. Looking at the individual components of velocity, (e, f) show the variance in the i component of the velocity. This field is very similar to the variance in velocity magnitude. However (g) and (h) representing the variation in the j component of the velocity are very different for the single hole and the auxiliary hole configurations. Along the central plane, there is very less lateral variation of velocity for the single hole case. In contrast, for the auxiliary hole case, there is a strong variation in the j component at the exit of the hole, and this can be attributed to a strong negative pressure gradient which attracts the jet from the auxiliary hole into the axis of the main hole. The periodic oscillation of sucking in the left and right auxiliary hole jet into the mainstream is the cause of this high variance at the jet exit. The k component of the velocity shows similar variance for the two hole configurations. Due to the enhanced mixing between the jet and the main hole caused by the Kelvin-Helmholtz instabilities, the maximum variation happens at the edges of the ejected jet (windward and leeward side). The combination of the variation of the three velocity components represent the overall wake region and the eventual mixing zones in the central plane.

Figure 6.15 shows the evolution of the mean helicity through the presentation of the front view (upstream of the hole). Helicity is defined as the product of the velocity and vorticity which is not only an indicator of the vortex intensity at a point but also an indicator of the direction of flow rotation (clockwise or anti-clockwise). In this figure the YZ plane is shown at (a)X/D=-1, (b)X/D=0, (c)X/D=1, (d)X/D=3. From figure (a) one can see the beginning of the CRVP in the auxiliary holes. From figure (b) the nascent stages of the single hole configuration and the main hole of the auxiliary hole configuration are seen. Notable differences in the intensity and form of the CRVP structure is seen. The auxiliary hole CRVPs position themselves over the CRVP of the main hole, with the sides have opposite signs of helicity. The effect of this is seen in figure (c) (Figure zoomed on purpose to show the features better) where the auxiliary hole configuration presents an overall reduced helicity intensity while remaining close to the wall. This is due to the auxiliary hole jets staying above the main hole jet which prevents the upward movement of the jet. This feature is not present in the single hole case and hence the CRVP promotes the upward movement of the jet, all the while dragging the main flow into the jet stream. Further downstream at X/D=3, the over all intensity of the CRVP vortex is reduced, but the single hole case continues to rise upwards. In the case of the auxiliary hole configuration, the rate of increase in the height of the flow remains lower as compared to the single hole case. For example, in Figure (c), the single hole case CRVP is higher by 0.5D in height along Z direction as compared to auxiliary hole case.

This explanation is supported by an instantaneous velocity and vorticity field vector visualisation in figure 6.16 showing the YZ plane at X/D=3. The figure (a) shows the velocity vector field of the single hole case and (b) shows the corresponding vortex vector field. The direction of the rotation of the flow is markedly seen from the two figures and the CRVP can be identified. The CRVP of the auxiliary hole system represented in (c) and (d) is a more complex. The main hole CRVP shows an opposite direction to the rotation of the auxiliary holes. The effect is a reduced vortex intensity in the entire system (figure (d)) as compared to the single hole system (figure (b)). To further reinforce this point, the instantaneous iso-contours of the Q-criterion are presented. It is defined as

$$Q = (||\Omega||^2 - ||S||^2) \tag{6.2}$$

where Ω is known as the rotation rate or vorticity tensor and S is the strain rate. Positive values of Q represent presence of pure rotation.

Constant values of $Q=Uc^2/D^2$ colored with mean helicity values to identify the direction of rotation are shown in the figures 6.17 and 6.18. In figure 6.17, a top view of the iso-contours of the Q-criterion are presented. The single hole case clearly highlights various coherent structures like the development of the horseshoe vortex upstream of the hole, jet-shear layer vortices and the CRVP formation at the edges of the hole exit. The prominent negative and positive arms of the CRVP eventually mix at downstream locations at X/D>2 and it is difficult to identify coherent structures. After this point, the mixing is three dimensional and there is no preferred direction. The figure in the bottom, the auxiliary hole configuration shows the development of horse shoe vortices upstream of each of the three holes. The formation of the jet-shear layer vortex system for the main hole is seen further downstream. The most notable feature is the positioning and

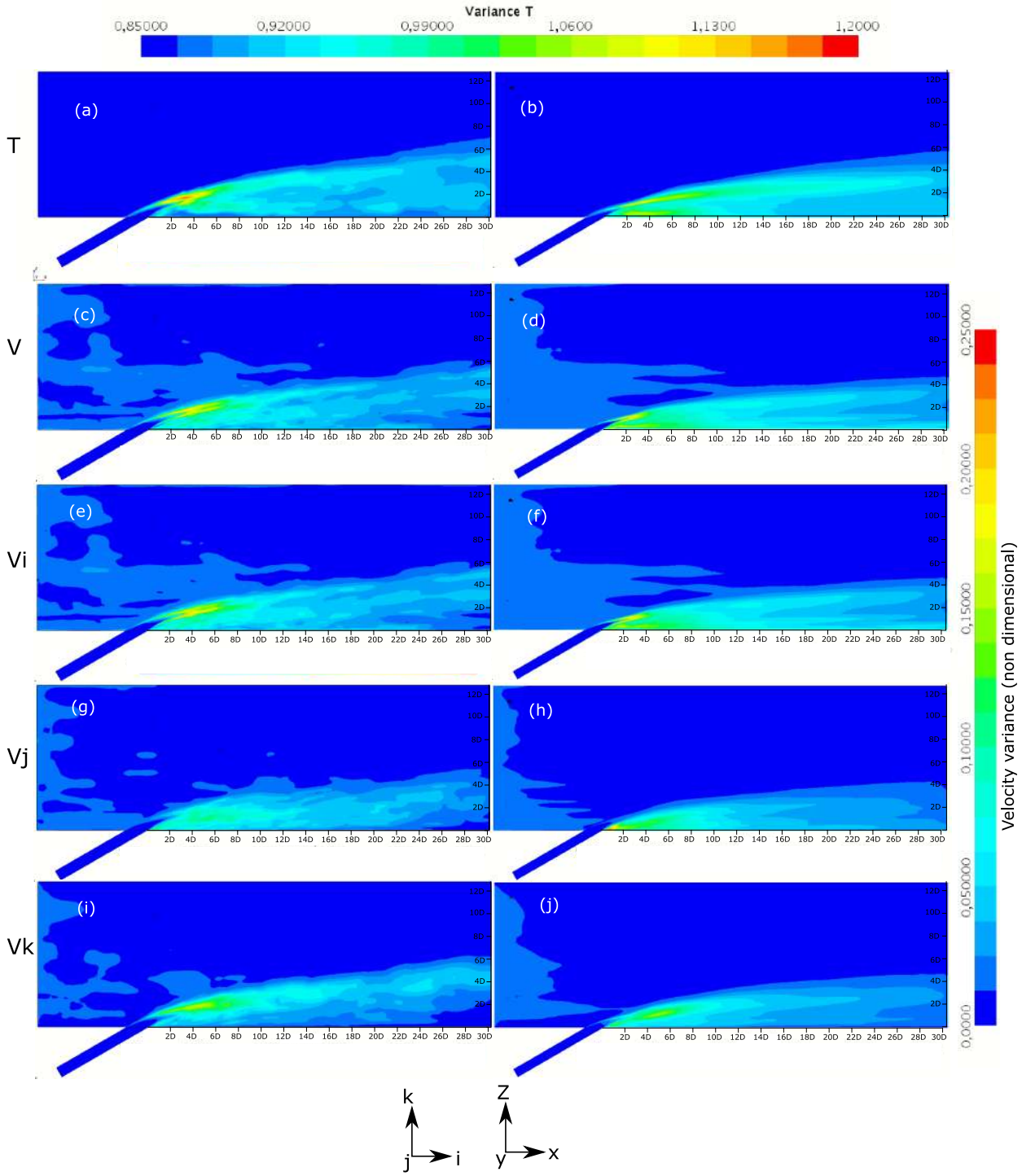

Figure 6.14: Variance contours for the single hole configuration and auxiliary hole configuration in the central plane. (a) and (b) present the variance in temperature; (c) and (d) present the variance in velocity magnitude; (e) and (f) present the variance in the i component of velocity; (g) and (h) present the variance in the j component of velocity; (i) and (j) present the variance in the k component of velocity.

the interaction of the CRVPs arising from the auxiliary holes and the main hole. The negative arm of the main hole is positioned near the positive arm of the left auxiliary hole and the positive arm of the main hole CRVP is positioned near the negative arm of the right auxiliary hole CRVP. This as explained in the earlier sections, helps in reducing the strength of the overall CRVP of the auxiliary hole system as compared to the single hole system.

Figure 6.18 further adds clarity to the explanation of why the CRVP height and intensity of the auxiliary hole system is lower. The jet ejecting from the single hole case directly meets the freestream and almost immediately the mixing process happens through the formation of the jet-

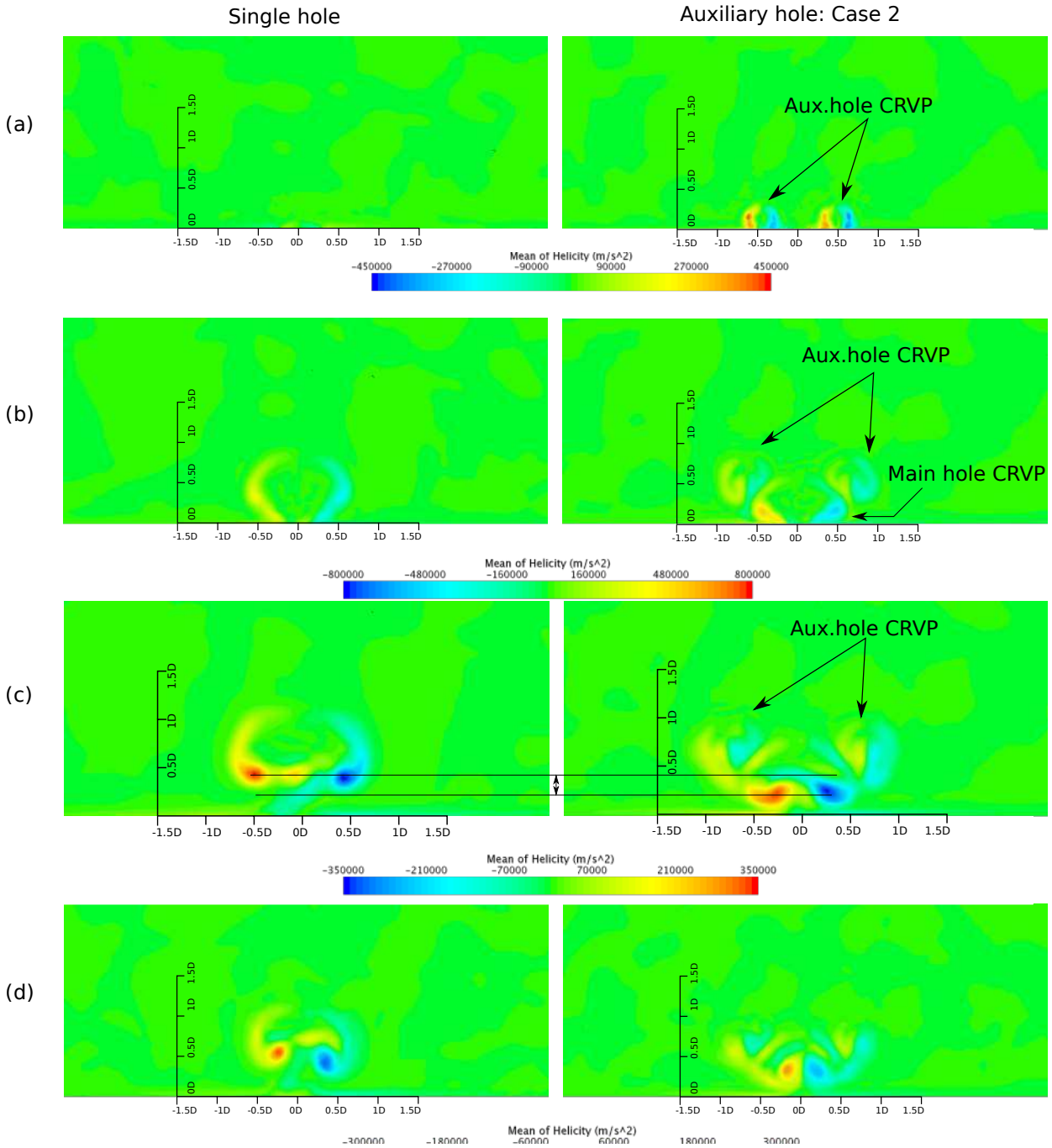

Figure 6.15: Front view of the mean helicity contours for the single hole and the auxiliary hole configuration at various planes (a) X/D=-1, (b) X/D=0, (c) X/D=1, (d) X/D=3.

shear layer vortices. Additionally, there are no barriers to prevent the jet from rising higher in Z direction nor protection in the lateral sides. However in the case of the auxiliary hole arrangement, the jets with high velocity ejecting from the auxiliary holes are the first to be in contact with the main flow and experience a force pushing them towards the main flow direction. Just downstream of these holes, the main hole jet is ejected outwards but due to the protection from the auxiliary hole jets in the lateral directions which also provide a slight downward force helping the main hole jet to stay closer to the wall. The downward force is due to the pulling action of the opposite pairing of the arms of the CRVP in the main hole and auxiliary hole in addition to the downward pushing imparted by the main flow on the auxiliary hole jets.

The entire explanation is summarised in the figure 6.19 which is a schematic representation of the single hole and auxiliary hole CRVP formation and evolution. The entire process can be summarised as

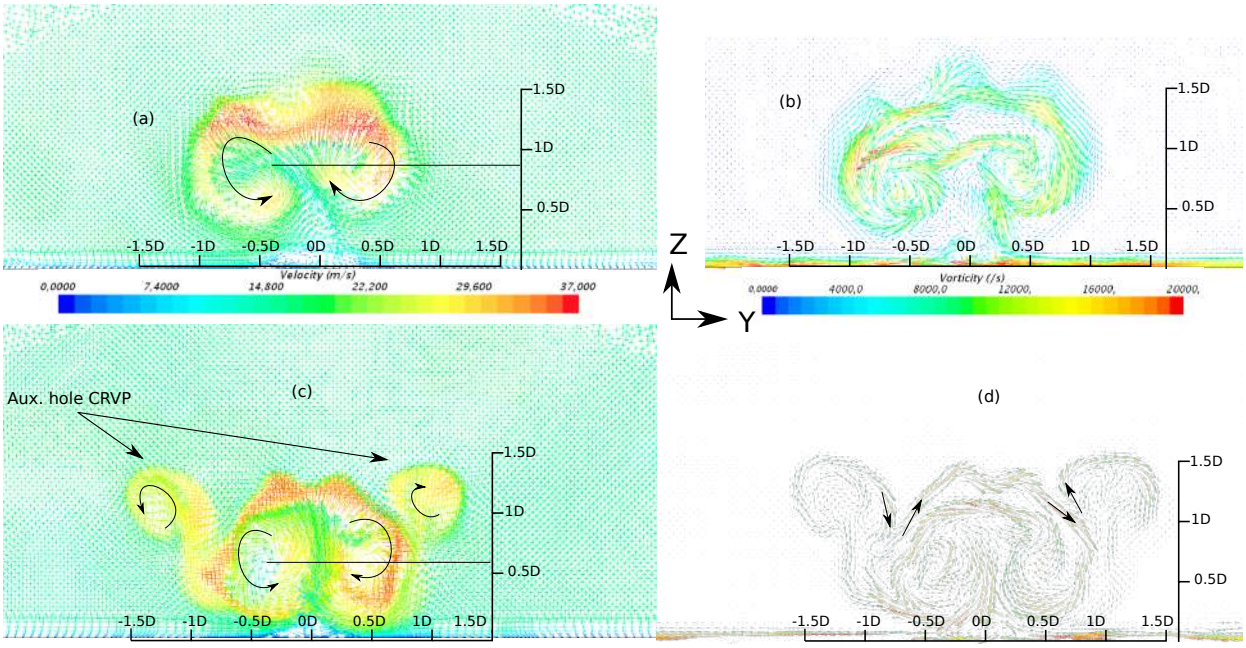

Figure 6.16: Instantaneous velocity (a, c) and vorticity (b,d) contours for the single hole and auxiliary hole configuration at X/D=3 plane. Figures (a) and (b) represent the single hole case, while (c) and (d) represent the auxiliary hole configuration.

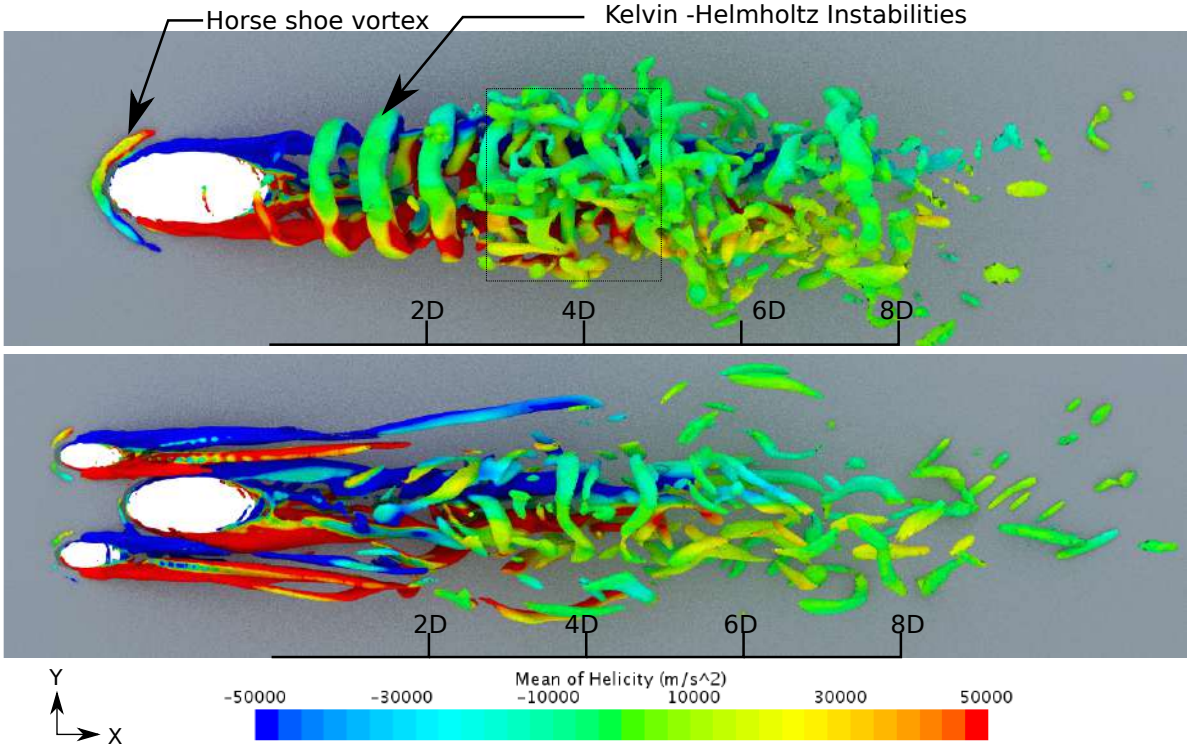

Figure 6.17: Top view of the iso-contours of Q-criterion colored with helicity values. Note: the color bar is limited to -50000 and 50000 to better highlight the vorticity features of the film cooling configurations.

- The major contribution to the CRVP intensity is the shear experienced by the ejected jet on its sides, which decide the direction of the CRVP rotation.
- The initial vortex is aligned in a plane horizontal to the wall supporting the hole (Z/D $<$ 0.5). At later stages, the bending of the jet due to the momentum of the main flow causes the CRVP structure to bend along also.
- At locations that are downstream (X/D$>$ 3) from the hole, it can be noticed that the CRVP

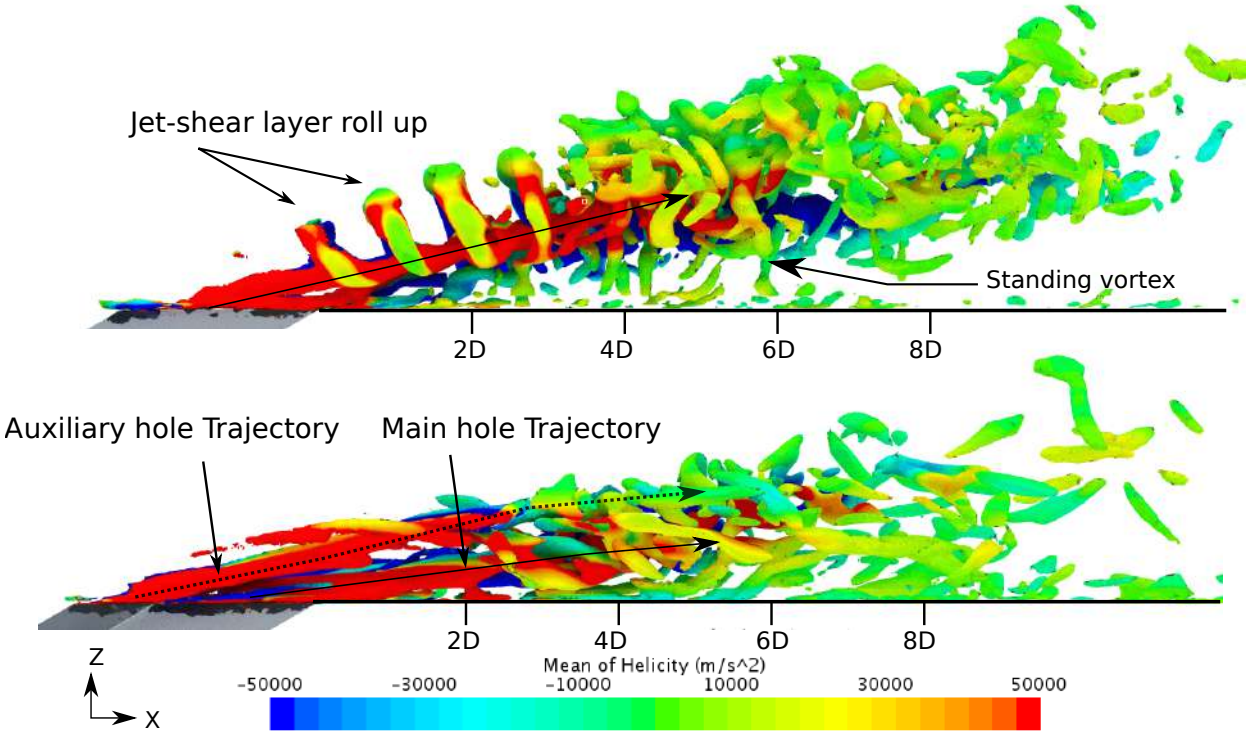

Figure 6.18: Side view of the iso-contours of Q-criterion colored with helicity values. Note: the color bar is limited to -50000 and 50000 to better highlight the vorticity features of the film cooling configurations.

is completely perpendicular to the wall.

- This perpendicularity promotes the ingestion of the hot main flow into the cold jet axis, effectively reducing the effectiveness of the cold injected jet near the wall. This means more mixing which is detrimental to the film cooling process.
- The auxiliary hole configuration is designed to reduce the height and intensity of the CRVP. The idea is to protect as much as possible the sides of the main hole from the shearing due to the interaction of the jet and the main flow.
- The relative velocity is drastically reduced due to the presence of the auxiliary hole jets and hence the shear force is also reduced. Additionally, the negative-positive arm interaction of the CRVPs in the main hole and auxiliary hole jets contribute to the reduction in the CRVP intensity of the main hole.

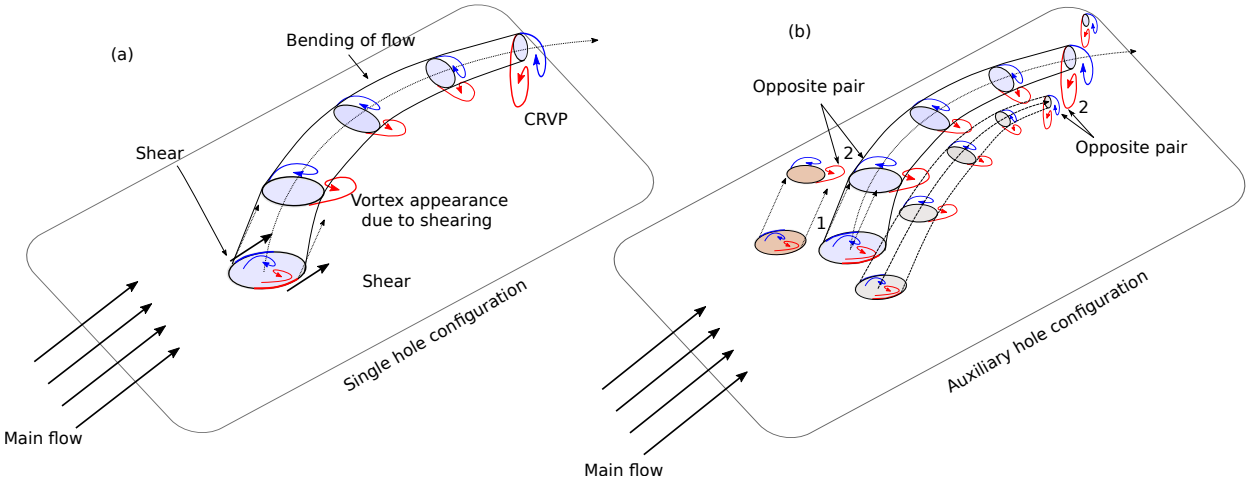

Figure 6.19: Illustration of the working mechanism in the single hole and auxiliary hole configurations.

In this chapter, results from Large Eddy Simulations are presented to compliment the information obtained in chapter 5 through experiments. The comparisons between the experiments and simulations show very good coherence in the turbulent structures. The experiments also validate the LES simulations through the temperature contours obtained. Further analysis have been made using the validated LES simulations to understand the flow in the auxiliary hole configuration. The key takeaways from the velocity and vorticity visualisations show that the CRVP of the auxiliary hole system has a much reduced intensity as compared to the single hole case and also the trajectory of the cold injected jet stays closer to the wall, outperforming the single hole case. Through this study, one can propose the working mechanisms of the auxiliary hole system.

Chapter 7

Summary and perspectives

Concluding remarks are provided in this chapter. An overview of the activities carried out in the thesis and the results obtained are presented. The perspectives and the industrial implications due to this work are highlighted and the chapter ends by providing key points from the study.

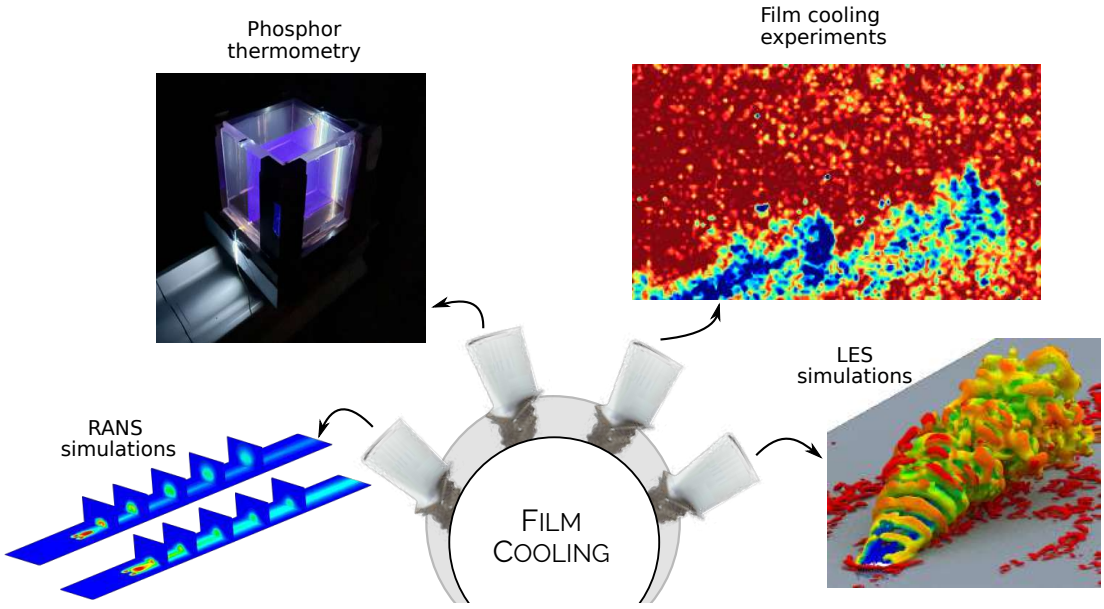

Figure 7.1: Various activities carried out in the framework of this thesis.

Contents

7.1 General synthesis 122
7.1.1 Overview of objectives 122
7.1.2 RANS studies 122
7.1.3 Phosphor thermometry development 122
7.1.4 Experimental film cooling studies 123
7.1.5 LES simulations 123
7.2 Perspectives 123

7.1 General synthesis

7.1.1 Overview of objectives

Film cooling of the gas turbine blades are an absolute necessity to maintain the turbine blade temperatures at acceptable levels. However, the use of the relatively colder air from the compressor stage for the film cooling process is detrimental to the overall efficiency of the engine as there is lesser amount of air available for the combustion process. The aerodynamic characteristics of the jet exiting the film cooling hole have an immense implication on the thermal film cooling performance. Hence this thesis focused on the film cooling optimisation methods to improve the usage of this limited bleed air obtained by studying a recent novel film cooling arrangement called the auxiliary film cooling configuration where a single main hole is supported by two smaller adjacent holes around the main hole.

Current practices in film cooling

Current state of the art film cooling configurations used in the recent gas turbine blades are very intricate and difficult to manufacture. Various hole shapes have been analysed to try and mitigate the Counter Rotating Vortex Pair (CRVP) which is detrimental to the film cooling process. Numerous numerical and experimental analysis have been made to estimate the performances of innovative hole shapes like the fan shaped hole, crescent shaped hole and more recently film cooling holes that are placed on slots, trenches and protrusions aiming to obtain better aerodynamic features aiding the film cooling process.

7.1.2 RANS studies

Before conducting expensive experimental tests on the proposed film cooling configuration, an overall idea of the expectations from the auxiliary hole system was necessary. Hence RANS simulations using OpenFOAM using K-ω SST turbulence model was conducted to ascertain certain critical centerline and laterally averaged parameters like the adiabatic film cooling effectiveness. The results obtained for two auxiliary hole configurations are presented in conjunction with experimental and numerical simulations for a single hole configuration. The boundary conditions for all the tested configurations are obtained from the work of Sultan (2011) who studied a jet emanating from an inclined single cylindrical hole at different blowing ratio regimes (M= 0.65, 1, 1.25). The auxiliary hole configuration where the auxiliary holes were spaced at 1.5D apart from each other (Case 2) outperformed another auxiliary hole configuration where the holes were spaced 1D apart from each other (Case 1). The two systems showed superior adiabatic film cooling effectiveness for all blowing ratios than the simple single hole configuration although all the cases had the same injected mass flow. Analysis of the mean vortex fields showed that the auxiliary hole configuration had much lower vorticity values in the entire domain and the flow traced by the jet stayed attached or remained closer to the wall as compared to the single hole case. The outcome from these studies was that the auxiliary hole configuration case 2 compared to the single hole case showed an augmentation of 65% in adiabatic film effectiveness in the centerline at M=0.65 (attachment regime), 149% at M=1 (re-attachment regime) and a maximum of 184% for M=1.25 (penetration regime). This gave a preliminary validation of the proposed configuration and further film cooling analysis were conducted on the case 2 auxiliary hole configuration as it showed higher adiabatic film cooling effectiveness than the case 1 auxiliary hole configuration.

7.1.3 Phosphor thermometry development

The development of phosphor thermometry using ZnO phosphor particles is explained subsequently. This is a major part of the thesis which describes a detailed analysis of the ZnO phosphor emission properties and the preliminary studies are conducted in water. A special Rayleigh-Benard test cell is built so as to simplify the phosphor thermometry development process. Eventually, the temporal and spectral methods to determine fluid temperature are studied extensively. Current

time dependent methods require a number of cameras to capture the quick emission decay generally. However, an improved temporal method using the rise time and decay time of the phosphor is explored and described which requires only two cameras. One of the major objectives of the thesis is to explore the possibility to conduct 2-D fluid temperature measurements using a single camera which is a novelty of this thesis. The spectral intensity ratio method using bandpass filters in an Optosplit device has been conducted and the calibration procedure is described in detail. The developed image processing code used to post process the raw acquired images were put to test using a natural convection test case, the Rayleigh-Benard convection. The temperature precision by using this method was of the order of 5-10% depending on the working temperature. This test case validated the calibration procedure followed and the successful implementation of spectral intensity ratio phosphor thermometry was assured. The entire procedure which was conducted in water could hence be translated to study film cooling configurations as the working principle of the phosphor remains the same in air and water.

7.1.4 Experimental film cooling studies

The film cooling studies were conducted on a newly constructed high temperature wind tunnel called the BATH at the PROMETEE site. This complex test bench required intensive calibration tests to determine its velocity and thermal characteristics. In the framework of this thesis, various metrology systems like pitot-static tube, thermocouples, pressure sensors, hot-wire anemometer, particle image velocimetry were employed to ascertain the working envelope and characteristics of the BATH test bench. The film cooling studies were conducted by using the electric heater alone so as to stay within the limits of the ZnO phosphor working temperatures. Three film cooling configurations as in the RANS study were used for analysis. A cold jet seeded with ZnO particles was injected in a main seeded crossflow at 150°C with a blowing ratio M=3. This blowing ratio was used due to the better visualisation possible due to high penetration of the injected cold jet. High resolution 2-D temperature contour results were obtained through a series of experiments for the three test cases. The key learning from this study was that the auxiliary hole system has very favourable flow characteristics as compared to the single hole case, as the cold jet stays closer to the wall. Additionally, the injected jet in the auxiliary hole case travels longer distance (X/D > 15) than that of the single hole case. The possibility of identifying key coherent structures like the jet-shear layer vortices show the fidelity of the phosphor thermometry technique.

7.1.5 LES simulations

Highly resolved Large Eddy Simulations were performed to understand why the auxiliary hole system shows improved performance than the single hole case. The comparison of the 2-D temperature flow fields with LES showed good similarities in instantaneous and mean flow fields. This comparison helps us to validate the phosphor thermometry using LES simulations. In search of better explanations on the flow physics of the auxiliary hole system, the instantaneous temperature, velocity and variance of temperature and velocity scalar fields were analysed. The vortex field visualisation (scalar and vector) at different planes along the flow direction showed that the intensity and height of the CRVP in the auxiliary hole configuration was lower as compared to single hole system due to the proximity of the oppositely signed CRVP arms of the main hole jet and the auxiliary hole jet on either side of the main hole. Iso-contours of the Q-criterion reinforces the explanations.

7.2 Perspectives

Through this work, the possibility of using phosphor thermometry for film cooling studies have been demonstrated. As in every scientific problem, there is a constant room for improvement. Concerning the perspectives on aero-thermal studies of film cooling problem, few suggestions can be proposed.
In this thesis, the positioning of the auxiliary holes upstream of the main hole was justified by the reasoning that having two smaller jets in front of the main hole jet can reduce the shearing forces

experienced by the main hole jet, hence reducing the CRVP intensity. However, other geometric positions of the auxiliary holes with respect to the main hole (upstream, sideways positioning) merit analysis. With respect to LES simulations, different blowing ratio regimes (for example, M=0.5, M=1, M=1.5) can be tested to ascertain if the flow features are different for the auxiliary hole configuration.
Additionally, the near-wall temperature and velocity profiles could be compared and studied through experimental and RANS/LES simulations. However, it is difficult to experimentally study the near wall region due to the high reflectivity of phosphor particles deposited on the wall.
The temporal study of LES results could shed light on the characteristic frequency of all kinds of coherent structures seen in the Jet In Cross-Flow.
Conjugate heat transfer (conduction-convection coupled) studies including the thickness of the wall could provide complete comprehension of the global mechanism of film cooling.

Regarding the measurement technique, few perspectives are identified. The phosphor thermometry implemented could be coupled with simultaneous velocity measurements through PIV. In this current thesis, the detector and laser system used prevented the simultaneous measurements. However, due to the use of discrete particles, PIV measurements are surely possible with the right equipment.
Since the phosphor thermometry was developed for the first time at the laboratory, there was a need to use huge quantities of seeding particles to perfect the technique. ZnO particles were chosen due to the easy availability and cost effectiveness. However, ZnO phosphors are a serious limitation to the working temperatures of the film cooling problem. Other particles like the BAM:Eu which can be used at higher temperatures and with larger decay times can help in film cooling analyses at much higher temperatures with better precision.
The temporal methods which require more number of cameras can provide better temperature precision than that of the spectral methods. The new method described in section 4.6.5 based on the rise time and decay time of the phosphor is a serious candidate for improved phosphor thermometry. Different filter combinations can be tested for ZnO phosphors while performing spectral intensity ratio method. The emission intensity captured vs temperature sensitivity compromise is a delicate balance and requires optimisation.
The lens and the optics in the Optosplit II device need to be adapted to the emission spectrum of the phosphor used. Lower transmissivity of the emission through the optics could lead to reduced temperature precision.
An important consideration is the time resolved analysis using phosphor thermometry measurements for film cooling as the results obtained through this method can be very easily compared with those of LES or DNS simulations.

To conclude, auxiliary hole film cooling configuration is a promising technique to improve aircraft gas turbine engine performance as has been proved through RANS and LES numerical simulations and experimental analysis using phosphor thermometry which provided high resolution temperature contours. Phosphor thermometry which is currently in nascent stages has immense potential to replace classical PIV systems to obtain time-resolved simultaneous velocity and temperature flow fields.

References

Abou Nada, Fahed, Aldén, Marcus & Richter, Mattias 2016 Investigation of the effect of engine lubricant oil on remote temperature sensing using thermographic phosphors. *Journal of Luminescence* **179**, 568–573.

Abram, Christopher, Fond, Benoit & Beyrau, Frank 2015 High-precision flow temperature imaging using zno thermographic phosphor tracer particles. *Optics express* **23** (15), 19453–19468.

Abram, Christopher, Fond, Benoit, Heyes, Andrew L & Beyrau, Frank 2013 High-speed planar thermometry and velocimetry using thermographic phosphor particles. *Applied Physics B* **111** (2), 155–160.

Abram, Christopher, Pougin, Miriam & Beyrau, Frank 2016 Temperature field measurements in liquids using zno thermographic phosphor tracer particles. *Experiments in Fluids* **57** (7), 115.

Addad, Yacine, Gaitonde, Ulka, Laurence, Dominique & Rolfo, Stefano 2008 Optimal unstructured meshing for large eddy simulations. In *Quality and reliability of large-eddy simulations*, pp. 93–103. Springer.

Adrian, Ronald J & Westerweel, Jerry 2011 *Particle image velocimetry*. Cambridge university press.

Andreopoulos, Jannis & Rodi, Wolfgang 1984 Experimental investigation of jets in a crossflow. *Journal of Fluid Mechanics* **138**, 93–127.

Armfield, Jeffrey S, Graves, RL, Beshears, DL, Cates, Michael R, Smith, TV & Allison, SW 1997 Phosphor thermometry for internal combustion engines. *Tech. Rep.*. SAE Technical Paper.

Azzi, Abbes & Jubran, Bassam A 2007 Numerical modelling of film cooling from converging slot-hole. *Heat and mass transfer* **43** (4), 381–388.

Barigozzi, Giovanna, Franchini, Giuseppe, Perdichizzi, Antonio & Ravelli, Silvia 2010 Film cooling of a contoured endwall nozzle vane through fan-shaped holes. *International Journal of Heat and Fluid Flow* **31** (4), 576–585.

Basset, Alfred Barnard 1887 On the motion of a sphere in a viscous liquid. *Proceedings of the Royal Society of London Series I* **43**, 174–175.

Beale, Sam 2012 Precision engineering for future propulsion and power systems: a perspective from rolls-royce. *Philosophical Transactions of the Royal Society A: Mathematical, Physical and Engineering Sciences* **370** (1973), 4130–4153.

Blanchard, JN, Brunet, Y & Merlen, A 1999 Influence of a counter rotating vortex pair on the stability of a jet in a cross flow: an experimental study by flow visualizations. *Experiments in fluids* **26** (1-2), 63–74.

Bogard, David G & Thole, Karen A 2006 Gas turbine film cooling. *Journal of propulsion and power* **22** (2), 249–270.

Boussinesq, JV 1885 Sur la resistance d'une sphere solide. *CR Hebd. Seanc. Acad. Sci. Paris* **100**, 935.

Boyce, Meherwan P 2011 *Gas turbine engineering handbook*. Elsevier.

Brübach, J, Patt, A & Dreizler, A 2006 Spray thermometry using thermographic phosphors. *Applied Physics B* **83** (4), 499.

Bunker, Ronald S 2005 A review of shaped hole turbine film-cooling technology. *J. Heat Transfer* **127** (4), 441–453.

Cortelezzi, Luca, Karagozian, Ann R *et al.* 2001 On the formation of the counter-rotating vortex pair in transverse jets. *Journal of Fluid Mechanics* **446**, 347–374.

Dexter, D LSCHULMANJH & Schulman, James H 1954 Theory of concentration quenching in inorganic phosphors. *The Journal of Chemical Physics* **22** (6), 1063–1070.

Dragomirov, Plamen, Mendieta, Aldo, Abram, Christopher, Fond, Benoît & Beyrau, Frank 2018 Planar measurements of spray-induced wall cooling using phosphor thermometry. *Experiments in Fluids* **59** (3), 42.

Ely, Marc J & Jubran, BA 2008 A numerical study on increasing film cooling effectiveness through the use of sister holes. In *Turbo Expo: Power for Land, Sea, and Air*, , vol. 43147, pp. 341–350.

Ely, Marc J & Jubran, BA 2009 A numerical evaluation on the effect of sister holes on film cooling effectiveness and the surrounding flow field. *Heat and Mass Transfer* **45** (11), 1435–1446.

Ely, Marc J & Jubran, BA 2010 A parametric study on the effect of sister hole location on active film cooling flow control. In *Turbo Expo: Power for Land, Sea, and Air*, , vol. 43994, pp. 1301–1311.

Ely, Marc J & Jubran, BA 2012 Film cooling from short holes with sister hole influence. In *Turbo Expo: Power for Land, Sea, and Air*, , vol. 44700, pp. 1185–1196. American Society of Mechanical Engineers.

Fan, Luming, Gao, Y, Hayakawa, A & Hochgreb, Simone 2017 Simultaneous, two-camera, 2d gas-phase temperature and velocity measurements by thermographic particle image velocimetry with zno tracers. *Experiments in Fluids* **58** (4), 34.

Fearn, Richard & Weston, Robert P 1974 *Vorticity associated with a jet in a cross flow*, , vol. 12.

Fond, Benoit, Abram, Christopher & Beyrau, Frank 2015 Characterisation of the luminescence properties of bam: Eu 2+ particles as a tracer for thermographic particle image velocimetry. *Applied Physics B* **121** (4), 495–509.

Fond, Benoit, Abram, Christopher, Heyes, Andrew L, Kempf, Andreas M & Beyrau, Frank 2012 Simultaneous temperature, mixture fraction and velocity imaging in turbulent flows using thermographic phosphor tracer particles. *Optics express* **20** (20), 22118–22133.

Frattina, Valerio 2019 Development and application of simultaneous 2d flow velocity and gas temperature measurements using thermographic phosphors under engine-relevant conditions. PhD thesis, Université Paris-Saclay; Universität Duisburg-Essen.

Fric, TF & Roshko, A 1994 Vortical structure in the wake of a transverse jet. *Journal of Fluid Mechanics* **1994**, 1–47.

Gogineni, Sivaram, Pestian, David, Rivir, Richard & Goss, Larry 1996 Piv measurements of flat plate film cooling flows with high free stream turbulence. In *34th Aerospace Sciences Meeting and Exhibit*, p. 617.

Gritsch, M, Schulz, A & Wittig, S 1998 Adiabatic wall effectiveness measurements of film-cooling holes with expanded exits .

Han, Je-Chin, Dutta, Sandip & Ekkad, Srinath 2012 *Gas turbine heat transfer and cooling technology*. CRC press.

Harrison, Katharine L & Bogard, David G 2008 Comparison of rans turbulence models for prediction of film cooling performance **43147**, 1187–1196.

Hasegawa, Ryo, Sakata, Ichiro, Yanagihara, Hiromichi, Aldén, Marcus & Johansson, Bengt 2008 Quantitative analysis of the relation between flame structure and turbulence in hcci combustion by two-dimensional temperature measurement. *Tech. Rep.*. SAE Technical Paper.

Hasegawa, R, Sakata, I, Yanagihara, H, Johansson, Bengt, Omrane, Alaa & Aldén, Marcus 2007 Two-dimensional gas-phase temperature measurements using phosphor thermometry. *Applied Physics B* **88** (2), 291–296.

Hasselbrink, Ernest F & Mungal, MG 2001 Transverse jets and jet flames. part 1. scaling laws for strong transverse jets. *Journal of Fluid Mechanics* **443**, 1–25.

Haven, Brenda A & Kurosaka, Mitsuru 1997 Kidney and anti-kidney vortices in crossflow jets. *Journal of Fluid Mechanics* **352**, 27–64.

Heidmann, James D & Ekkad, Srinath 2008 A novel antivortex turbine film-cooling hole concept. *Journal of turbomachinery* **130** (3).

Hertle, Ellen, Will, Stefan & Zigan, Lars 2017 Characterization of yag: Dy, er for thermographic particle image velocimetry in a calibration cell. *Measurement Science and Technology* **28** (2), 025013.

Javadi, A, Javadi, K, Taeibi-Rahni, M & Darbandi, M 2003 A new approach to improve film cooling effectiveness using combined jets. *Momentum* **2** (2).

Jenkins, Tom, Wu, Frank & Turner, Kevin 2008 On the development of flow thermometry imaging for high temperatures using thermographic phosphors. In *50th AIAA Aerospace Sciences Meeting including the New Horizons Forum and Aerospace Exposition*, p. 405.

Jordan, Jonathan & Rothamer, David A 2013 Pr: Yag temperature imaging in gas-phase flows. *Applied Physics B* **110** (3), 285–291.

Jovicic, Gordana, Zigan, Lars, Will, Stefan & Leipertz, Alfred 2014 Phosphor thermometry in turbulent hot gas flows applying dy: Yag and dy: Er: Yag particles. *Measurement Science and Technology* **26** (1), 015204.

Kalghatgi, Prasad & Acharya, Sumanta 2015 Improved film cooling effectiveness with a round film cooling hole embedded in a contoured crater. *Journal of Turbomachinery* **137** (10), 101006.

Kali, EH, Brun, C & Métais, O 2010 Large eddy simulation of a rectangular turbulent jet in crossflow. In *Direct and Large-Eddy Simulation VII*, pp. 89–93. Springer.

Kamotani, Yasuhiro & Greber, Isaac 1972 Experiments on a turbulent jet in a cross flow. *AIAA journal* **10** (11), 1425–1429.

Karagozian, AR 1986 An analytical model for the vorticity associated with a transverse jet. *AIAA journal* **24** (3), 429–436.

Keffer, JF & Baines, WD 1963 The round turbulent jet in a cross-wind. *Journal of Fluid Mechanics* **15** (4), 481–496.

Kelso, Richard Malcolm, Lim, TT & Perry, AE 1996*a* An experimental study of round jets in cross-flow. *Journal of fluid mechanics* **306**, 111–144.

Kelso, R. M., Lim, T. T. & Perry, A. E. 1996*b* An experimental study of round jets in cross-flow. *Journal of Fluid Mechanics* **306**, 111–144.

Kim, Dong, Yi, Seung Jae, Kim, Hyun Dong & Kim, Kyung Chun 2017 Simultaneous measurement of temperature and velocity fields using thermographic phosphor tracer particles. *Journal of Visualization* **20** (2), 305–319.

Knappe, Christoph, Algotsson, Martin, Andersson, Peter, Richter, Mattias, Tunér, Martin, Johansson, Bengt & Aldén, Marcus 2013 Thickness dependent variations in surface phosphor thermometry during transient combustion in an hcci engine. *Combustion and flame* **160** (8), 1466–1475.

Lawrence, Martin, Zhao, Hua & Ganippa, Lionel 2013 Gas phase thermometry of hot turbulent jets using laser induced phosphorescence. *Optics express* **21** (10), 12260–12281.

Lee, David S, Fahey, DW, Skowron, Agniezka, Allen, MR, Burkhardt, Ulrike, Chen, Q, Doherty, SJ, Freeman, S, Forster, PM, Fuglestvedt, J *et al.* 2021 The contribution of global aviation to anthropogenic climate forcing for 2000 to 2018. *Atmospheric Environment* **244**, 117834.

Lee, Hyunchang, Böhm, Benjamin, Sadiki, Amsini & Dreizler, Andreas 2016 Turbulent heat flux measurement in a non-reacting round jet, using bam: Eu 2+ phosphor thermography and particle image velocimetry. *Applied Physics B* **122** (7), 209.

Lenzi, T, Palanti, L, Picchi, A, Bacci, T, Mazzei, L, Andreini, A, Facchini, B & Vitale, I 2019 Time-resolved flow field analysis of effusion cooling system with representative swirling main flow. In *ASME Turbo Expo 2019: Turbomachinery Technical Conference and Exposition*. American Society of Mechanical Engineers Digital Collection.

Lim, TT, New, TH & Luo, SC 2001 On the development of large-scale structures of a jet normal to a cross flow. *Physics of fluids* **13** (3), 770–775.

Lindén, Johannes, Takada, N, Johansson, Bengt, Richter, Mattias & Aldén, Marcus 2009 Investigation of potential laser-induced heating effects when using thermographic phosphors for gas-phase thermometry. *Applied Physics B* **96** (2-3), 237–240.

Mahesh, Krishnan 2013 The interaction of jets with crossflow. *Annual review of fluid mechanics* **45**, 379–407.

Mayhew, James E, Baughn, James W & Byerley, Aaron R 2003 The effect of freestream turbulence on film cooling adiabatic effectiveness. *International Journal of Heat and Fluid Flow* **24** (5), 669–679.

Milani, Pedro M, Ching, David S, Banko, Andrew J & Eaton, John K 2020 Shear layer of inclined jets in crossflow studied with spectral proper orthogonal decomposition and spectral transfer entropy. *International Journal of Heat and Mass Transfer* **147**, 118972.

Muppidi, Suman 2006 Direct numerical simulations and modeling of jets in crossflow. *Ph. D. Thesis* .

Neal, Nicholas James, Jordan, Jonny & Rothamer, David 2013 Simultaneous measurements of in-cylinder temperature and velocity distribution in a small-bore diesel engine using thermographic phosphors. *SAE International Journal of Engines* **6** (1), 300–318.

New, TH, Lim, TT & Luo, SC 2006 Effects of jet velocity profiles on a round jet in cross-flow. *Experiments in Fluids* **40** (6), 859–875.

Nicoud, Franck & Ducros, Frédéric 1999 Subgrid-scale stress modelling based on the square of the velocity gradient tensor. *Flow, turbulence and Combustion* **62** (3), 183–200.

Ojo, Anthony O, Fond, Benoit, Abram, Christopher, Van Wachem, Berend GM, Heyes, Andrew L & Beyrau, Frank 2017 Thermographic laser doppler velocimetry using the phase-shifted luminescence of bam: Eu 2+ phosphor particles for thermometry. *Optics Express* **25** (10), 11833–11843.

Ojo, Anthony O, Fond, Benoit, Van Wachem, Berend GM, Heyes, Andrew L & Beyrau, Frank 2015 Thermographic laser doppler velocimetry. *Optics letters* **40** (20), 4759–4762.

Omrane, Alaa, Juhlin, Greger, Ossler, Frederik & Aldén, Marcus 2004*a* Temperature measurements of single droplets by use of laser-induced phosphorescence. *Applied optics* **43** (17), 3523–3529.

Omrane, Alaa, Petersson, Per, Aldén, Marcus & Linne, MA 2008 Simultaneous 2d flow velocity and gas temperature measurements using thermographic phosphors. *Applied Physics B* **92** (1), 99–102.

Omrane, Alaa, Santesson, Sabina, Aldén, Marcus & Nilsson, Staffan 2004*b* Laser techniques in acoustically levitated micro droplets. *Lab on a Chip* **4** (4), 287–291.

Omrane, Alaa, Särner, Gustaf & Aldén, Marcus 2004*c* 2d-temperature imaging of single droplets and sprays using thermographic phosphors. *Applied Physics B* **79** (4), 431–434.

Oseen, CW 1927 Hydromechanik. *Leipzig: Akademische* .

Park, Sehjin, Chung, Heeyoon, Choi, Seok Min, Kim, Seon Ho & Cho, Hyung Hee 2017 Design of sister hole arrangements to reduce kidney vortex for film cooling enhancement. *Journal of Mechanical Science and Technology* **31** (8), 3981–3992.

Park, Soon Sang, Park, Jung Shin, Lee, Sang Hoon, Moon, Young Gi & Kwak, Jae Su 2014 Effect of anti-vortex hole angle on the flat plate film cooling effectiveness. *The KSFM Journal of Fluid Machinery* **17** (5), 5–10.

Perry, AE 1982 Hot-wire anemometry," oxford university press, new york .

Pratte, Bruce D & Baines, W Douglas 1967 Profiles of the round turbulent jet in a cross flow. *Journal of the Hydraulics Division* **93** (6), 53–64.

Raffel, Markus, Willert, Christian E, Scarano, Fulvio, Kähler, Christian J, Wereley, Steve T & Kompenhans, Jürgen 2018 *Particle image velocimetry: a practical guide*. Springer.

Ramesh, Sridharan, Ramirez, David Gomez, Ekkad, Srinath V & Alvin, Mary Anne 2016 Analysis of film cooling performance of advanced tripod hole geometries with and without manufacturing features. *International Journal of Heat and Mass Transfer* **94**, 9–19.

Roache, Patrick J 1998 *Verification and validation in computational science and engineering*, , vol. 895. Hermosa Albuquerque, NM.

Rothamer, DA & Jordan, J 2012 Planar imaging thermometry in gaseous flows using upconversion excitation of thermographic phosphors. *Applied Physics B* **106** (2), 435–444.

Ruiz, AM, Lacaze, G & Oefelein, JC 2015 Flow topologies and turbulence scales in a jet-in-cross-flow. *Physics of Fluids* **27** (4), 045101.

Särner, Gustaf, Richter, Mattias & Aldén, Marcus 2008 Two-dimensional thermometry using temperature-induced line shifts of zno: Zn and zno: Ga fluorescence. *Optics letters* **33** (12), 1327–1329.

Sau, Amalendu, Sheu, Tony WH, Hwang, Robert R & Yang, WC 2004 Three-dimensional simulation of square jets in cross-flow. *Physical review E* **69** (6), 066302.

Sau, R. & Mahesh, K. 2008 Dynamics and mixing of vortex rings in crossflow. *J. Fluid Mech.* **604**, 389–409.

Schmidt, Donald L & Bogard, David G 1996 Effects of free-stream turbulence and surface roughness on film cooling. In *Turbo Expo: Power for Land, Sea, and Air*, , vol. 78750, p. V004T09A049. American Society of Mechanical Engineers.

Schreivogel, Peter, Abram, Christopher, Fond, Benoit, Strausswald, Michael, Beyrau, Frank & Pfitzner, Michael 2016 Simultaneous khz-rate temperature and velocity field measurements in the flow emanating from angled and trenched film cooling holes. *International Journal of Heat and Mass Transfer* **103**, 390–400.

Shigeo Shionoya, William M. Yen, Hajime Yamamoto 2006 *Phosphor Handbook*, 2nd edn. CRC Press.

Silano, G, Sreenivasan, KR & Verzicco, Roberto 2010 Numerical simulations of rayleigh–bénard convection for prandtl numbers between 10- 1 and 104 and rayleigh numbers between 105 and 109. *Journal of fluid mechanics* **662**, 409–446.

Smith, Lance, Karim, Hasan, Etemad, Shahrokh, Pfefferle, William C *et al.* 2006 The gas turbine handbook .

Someya, Satoshi, Okura, Yasuhiro, Uchida, Mitsunori, Sato, Yoshihisa & Okamoto, Koji 2012 Combined velocity and temperature imaging of gas flow in an engine cylinder. *Optics Letters* **37** (23), 4964–4966.

Sultan, Qaiser 2011 Caractérisation expérimentale aérothermique d'un jet pulsé débouchant dans un écoulement transversal : Influence du nombre de Strouhal d'excitation sur le refroidissement de paroi par film. Theses, ISAE-ENSMA Ecole Nationale Supérieure de Mécanique et d'Aérotechique - Poitiers.

Sultan, Q, Lalizel, G, Fénot, M & Dorignac, E 2011 Experimental time-resolved study of the interaction between a pulsating injectant and a steady cross-flow: aerodynamics of film cooling. *Experiments in fluids* **51** (5), 1245–1259.

Sultan, Qaiser, Lalizel, Gildas, Fénot, Matthieu & Dorignac, Eva 2017 Influence of coolant jet pulsation on the convective film cooling of an adiabatic wall. *Journal of Heat Transfer* **139** (2).

Tabei, Masatoshi, Shionoya, Shigeo & Ohmatsu, Hideki 1975 Mechanism of the killer effect of iron-group ions on the green luminescence in zns: Cu, al phosphors. *Japanese Journal of Applied Physics* **14** (2), 240.

Takada, Noriyuki, Sakata, Ichiro, Yanagihara, Hiromichi, Lindén, Johannes, Richter, Mattias, Aldén, Marcus & Johansson, Bengt 2009 Two-dimensional temperature measurements in diesel piston bowl using phosphor thermometry. *Tech. Rep.*. SAE Technical Paper.

Tan, ZP, Lubarsky, E, Bibik, O, Shcherbik, D & Zinn, BT 2013 Fuel jet in cross-flow: Experimental study of fuel concentration and temperature distributions at elevated temperature of the crossing flow using planar laser-induced phosphorescence. In *ILASS Americas, 25th Annual Conference on Liquid Atomization and Spray Systems, Pittsburgh, USA*.

Tan, Zu Puayen, Lubarsky, Eugene, Bibik, Oleksandr, Shcherbik, Dmitriy & Zinn, Ben T 2014 Application of planar laser-induced phosphorescence to investigate jet-a injection into a cross-flow of hot air. In *Turbo Expo: Power for Land, Sea, and Air*, , vol. 45752, p. V006T06A005. American Society of Mechanical Engineers.

Valori, Valentina 2018 Rayleigh-bénard convection of a supercritical fluid: Piv and heat transfer study .

Van Lipzig, JPJ, Yu, M, Dam, NJ, Luijten, CCM & de Goey, LPH 2013 Gas-phase thermometry in a high-pressure cell using bamgal 10 o 17: Eu as a thermographic phosphor. *Applied Physics B* **111** (3), 469–481.

Virginia 2018 Evolution of gas turbine blade temperature (turbine inlet temperature (tet). wadley research group, university of virginia. (https://www2.virginia.edu/ms/research/wadley/high-temp.html).

Witkowski, Dustin, Rothamer, David A, Lynch, Amy & Belovich, Vince 2013 Measurements of the temperature and velocity fields in a free shear flow between a vitiated stream and clean air stream using a pr: Yag thermographic phosphor. *Measurements* .

Wu, Hong, Cheng, Huichuan, Li, Yulong, Rong, Chengjun & Ding, Shuiting 2016 Effects of side hole position and blowing ratio on sister hole film cooling performance in a flat plate. *Applied Thermal Engineering* **93**, 718–730.

Yang, Peizhi, Deng, Peizhen & Yin, Zhiwen 2002 Concentration quenching in yb: Yag. *Journal of luminescence* **97** (1), 51–54.

Yin, Zhiyao, Fond, Benoit, Eckel, Georg, Abram, Christopher, Meier, Wolfgang, Boxx, Isaac & Beyrau, Frank 2017 Investigation of bam: Eu2+ particles as a tracer for temperature imaging in flames. *Combustion and Flame* **184**, 249–251.

Yokomori, Takeshi, Nagai, Haruko, Shiratori, Hiroshi, Shino, Naoki, Fujisawa, Naoki & Hirasawa, Taro 2015 Simultaneous measurements of phosphor thermometry and piv for high-temperature gas flows. *Tech. Rep.*. SAE Technical Paper.

Yuan, Lester L, Street, Robert L & Ferziger, Joel H 1999 Large-eddy simulations of a round jet in crossflow. *Journal of Fluid Mechanics* **379**, 71–104.

Yuen, CHN & Martinez-Botas, RF 2003 Film cooling characteristics of a single round hole at various streamwise angles in a crossflow: Part i effectiveness. *International Journal of Heat and Mass Transfer* **46** (2), 221–235.

Zentgraf, Florian, Stephan, Michael, Berrocal, Edouard, Albert, Barbara, Böhm, Benjamin & Dreizler, Andreas 2017 Application of structured illumination to gas phase thermometry using thermographic phosphor particles: a study for averaged imaging. *Experiments in Fluids* **58** (7), 82.

Synthèse

Introduction

Ce chapitre présente les objectifs et le contenu de cette thèse. Les moteurs à turbine à gaz sont les systèmes de propulsion les plus couramment utilisés dans les avions commerciaux et militaires modernes. Grâce à diverses avancées technologiques, des augmentations drastiques des rendements de cycle ont été rendues possibles depuis l'avènement du turboréacteur. Cette thèse porte sur l'amélioration d'une technique de refroidissement externe des aubes de turbine appelée film de refroidissement afin d'améliorer le rendement global du moteur.
Le refroidissement par film a pour but de fournir une couche d'air de refroidissement, extrait de l'étage du compresseur, sur la surface de l'aube de turbine afin de limiter le contact de la paroi de l'aube de turbine avec les gaz chauds du flux principal. Une configuration de trou de refroidissement de film non conventionnelle récente appelée configuration de trou auxiliaire est présentée. Le chapitre d'introduction présente brièvement le contenu de chaque chapitre. Une première étude RANS est menée à l'aide d'OpenFOAM 7 pour analyser le fonctionnement de la configuration du trou auxiliaire et pour comparer ses caractéristiques aéro et thermiques par rapport à un seul trou. Pour mieux comprendre la physique de l'interaction des structures cohérentes, une technique de thermométrie récente appelée thermométrie au phosphore ('Phosphor thermometry') est développée pour la première fois à l'Institut P'. Cette technique peut fournir un champ de température 2D dans un écoulement. Le développement métrologique original de cette thèse est de n'utiliser qu'une seule caméra associée à l'écriture d'un code de post-traitement des images brutes et à la mise au point d'un processus d'étalonnage robuste bien défini. La thermométrie au phosphore à l'oxyde de zinc est développée sur une cellule de test où les particules de ZnO sont en suspension dans l'eau. La méthode de thermométrie validée est ensuite réutilisée pour étudier la technique de refroidissement par film où l'écoulement dont on veut mesurer la température est alors de l'air. Des expériences de refroidissement de film sont menées dans un tout nouveau banc d'essai appelé BATH (Banc Aéro-THermique) à l'Institut P'.
Des simulations LES sont réalisées pour comprendre le champ d'écoulement instantané dans le problème de refroidissement par film et également pour visualiser le champ volumique de l'agencement de refroidissement par film. Une description de l'écoulement pour la configuration du trou auxiliaire est proposée et comparée aux expériences relatives à un trou unique. La figure 7.2 fournit une synthèse des tâches réalisées dans le cadre de cette thèse.

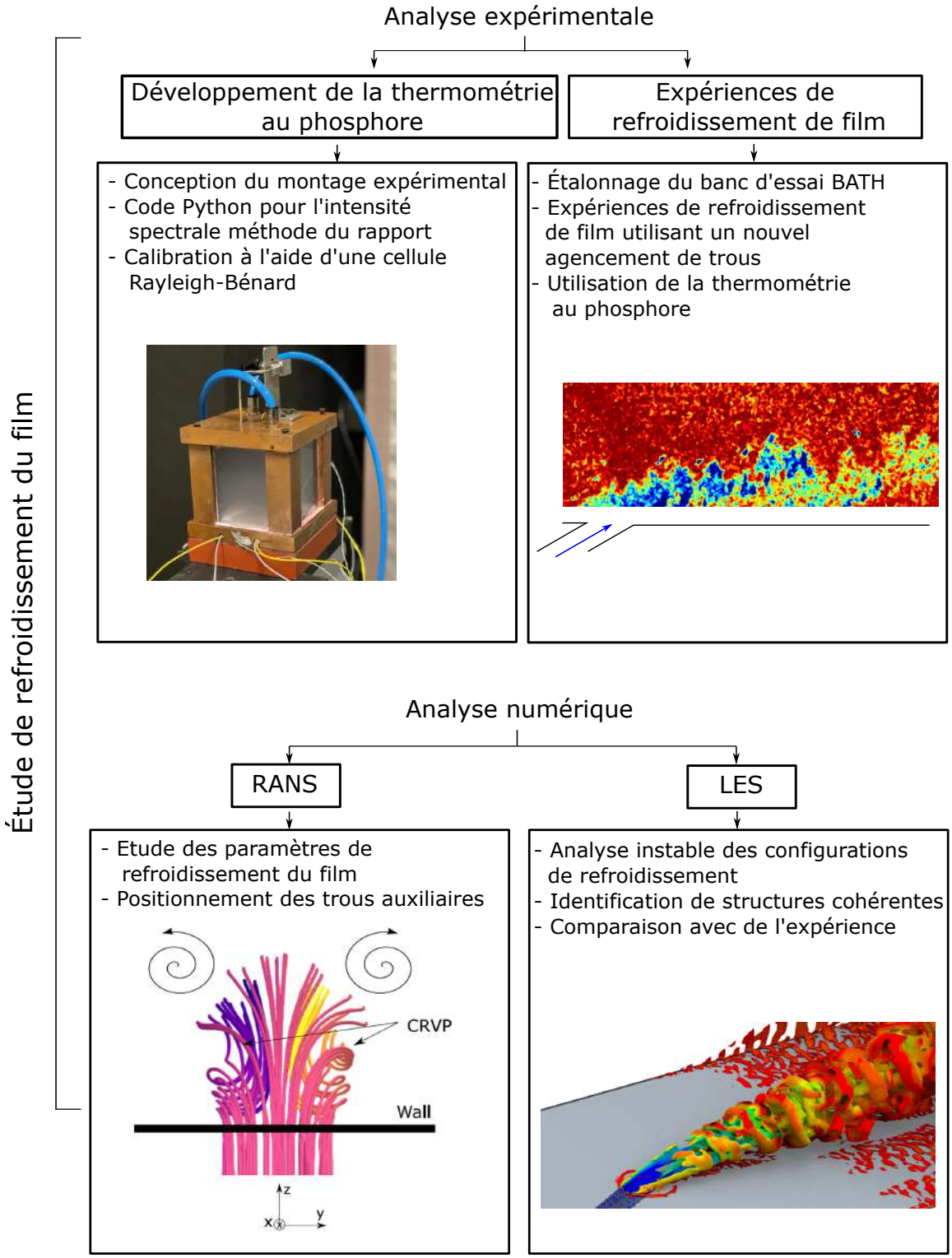

Figure 7.2: Aperçu des travaux réalisés dans cette thèse

Revue de la littérature du système Jet In Cross-Flow

Ce chapitre, présente le concept de Jet in Cross-Flow (JICF). Les différents paramètres de similarité impliqués dans la caractérisation d'une telle configuration sont discutés. Une courte revue bibliographique des différentes structures de vortex qui se forment en raison de l'interaction d'un jet injecté et du courant principal est fournie. Enfin, les différents facteurs affectant les performances de refroidissement du film et les méthodes pour améliorer l'efficacité du refroidissement du film trouvés dans la littérature sont discutés en mettant l'accent sur la configuration de refroidissement du film des trous auxiliaires.

Des paramètres importants tels que le rapport de soufflage M et l'efficacité de refroidissement du film adiabatique η sont introduits.

$$M = \frac{\rho_c U_c}{\rho_\infty U_\infty}$$

$$\eta = \frac{T_\infty - T_{aw}}{T_\infty - T_c}$$

L'interaction du flux principal avec le jet d'éjection crée quatre systèmes de vortex principaux, comme le montre la représentation classique d'un jet en flux croisé dans la figure 7.3 sont répertoriés ci-dessous.

- Vortex en fer à cheval
- Tourbillons de sillage ou tourbillons stationnaires
- Tourbillons de la couche de cisaillement
- Paire de tourbillons contra-rotatifs (Counter Rotating Vortex Pair, CRVP)

Parmi ceux-ci, le CRVP est identifié comme ayant l'effet le plus néfaste sur le processus de refroidissement du film. Il est donc nécessaire de réduire l'intensité et la hauteur du CRVP.

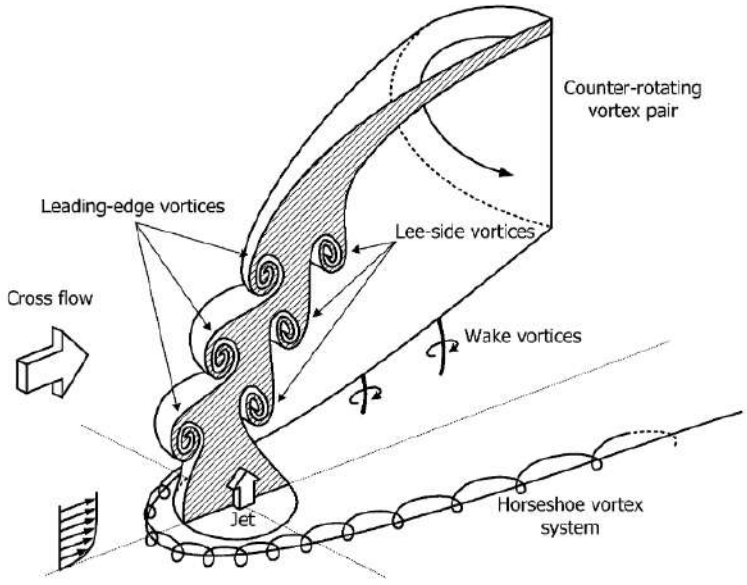

Figure 7.3: Représentation de JICF avec des systèmes de vortex New *et al.* (2006)

Optimisation de la position des trous auxiliaires : étude RANS

Dans ce chapitre, des simulations RANS sont effectuées d'une part pour optimiser la position spatiale des trous auxiliaires par rapport au trou principal, d'autre part pour tester les performances de deux configurations de trous auxiliaires. Une brève introduction est suivie d'une description de la géométrie et de la configuration numérique. Les résultats sur les caractéristiques aérodynamiques des différents systèmes sont discutés et leurs implications sur le comportement thermique sont mises en évidence. Il est nécessaire d'optimiser le nombre de cas géométriques étudiés expérimentalement car le coût de fabrication et de fonctionnement du banc d'essai peut être important. Ainsi, des simulations RANS moyennées dans le temps ont été réalisées afin d'avoir une première optimisation de la forme et de l'emplacement des trous. Trois configurations géométriques de trous (trou unique de base et deux configurations de trous auxiliaires) sont testées pour trois rapports de soufflage différents (M = 0,65, 1, 1,25). Chaque taux de soufflage correspond à une configuration d'écoulement : écoulement attaché à la paroi, décollement et rattachement de l'écoulement à la paroi et pénétration de l'écoulement injecté dans l'écoulement principal. Des études expérimentales sur un seul trou cylindrique ont été menées par Sultan *et al.* (2011). Les résultats expérimentaux des cas stables sont utilisés comme référence pour comparer et valider la procédure utilisée pour effectuer les simulations.

Grâce à cette étude RANS utilisant OpenFOAM 7, une analyse qualitative et quantitative de quelques paramètres moyennés dans le temps jugeant l'efficacité d'un système de refroidissement par film est effectuée :

- Efficacité de refroidissement par film adiabatique
- Évolution moyenne du tourbillon
- Coefficient de transfert de chaleur
- Réduction nette du flux de chaleur
- Visualisations de champ de vitesse, température

Les contours de température de paroi adiabatique ont montré des caractéristiques de refroidissement du film améliorées pour le cas du trou auxiliaire et validées par l'évolution de l'efficacité du refroidissement du film adiabatique le long de la ligne médiane et moyennée latéralement. Dans certaines régions, une amélioration d'environ 265% de l'efficacité du refroidissement du film adiabatique a été obtenue en utilisant la configuration de trou non conventionnelle. L'analyse aérodynamique a montré que l'intensité du tourbillon dans la configuration des trous auxiliaires était inférieure à celle du trou unique. L'analyse de la couche limite a également montré que l'écoulement injecté restait plus près de la paroi et avait des températures plus basses en proche paroi par rapport au cas à un seul trou. La figure 7.4 montre les lignes de courant du flux principal superposées au contour de température non-dimensionnel. Avec cette analyse RANS, on peut conclure sur la dimension et la position des modules de refroidissement par film à tester expérimentalement et avoir une idée globale des résultats à attendre. Par conséquent, cette configuration sera utilisée sur le banc d'essai BATH pour l'analyse expérimentale du refroidissement du film.

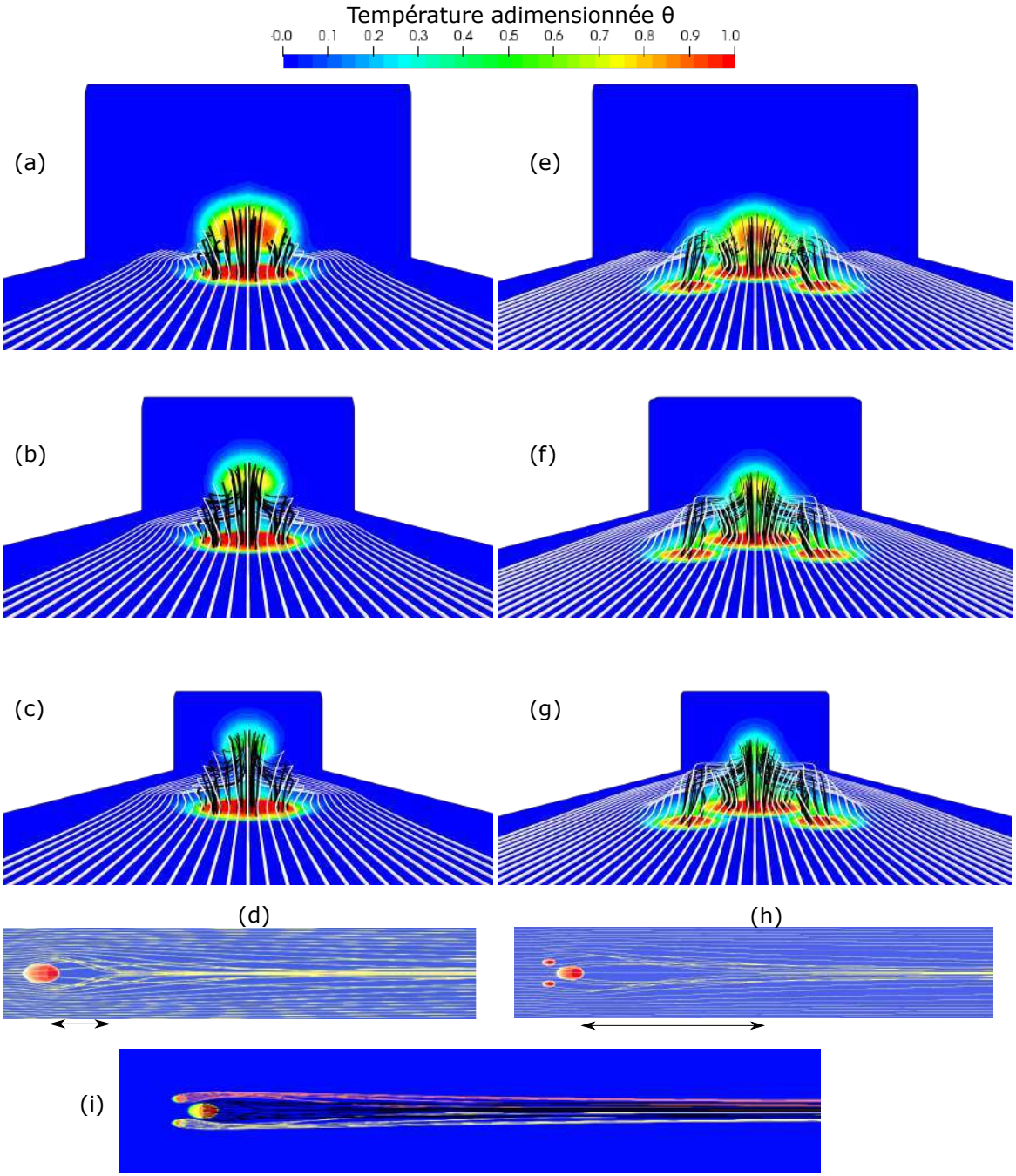

Figure 7.4: Visualisation des lignes de courant de l'écoulement principal et de l'écoulement injecté pour le cas du trou unique (a-d) et le cas des trous auxiliaires 2 (e-i) à différents plans :(a,e) X/D=1 ; (b, f) X/D=3 ; (c,g) X/D=5 avec les contours de température sur les plans. Les figures (g) et (h) montrent la vue de dessus des lignes de courant de l'écoulement principal près de la paroi, et (i) les lignes de courant du jet injecté dans la configuration des trous auxiliaires 2.

Nouvelle technique de thermométrie : thermométrie au phosphore

Ce chapitre se concentre sur la thermométrie du phosphore pour mesurer les champs d'écoulement de température instantanée. Les notions des principes de fonctionnement du phosphore sont introduites. Les propriétés du phosphore et les manières d'effectuer l'étalonnage de la température sont expliquées. Le contenu principal de ce chapitre est l'étude du phosphore d'oxyde de zinc pour ses propriétés, la discussion des différentes méthodes explorées pour mettre en œuvre l'étalonnage de la température et la description procédurale de la méthode du rapport d'intensité spectrale bicolore. La validation de cette méthode se fait à l'aide d'un cas test de convection naturelle de Rayleigh-Benard.

Les particules de luminophore absorbent le rayonnement incident I_0 et sont excitées vers des états d'énergie temporaires plus élevés. Elles reviennent aux états d'énergie inférieurs par émission de rayonnement, et pour effectuer la thermométrie du phosphore, les luminophores avec émission dans le spectre visible sont préférés.

Le nombre de photons émis lors de l'excitation par un laser dépend de divers facteurs telles que la température du fluide de travail T, la concentration locale χ de particules, l'intensité de la nappe laser I_0 travaillant à la longueur d'onde λ_0 et l'émission inhérente propriété du luminophore utilisé σ. L'intensité d'émission I est donnée par l'expression :

$$I(\lambda, x, y, z, T) \approx \underbrace{I_0(\lambda_0, x, y, z)}_{(1)} \underbrace{\sigma(\lambda_0, T)}_{(2)} \underbrace{exp(\chi(x, y, z)d)}_{(3)} \underbrace{\chi(x, y, z)}_{(4)}$$

Dans l'équation ci-dessus, l'intensité d'émission dépend donc de (1) la longueur d'onde et l'intensité du laser, (2) les caractéristiques du phosphore, (3) l'absorption locale due à l'effet Beer-Lambert et (4) la concentration locale de particules de phosphore. En plus de ces paramètres, des facteurs telles que l'efficacité du détecteur, la transitivité de l'optique et la direction dans laquelle le rayonnement est émis lors de l'excitation jouent également un rôle sur l'intensité d'émission détectée.

Pour effectuer une thermométrie de phosphore 2D, il existe plusieurs types de phosphore. La table 7.1 en donne quelques uns ainsi que leurs propriétés, notamment leur plage de température. Pour notre étude dont les températures peuvent aller jusqu'à 500 K, nous retenons l'oxyde de zinc qui permet des mesures de température entre 300 et 500K. Une analyse de ses propriétés d'émission est effectuée pour étudier l'influence de la variation de concentration, d'intensité laser et de température.

Table 7.1: Phosphor types et applications

No	Phosphor	τ	Laser excitation (nm)	Spectral emission (nm)	Temperature (K)	Strategy
1	$Mg_4FGeO_6 : Mn^{4+}$	3ms	266,355,385	632-657	700-1050	IR,LT
2	$La_2O_2S : EU^{3+}$	12 μs	355,337	512	300-600	LT,IR
3	$Y_3Al_5O_{12} : Dy^{3+}$	1ms	355	458/497	400-1700	LT,IR
4	$Y_2O_3 : EU^{3+}$	1ms	266,355,532	512,538,624	300-900	LT
5	BAM: EU^{2+}	1 μs	355,375,266,376	460	300-900	LT,IR
6	**ZnO: Zn**	<1ns	355,266	389,510	300-500	IR
7	$Y_2O_2S : Er^{3+}, Yb^{3+}$	50 μs	980	500-540/540-575	300-600	LT,IR
8	YAG: Pr^{3+}	190 μs	266	484/610	300-750	IR
9	ZnO:Ga	<1ns	355	386	300-600	IR
10	$YVO_4 : EU^{3+}$	300 μs	355	535-592/618-620	650-930	IR,LT

La figure 7.5 montre qu'il existe deux manières d'utiliser la phosphorescence pour mesurer un champ de température, soit par l'évolution temporelle de la phosphorescence, soit par l'évolution spectrale. Ces deux techniques sont détaillées pour le luminophore ZnO. Une méthodologie d'étalonnage fiable soit pour la méthode temporelle soit pour la méthode spectrale est donc développée et utilisable pour toute application de thermométrie au phosphore. Par souci de simplicité, ce processus d'étalonnage est mis au point sur une petite cavité remplie d'eau dont il est facile de maitriser et de mesurer la température.

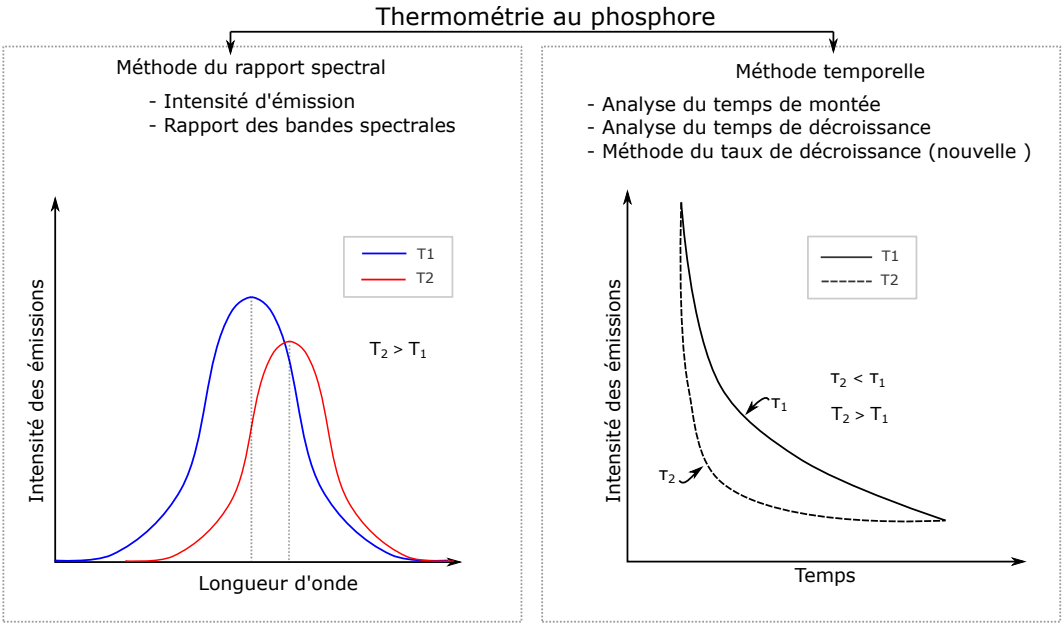

Figure 7.5: Méthodes pour effectuer la thermométrie au phosphore

La méthode temporelle exploite la dépendance de la température au temps de décroissance de l'émission du ZnO. Au cours de cette thèse, il est proposé une autre technique d'exploitation de cette dépendance de la température au temps de croissance et décroissance de l'émission du phosphore. L'idée est de corréler le rapport croissance/décroissance de l'émission du ZnO et la température. L'avantage essentiel de cette méthode est que seulement deux caméras sont nécessaires et non plusieurs comme dans le cas où seule la décroissance de l'émission est considérée. La méthode du rapport d'intensité spectrale est basée sur l'exploitation de la dépendance à la température du spectre d'émission. A cette fin, un dispositif Optosplit II est utilisé pour diviser le rayonnement émis en deux chemins qui traversent deux filtres passe-bande différents et produisent deux images sur la même caméra. Une procédure d'étalonnage détaillée est décrite pour cette méthode et validée à l'aide d'un cas de test de convection naturelle. Un exemple d'application de la procédure d'étalonnage est illustré dans la figure 7.6.

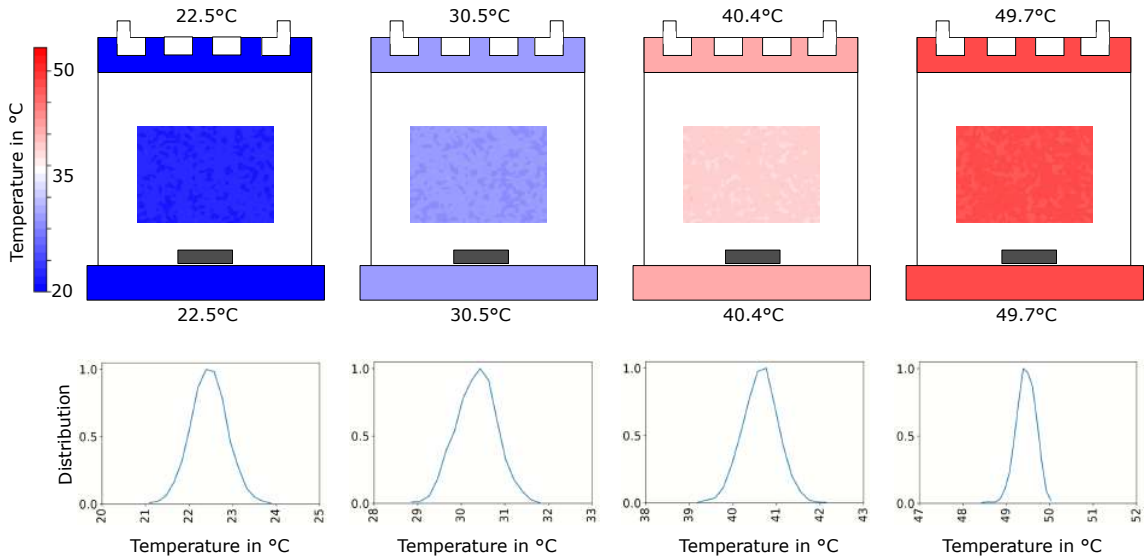

Figure 7.6: Validation du processus d'étalonnage en testant le processus dans des cas à température constante à différentes températures. Une distribution de fréquence de la température pour l'ensemble de la zone d'étalonnage est indiquée sous chaque cas.

L'ensemble du processus avec le code d'étalonnage validé pour effectuer la thermométrie du phosphore peut être utilisé pour étudier expérimentalement le refroidissement du film.

Analyse des configurations de refroidissement par film à l'aide de méthodes expérimentales

Ce chapitre traite de l'analyse expérimentale du refroidissement par film. La configuration du trou auxiliaire et la configuration du trou cylindrique unique sont testées sur le banc d'essai BATH (figure 7.7). La description du banc d'essai innovant BATH est fournie. Le banc d'essai étant utilisé pour la première fois, la caractérisation de l'écoulement dans la section d'essai est effectuée pour étudier les profils de vitesse et de température. Finalement, les configurations de refroidissement par film sont testées à l'aide de la thermométrie au phosphore du rapport d'intensité spectrale comme décrit au chapitre 4 pour visualiser les champs de température.

Figure 7.7: Illustration des modules de refroidissement par film utilisés dans cette thèse et leur forme de trou correspondante de la vue de dessus est montrée en dessous de chaque module avec leurs paramètres géométriques.

Le banc d'essai BATH est une soufflerie à circuit ouvert qui vise à reproduire les conditions de débit et de température rencontrées dans les moteurs aéronautiques au sein de la veine d'essai. Le banc utilise une combustion contrôlée air-kérosène pour recréer ces conditions. Le banc d'essai BATH étant utilisé pour la première fois, un étalonnage approfondi est effectué. Le débit massique peut varier entre 100g/s et 1500g/s, la température peut varier de 20°C 'a 250°C en utilisant le réchauffeur électrique seul et jusqu'à 1200°C avec la combustion allumée. Ces mesures montrent que les niveaux de turbulence sont inférieurs à 10%. Pour les expériences de refroidissement par film, un rapport de soufflage M=3 est étudié. Pour cette valeur de taux de soufflage, la hauteur de pénétration du jet dans l'écoulement principal est importante. Ainsi la visualisation du champ de température tout au long de la trajectoire du jet est rendue plus aisée. De plus, les structures cohérentes sont amplifiées et contribuent à une meilleure identification et quantification. La table 7.2 récapitule toutes les conditions aux limites des expériences effectuées. Les champs de température à différents plans dans la direction latérale montrent des structures d'écoulement très détaillées. Il est possible d'identifier les structures tourbillonnaires responsables du mélange comme dans la figure 7.8.

Table 7.2: Conditions limites

Paramètre	Cross-flow	Jet
Débit massique	310g/s	4.45g/s
Température	150°C	20°C
Densité	0.83kg/m^3	1.32kg/m^3
Pression	1.2Bar	1.2Bar
Vitesse (théorique)	12.8m/s	27.5m/s
Taux de soufflage 'M'	3	
Rapport de densité	1.45	

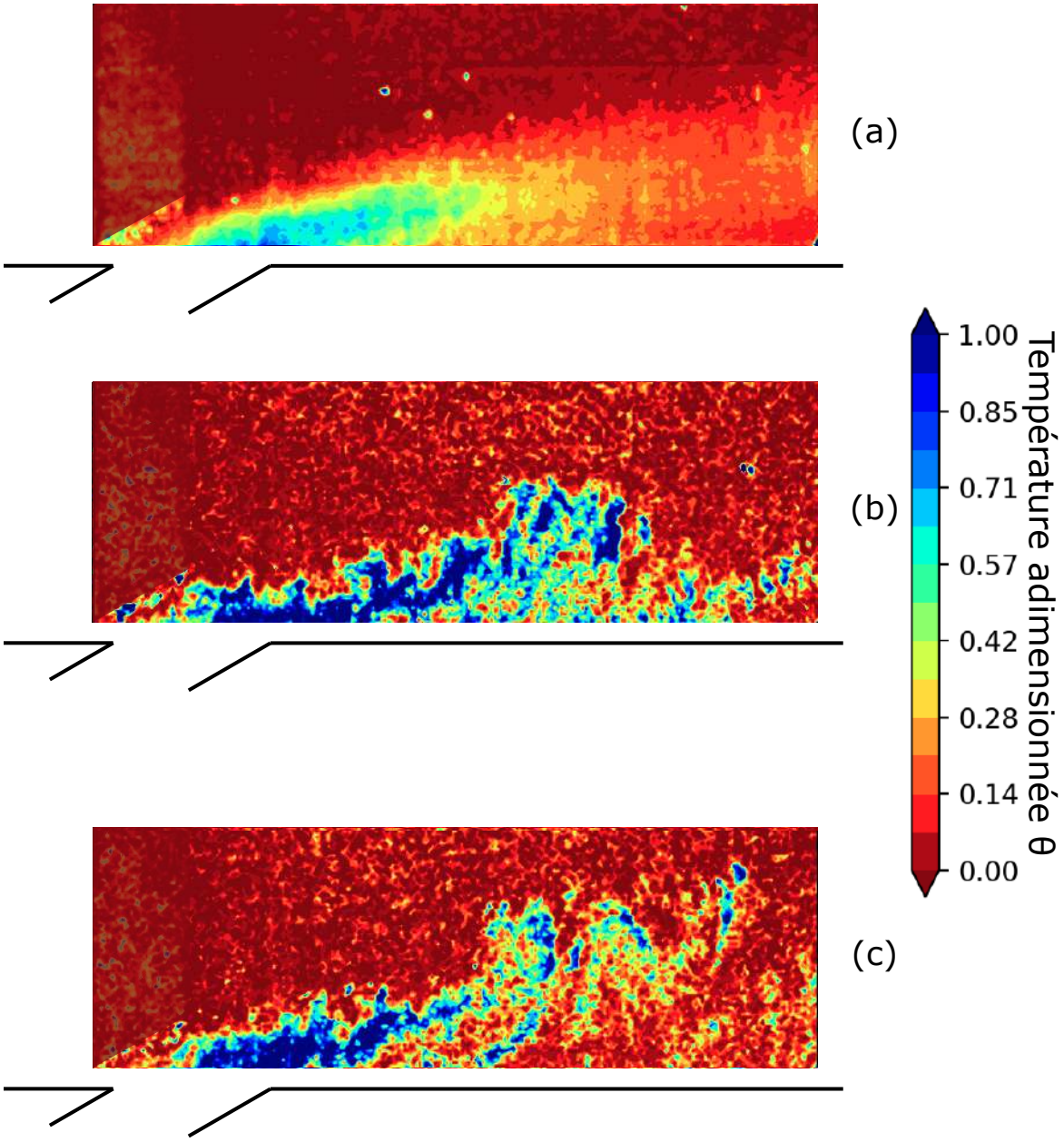

Figure 7.8: Thermométrie au phosphore: contours de température non dimensionnels pour M=3 pour le cas d'un seul trou à Y/D=0,4. (a) Champ d'écoulement moyen. (b,c) Les champs température instantanés

Simulations résolues en temps par LES et analyse physique des écoulements

L'utilisation des simulations LES facilite l'analyse instationnaire du problème de refroidissement du film. En fait, comme la majeure partie de l'énergie de l'écoulement est contenue dans les grands tourbillons, la résolution de ces grands tourbillons et la modélisation des petits tourbillons isotropes est le meilleur compromis entre un écoulement hautement résolu et une utilisation acceptable des ressources de calcul. Divers paramètres (les mêmes que ceux présentés au chapitre 3) telles que la température adimensionnelle θ, l'efficacité de la paroi adiabatique, les caractéristiques du vortex, le critère Q et les champs de vitesse sont analysés. Les simulations sont conduites au rapport de soufflage M=3. Le choix du rapport de soufflage, comme dit précédemment, a été fait en raison d'une visualisation plus facile des structures cohérentes et parce que l'efficacité adiabatique du film est très faible pour les cas de trous simples à cause de la pénétration du jet (figure 7.9).

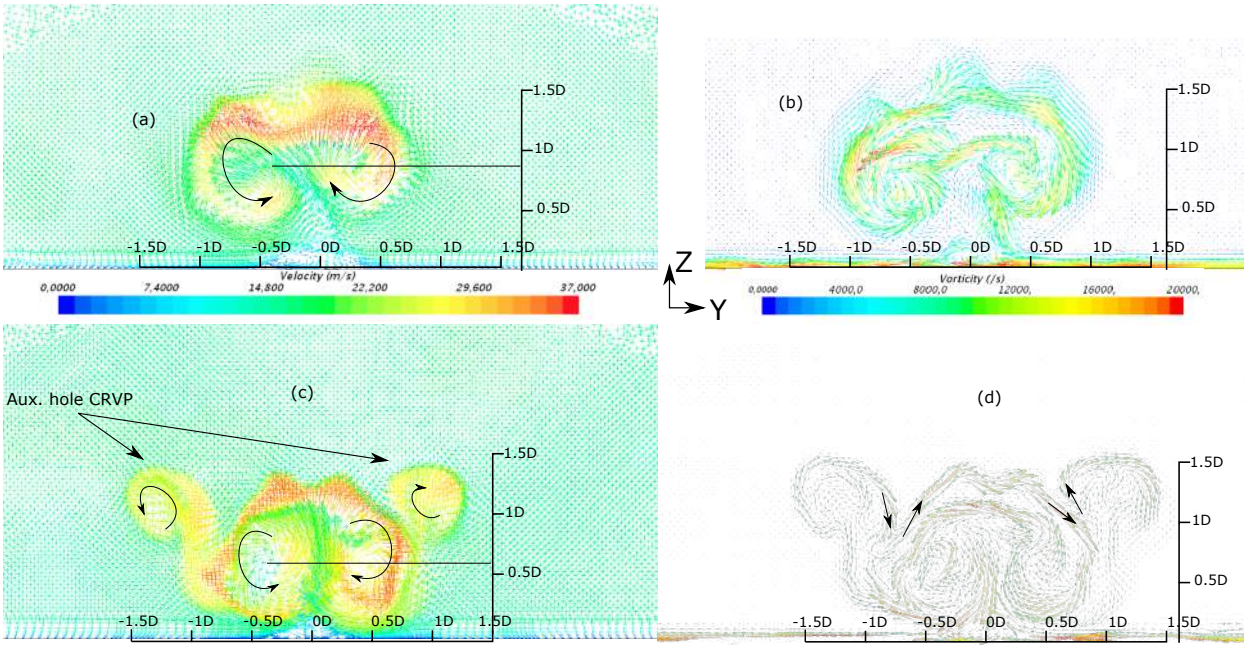

Figure 7.9: Contours de vitesse instantanée (a, c) et de vorticité (b, d) pour la configuration à trou unique et trou auxiliaire au plan X/D=3. Les figures (a) et (b) représentent le cas d'un seul trou, tandis que (c) et (d) représentent la configuration du trou auxiliaire.

Les résultats des simulations aux grandes échelles sont présentés pour compléter les informations obtenues au chapitre 5 par le biais d'expériences. Les comparaisons entre les expériences et les simulations montrent une très bonne cohérence tant sur les contours de température que sur les structures turbulentes (figure 7.10). Cette concordance entre les expériences et les simulations nous ont permis d'effectuer des analyses plus approfondies grâces aux simulations LES et comprendre ainsi la topologie de l'écoulement dans la configuration du trou auxiliaire. Les principales conclusions des visualisations de vitesse et de vorticité montrent que le CRVP du système de trous auxiliaires a une intensité beaucoup plus réduite par rapport au cas à un seul trou et que la trajectoire de l'écoulement froid injecté reste en plus proche paroi par rapport au cas à un seul trou. A travers cette étude, on peut proposer les mécanismes de fonctionnement du système de trous auxiliaires. La présence des bras rotatifs positif et négatif du jet du trou auxiliaire et du jet du trou principal est la principale raison de la réduction de l'intensité du vortex de l'ensemble du système (Figure 7.11).

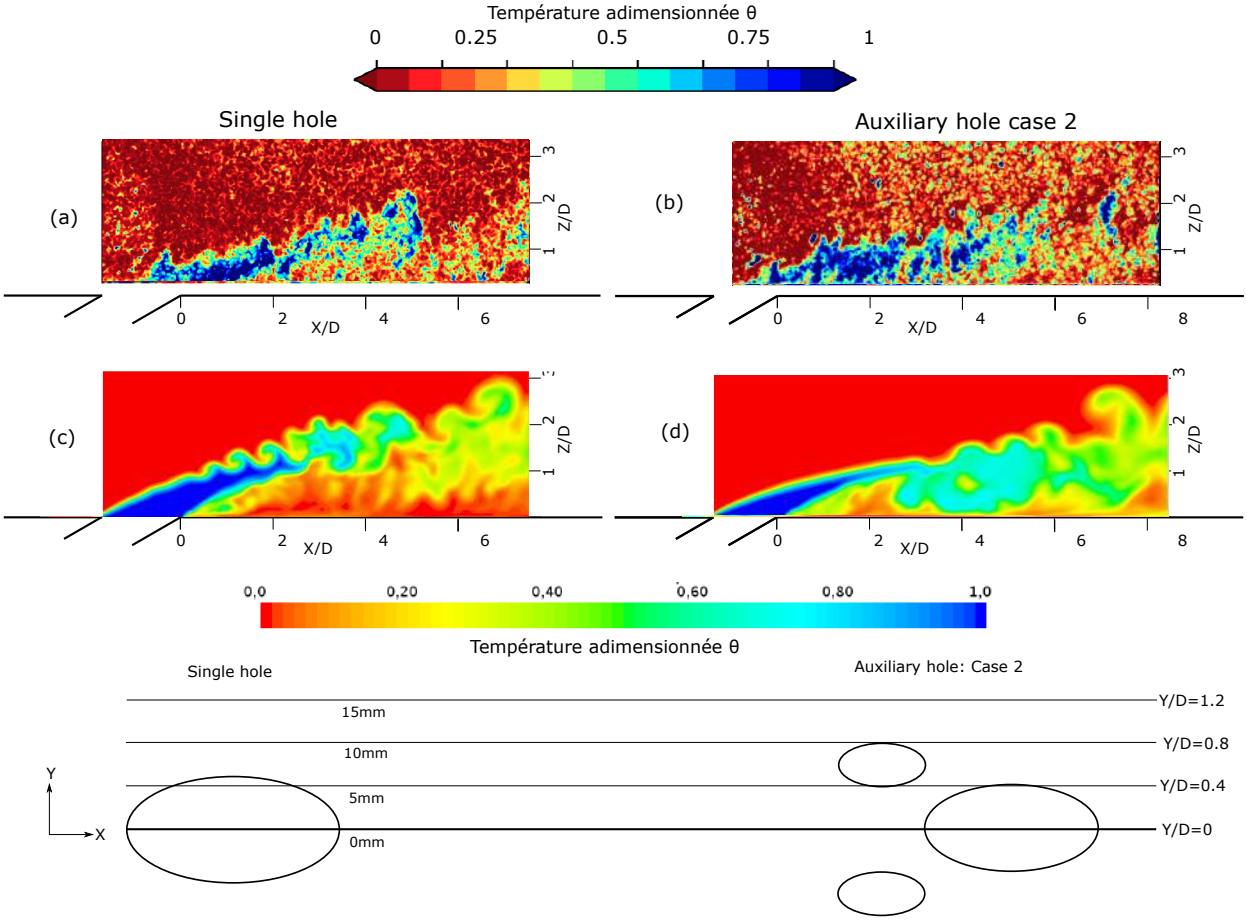

Figure 7.10: Contours de température 2D instantanés non dimensionnels dans le plan XZ à **Y/D=0** pour la configuration à un seul trou (a et c) et la configuration à trou auxiliaire (b et d). Les figures (a) et (b) sont obtenues expérimentalement à l'aide de la thermométrie au phosphore et (c) et (d) sont obtenues par des simulations LES.

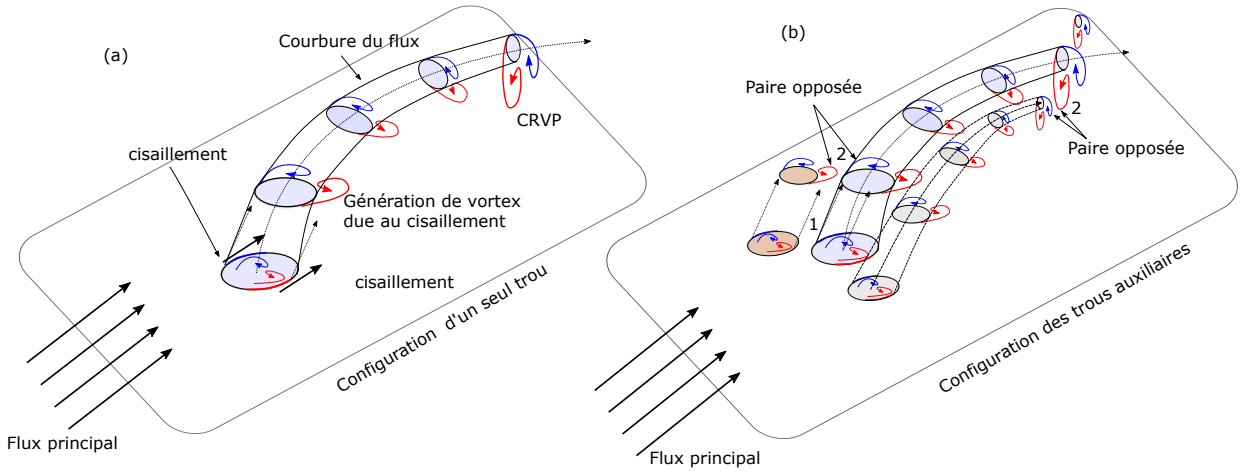

Figure 7.11: Illustration du mécanisme dans les configurations à trou unique et à trou auxiliaire.

Conclusions et perspectives

Le refroidissement par film des aubes de turbine à gaz est une nécessité absolue pour maintenir les températures des aubes de turbine à des niveaux acceptables. Cependant, l'utilisation de l'air relativement plus froid de l'étage du compresseur pour le processus de refroidissement par film est préjudiciable à l'efficacité globale du moteur car il y a moins de quantité d'air disponible pour le processus de combustion. Les caractéristiques aérodynamiques du jet sortant du trou de refroidissement du film ont une immense implication sur les performances de refroidissement du film thermique. Par conséquent, cette thèse s'est concentrée sur les méthodes d'optimisation du refroidissement par film pour améliorer l'utilisation de cet air de prélèvement limité obtenu en étudiant un nouvel agencement récent de refroidissement par film appelé configuration de refroidissement par film auxiliaire où un seul trou principal est soutenu par deux trous adjacents plus petits autour du trou principal.

La configuration de refroidissement par film de trous auxiliaires est une technique prometteuse pour améliorer les performances des moteurs à turbine à gaz des avions, comme cela a été prouvé par des simulations numériques RANS et LES et une analyse expérimentale utilisant la thermométrie au phosphore qui a fourni des contours de température à haute résolution. La thermométrie du phosphore, qui en est actuellement à ses débuts, a un immense potentiel pour remplacer les systèmes PIV classiques afin d'obtenir des champs d'écoulement de vitesse et de température simultanés résolus dans le temps.

En ce qui concerne les simulations LES, différents régimes de rapport de soufflage (par exemple, $M = 0{,}5$, $M = 1$, $M = 1{,}5$) peuvent être testés pour déterminer si les caractéristiques d'écoulement sont différentes pour la configuration du trou auxiliaire. La thermométrie au phosphore pourrait être couplée à des mesures de vitesse simultanées via la PIV.

Abstracts

Contribution to aerothermal study of a film cooling geometric design using ZnO phosphorescence thermography and numerical simulations

Film cooling of aircraft gas turbine blades has been in use since a few decades now to improve the Turbine Inlet Temperature (TIT) and to extend the life time of the turbine blade. Additionally, stringent emission norms stipulate the improvement of overall efficiency of the gas turbine engine and hence the need to improve film cooling process. Film cooling is a technique where a cold jet is injected through discrete holes on the surface of the turbine blade, so as to form a layer of cool air over the surface of the blade, effectively protecting the blade from high temperature crossflows arising from the combustion chamber. This problem can be viewed as a Jet In Cross-Flow (JICF) phenomena where the the interaction of the crossflow with a jet injected perpendicular or at an angle creates a system of vortices. One of the most important vortex systems in this arrangement is the Counter Rotating Vortex Pair arising from the shear forces at the sides of the ejecting jet with the crossflow primarily. The bending of the jet along the direction of the crossflow promotes the CRVP to ingest hot cross-flow into the jet stream which reduces the effectiveness of the film cooling system. Hence, in this study, an auxiliary hole system is studied experimentally and numerically to reduce the intensity and the height of the CRVP which eventually helps in an augmented adiabatic film cooling effectiveness. The auxiliary holes placed upstream of the main film cooling hole reduces the intensity of the main hole CRVP due to the reduction in the shear forces experienced by the jet emanating from the main hole. In this thesis numerical analysis through RANS study using k-ω SST turbulence model to have a preliminary understanding of the auxiliary hole system and a detailed understanding of the flow structure using Large Eddy Simulation are performed. The highlight of this work is the development of single camera phosphor thermometry using the spectral intensity ratio method. This technique allows the measurement of the instantaneous and mean flow temperature non-intrusively. A detailed analysis of the emission properties of ZnO phosphor upon excitation by a 266nm laser is described. A calibration procedure for the intensity ratio method is defined and it is tested using a Rayleigh-Bénard natural convection process. This phosphor thermometry procedure with the validated code is implemented on the new BATH test Rig to study film cooling arrangements. Three different configurations are tested for their aero-thermal characteristics at penetration blowing ratio regime. Analysis of the experimental and numerical results help in identifying key vortex structures, leading to the better understanding of reasons for the augmentation of film cooling effectiveness in the auxiliary hole system compared to a classical simple cylindrical hole.

Keywords: Gas turbine engines, film cooling, heat transfer, zinc oxide phosphor thermometry, aero-thermal analysis, JICF, CRVP

Caractérisation aérothermique expérimentale des configurations de refroidissement du film à l'aide de la thermométrie au phosphore ZnO.

Le refroidissement par film des aubes de turbine à gaz d'avion est utilisé depuis quelques décennies pour améliorer la température d'entrée de la turbine (TIT) et prolonger la durée de vie de l'aube de turbine. De plus, des normes d'émission strictes stipulent l'amélioration de l'efficacité globale du moteur à turbine à gaz et donc la nécessité d'améliorer le processus de refroidissement par film. Le refroidissement par film est une technique où un jet froid est injecté à travers des trous discrets sur la surface de l'aube de turbine, de manière à former une couche d'air froid sur la surface de l'aube, protégeant efficacement l'aube des flux croisés à haute température résultant de la combustion. chambre. Ce problème peut être considéré comme un phénomène de 'Jet In Cross-Flow' (JICF) où l'interaction du flux croisé avec un jet injecté perpendiculairement ou avec un angle crée un système de vortex. L'un des systèmes de vortex les plus importants dans cet agencement est la paire de vortex contrarotatifs résultant des forces de cisaillement sur les côtés du jet d'éjection avec le flux croisé principalement. La courbure du jet le long de la direction de l'écoulement primaire encourage le CRVP à ingérer un écoulement croisé chaud dans le courant de jet, ce qui réduit l'efficacité du système de refroidissement par film. Par conséquent, dans cette étude, un système de trous auxiliaires est étudié expérimentalement et numériquement pour réduire l'intensité et la hauteur de la CRVP, ce qui contribue finalement à augmenter l'efficacité du refroidissement du film adiabatique. Les trous auxiliaires placés en amont du trou de refroidissement du film principal permettent de réduire l'intensité du trou principal CRVP du fait de la réduction des forces de cisaillement subies par le jet émanant du trou principal. Dans cette thèse, une analyse numérique via une étude RANS utilisant un modèle de turbulence k-ω SST pour avoir une compréhension préliminaire du système de trous auxiliaires et une compréhension détaillée de la structure de l'écoulement à l'aide de la simulation des grands tourbillons est effectuée. Le point culminant de ce travail est le développement de la thermométrie au phosphore à caméra unique en utilisant la méthode du rapport d'intensité spectrale. Cette technique permet la mesure de la température de départ instantanée et moyenne de manière non intrusive. Une analyse détaillée des propriétés d'émission du phosphore ZnO lors de l'excitation par un laser de 266 nm est décrite. Une procédure d'étalonnage pour la méthode du rapport d'intensité est définie et elle est testée à l'aide d'un procédé de convection naturelle Rayleigh-Bénard. Cette procédure de thermométrie au phosphore avec le code validé est implémentée sur le nouveau banc d'essai BATH pour étudier les dispositions de refroidissement du film. Trois configurations différentes sont testées pour leurs caractéristiques aérothermiques au régime de taux de soufflage de pénétration. L'analyse des résultats expérimentaux et numériques aide à identifier les structures de vortex clés, conduisant à une meilleure compréhension des raisons de l'augmentation de l'efficacité du refroidissement du film dans le système de trous auxiliaires par rapport à un trou cylindrique simple classique.

Mots clés : moteurs à turbine à gaz, refroidissement par film, transfert de chaleur, phosphore thermométrie à l'oxyde de zinc , analyse aérothermique, JICF, CRVP